



UiT The Arctic University of Norway

Dynamic Analysis of Herøysund Bridge using Finite Element Modelling and Operational Modal Analysis

Dr. Harpal Singh, Dr. Giuseppe Occhipinti and Daniele Storni

A Technical Report, December 2024





Technical Report

Dynamic Analysis of Herøysund Bridge using finite element modelling and operational modal analysis

VERSION

2

DATE

23-12-2024

AUTHORS

Dr. Harpal Singh, Daniele Storni and Dr. Giuseppe Occhipinti

CLIENTSNordland Fylke Kommune
Statens Vegvesen**PROJECT NAME**

Herøy FoU

PROJECT NUMBER

100397

SUMMARY

This report contains the summary of dynamic analysis of Herøysund Bridge using finite element modelling and field work results of operational modal analysis campaign. Detailed work and results of master thesis can be found in the attached documents. This report contains results that are confidential and will be published in the coming year. A permission from project owners that is Nordland Fylke Kommune, Statens Vegvesen and UiT The Arctic University of Norway is required for using and findings in this report.

PREPARED BY

Dr. Harpal Singh

SIGNATURE**CHECKED BY**

Dr. Giuseppe Occhipinti

EDITED BY

Daniele Storni

APPROVED BY

Jørn Eldby

REPORT NUMBER

2024:00001

CLASSIFICATION

Confidential

USE

Internal



*Our heartfelt gratitude is extended to **Per Ove Ravatsås** from Nordland Fylkes Kommune and **Dr. Roy Antonsen** from SINTEF Narvik (formerly Statens Vegvesen). Their unwavering dedication and tireless efforts have illuminated the path to securing vital funding for the Herøy FoU research project. Their contributions not only support our research endeavours but also inspire a collaborative spirit that will resonate through the corridors of innovation.*



About the Authors

Dr. Harpal Singh

Dr. Harpal Singh is associate professor at UiT - The Arctic University of Norway. He obtained his Ph.D. degree from UiT in engineering science and applied mathematics. His research focuses on the advancement of structural health monitoring within civil engineering, particularly concerning vital infrastructures such as bridges, high-rise buildings, heritage buildings and dams. His expertise lies in the application of vibrational analysis methodologies to determine the dynamic behaviour of the structures. Utilization of such techniques enables the monitoring of the civil engineering infrastructure in real-time. This can help to identify signatures of probable failures that can lead to structural collapse. Furthermore, Dr Singh demonstrates a profound interest in the development and implementation of artificial intelligence and machine learning based algorithms. These cutting-edge technologies can automate data processing and analysis that can enhance efficiency and accuracy in structural assessment. At present he is also a project manager at UiT Narvik for a project Herøy FoU that is funded by Nordland Fylke and Statens Vegvesen. He is also project manager for research project Health Monitoring of Concrete Bridges which is funded by Troms Fylke Kommune. Internationally, he collaborates with Sweden, Italy, Georgia, Kazakhstan and India for research co-operation. He has been invited as guest speaker in various conferences and universities.



Dr. Giuseppe Occhipinti

Dr. Giuseppe Occhipinti obtained his PhD in structural engineer at the University of Catania. He was visiting student at Computational Structural Mechanics group at Imperial College of London. He obtained the II level master's degree from Sapienza University of Rome in Diagnostic Analysis and Monitoring of Structures and Infrastructures with honours. He contributed to research at the National Research Council (IGAG-CNR), where he developed simplified continuous beam models for determining the structural operability of strategic buildings; at the University of Rome "Sapienza" for the finite element modelling and the seismic and vibrational isolation of the Sarcophagus of the Spouses (~520 BC) preserved at the ETRU museum; at the INGV Urban Seismic Observatory as a consultant for the aspects of structural engineering in the field of seismic monitoring of structures and infrastructures; at the University of Roma Tre for the development of software for the model updating of finite element models; with private companies for the dynamic modelling and identification of structures and infrastructures. With more than twenty years of experience his main topics are assessment and retrofitting of existing structures, nonlinear numerical modelling, model updating and SHM. He is the author of several scientific publications in international journals and conferences. He is II level certified experimentalist for non-destructive testing and dynamic testing.



Daniele Storni (UiT PhD student)

With over ten years of experience in developing and implementing learning algorithms, he has a background in Economics and Management with a specialization in financial markets. He completed a second level master's degree in Big Data Analytics and Machine Learning at Luiss University in Rome, where he specialized in Bayesian techniques and deep learning for advanced time series analysis. Currently, he is conducting research at the Department of Computer Science and Computational Engineering at UiT The Arctic University of Norway, focusing on dynamic structural analysis and the development of decision support systems for structural monitoring of bridges. He is committed to developing innovative solutions in the SHM sector, applying advanced data analysis techniques to enhance the safety, reliability, and resilience of infrastructures.



Acknowledgement

This technical report would not have been possible without the generous funding provided by Nordland County and Statens Vegvesen. We would like to express our sincere appreciation to the collaborative efforts of the researchers and administration from NTNU, Sintef Narvik, and UiT Narvik that contributed to the project, Herøy FoU.

A special thanks goes to Wise Robotics from Italy for their invaluable contribution to the field work, which was essential for the success of this project. We are also grateful to Heine André Rokås from Nordland Fylke and Nils Göran Åhlin from PEAB for their unwavering support during the project activities in the field.

We would like to acknowledge Per Ove Ravatsås from Nordland Fylke and Dr. Roy Antonsen from SINTEF Narvik (previously Statens Vegvesen) for their dedicated efforts their respective organizations, which greatly facilitated the progress in the research concerning structural health monitoring of bridges.

Moreover, I want to thank Prof. Lars-Erik Persson and Prof. Natasha Samko for their help and support that has further led to the advancement in the engineering mathematics concerning Fourier based methods and Bayesian approach in signal processing techniques.

Lastly, I would like to thank everyone involved for their collaboration, support, and dedication to advancing our understanding in this important field.

Dr. Harpal Singh
Place: Dublin, California
Date: 23/12/2024



Project Contributions

Dr. Harpal Singh: Project manager of Herøy FoU at UiT Narvik.

Jørn Eldby: Project Administration of Herøy FoU at UiT Narvik.

Wenche Svea: Project Support Administration at UiT Narvik.

Boy-Arne Persson Buyle: Project support from concrete lab at UiT Narvik.

Dr. Iveta Novakova: Contribution on WP2 from UiT Narvik.

Daniele Storni: Project manager from Wise Robotics for the OMA campaign.

Dr. Giuseppe Occhipinti: Project Engineer from Wise Robotics for the OMA campaign.

Guido Battistella: Technician from Wise Robotics for the OMA campaign.

Dr. Daniel Cantero: Project Leader Herøy FoU, NTNU.

Dr. Roy Antonsen: Project Owner from Statens Vegvesen (Now SINTEF Manager).

Karla Hornbostel: Project Manager from Statens Vegvesen.

Per Ove Ravatsås: Project Owner from Nordland Fylke.

Heine Andrè Rokås: Project support from Nordland Fylke.

Nils Göran Åhlin: Project support from PeAB.

Dr. Vanni Nicoletti: Master thesis co-supervision from Marche University, Italy.

Dr. Aleksander Pedersen: Master thesis co-supervision from UiT Narvik.



Summary

1	Introduction	21
1.1	State of bridge infrastructure in Norway.....	21
1.2	Herøy FoU.....	27
1.3	Project schedule of the project and responsible people	27
1.4	How the report is organized	28
2	The Herøysund Bridge	33
3	Model-based approaches for the Herøysund bridge	39
3.1	Introduction	39
3.2	Discrete Macro-Element Method (HISTRA).....	39
3.3	FEM Beam like approach (ANSYS).....	46
3.4	FEM linear shell-like approach (LUSAS).....	50
3.5	FEM Shell-based approach (ANSYS)	53
3.6	FEM damage modelling (ANSYS).....	58
4	Operational Modal Analysis OMA	65
4.1	Introduction	65
4.2	Theory and Methods	67
5	Instrumentation, data acquisition and data processing on the Herøysund	71
bridge		
5.1	Introduction	71
5.2	Data Acquisition	75
5.2.1	Time Synchronization and Data Integrity	75
5.2.2	Sampling Frequency and Duration.....	76
5.3	Data Processing	76
6	The OMA campaign	79
6.1	Introduction	79
6.2	Use of FEM and DMEM models for defining the sensor layout.....	81
6.3	Sensor placement.....	84
6.4	OMA results.....	90
6.5	Analysis of the Natural Frequency of a Bridge Using Statistical Methods.....	94
7	Challenging problems and proposed solutions	107
7.1	Optimal Sensor Placement	107
7.2	Model updating.....	110
8	Conclusions and Lessons Learnt.....	115
9	Dissemination of Knowledge	125
9.1	Meetings and fieldwork Herøy FoU	125
9.2	Public lectures and research discussions.....	125
9.3	Conferences.....	126
9.4	Publications.....	126
9.5	Master Thesis.....	127
9.6	PhD thesis.....	127
10	References.....	131
11	Appendix 1: Sensor placement survey.....	137
12	Appendix 2: Sensors' operating guide.....	175
13	Appendix 3: Sensors Technical drawings.....	185
14	Appendix 4: Sensors Calibration Certificate	189



LIST OF FIGURES

Fig. 1 Histogram of the state of Norwegian bridges in logarithmic scale [2].	22
Fig. 2 State of bridges in northernmost Norwegian counties of Nordland, Troms and Finnmark [2].	22
Fig. 3 Histogram of bridges grouped by build decade in northernmost Norwegian counties [2].	23
Fig. 4 The bridges in the Nordland County [2].	24
Fig. 5 The bridges in the northern Nordland County and southern Troms and Finnmark county [2].	25
Fig. 6 The bridges in the northern Troms and Finnmark county [2].	26
Fig. 7 Picture of Herøysund bridge.	34
Fig. 8 Overview of the bridge including axes and dimensions [6].	34
Fig. 9 Geometry of the main pillar pressure plates [7].	35
Fig. 10 Top deck cross section profiles of bridge spans 1-7 all dimensions in mm [8].	35
Fig. 11 The 1971 Drawings of Herøysund bridge parts [9].	36
Fig. 12 Exploded view of Herøysund bridge parts [9].	36
Fig. 13 Advances in the mechanical scheme adopted in the proposed macro-element approach: (A) plane element, (B) regular three-dimensional element, (C) irregular 3D element, (D) irregular 3D element with interfaces on all faces [12].	40
Fig. 14 Transversal nonlinear links: (a) fiber calibration for a single masonry strip, (b) cyclic behaviour related to the flexural response; Calibration of the shear-sliding response: (c) in-plane and (d) out-of-plane nonlinear links [19].	41
Fig. 15 Calibration of diagonal nonlinear link: (a) equivalent macroelement and (b) Cyclic constitutive law for diagonal nonlinear links [19].	41
Fig. 16 DMEM model of the bridge, global top view.	42
Fig. 17 DMEM model of the bridge, global bottom view.	42
Fig. 18 Details of the half joint connections.	43
Fig. 19 Detail of one of the central piers.	43
Fig. 20 Elastic concrete properties.	44
Fig. 21 HISTRA BRIDGE DMEM model modal shapes.	45
Fig. 22 Mode 1 on the solid model matched by 99,5% with mode 1 on the beam model. Frequency error: -4,3%. [21].	46
Fig. 23: Mode 2 on the solid model matched by 98,8% with mode 2 on the beam model. Frequency error: -18,9%. [21].	47
Fig. 24: Mode 3 on the solid model matched by 99,4% with mode 3 on the beam model. Frequency error: 1%. [21].	47
Fig. 25: Mode 5 on the solid model matched by 99,3% with mode 5 on the beam model. Frequency error: 5,5%. [21].	47
Fig. 26: Mode 4 on the solid model matched by 99,1% with mode 6 on the beam model. Frequency error: -17,4%. [21].	48
Fig. 27: Mode 7 on the solid model matched by 94% with mode 7 on the beam model. Frequency error: -6,4%. [21].	48
Fig. 28: Mode 1 on the solid model matched by 97,7% with mode 1 on the beam model. Frequency error: -12,5%. [21].	48
Fig. 29: Mode 10 on the solid model matched by 94,3% with mode 12 on the beam model. Frequency error: -2,6%. [21].	49
Fig. 30: Mode 9 on the solid model matched by 93,5% with mode 14 on the beam model. Frequency error: -10,5%. [21].	49

Fig. 31: Mode 16 on the solid model matched by 97,8% with mode 18 on the beam model. Frequency error: 3,9%. [21].	49
Fig. 32: Mode 15 on the solid model matched by 93,6% with mode 20 on the beam model. Frequency error: -14,5%. [21].	50
Fig. 33 Section assignment.	51
Fig. 34 Material Assignment.	51
Fig. 35 Shell and Solid model transformation [23].	54
Fig. 36 3D-Solid and 3D Shell bridge geometry [23].	54
Fig. 37 3D-Solid model joints across all pillars [23].	56
Fig. 38 Shell model joints across all pillars [23].	56
Fig. 39 MAC Index matrix for Solid and Shell model matched modes [23].	58
Fig. 40 Photos of some of the cracks identified on Herøysund bridge [9].	60
Fig. 41 Location of cracks in the model [9].	60
Fig. 42 Stochastic framework used in Operational Modal Analysis [24].	66
Fig. 43 PCB 393B12 Accelerometer.	71
Fig. 44 Cabin office by the bridge.	73
Fig. 45 Server.	73
Fig. 46 Sensors and DAQ before mounting.	74
Fig. 47 Local DAQ placed under the bridge.	74
Fig. 48 Example of sensor placement under the bridge.	75
Fig. 49 Herøysund bridge, lateral view (Herøysund bru, korrosjon av etterspent armering FoU-programmet Bedre Bruvedlikehold 2017-2021, Statens Vegvesen Rapport Nr.843).	80
Fig. 50 a) Construction phase (1966), b) upgrading work (2020) (https://www.wikiwand.com/no/Herøysundet_bru).	80
Fig. 51 Herøysund Bridge, image and section (Herøysund bru, korrosjon av etterspent armering FoU-programmet Bedre Bruvedlikehold 2017-2021, Statens Vegvesen Rapport Nr.843).	80
Fig. 52 LUSAS shell model modal shapes.	82
Fig. 53 HISTRA BRIDGE DMEM model modal shapes.	83
Fig. 54 Configuration of the T-shape plate and FEM results.	84
Fig. 55 Three tests layouts.	86
Fig. 56 Control of the sensor orientation.	86
Fig. 57 PSD results for the X direction.	87
Fig. 58 Sensors' layout.	88
Fig. 59 Example of triaxial point of measure.	89
Fig. 60 Stabilization diagram of estimated state space models, SSI-UPC.	90
Fig. 61 Modal Assurance Criteria.	92
Fig. 62 Frequencies tracking.	93
Fig. 63 Time series plot of the first six natural frequencies of the system.	94
Fig. 64 Histograms and densities of the frequencies time series.	95
Fig. 65 Quantile-Quantile Plot of the frequencies.	96
Fig. 66 Raw time series along with processed time series after outlier removal.	97
Fig. 67 QQ-plot after outlier removal.	98
Fig. 68 Model prediction and uncertainties estimation for f1.	99
Fig. 69 Model prediction and uncertainties estimation for f2.	99
Fig. 70 Model prediction and uncertainties estimation for f3.	99
Fig. 71 Model prediction and uncertainties estimation f4.	100
Fig. 72 Model prediction and uncertainties estimation for f5.	100
Fig. 73 Model prediction and uncertainties estimation for f6.	100
Fig. 74 Trend and seasonalities estimation for f1.	101

Fig. 75 Trend and seasonalities estimation for f2.	101
Fig. 76 Trend and seasonalities estimation for f3.	102
Fig. 77 Trend and seasonalities estimation for f4.	102
Fig. 78 Trend and seasonalities estimation for f5.	103
Fig. 79 Trend and seasonalities estimation for f6.	103
<i>Fig. 80 Ten final sensor location for model WPT [8].</i>	<i>108</i>
<i>Fig. 81 Ten sensor locations for model WPT EFI-DPR method [8].</i>	<i>108</i>
<i>Fig. 82 Ten final sensor location for model WNPT [8].</i>	<i>109</i>
<i>Fig. 83 Ten sensor location for model WNPT EFI-DPR method [8].</i>	<i>109</i>
Fig. 84 Graphical comparison of frequencies.	115
Fig. 85 Sensor layout.	117
Fig. 86 Histogram of the identified frequencies.	118
Fig. 87 Relevant variations.	119
Fig. 88 Comparison of the three modal shapes identified at a) 14:30 and b) 15:00, 20 th June 2023.	120
Fig. 89 Comparison of the three modal shapes identified at a) 22:00 and b) 22:30, 21 st June 2023.	120
Fig. 90 Comparison of the three modal shapes identified at a) 05:30 and b) 06:00, 22 nd June 2023.	121
Fig. 91 Comparison of the three modal shapes identified at a) 14:30 and b) 15:00, 23 rd June 2023.	121
Fig. 92 Model prediction and uncertainties estimation for f1.	122



LIST OF TABLES

Table 1 CPU time comparison for modal analysis [21].....	50
Table 2 Elastic material properties.....	51
Table 3 Modal results.....	52
Table 4 Factors influencing the deformation in Solid and Shell models [23].	55
Table 5 Material properties for models in numerical simulations [23].....	55
Table 6 Bridge data (https://www.wikiwand.com/no/Herøysundet_bru).....	79
Table 7 Sensors' placements.....	88
Table 8 Global modes	91
Table 9 Comparison of preliminary models and OMA results	91
Table 10 Updated values of Selected parameters [28].....	111
Table 11 Frequencies values	116





Chapter 1

Introduction



1 Introduction

Worldwide aging of the civil infrastructure presents significant challenges, necessitating the development of new research techniques to address these problems effectively. Municipalities and governments are increasingly allocating more time and budget towards the maintenance, repair, and construction of new structures to replace deteriorated or damaged infrastructure, ensuring that reliable services are provided to citizens. The deterioration of buildings and civil engineering structures can be caused by several factors such as:

- Degradation induced by environmental factors
- Improper understanding of initial boundary conditions
- Lack of maintenance practices
- Use of bad materials

For example, in Germany, the estimated value of all the constructed infrastructure is approximately €20 trillion, if we assume a lifespan of 100 years for this infrastructure, the replacement rate is estimated to be around €200 billion annually [1]. The American Society of Civil Engineers conducted a detailed study on the nation's infrastructure and found that an estimated \$2 trillion in investment will be necessary over the next decade to avoid the risks associated with aging infrastructure in USA. Further, it was reported that 9.1% of bridges in the USA were structurally deficient as of 2016. An estimated \$123 billion is required for the rehabilitation of these bridges [1].

These challenges require immediate attention and action. An increased investment and innovative new research techniques could be useful to ensure the safety of infrastructure systems, for enhancing public service delivery sustainably.

1.1 State of bridge infrastructure in Norway

The growth, particularly in the sparsely populated areas of northern Norway, is imposing increasing demands on bridge infrastructure. Therefore, aging infrastructure should be rigorously tested and maintained to accommodate these increased loads. Failure of such infrastructure could not only result in significant economic losses and can pose risks to human safety.

The Norwegian newspaper Verdens Gang (VG) got access to a report from Statens Vegvesen (The Norwegian Public Roads Administration) in 2017. This report highlighted the state of 16,791 bridges in Norway and how they are classified as missing inspection, delayed renovation, serious and critical. VG discovered that half of these bridges lack adequate inspection [2]. Moreover, around 1,087 bridges have been identified as having serious or critical damage, with respect to Statens Vegvesen's internal classification system. Furthermore, the government-owned broadcasting channel NRK revealed that approximately 1,000 bridges in Norway still do not meet established standards [2].

The authors of [2], did analysis of this data available on the VG website, and presented an overview of all bridges in Norway, displayed on a logarithmic scale in Fig. 1.

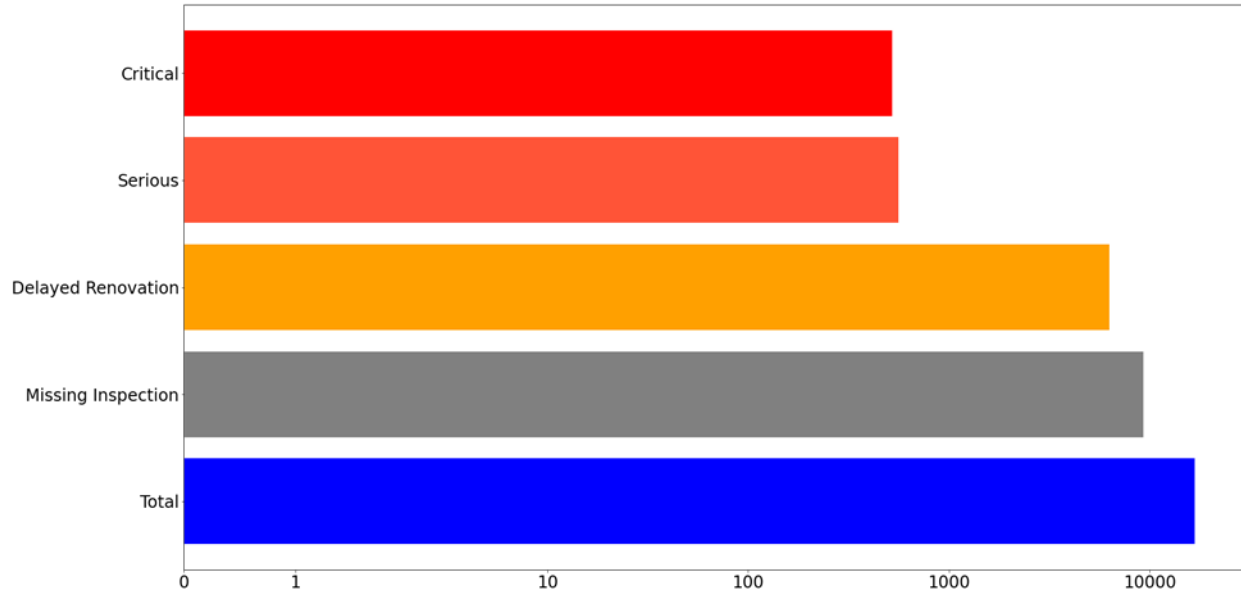


Fig. 1 Histogram of the state of Norwegian bridges in logarithmic scale [2].

A comprehensive study that maps the clusters of bridges located in Nordland, Troms, and Finnmark counties is presented in [2] where a significant portion of the seafood industry is concentrated. Histograms illustrating the condition of all bridges in northern Norway are provided in Fig. 2 and histograms of bridges grouped by build decade in northern Norway is presented in Fig. 3.

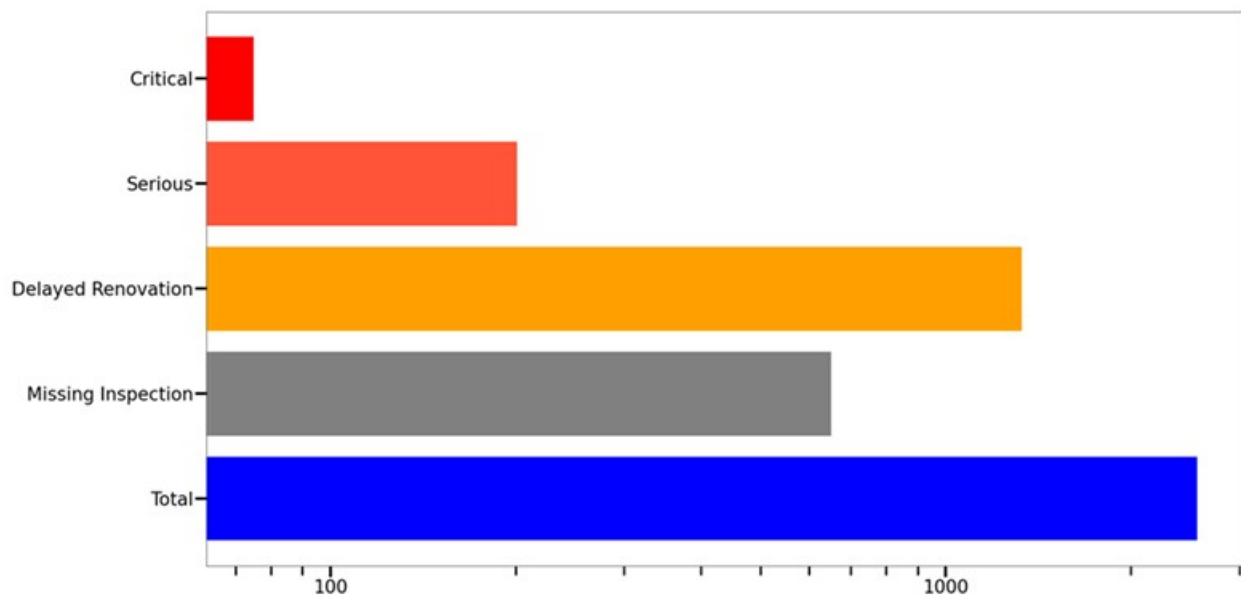


Fig. 2 State of bridges in northernmost Norwegian counties of Nordland, Troms and Finnmark [2].

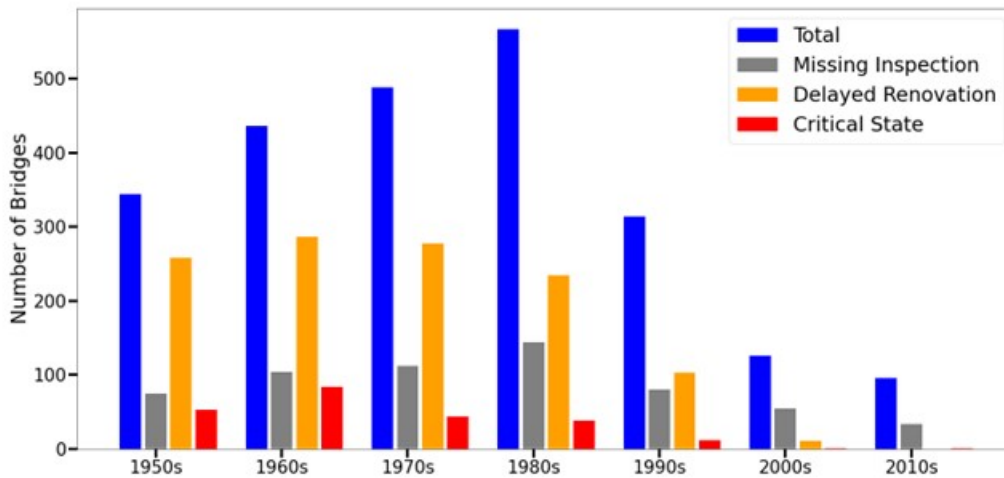


Fig. 3 Histogram of bridges grouped by build decade in northernmost Norwegian counties [2].

Norway has an extensive geography, therefore the area of focus spanning from Nordland to Finnmark, is divided into three distinct regions so as to have improved visualization. The following figures highlight the severity of the infrastructure challenges in northern Norway.

- Fig. 4 covers the region from latitude 57 degrees (the border of Nordland and Trøndelag) to latitude 66 degrees, that is passing through Bodø.
- Fig. 5 encompasses a geographical area from Bodø that is latitude 66 degrees to latitude 68 degrees.
- Fig. 6 covers Finnmark and Troms, starting from latitude 68 degrees and extending to latitude 69 degrees through Nordkapp.

In all these visualizations, hexagonal blocks show the density of bridges that lack inspection, while red circles represent bridges that are being classified as critical or serious condition by length of span.

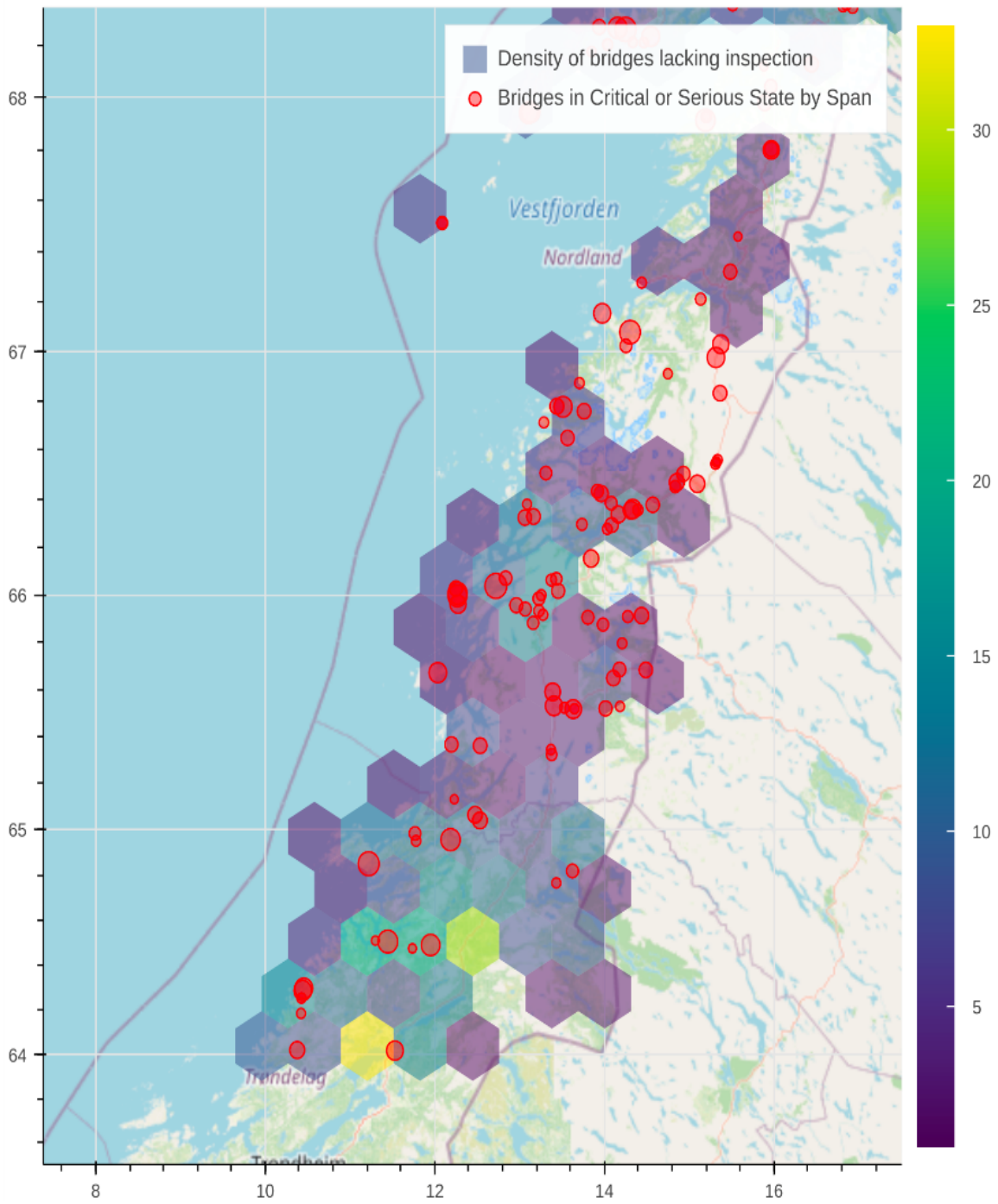


Fig. 4 The bridges in the Nordland County [2].

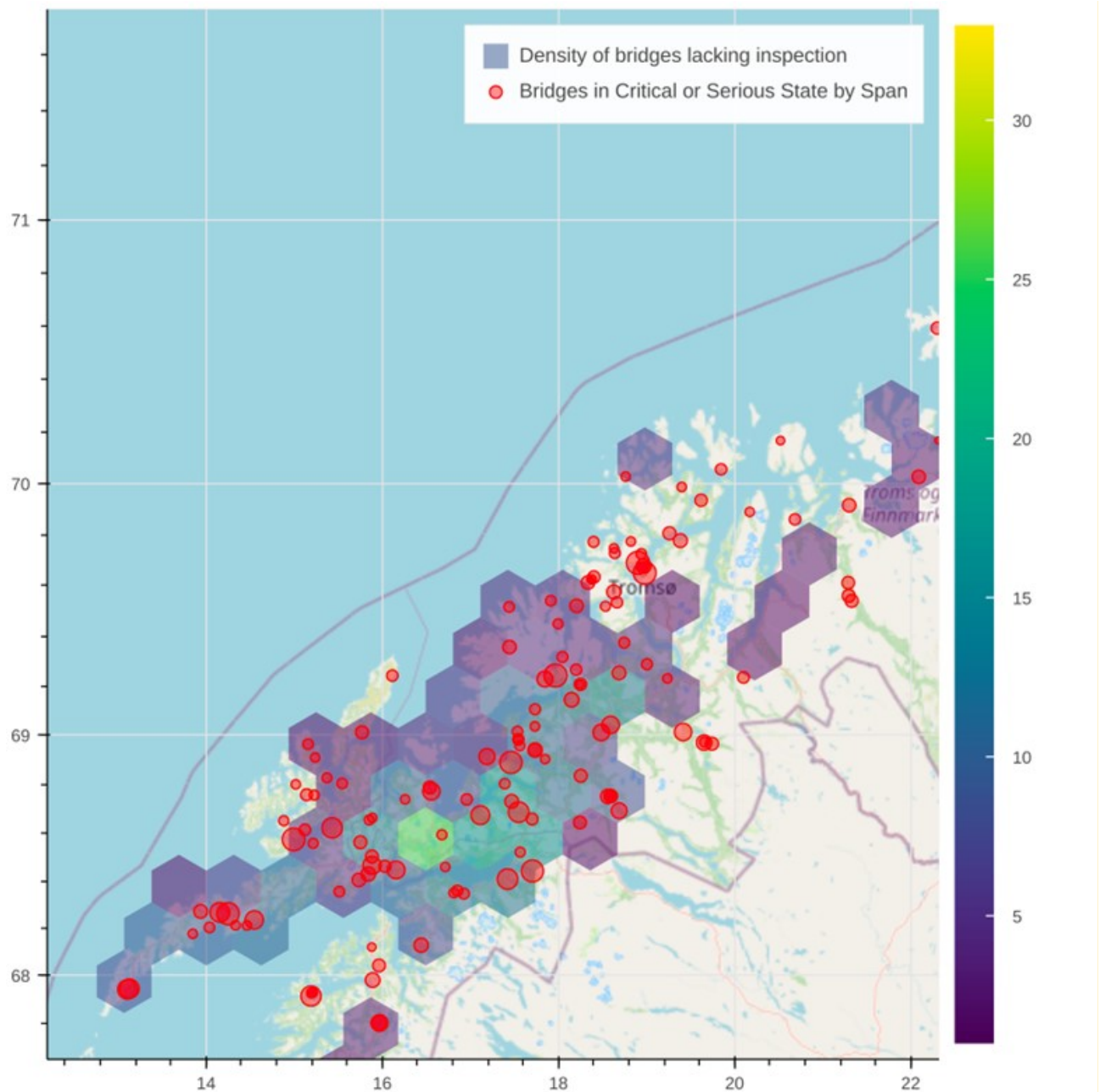


Fig. 5 The bridges in the northern Nordland County and southern Troms and Finnmark county [2].

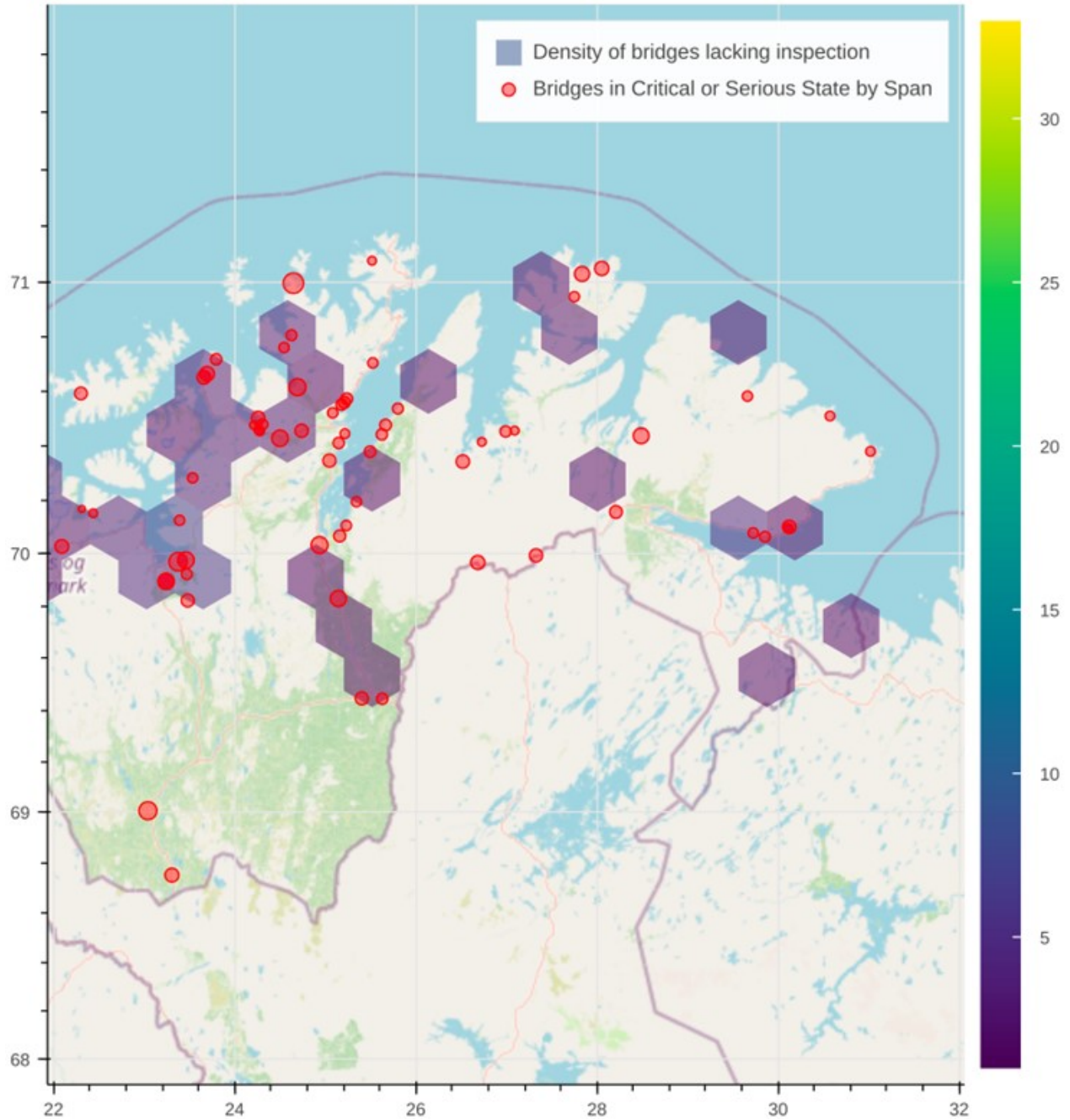


Fig. 6 The bridges in the northern Troms and Finnmark county [2]

Statens Vegvesen has prioritized the inspection and repair of bridges identified as critical or seriously damaged, in response to the urgent need for infrastructure maintenance. During such an activity, a significant structural issue was discovered in 2019 on the Herøysund Bridge, that is located on the west coast of Nordland County in Norway. As a result, the authorities prohibited special transport from crossing the bridge and started the rehabilitation work on the old bridge. Furthermore, a greater damage than first thought was discovered during this rehabilitation of the old bridge.

As a result, in 2020, Nordland County together with Statens Vegvesen, initiated plans to construct a new bridge that will be situated just south of the existing Herøysund Bridge. The construction of new bridge was projected to cost approximately 270 million NOK [2]. Moreover, maintenance and reinforcement work will be carried out on the current Herøysund Bridge to ensure its safety and usability until the new bridge become operational. Reduced speed regulations were imposed on the special heavy cargo. According to the Nordland County website the construction of new Herøysund bridge is now finished and it has been opened for traffic on 12 November 2024.

1.2 Herøy FoU

The old Herøysund bridge in Nordland was chosen as a test pilot to find out how bridge disaster can be prevented in future. UiT The Arctic University of Norway, NTNU, SINTEF Narvik, Nordland Fylkes Kommune and Statens Vegvesen collaborated on a research project titled Herøy FoU that had a budget of just under 6 million NOK. UiT The Arctic University of Norway contributed on Work Package 1 i.e. Structural Health Monitoring and Work Package 2 i.e. Corrosion inspection, assessment and repair.

This report focuses on ambient vibration measurements and operational traffic loading using operational modal analysis (OMA).

1.3 Project schedule of the project and responsible people

Phase	Activity	Start Date	End Date	Responsible
Preparation of fieldwork	Procurement of Hardware and Services	28/11/2022	30/05/2023	HS
	Master thesis topics preparation	13/10/2022	02/12/2023	HS
Master Thesis	Review and application of optimal sensor placement method on Herøysund Bridge	02/01/2023	15/05/2023	HS
	Beam based finite element modelling of Herøysund Bridge	02/01/2023	15/05/2023	HS
	Shell based finite element modelling of Herøysund Bridge	02/01/2023	15/05/2023	HS
Courses	Road Safety Course Level1	23/05/2023	24/05/2023	HS
	Working on construction Site	13/06/2023	13/06/2023	PR
	Working on Scaffoldings	14/06/2023	14/06/2023	PR
Spot Analysis Campaign	Planning of Activity	14/11/2022	05/05/2023	HS, DS & GO
	Safe Job Analysis	15/05/2023	25/05/2023	HS
Field Work Spot Analysis	Testing of Equipment on arrival	11/06/2023	13/06/2023	DS & GO
	Installation of Equipment	15/06/2023	17/06/2023	DS & GO
	Data Collection	18/06/2023	28/06/2023	DS & GO
	Preliminary Data Processing and Validation of Results	20/06/2023	21/06/2023	GO
Permanent Installation Campaign	Planning of Activity and procurement of new equipment	21/06/2023	29/06/2023	HS, DS & GO
	Installation of Equipment	29/06/2023	03/07/2023	DS

	Validation of the data collection	03/07/2023	03/07/2023	GO
	Designing of Digital Platform			DS & GO
	Frequency Tracking on digital platform			DS & GO
Review with Stakeholders	Herøy FoU plenary meeting	05/12/2023	06/12/2023	JE
Demounting of System		15/01/2024	16/01/2024	HS & JE
Master Thesis	Numerical modelling of damage conditions on Herøysund Bridge in Herøy Municipality, Nordland, Norway	05/01/2024	15/05/2024	HS
	Development of digital twin of Herøysund Bridge using finite element model updating	05/01/2024	15/05/2024	HS
Data Analysis	Preliminary processing			GO
	Modal parameter identification			GO
Reporting	Prepare Findings	11/09/2024	27/09/2024	HS
	Report Writing	04/11/2024	20/11/2024	HS, DS & GO
	Presentation of Work	27/11/2024	27/11/2024	HS, DS & GO
	Report Submission Version 1	25/11/2024	25/11/2024	HS
	Final Report Submission Version 2	23/12/2024	23/12/2024	HS

Responsible People

	Name	Institution	Role	Email
1.	Per Ove Ravatsås	NFK	Project Owner	perrav@nfk.no
2.	Heine André Rokås	NFK	Project Support	heirok@nfk.no
3.	Dr. Harpal Singh (HS)	UiT	Project Manager	harpal.singh@uit.no
4.	Jørn Eldby (JE)	UiT	Project Administration	jorn.eldby@uit.no
5.	Daniele Storni (DS)	WR	Project Manager	daniele.s@wls3.com
6.	Dr. Giuseppe Occhipinti (GO)	WR	Structural Engineer	ing.giuseppe.occhipinti@gmail.com
7.	Guido Battistella	WR	Technician	gbattistella@sitie.it
8.	Nils Göran Åhlin	PEAB	Project Support	nils.goran.ahlin@peab.no

1.4 How the report is organized

This report is organized into ten chapters. The introduction presents the state of the bridge infrastructure in Norway and provides a basic overview of Herøy FoU research project and the project management schedule of the WP1.A3 model development and updating from ambient vibration measurements. In Chapter 2 Herøysund bridge is described in detail.

Further, Chapter 3 focuses on model-based approaches, detailing the results from various Finite Element (FE) models, including those developed in LUSAS, discrete macro-element model, shell-based FEM,



beam-based FEM, and numerical modeling of damage conditions on the Herøysund Bridge. This chapter also includes various theoretical aspects of model based structural damage identification and literature review of various topics concerning structural health monitoring.

Chapter 4 presents the theoretical background of data-driven operational modal analysis (OMA) approaches, primarily discussing Stochastic Subspace Identification (SSI) and Frequency Domain Decomposition (FDD). The instrumentation used for the OMA activities is explained in detail in Chapter 5, along with the data acquisition system and data processing techniques. Chapter 6 details the OMA campaign, sensor placement including results from the first ten days of fieldwork.

Challenging problems concerning optimal sensor placement and finite element model updating including some basic results is discussed in Chapter 7. Chapter 8 summarizes the overall project activities, including conclusions and lessons learned. Further, Chapter 9 addresses the dissemination of knowledge acquired throughout the project. The references used are listed in Chapter 10. This report includes 4 Appendix; A1: Sensor placement on field, A2: Sensor operating guide, A3: Sensor technical drawings and A4: Sensor calibrations.



Chapter 2

The Herøysund Bridge



2 The Herøysund Bridge

The Herøysund bridge (Fig. 7) is a cast-in-place concrete post-tensioned bridge with seven axes consisting of five pillars and two land vessels, a bridge plate, and two concrete load-bearing beams (see Fig. 8, Fig. 9, Fig. 10, Fig. 11, Fig. 12). The post tensioning system is installed on four axes, including the middle axes and the corresponding axes (axes 3 to 6). The bridge connects the two islands of Nord Herøy and Sør-Herøy to country road 828 along the coast of Helgeland in northern Norway. It has a length of 154.5 metres and a width of 5.3 metres. The bridge was completed and opened to traffic in 1966. The main span (axes 4 to 5) measures 60 metres in length and was constructed according to weight regulations 2/1958. There are two pressure plates positioned at the main pillars (axis 4 and 5). The primary portion of the bridge, from axis 3 to axis 6, is braced. The viaducts are girder structures with lax reinforcement. There is no excess reinforcement along the length of the beams. Since the bridge was constructed in the 1960s, there is no access to the original construction calculations. It is presumed that the cross-section has been dimensioned so that tensile stresses do not occur in the cross section of the bridge.

In 2017, it was discovered that the bridge's construction was flawed due to excessive chlorides in the concrete that could corrode the rebars and tendons. In addition, there were cracks on the beams distributed over approximately 15 metres in the middle of the main span, with the largest fracture measuring between 0.5 millimetres and 0.9 millimetres at the foot of the beams. The bridge is also subject to increased traffic volumes, which may have resulted in increased tensile forces in the bridge since it was constructed and because of its intended use [3].

Due to this, it was decided to restore the bridge with cathodic protection and mechanical repairs. During the rehabilitation of the bridge in 2020, additional damages and construction flaws were discovered, despite the bridge's strengthening. It was discovered that the channels for the post-tensioned tendons were inadequately injection grouted, with only about 50% injection grout in some areas. In addition, some of the tendons in the post-tensioning system were corroded, and some of the wires' threads were fractured [4]. The capacity of the post tensioning system may be nullified by a lack of injection and subpar grouting. This results in an excessive utilization of the moment capacity in sections of the primary span [5].

The bridge will remain accessible until 2024, when the replacement bridge is scheduled to open. There are restrictions on heavier traffic, so the utmost weight is limited to 50 tonnes. The bridge is slated for demolition after the new bridge is fully functional and opened, and the scientific work is finished.



Fig. 7 Picture of Herøysund bridge.

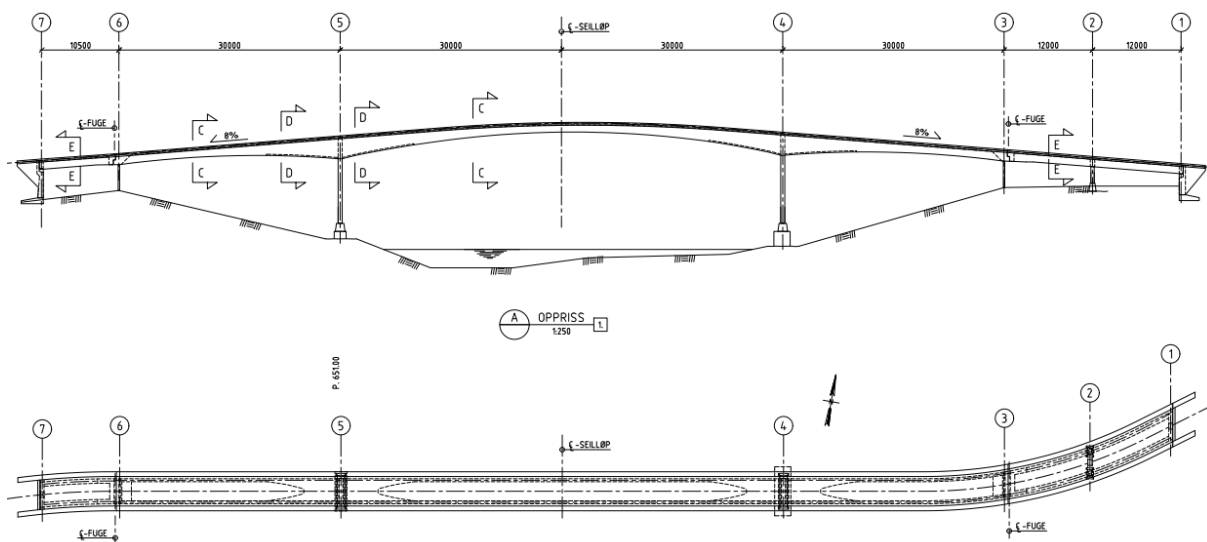


Fig. 8 Overview of the bridge including axes and dimensions [6].

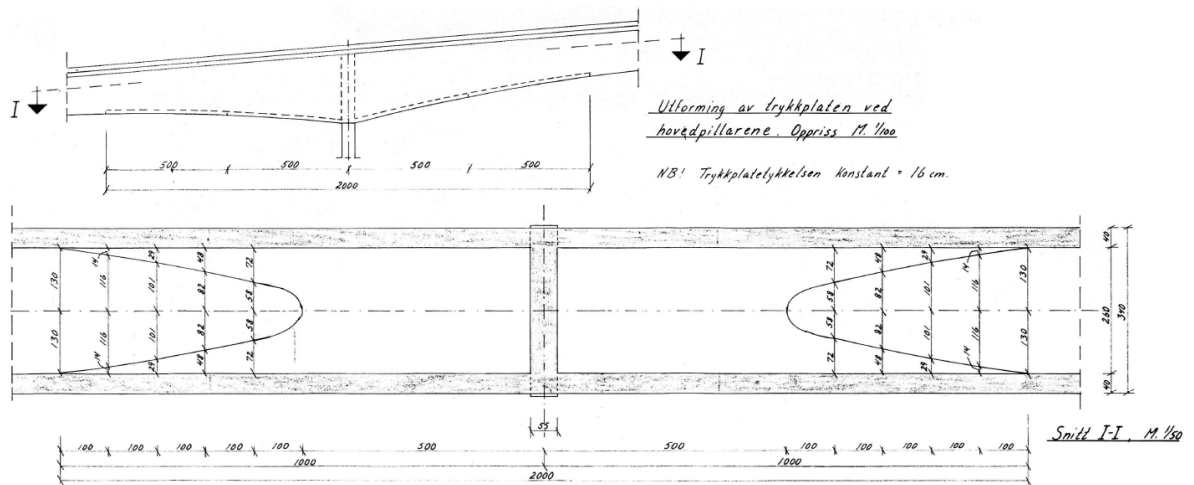


Fig. 9 Geometry of the main pillar pressure plates [7].

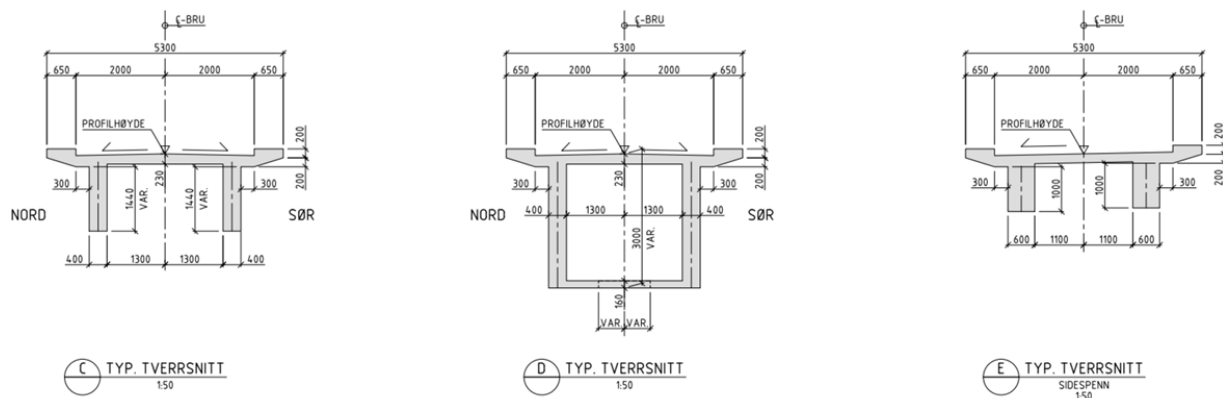


Fig. 10 Top deck cross section profiles of bridge spans 1-7 all dimensions in mm [8].

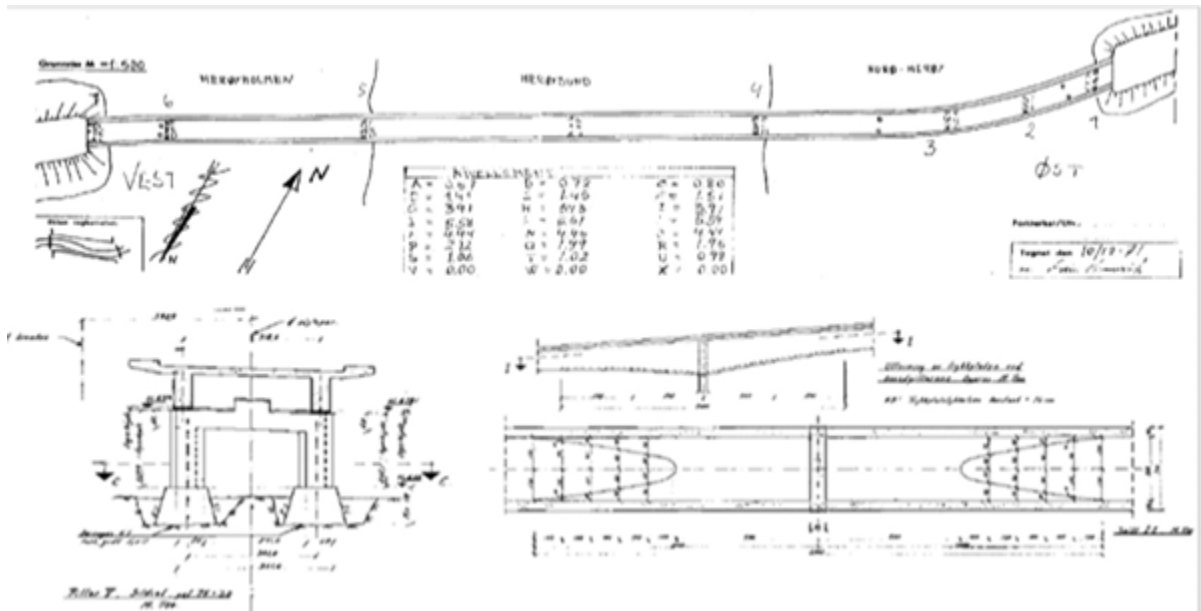


Fig. 11 The 1971 Drawings of Herøysund bridge parts [9].

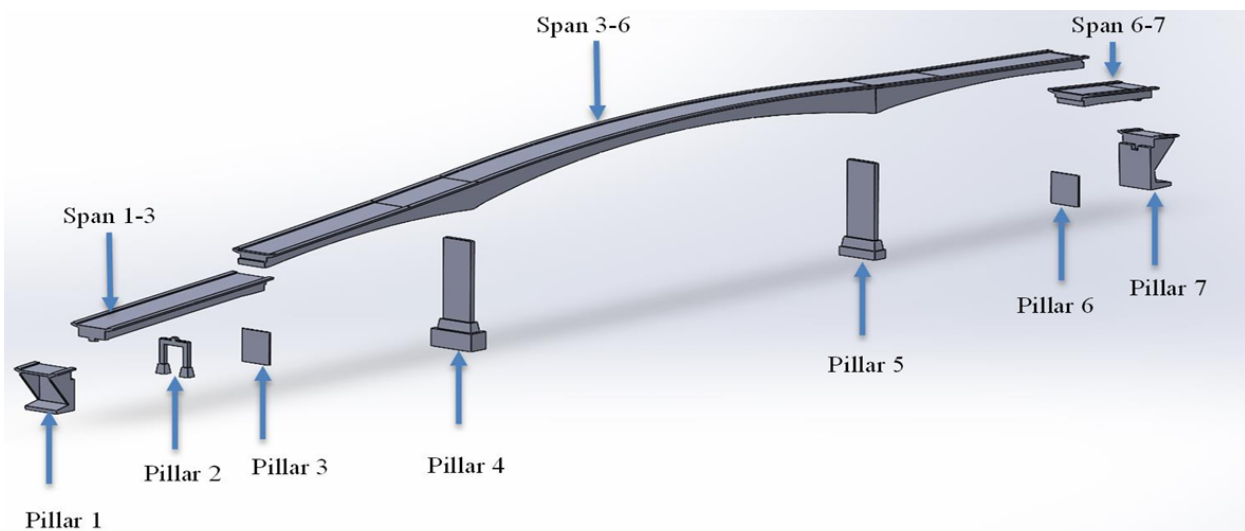


Fig. 12 Exploded view of Herøysund bridge parts [9].

Chapter 3

Model-based Approaches for the Herøysund bridge



3 Model-based approaches for the Herøysund bridge

3.1 Introduction

The assessment of existing concrete bridges represents a crucial aspect in the correct management and maintenance of road and railway infrastructures. For numerical modelling of reinforced concrete elements in the nonlinear field requires the adoption of sophisticated although robust models, if a reliable assessment of the seismic performance is needed. Uniaxial elements cannot be adopted for studying complex bridges and two- or three-dimensional elements must be considered. Those structures need accurate modelling even though the explicit modelling of concrete and steel bars would make the simulations too cumbersome for many practical applications. This aspect may be key considering the large number of bridges that have to be assessed in Italy. Recently, a more optimized and less computationally burden method has been applied for analysing masonry bridges that are still a key part of the European infrastructure network. The numerical approach is named Discrete Macro-Element Model (DMEM) (Cannizzaro, et al., 2018).

Research on detecting structural damage has been an interesting topic for decades. Among them, the vibration-based damage detection method as a global technique is especially pervasive. The present survey reviewed the state-of-the-art on the framework of vibration-based damage identification and severity estimation. The survey is mainly focused on model-based procedures.

Deterioration and degradation of structures are of great concerns worldwide. The deficient structures can potentially endanger the safety and economical use of the infrastructure system and even develop into structure failures if the damage is not detected in the early stage. Structural Health Monitoring can be considered as part of the more general Non-Destructive Test methods. Most non-destructive damage detection methods can be categorized as either local or global techniques. Unfortunately, the non-destructive testing (NDT) methods, requires that the damage is known a priori and that the portion of the structure being inspected is readily accessible. Subjected to these limitations, the local NDT methods can only detect damage on or near the surface of the structure [10].

According to the literature [11] structure damage identification can be classified into four levels:

- **Level 1:** Determination that damage is present in the structure (damage occurrence).
- **Level 2:** Level 1 and determination of the geometric location of the damage (damage location).
- **Level 3:** Level 2 and quantification of the severity of the damage (damage severity).
- **Level 4:** Level 3 and prediction of the remaining service life of the structure (service life and decision making).

3.2 Discrete Macro-Element Method (HISTRA)

The Discrete Macro-Element Method DMEM [12] was originally developed for simulating in-plane and out-of-plane nonlinear response of masonry structures. In the last decade, the method was applied to masonry buildings [13, 14, 15], churches [16, 17] and arch bridges [12, 18]. In the DMEM approach each

not rigid macro-element interacts with the adjacent elements through nonlinear distributed zero-thickness interfaces. Fig. 13 graphically describes the macro-element developments. The method was introduced in 2005 by Calìo et al. [13], for in-plane nonlinear response of masonry walls only, Fig. 13 (A). Originally the kinematic was described by 6 degrees of freedom related to the rigid body motion plus 1 governing the shear element deformability. Later, it was extended by adding three additional degrees-of-freedom and further nonlinear links in order to account for the three-dimensional mechanical behaviour published in 2017 [15], Fig. 13(B). Curved geometries required a further enrichment towards a more general shell macro-element, qualitatively reported in Fig. 13 (C) and (D), that were introduced in 2016 [16] and 2017 [17], respectively.

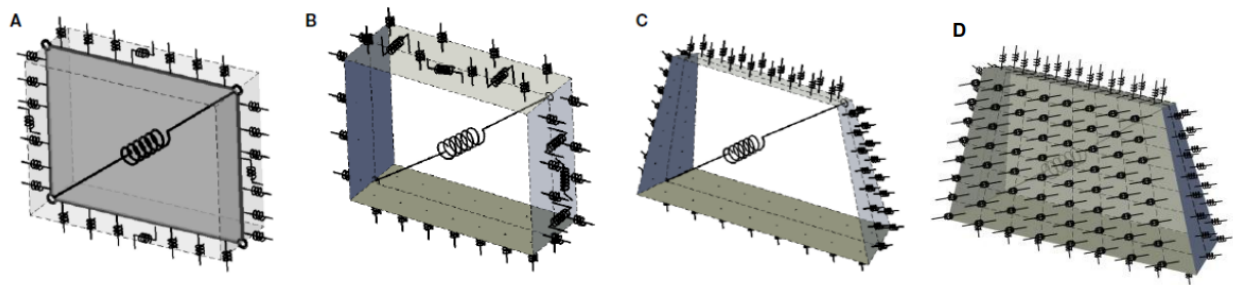


Fig. 13 Advances in the mechanical scheme adopted in the proposed macro-element approach: (A) plane element, (B) regular three-dimensional element, (C) irregular 3D element, (D) irregular 3D element with interfaces on all faces [12].

The transversal nonlinear links of the interface elements simulate the in-plane and the out-of-plane flexural behaviour of the connected panels. Each link represents a strip corresponding to 2 adjacent elements along a given material direction. The calibration of each link is conducted by means of a fiber discretization approach that provides a couple of nonlinear links in series, which are further replaced by an equivalent one (Fig. 6a). The hysteretic behaviour (Fig. 6b) defined for the transversal nonlinear links was adapted from the cyclic constitutive model. The nonlinear links located at the interface elements (Fig. 6c) aim at simulating the shear-sliding and torsion responses. The behaviour of the link in the pre-yielding phase is kept rigid. On the other hand, the out-of-plane shear deformability is solely simulated by 2 additional nonlinear links along the thickness of the interface element (Fig. 6d). The calibration procedure is based on an elastoplastic constitutive law (Fig. 6e). The diagonal nonlinear link is mainly associated with the in-plane shear-diagonal response (Fig. 7a). The hysteretic constitutive law that governs the cyclic response of the diagonal nonlinear links is based on the Takeda (Takeda, et al., 1970) model (Fig. 7b). A more detailed description of calibration assumption and procedure, constitutive laws and cyclic rules is reported in previous works [19, 15, 13].

As introduced, the first attempt to the extension of the macro-element to concrete structures is presented in this paper. An opportune number of 1D trusses, which simulate the reinforcement bars, can be introduced between two macro-elements (QUAD). Each truss is calibrated for simulating a certain number of reinforcement steel bars. The truss properties (ϵ_{ut} , E_t) are equal to the rebars ultimate values (ϵ_{us} , E_s) times the ratio between the bar (l_b) and the truss (l_t), lengths. The discretization of a reinforced concrete element is sketched in Fig. 8.

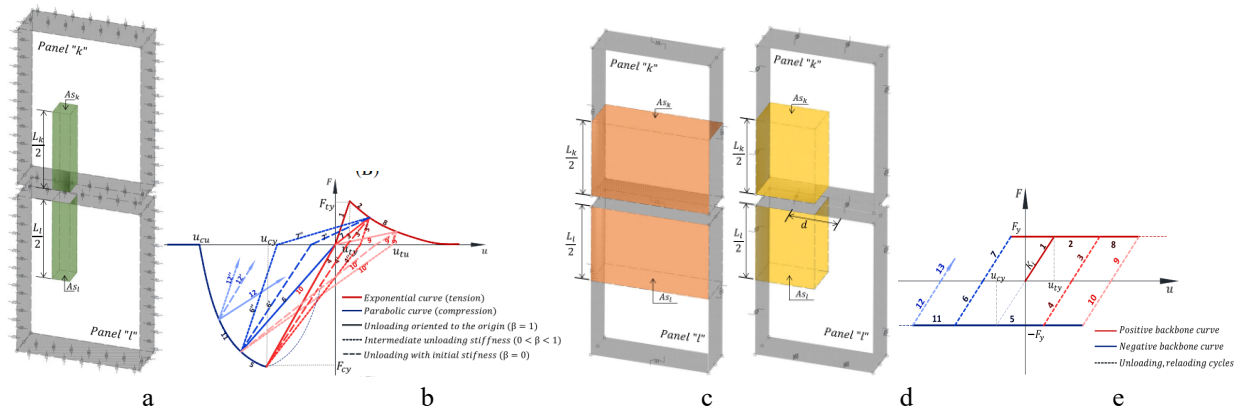


Fig. 14 Transversal nonlinear links: (a) fiber calibration for a single masonry strip, (b) cyclic behaviour related to the flexural response; Calibration of the shear-sliding response: (c) in-plane and (d) out-of-plane nonlinear links [19].

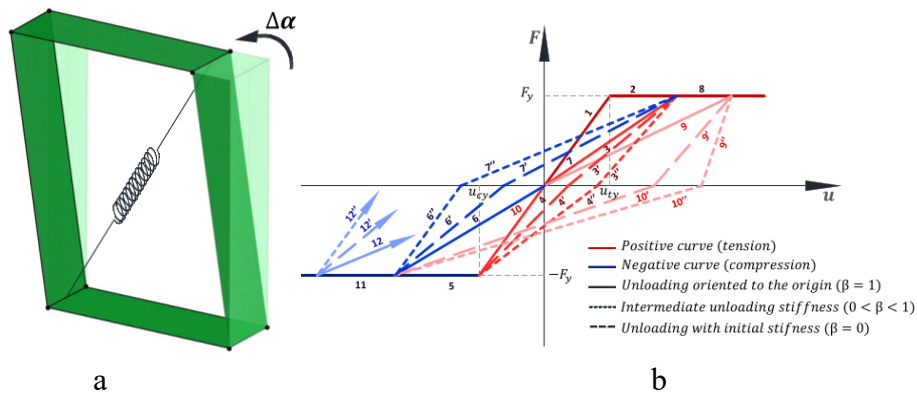


Fig. 15 Calibration of diagonal nonlinear link: (a) equivalent macroelement and (b) Cyclic constitutive law for diagonal nonlinear links [19].

The method was adopted for modelling the bridge (Fig. 16, Fig. 17, Fig. 18, Fig. 19) in the elastic behaviour. Even if the method allows for simulating nonlinear reinforced concrete [20] it wasn't necessary in this case.

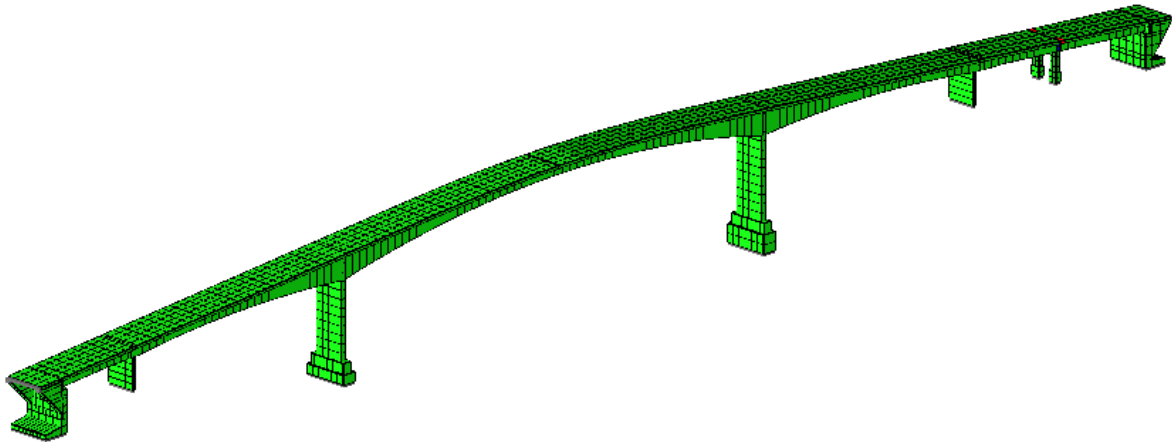


Fig. 16 DMEM model of the bridge, global top view.

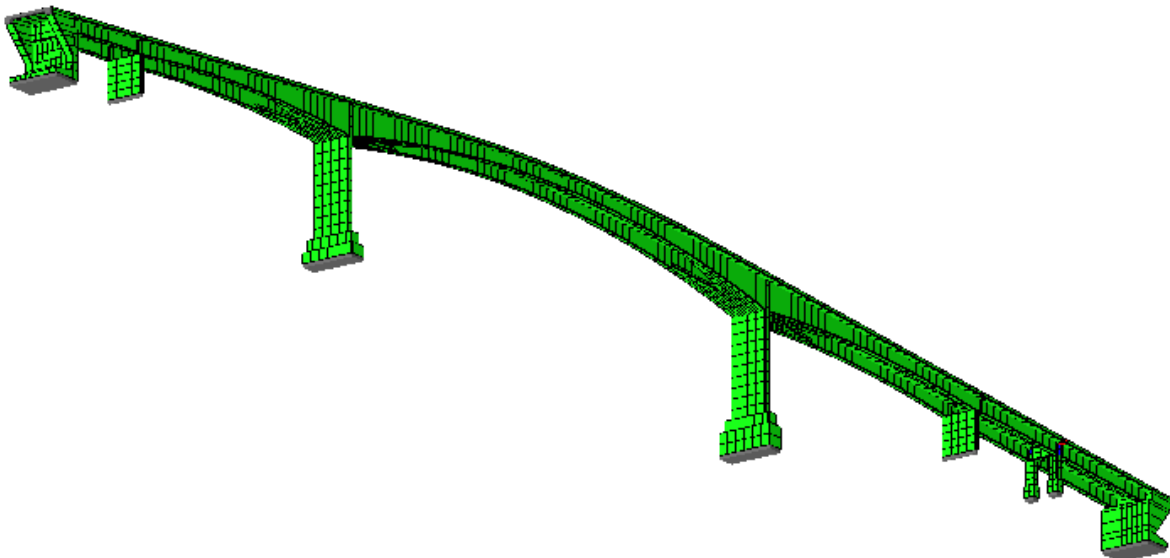


Fig. 17 DMEM model of the bridge, global bottom view.

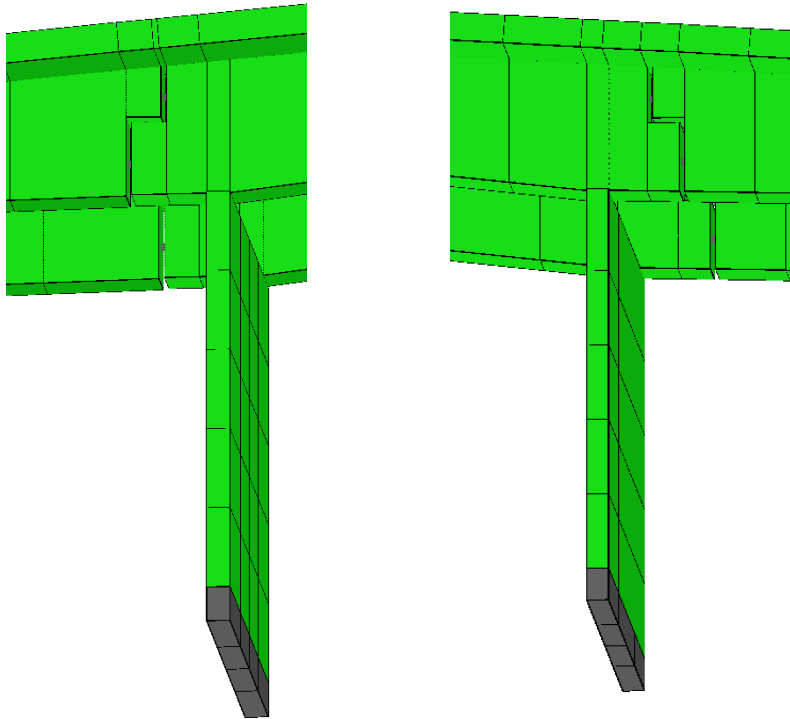


Fig. 18 Details of the half joint connections.

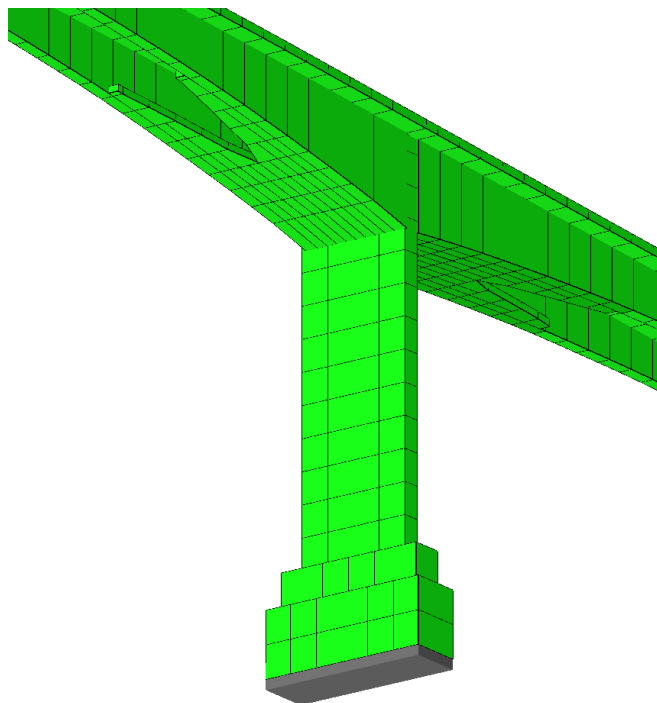


Fig. 19 Detail of one of the central piers.

The material has been assumed linear with properties that are reported in the following figures (Fig. 20).

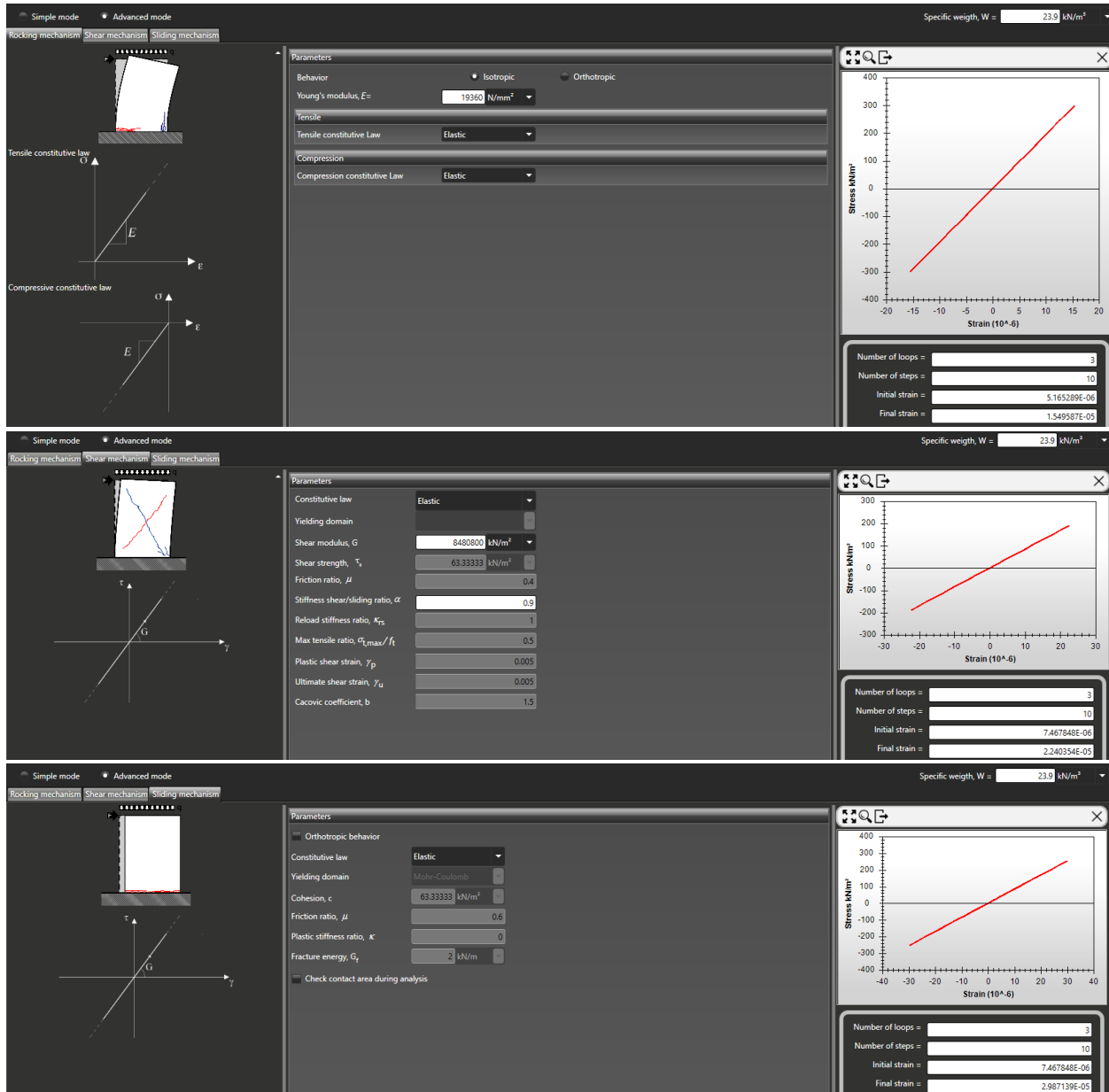


Fig. 20 Elastic concrete properties.

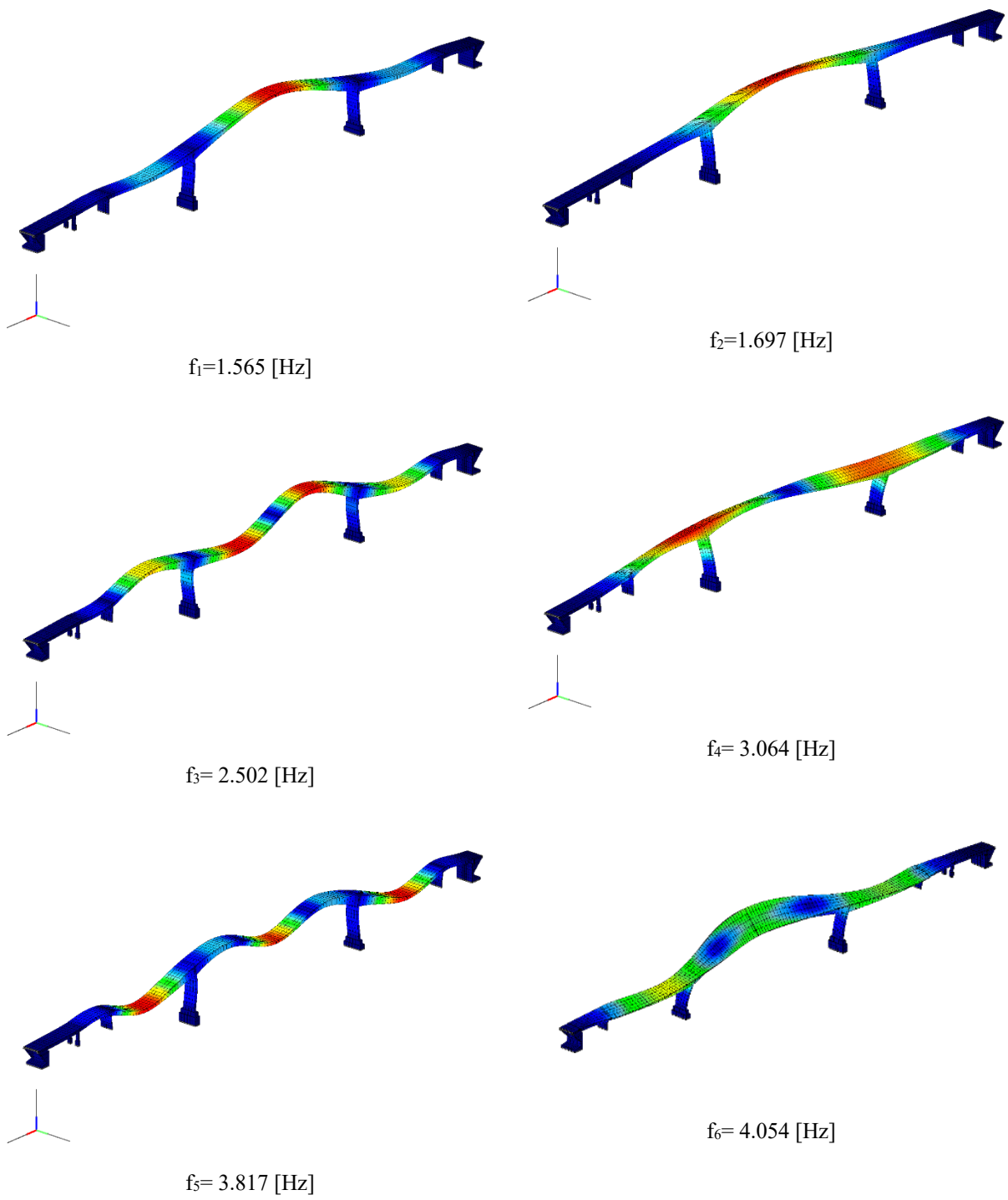


Fig. 21 HISTRA BRIDGE DMEM model modal shapes.

3.3 FEM Beam like approach (ANSYS)

In the thesis, **Beam Based Finite Element Modelling of Herøysund Bridge** by Patrick Norheim Berg and tutored by prof. Harpal Singh (UiT Narvik), the candidate aimed to create two finite element models of the post-tensioned concrete Herøysund Bridge. Initially, a solid element model was developed using documentation from the bridge's construction. Following this, a beam element model was constructed using the solid model as a foundation. These models underwent structural analysis, which applied boundary conditions, joints, mass, gravity, asphalt, railings, and the post-tensioning system. This structural analysis served as the pre-stress condition for a modal analysis of each model, aimed at determining the eigenfrequencies and corresponding mode shapes of the bridge models.

The results from both models were compared to reveal their similarities and identify which model provided the most reliable results. The modal assurance criterion was used for this comparison. Evaluated modes were then suggested for future comparison with operational modes that will be extracted from the bridge. The structural analysis results of the solid and beam models were consistent without the post-tensioning forces; however, once the post-tensioning forces were included, the static structural results showed significant variations in deflection.

The primary objective of this thesis—to model a solid and a beam model of Herøysund Bridge and extract modal analysis results—was achieved. There was good correspondence between the modal analysis results of the solid and beam models, with 11 out of 20 modes showing over 90% similarity in mode shapes and less than 20% frequency error. The results appeared realistic, as the mode shapes materialized as expected for a structure of Herøysund Bridge's scale and shape.

Here the 11 (from Fig. 22 to Fig. 32) modes that gave correspondence above 90% is shown side by side for a visual comparison of the mode shapes.

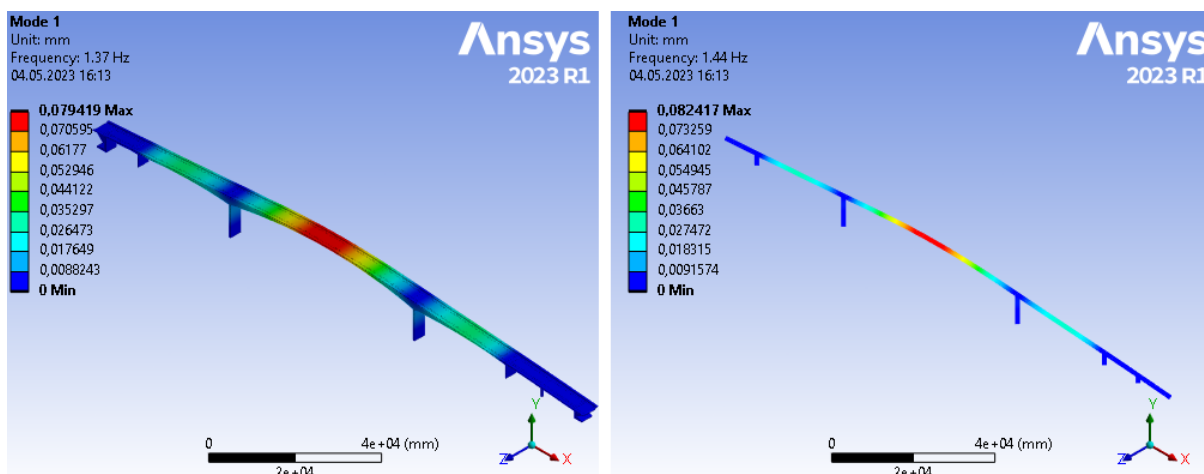


Fig. 22 Mode 1 on the solid model matched by 99,5% with mode 1 on the beam model. Frequency error: -4,3%. [21].

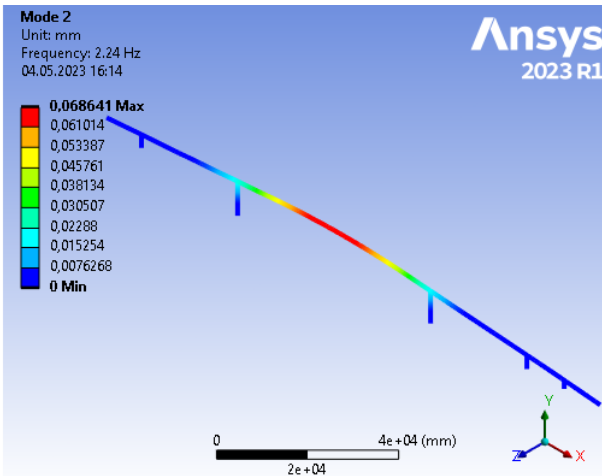
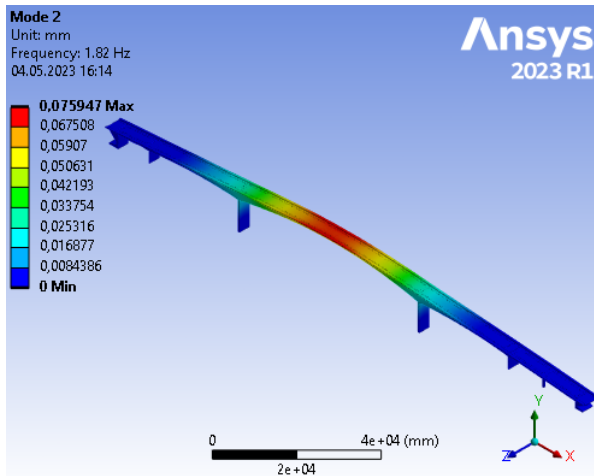


Fig. 23: Mode 2 on the solid model matched by 98,8% with mode 2 on the beam model. Frequency error: -18,9%. [21].

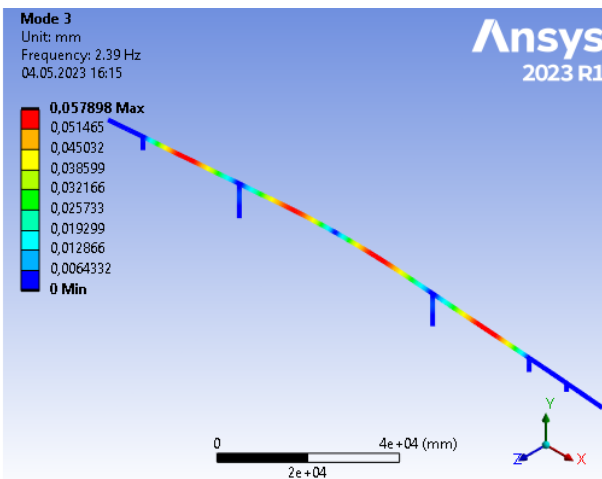
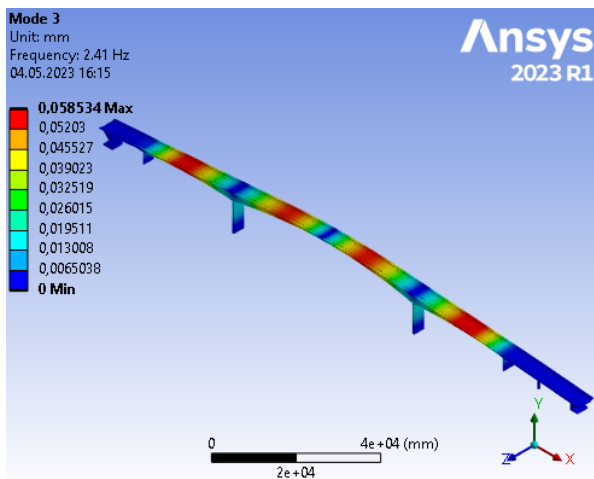


Fig. 24: Mode 3 on the solid model matched by 99,4% with mode 3 on the beam model. Frequency error: 1%. [21].

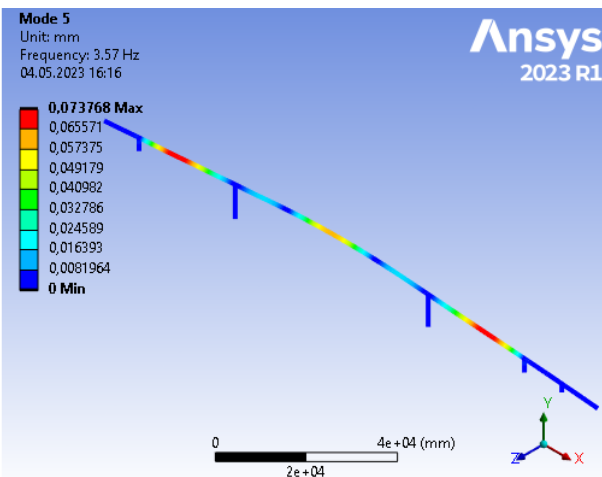
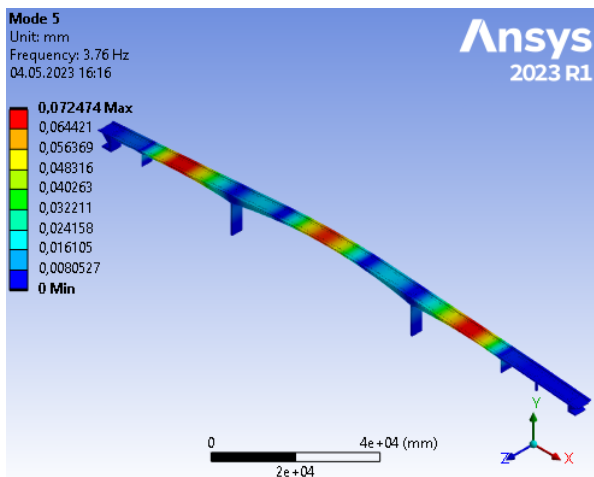


Fig. 25: Mode 5 on the solid model matched by 99,3% with mode 5 on the beam model. Frequency error: 5,5%. [21].

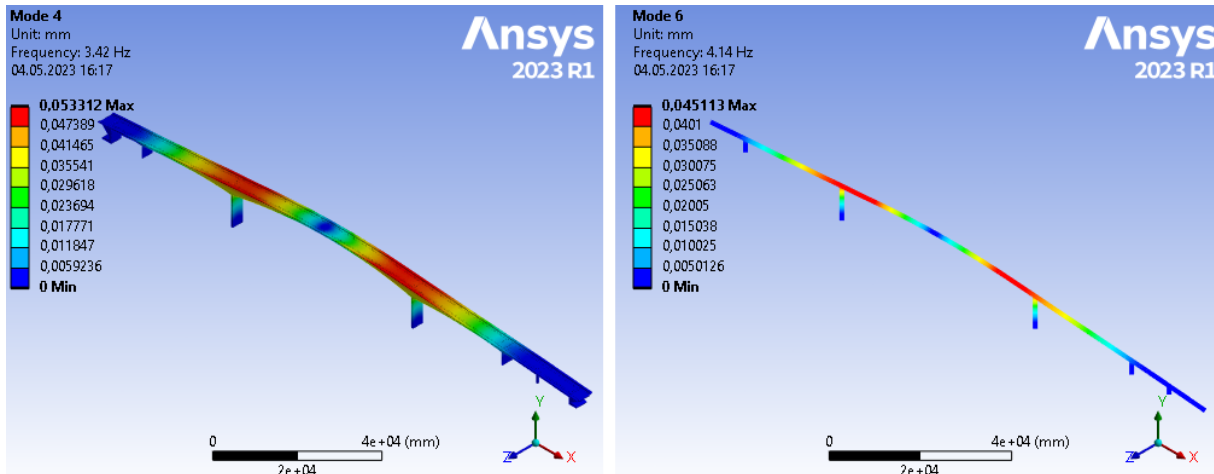


Fig. 26: Mode 4 on the solid model matched by 99,1% with mode 6 on the beam model. Frequency error: -17,4%. [21].

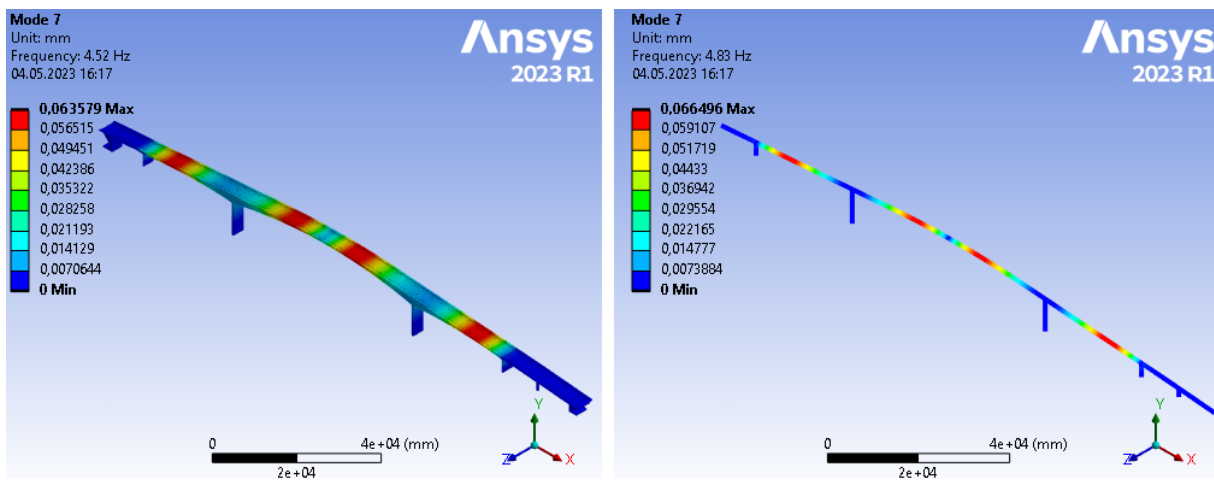


Fig. 27: Mode 7 on the solid model matched by 94% with mode 7 on the beam model. Frequency error: -6,4%. [21].

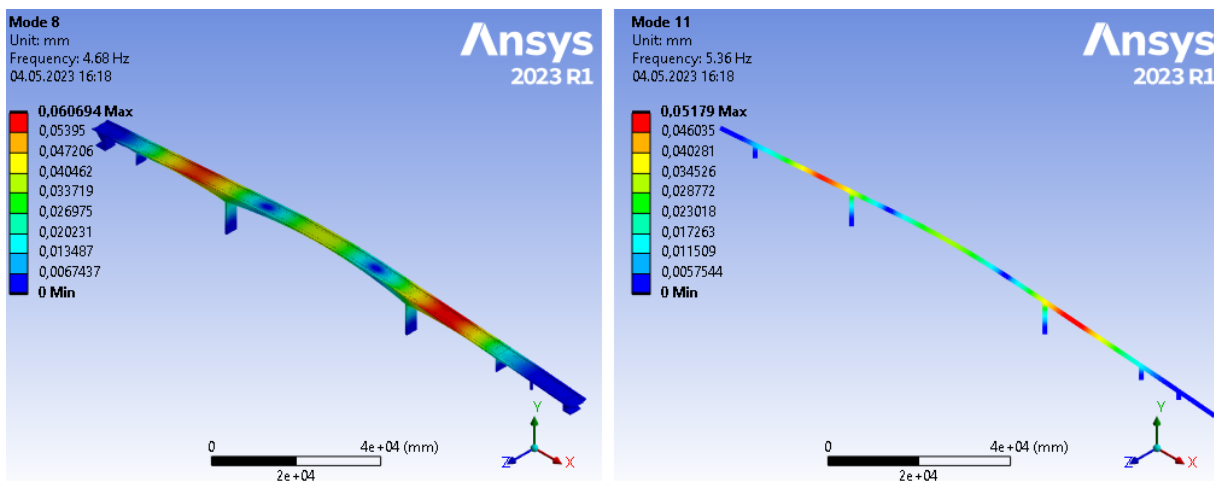


Fig. 28: Mode 1 on the solid model matched by 97,7% with mode 1 on the beam model. Frequency error: -12,5%. [21].

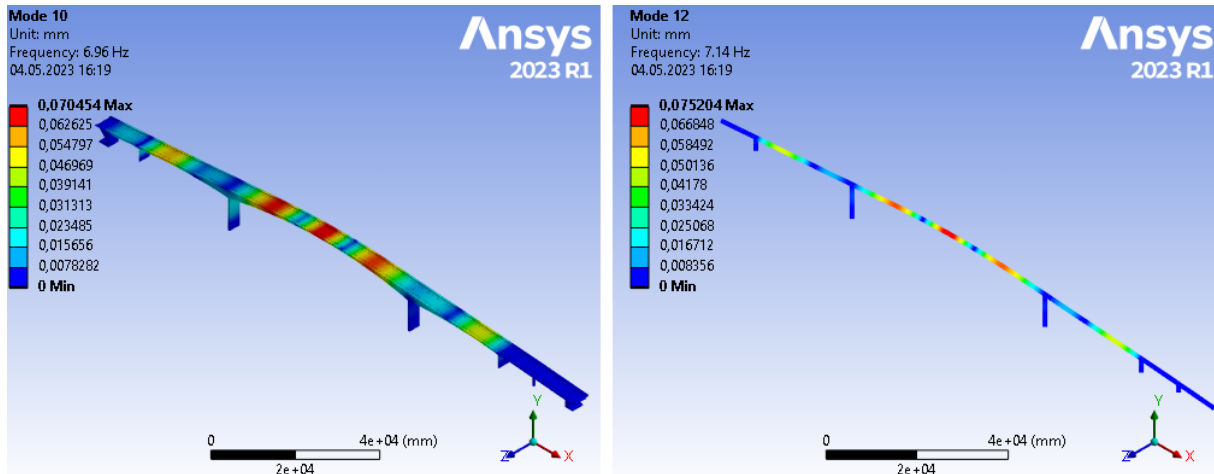


Fig. 29: Mode 10 on the solid model matched by 94,3% with mode 12 on the beam model. Frequency error: -2,6%. [21].

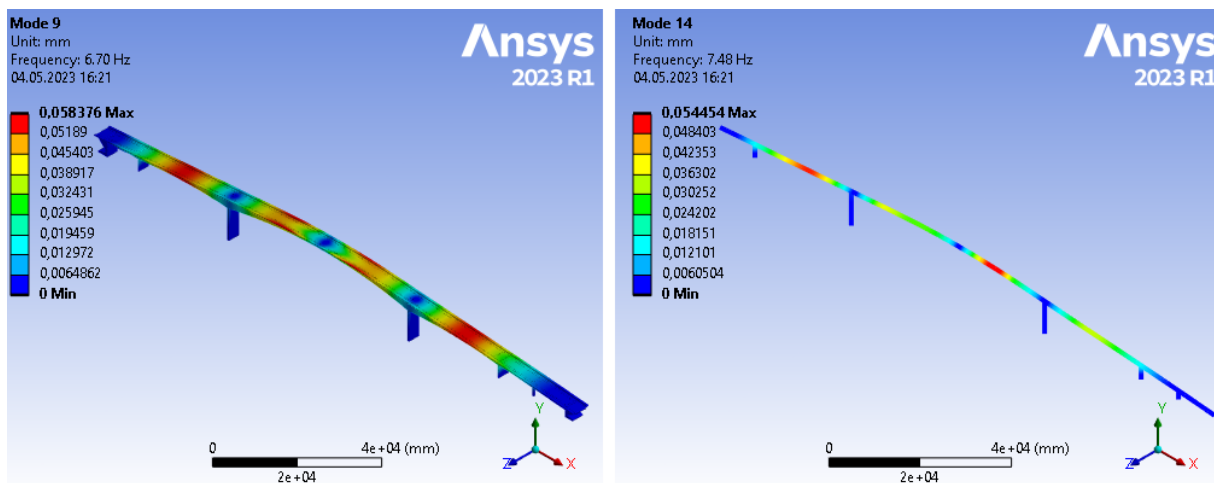


Fig. 30: Mode 9 on the solid model matched by 93,5% with mode 14 on the beam model. Frequency error: -10,5%. [21].

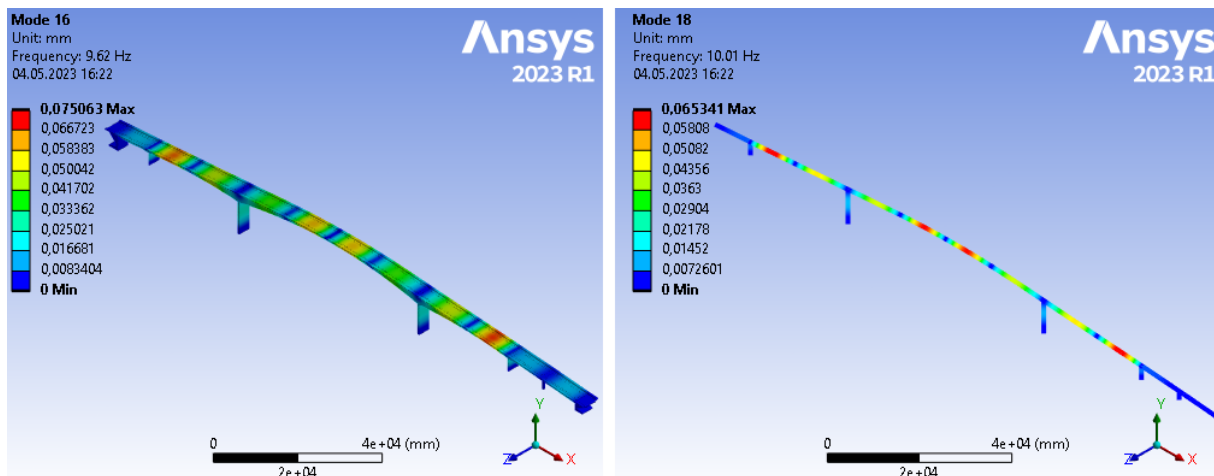


Fig. 31: Mode 16 on the solid model matched by 97,8% with mode 18 on the beam model. Frequency error: 3,9%. [21].

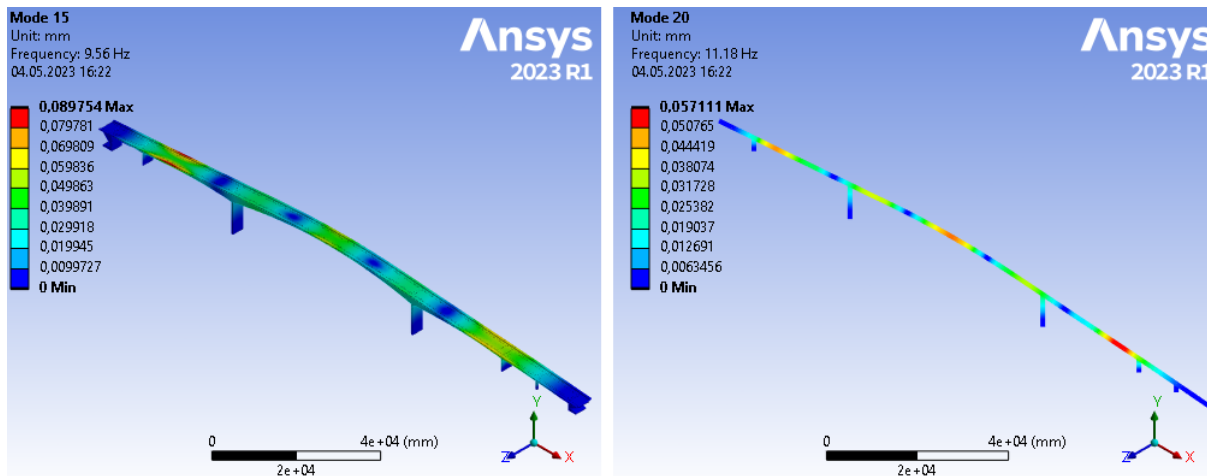


Fig. 32: Mode 15 on the solid model matched by 93,6% with mode 20 on the beam model. Frequency error: -14,5%. [21].

However, the results should be viewed with some scepticism due to missing details in the models, such as rebars (slack reinforcement), post-tensioned cables, creep and loss factors, and nonlinear joints. These details should be incorporated in more advanced models to enhance the reliability of the models' results.

The solid model required significantly more computational power and produced results that were more representative of a concrete bridge structure compared to the beam model. The solid element technology is based on a more precise theory (elasticity theory) compared to the beam theory (Timoshenko), which is a simplified technology that adds a cross-section to a line. Additionally, the beam model includes more simplifications than the solid model. Therefore, more confidence is placed in the solid model, although the beam model can be useful for quick analyses with low computational power requirements, for example, in situ on a laptop.

Table 1 CPU time comparison for modal analysis [21].

Parameter	Solid element model	Beam element model
Total CPU time for all threads	166,6 seconds	3,8 seconds
Sum of memory used on all processes	20406 MB	205 MB
Total amount of I/O written to disk	6.6 GB	0,1 GB
Total amount of I/O read from disk	84 GB	0,4 GB

3.4 FEM linear shell-like approach (LUSAS)

The LUSAS FEM [22] software was engaged for modelling the bridge in the elastic field. The model has been developed only with the aim of identifying the modal properties of the structure and defining the sensor layouts (from Fig. 33 to Fig. 34). Table 2 reports the adopted material properties.

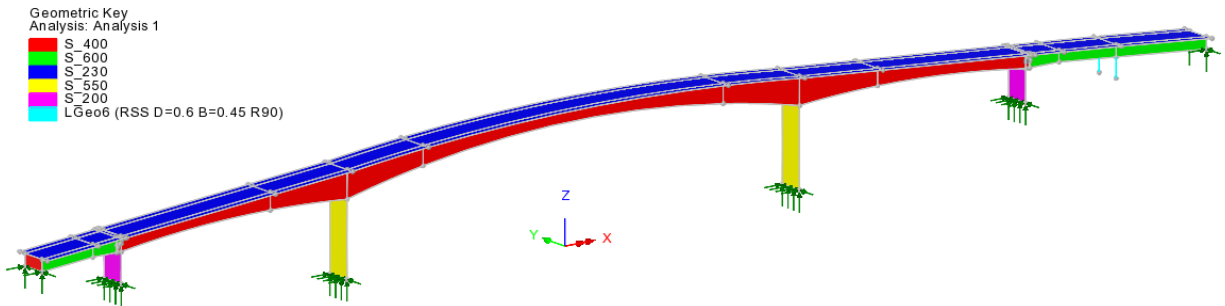


Fig. 33 Section assignment.

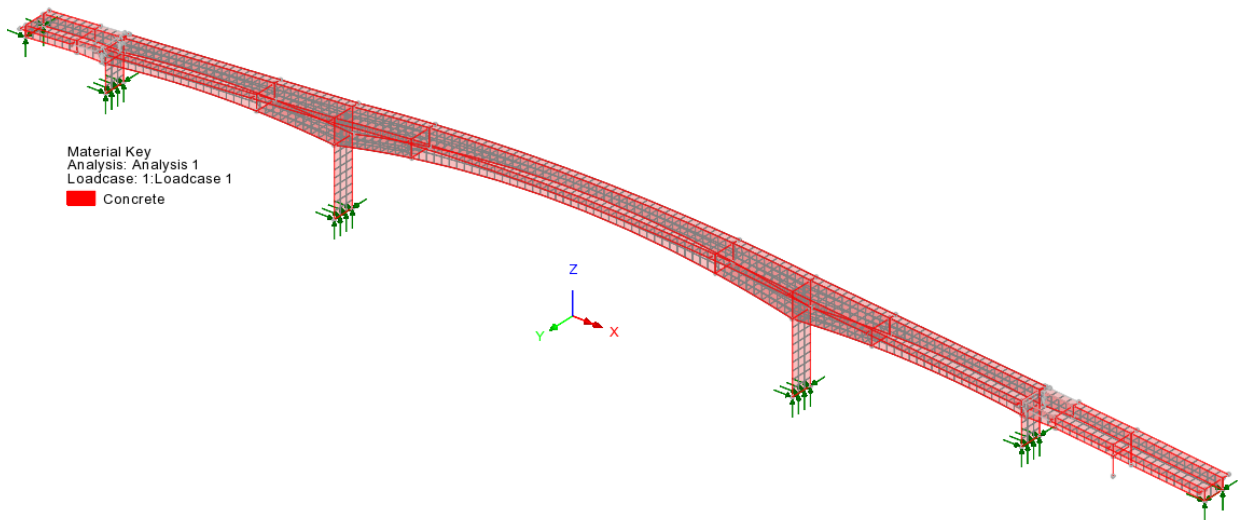


Fig. 34 Material Assignment.

Table 2 Elastic material properties

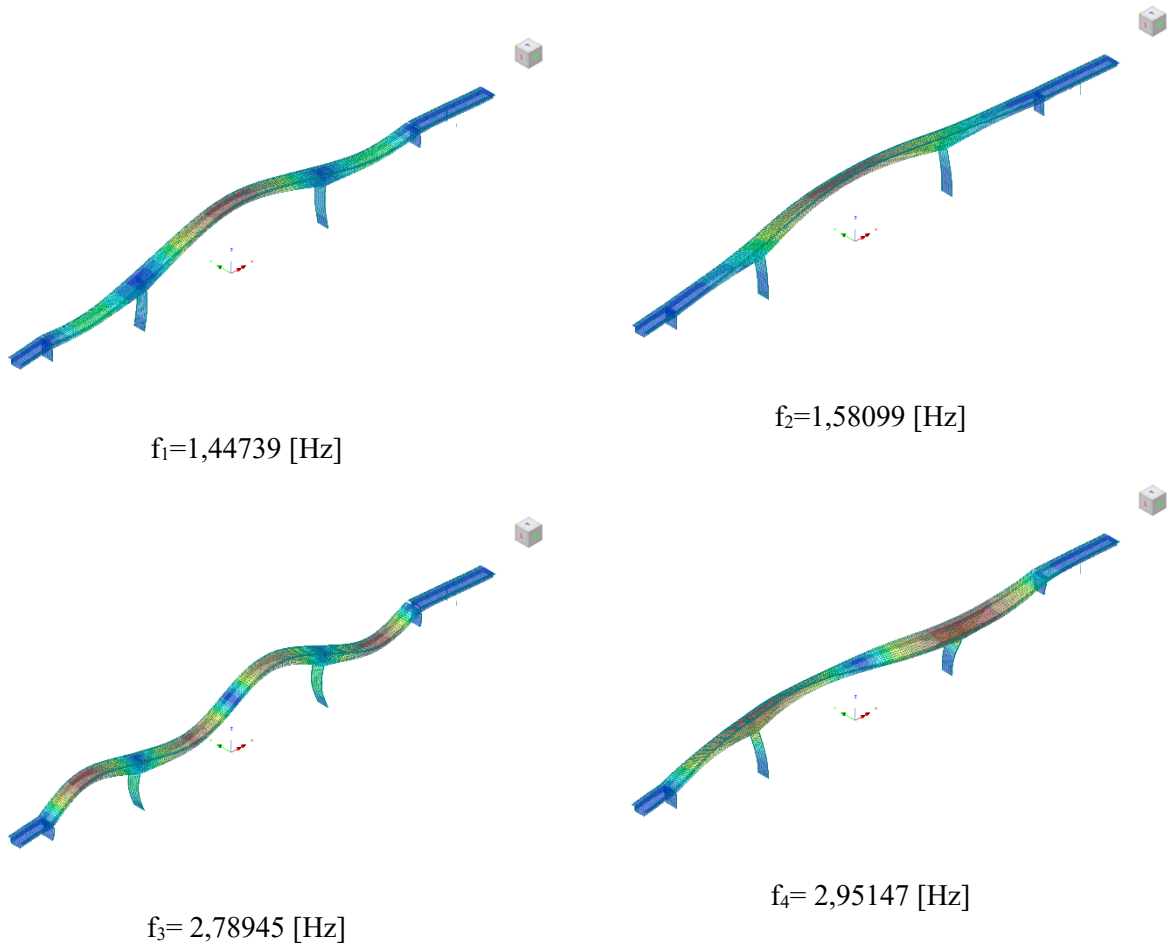
Elastic	
<input type="checkbox"/> Dynamic properties	
<input type="checkbox"/> Thermal expansion	
	Value
Young's modulus	19.36E3
Poisson's ratio	0.14
Mass density	2.39E-9

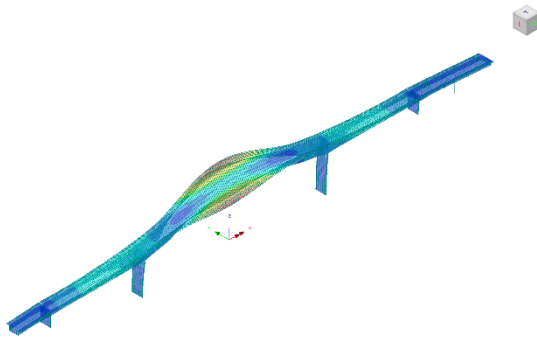
The LUSAS model was necessary for estimating the expected frequencies and the modal shapes. The use of preliminary numerical models helps to defining the sensor layout that has to be considered on the structure. In this case, the more relevant modal shapes are reported in

Table 3. In detail, the first and second modes are in-plane and out-of-plane flexural shapes at frequencies of $f_1=1,448$ [Hz] and $f_2=1,581$ [Hz]. The third mode is a second order in-plane flexural mode at the frequency of $f_3= 2,789$ [Hz]. The fourth mode is a torsional mode due to the out-of-plane piers behaviour

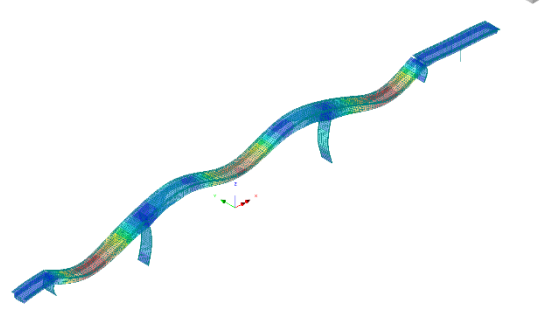
at $f_4= 2,952$ [Hz]. The fifth mode is a pure torsional at $f_5= 3,969$ [Hz]. Lastly, a third order in-plane flexural mode is placed at $f_6= 4,365$ [Hz].

Table 3 Modal results





$f_5 = 3,96883$ [Hz]



$f_6 = 4,36448$ [Hz]

3.5 FEM Shell-based approach (ANSYS)

The second master's thesis, **Shell-Based Finite Element Modelling of Herøysund Bridge** by Zeeshan Azad and tutored by prof. Harpal Singh (UiT Narvik), thoroughly examined the application of the Finite Element Method (FEM) to the numerical modal analysis of the Herøysund Bridge. It focused on the theoretical backdrop, construction process, FEM techniques, and Eurocode recommendations for concrete structures. This study aimed to demonstrate the utility of FEM in bridge analysis by utilizing ANSYS 2023 R1 to conduct a comprehensive numerical investigation of the bridge's technical specifications and design features.

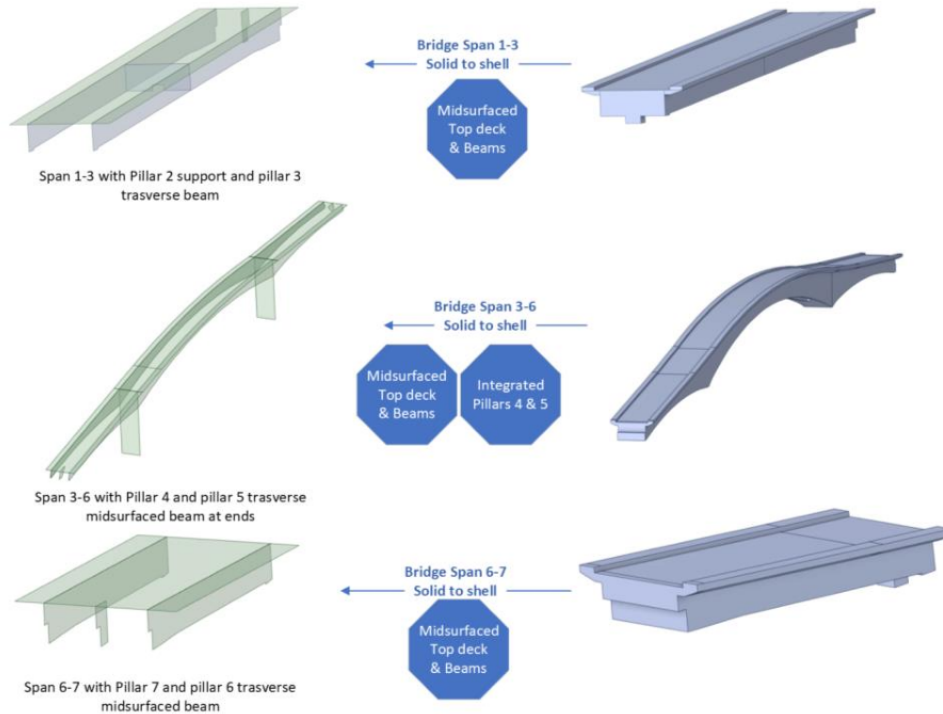


Fig. 35 Shell and Solid model transformation [23].

The thesis discussed the theoretical background, including the context of applying FEM for bridge design and main bridge construction techniques. It then examined the specific FEM approaches applied, along with their advantages and disadvantages. The Herøysund Bridge analysis employed a two-pronged strategy consisting of a 3D-Solid Model and a Shell Model (Fig. 35, Fig. 36). To forecast the physical behaviour of the structure, assumptions, modelling methodologies, and the incorporation of specific components such as pillars were applied to both approaches. The document described the complexity of bridge design, from the selection of units and materials through the development of connections and meshes.

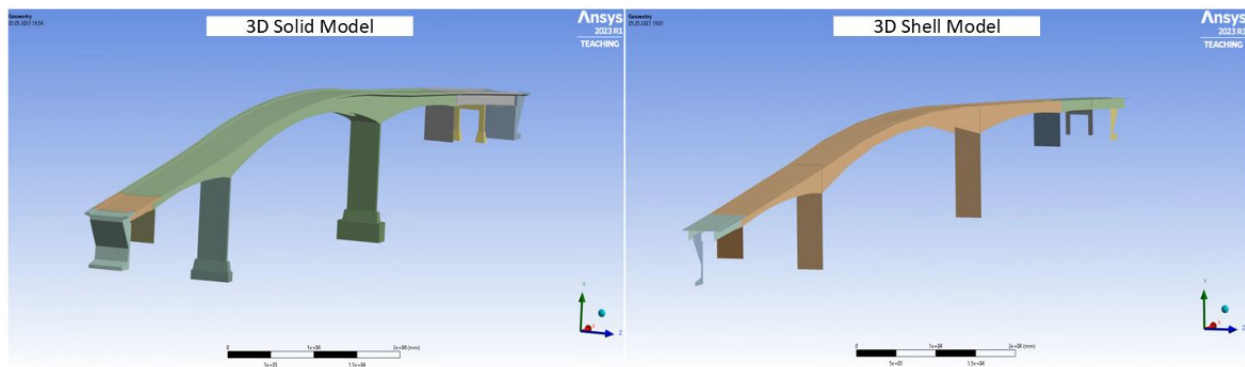


Fig. 36 3D-Solid and 3D Shell bridge geometry [23].

The full report also emphasized the importance of boundary conditions (Fig. 37, Fig. 38), examining the structural effects of standard earth gravity, post-tensioned load, and railing and asphalt load. The results section thoroughly explored the mode shapes and frequencies for the 3D-Solid and Shell models.

Table 4 Factors influencing the deformation in Solid and Shell models [23].

Factors	3D- Solid model	Shell model
Simplified geometry	Volume based elements	Thin surface elements
DOFs	3198967 DOFs	643243 DOFs
Stiffness Distribution	Higher	Lower
Boundary conditions	Applied to surfaces	Applied to edges
Load distribution	Higher loads on surfaces	Higher loads on edges

Table 5 Material properties for models in numerical simulations [23].

Properties	Concrete	Structural Steel
Density, Kg/mm^3	2.39e-06	7.85e-06
Young's Modulus, MPa	19360	2.00e+05
Poisson's Ratio	0.1414	0.3
Bulk Modulus, MPa	8998	1.67e+05
Shear Modulus, MPa	8480.8	76923
Tensile Ultimate Strength, MPa	1.1960	460
Tensile Yield Strength, MPa	1.0950	250
Isotropic Thermal Conductivity, $W/mm^{\circ}C$	0.002071	0.06050
Specific heat constant pressure, $mJ/Kg^{\circ}C$	9.36e+05	4.34e+05
Isotropic Resistivity, $ohm - mm$	5.85e+07	-
Secant Thermal Expansion Coeff.	-	1.20e-05

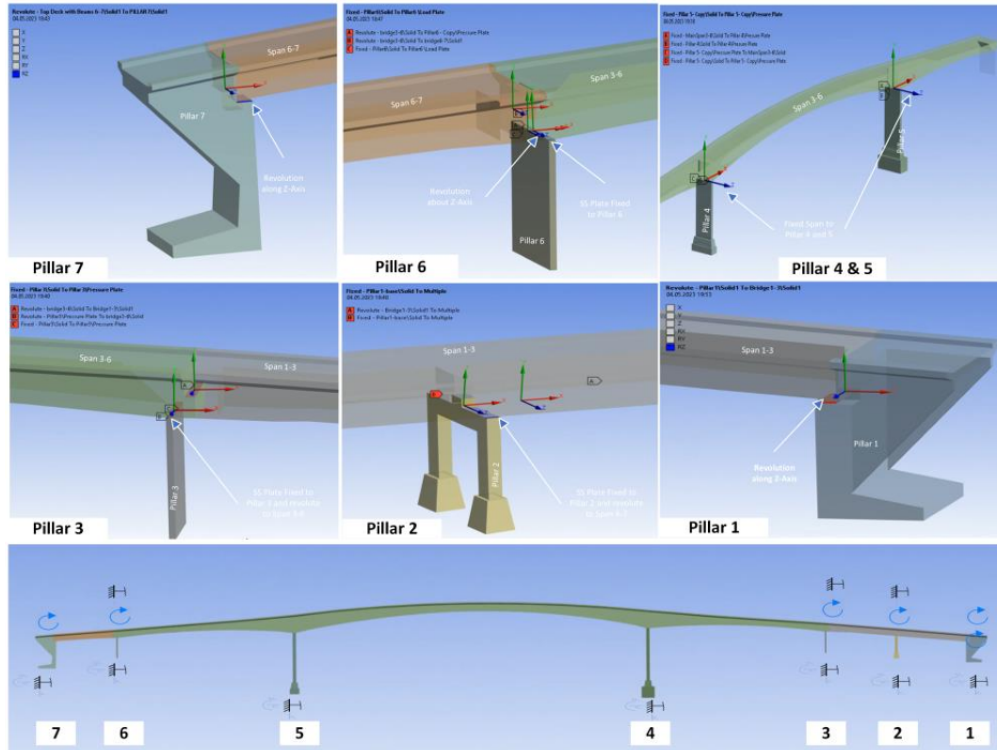


Fig. 37 3D-Solid model joints across all pillars [23].

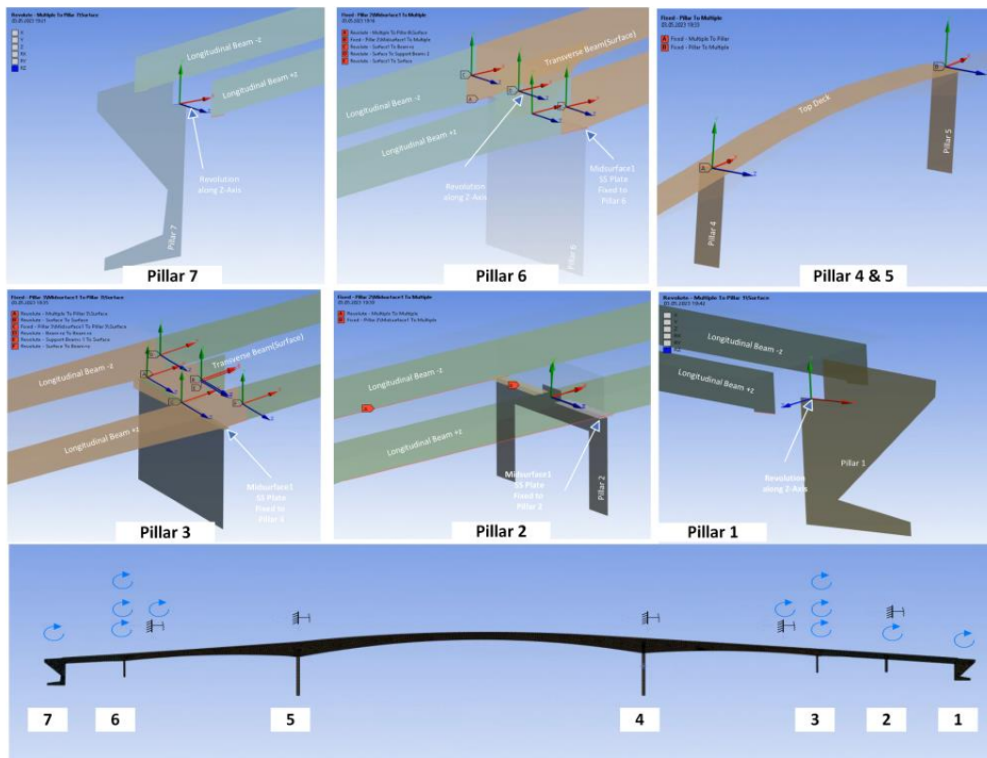


Fig. 38 Shell model joints across all pillars [23].

The Modal Assurance Criteria analysis compared modal frequencies across several modes, including flexural, transverse bending, and twist modes. The conclusion of the thesis included findings obtained from the study, implications for the Herøysund Bridge, detailed resonant frequencies of the structure, and a comparison of both modelling strategies. It also incorporated ideas for future research and guided the use of FEM 3D-Solid and Shell methods to design and construct more efficient, resilient, and durable bridge structures (Fig. 39).

The primary aim of this thesis was to provide an in-depth numerical prestressed modal analysis of 3D Solid and Shell models utilizing finite element modelling for Herøysund Bridge design. FEM was used to accurately predict structural deformations, modes, shapes, and modal frequencies in a post-tensioned concrete bridge structure. Developing a 3D solid model and extracting the Shell model through mid-surfacing yielded high similarity between models.

The Shell model required geometrical simplifications due to the different element types used in numerical simulation. The mass and volume control for models resulted in a percentage difference of 1.028%, which was negligible; however, the Shell model resulted in a mass distribution difference across the structure. Structural analysis revealed distinct deformations for 3D Solid and Shell models, with Shell models allowing more deformation than the Solid model. Another significant finding was that the defined joints, instead of default bonded joints, allowed the bridge connections to deform realistically.

The total deformation for the Solid model was in good agreement with the structural calculations from AAS Jacobsen, validating the Solid model. The total deformation of the 3D Solid model yielded a better representation of the physical structure. The prestressed modal analysis revealed distinct mode shapes and modal frequencies for 3D Solid and Shell models.

The study also explored differences in the modal frequencies across various modes, including flexural, transverse bending, and twist modes. The MAC correlation for Shell vs. Solid found that the MAC correlation for nine modes out of twenty was in good agreement (80-100%). Although the mode shapes were identical, they appeared in different sequences for the Shell model because of the mass distribution difference across different spans.

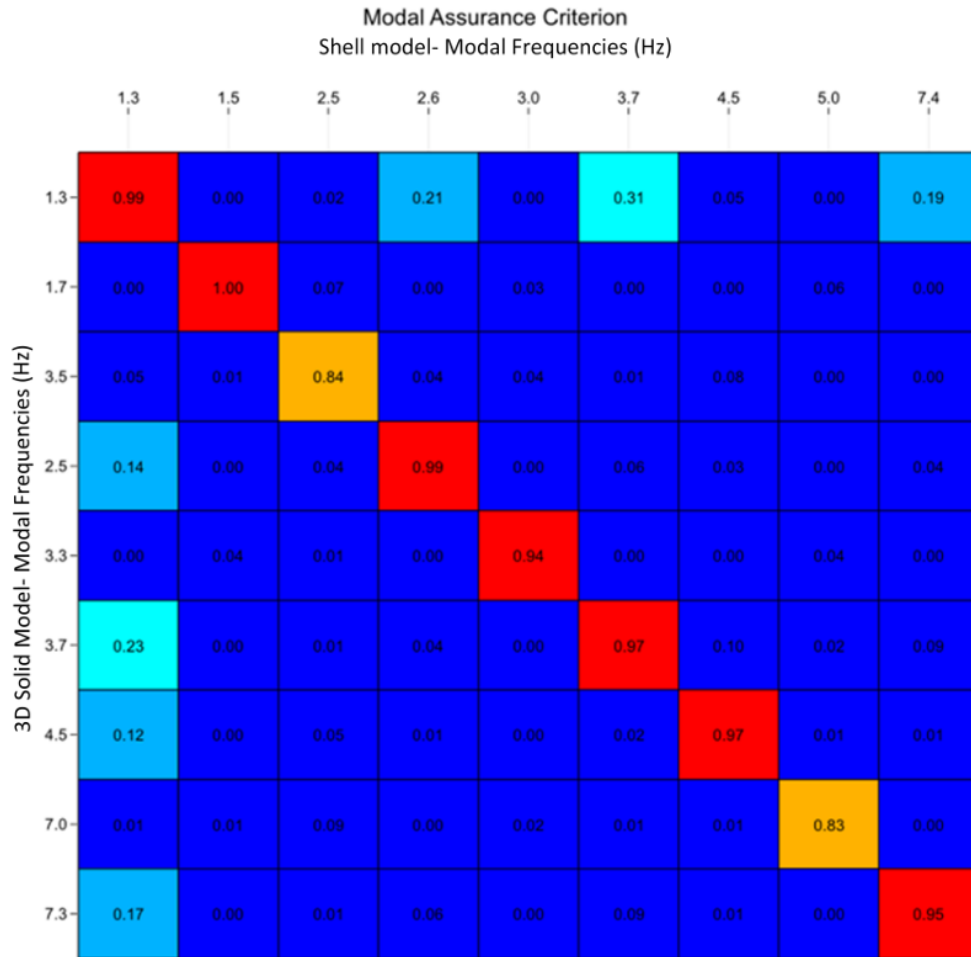


Fig. 39 MAC Index matrix for Solid and Shell model matched modes [23].

Despite the comprehensive analysis, the study had limitations such as limited post-tensioned tendons details, leading to assumptions; shell model geometrical limitations, leading to mass distribution differences; time constraints to dive deeper; and approximations in applying boundary conditions in ANSYS. The findings were significant for the Herøysund Bridge since the data obtained for both models would significantly contribute to comparing experimental vibration data with numerical results. This study also signified the credibility of the 3D Solid model strategy for complex concrete structures such as the Herøysund Bridge. Finally, the insights derived from this study underscored the importance of FEM in revolutionizing bridge design, leading to efficient and more reliable structures.

3.6 FEM damage modelling (ANSYS)

The thesis, **Numerical Modelling of Damage Conditions on Herøysund Bridge in Herøy Municipality, Nordland, Norway** by Christopher Odongo and tutored by prof. Harpal Singh (UiT Narvik), introduced the study of damage conditions. The usability of bridges is highly dependent on their safety conditions since they are subjected to various loads that might compromise their ability to withstand stresses over a prolonged period.

As a result, fracture failure analysis and dynamic response evaluations are essential for monitoring the behaviour of bridges, predicting their lifespan, and planning rehabilitation. This study aimed to investigate the structural behaviour of the Herøysund Bridge through analytical computation and numerical simulation of its damage conditions, focusing on fracture failure analysis and dynamic response.

The study began by developing a 3D solid model of the bridge, with induced cracks, in SolidWorks based on existing 2D drawings and photos taken at the actual bridge site. The Computer-Aided Design (CAD) model was then transferred to ANSYS Mechanical software for finite element analysis. An overview of the analytical computation of free and ambient vibration of idealized bridge structures was conducted alongside fracture failure inspections of the cracks. This aimed to deduce the theoretical concepts of dynamic response and crack growth analysis.

Subsequently, ANSYS finite element modelling was performed, focusing on crack propagation dynamics, modal parametric analysis, harmonic response, response spectrum, and random vibration reviews. Results were generated in terms of stress intensity factors (SIFs), strain energy release rate (J-integral) values of cracks, mode shapes, natural frequencies, phase angles, peak response locations, total and directional deformations, and equivalent stresses on the bridge model. Finally, the obtained results were discussed, and conclusions drawn.

This master's thesis project sought to investigate the damage conditions of the Herøysund Bridge through structural design modelling and finite element simulation. The project was accomplished through 3D modelling of the Herøysund Bridge and numerical simulation of static structural parametric evaluation of fracture mechanics, modal, and vibratory analysis. The structure was designed in SolidWorks considering all the available 2D drawings. Subsequently, numerical simulations of fractures, modal and vibratory parameters, such as harmonic response, response spectrum, and random vibration, were executed.

Seven cracks were induced in the structure, and their analysis was based on stress intensity factors (SIFs) and strain energy release rate (J-integral) values. Structural deformation and equivalent stress on the bridge due to loading were also determined. SIFs and J-integral values were compared against the fracture toughness (K_{1C}) and critical J-integral (J_C) values of concrete to determine which cracks were likely to propagate.

The analysis revealed that cracks 2, 4, 5, and 7 had zero probability of propagation, while cracks 1, 3, and 6 had a very high probability of propagation. Therefore, it was concluded that cracks 1, 3, and 6 were likely to cause structural failure of the Herøysund Bridge, while cracks 2, 4, 5, and 7 posed no structural failure risk (Fig. 40, Fig. 41).

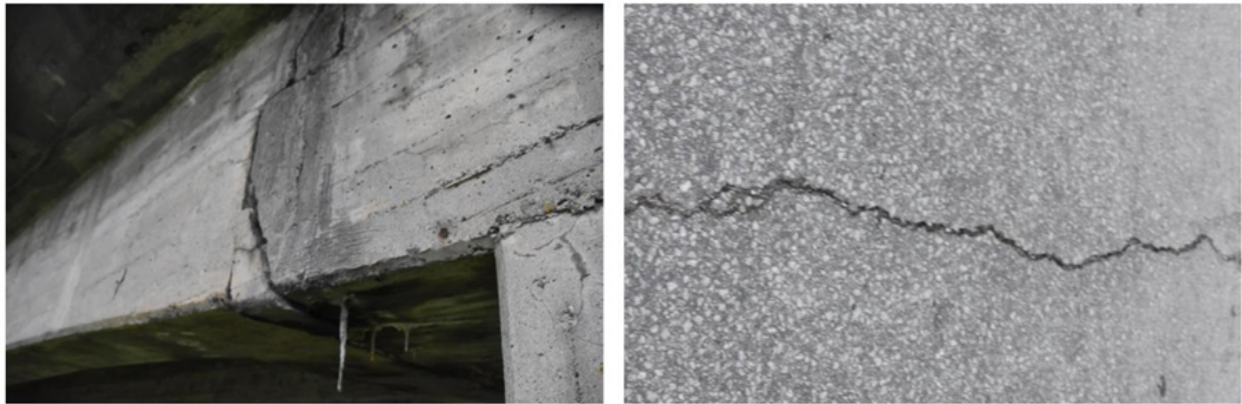


Fig. 40 Photos of some of the cracks identified on Herøysund bridge [9].

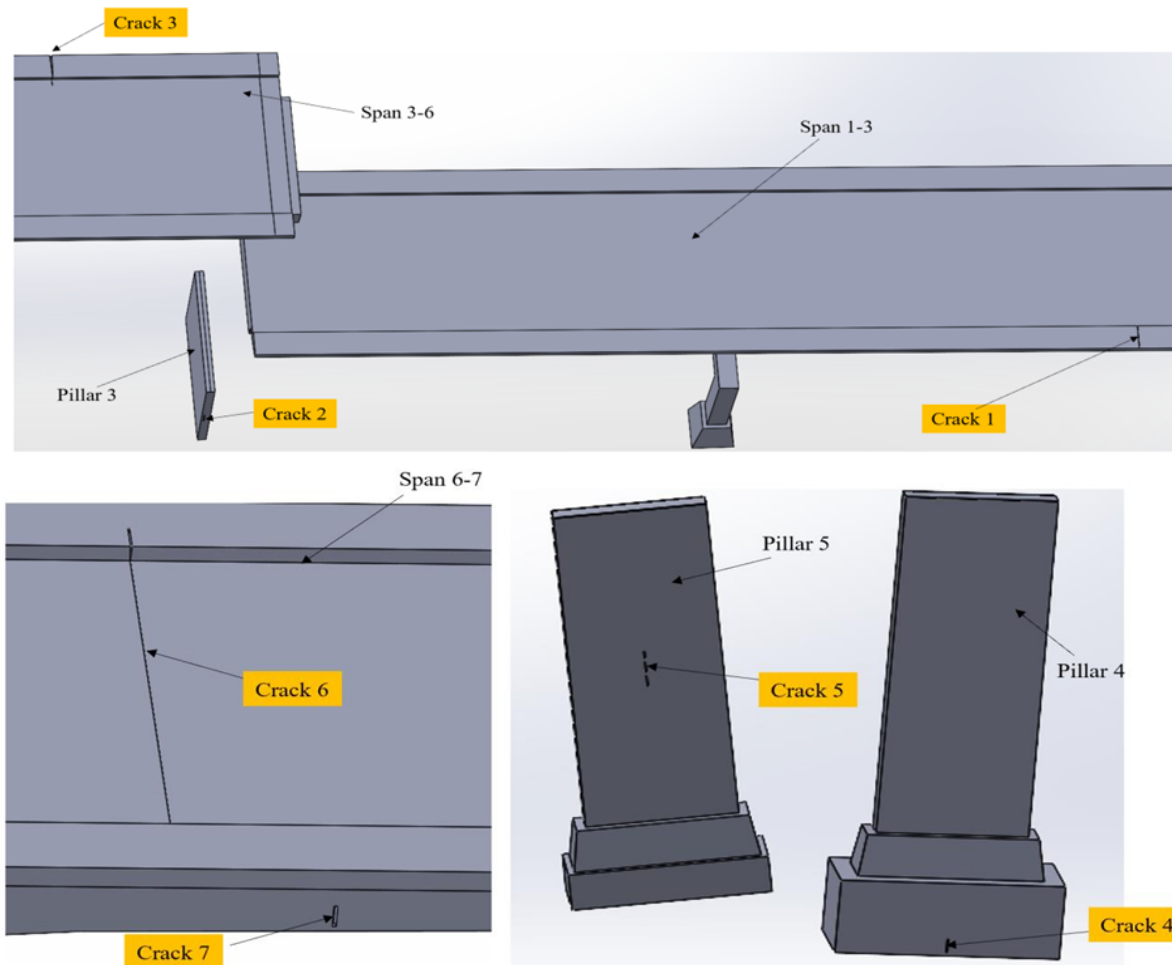


Fig. 41 Location of cracks in the model [9].

Additionally, dynamic response analysis of the bridge was conducted through modal analysis, harmonic response, response spectrum, and random vibration to investigate the bridge's behavior under loading. In modal analysis, flexural, transverse, and torsional deformation mode shapes were generated at varying frequencies. The lowest energy level mode 1 had a frequency of 1.4236 Hz, and the highest energy level mode 20 had a frequency of 11.493 Hz. Participation factor and effective mass were generated and applied to determine the translational and rotational excitation of the modes. It was discovered that transverse modes 2 and 8 had significant contributions.

Harmonic response analysis was performed to find the peak response location. The study disclosed that a peak response frequency of 1.4184 Hz and phase angle of 93.943° produced a maximum deformational amplitude of 0.59247 m on bridge span 3-5. The research affirmed the main bridge span 3-6 as the peak response location of the bridge. Frequency response velocity and acceleration were also performed, with peak response velocity found to be 5.287 m/s at a frequency of 1.4236 Hz, while peak response acceleration was 47.353 m/s^2 at a frequency of 1.4288 Hz. Total and directional deformation and equivalent stress on the bridge structure were investigated. Maximum directional and total deformation were experienced on bridge span 3-5 and minimal on bridge pillars 1 and 7. The maximum equivalent stress on the bridge was found on the load-bearing steel plate on pillar 6, and the minimum equivalent stress was encountered on bridge span 3-5.

Further, response spectrum and random vibration analysis of the Herøysund Bridge under loading were conducted. In response spectrum analysis, RS acceleration data was used to determine total and directional deformation, and directional velocity and acceleration of the bridge. The analysis found that total deformation, directional deformation, and directional velocity were optimal on the main bridge span 3-5, while directional acceleration was high on span 5-6. Maximum equivalent stress was experienced on the load-bearing steel plate on pillar 6. In random vibration analysis, input power spectral data (PSD) was applied to investigate probable deformation, stresses, and strain on the bridge. A 3-sigma (3σ) scale factor value with a probability of 99.73% was applied in this analysis. It was deduced that, 99.73% of the time, the directional deformation of the bridge would be greater than zero but would not exceed 1.5314 m in the x-axis direction and 1.9976 m in the y-axis direction. Similarly, the equivalent von Mises stress on the bridge would be greater than 99.078 kPa but less than 5.6655 GPa in the x-axis direction. Furthermore, the normal elastic strain of the bridge would be less than 0.10495 m/m in the x-axis, 0.097805 m/m in the y-axis, and 0.058221 m/m in the z-axis directions.

To sum up, structural deformation was highly prevalent in bridge spans 3-6 and minimal on bridge pillars 1 and 7 for all evaluated parameters. However, for equivalent stress analysis, it was identified that maximum equivalent stresses were experienced by the load-bearing steel plate on pillar 6 and minimal equivalent stresses on bridge spans 3-6. The average equivalent stresses obtained were much higher compared to the ultimate tensile strength and tensile yield strength of concrete, indicating a high possibility of structural failure of the Herøysund Bridge under the given dynamic loading conditions. Therefore, based on the findings and crack propagation results, the Herøysund Bridge is at high risk of structural failure, and precautionary measures must be undertaken to avert potential adversities.



Chapter 4

Operational Modal Analysis (OMA)



4 Operational Modal Analysis OMA

4.1 Introduction

Operational Modal Analysis (OMA) is used to identify Output-only systems, i.e., those for which it is possible to measure only the response of the dynamic system while the forcing (input) remains unknown. OMA techniques are convenient when estimating the dynamic properties of a structure, i.e., the natural frequencies, the vibration modes, and the damping from the dynamic responses [18].

OMA techniques are based on four basic assumptions [13] that must be verified to obtain reliable estimates:

- Structure time invariance;
- The forces should have broadband frequency spectra;
- The forces must be distributed over entire structure;
- The force must uncorrelated;
- The forces must be distributed on the entire structure.

This approach differs from experimental modal analysis because the forces acting on the structure are unknown. For this reason, it is necessary to model forces as stochastic processes [13]. The fundamental idea of OMA identification is that the structure to be tested is excited by excitations with approximately white noise characteristics, i.e. with energy distributed over a wide frequency range that covers the frequency range of the modal characteristics of the structure. In this stochastic framework the forces that excite the structures are assumed to be a stochastic Gaussian noise process. This type of process has a wide range of frequencies, each of which has the same energy level. However, it is very difficult for this hypothesis to be verified, since it is probable that some frequencies contained in the input have more energy than others and therefore its power spectral density is not flat.

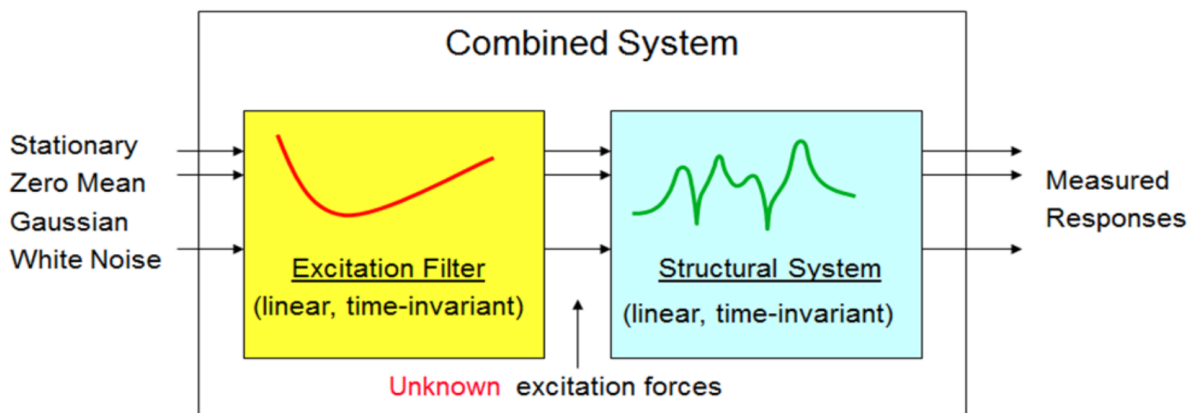
To deal with this problem, it is assumed that the input white noise is modelled by a linear filter that transforms the power spectral density into that of the unknown effective forcing which does not have the same energy on all frequencies [18]. Therefore, the structure's dynamic response will contain the characteristics of the structural system and those of the linear filter that models the Gaussian stochastic process hypothesized as input. By analysing the hypothesis underlying OMA, we can conclude that the system must be excited by a stochastic broadband input, so that all the modes of interest are adequately excited. It worth noting that the spectra resulting from the dynamic responses could contain peaks not related to the characteristics of the structural system [18].

The measured temporal signals can be processed in the time domain or in the frequency domain. Since the forcing function is unknown, it is not possible to calculate the frequency response function between the force and response signals. Instead, the analysis is based on correlation functions and spectral density functions estimated from the operational responses.

In conclusion, operational modal analysis allows, therefore, to exploit the environmental noise for structural identification, thus avoiding the use of special equipment (vibrating hammers, instrumented hammers, hydraulic or electrodynamic exciters) that directly excite the structure.

This results in a number of advantages:

- The test is quick and economical, since no equipment is needed to excite the structure,
- The measurements are carried out under the actual operating conditions of the structure, so the modal parameters obtained are representative of the dynamic behaviour of the structure in its actual conditions of use.
- The test does not interfere with the operation of the structure (so, for example, it is not necessary to close a bridge to traffic when it is being analysed).



The stochastic framework used in Operational Modal Analysis

Fig. 42 Stochastic framework used in Operational Modal Analysis [24].

There are many applications of OMA techniques, especially for monitoring the operating conditions of road infrastructures. Other applications can be found in the study of civil buildings, although with different degrees of success depending on the construction type used and the geometric characteristics of the structure.

Another very interesting field of application, which contributed to the development of these techniques, is that of wind turbines. In fact, one of the first algorithms, called NEXt, was developed by [25] precisely with the aim of studying the dynamics of wind turbines. It is worth noting that the application of OMA techniques to this specific area is not obvious, as for example the first assumption of structure time invariance is not respected, because in this case the structure is made up of several mobile parts in motion with respect to each other during the operational phase of the wind turbine.

Presence of harmonics and aeroelastic effects due to the rotating rotors [25]. There are multiple challenges to face when these techniques are applied in real cases which can lead to inaccurate estimates of modal

frequencies by up to 30% [26]. These differences are due to multiple factors, such as: the difficulty of modelling damping; the existing relationship between temperature and frequencies: the effect of the thermal factor must be considered to obtain a more accurate estimate of the natural frequencies. Variations or deviations in the distribution of masses and stiffnesses; the relationship between input intensity and the dynamic response of the system: Even assuming that the properties of the forcing are consistent with those previously described, the frequencies estimated in a certain time window can change due to a greater input intensity [27].

4.2 Theory and Methods

Frequency Domain Decomposition (FDD) is an output-only method useful for identifying the vibration frequencies and the corresponding mode shapes of a structural system starting from the accelerations recorded on the structure (output); it is based on the assertion that the eigenvectors, which represent the vibration modes, constitute a basis, being linearly independent, so that a linear combination of them can represent any displacement of the system and it is possible to decouple the components of the various modes. This last property can be applied to the system response, measured at each point where the accelerometer is positioned, or to the spectral density (Power Spectral Density, PSD) of the accelerometric history, through a singular value decomposition (Singular Value Decomposition, SVD) of the matrix that represents it at each frequency (Wall et al., 2003).

The frequencies and mode shapes provided by this procedure are more valid when the following conditions are verified:

- the excitation is a Gaussian white noise with zero mean and unit standard deviation.
- the identified mode shapes are orthogonal.
- the structure has a low damping coefficient (Brinker et al 2000).

In the FDD identification process, the first step is to estimate the power spectral densities (PSD) obtained through the Fourier transform of the autocorrelation signals. In particular, the PSD matrices are constructed by varying the frequency in the range of interest for the structure under examination and compatible with the sampling frequencies of the signals recorded by the accelerometers.

The second step consists in the singular value decomposition (SVD) of the matrix in which the PSDs of the input signals are allocated.

The singular values obtained from the SVD of the PSD matrix at each frequency are equal in number to the number of accelerometers used. They represent the energy contribution of the different structural modes at the specific frequency. The highest singular values indicate the dominant modes, while the associated singular vectors contain the information on the relative mode shapes.

The third step consists in the graphic representation of the spectrum of singular values from which it is possible to recognize the peaks representing the identified modes. In fact, the natural frequencies associated with a mode are identified graphically through the peak-picking technique. Each identified peak is

associated with a singular value to which the singular vectors correspond. At the frequencies where peaks in the singular values are observed (the natural frequencies), the first singular vector obtained by the SVD approximates well the mode shape associated with that frequency at the measurement points of the accelerometers.

Stochastic subspace identification (SSI) is a well-known operational modal analysis (OMA) algorithm. It is based on the state space representation of a linear time-invariant system. The SSI algorithm works only on measured output response data (the input excitation is not measured in OMA). From the point of view of modal parameter estimation, the estimation of the state transition matrix is most important since its eigenvalue decomposition reveals modal parameters.

Two variants of this algorithm are very popular in practice:

- data-driven (SSI-Data)
- covariance-driven (SSI-Cov)

These variants differ in terms of the data they operate on. SSI-Data operates directly on the response data, processing it to build the matrices needed for system identification. On the other hand, SSI-Cov requires that autocovariance functions are initially estimated from the output time series. It is precisely on these functions that SSI-Cov relies on the estimation of the modal parameters.

Stabilization Diagram: Dynamic identification methods in the time domain, especially those based on state-space theory, suffer from a fundamental problem: the a priori choice of the order of the dynamic system, i.e. the number of modes to be identified or degrees of freedom. Since modal analysis, in engineering practice, is applied to real structures, i.e., having an unlimited number of degrees of freedom, this aspect is vital to obtaining good results.

The most common practice to overcome this problem is to repeat the identification for different orders of the dynamic system, included in an a priori established interval. In this way, many values of the modal parameters are obtained, particularly the frequency, for each vibration mode. However, this inevitably leads to non-physical modes, called noise modes, which must be isolated from the real modes, and discarded from the results.

The procedure for isolating such spurious modes is based on the values of the modal parameters obtained for each chosen order; it involves introducing comparison parameters, for which a threshold acceptance value can be prudentially established. A set of parameters is introduced that take into account the percentage variation of frequency and damping ratio, and the so-called Modal Assurance Criterion (MAC) compares the modal shapes and assumes a value between 0 and 1, where it is 1 when the two modal shapes coincide.

Chapter 5

Instrumentation, data acquisition & data processing on the Herøysund Bridge



5 Instrumentation, data acquisition and data processing on the Herøysund bridge

5.1 Introduction

This chapter describes the instrumentation used in the dynamic identification campaign carried out in the Herøy FoU project. The characteristics of the data acquisition system, the adopted accelerometer sensors and the data processing methods to obtain accurate timing of the dynamic properties of the structure under investigation will be presented.

Accelerometer

The experimental campaign's objective is to estimate the structure's dynamic properties in conditions of environmental noise (AVT) and operating conditions, i.e. in the presence of human activity and during normal hours in which vehicular traffic is present. Considering that the intensity of the vibration induced on the structure in conditions of environmental noise is minimal, it was necessary to choose extremely sensitive instrumentation both with respect to the accelerometer part and to the analog-to-digital conversion control unit.

The sensitivity of Model 393b12, shown in Fig. 44, is 10,000 mV/g, making it capable of measuring even the slightest vibrations. Following the main features of the Model 393B12:



Fig. 43 PCB 393B12 Accelerometer.¹

- 1 **Sensitivity:** 10,000 mV/g ($\pm 10\%$)
- 2 **Frequency Range:** 0.15 to 1,000 Hz ($\pm 5\%$)
- 3 **Measurement Range:** ± 0.5 g peak
- 4 **Broadband Resolution:** 0.000008 g rms
- 5 **Environmental Durability:** Operating temperature range from -45 to $+82$ °C, with a shock limit of $\pm 5,000$ g peak

¹ <https://www.pcb.com/products?m=393b12>

These accelerometers are hermetically sealed in stainless steel housings, providing robustness and longevity in outdoor environments. They are equipped with a 2-pin MIL-C-5015 top connector and a 1/4-28 female mounting thread, facilitating secure and stable installation on bridge structures.

LEAP 8-32

The Quakebots LEAP DAQ system, designed with a serverless architecture, operates independently without the need for a central server, increasing its versatility and allowing it to operate in a variety of remote locations. An integrated firewall, AES-256 payload encryption, and IP whitelisting are cybersecurity features that protect the system and recorded data, ensuring safe operation in potentially harsh environments.

With a dual-core ARM CPU up to 866 MHz, 512 MB of DDR3 RAM, and 8 GB of eMMC storage, the DAQ hardware configuration is robust. An FPGA module ensures efficient and reliable performance because it is dedicated exclusively to the ADC processes for data acquisition. The system has eight RJ45 differential input ports that support different voltage ranges (± 1 V, ± 3.3 V, ± 5 V, and ± 10 V) and allow specific software configuration for each input port to meet various sensor requirements. Each sensor port also has a 12V power supply that can be configured as needed.

The DAQ supports flexible deployment data transmission and integration modes, such as cloud storage, direct server control, and automatic data transfer to single or multiple servers. It also enables precise time synchronization via configurable NTP servers, ensuring data consistency across multiple channels and locations.

Server

The Compute Module MIC-7700, used in the Herøy FoU DAQ system, is a robust modular platform that supports Intel® 6th/7th Gen Core™ i CPUs (LGA1151) and operates on either Q170 or H110 chipsets. This module provides reliable computing power and operates efficiently across a temperature range of -10 to 50 °C. With dual LAN ports (Gigabit Ethernet) and multiple USB 3.0/2.0 ports, it ensures high-speed data transfer and seamless connectivity with various peripheral devices, including sensors and other DAQ components.

The module includes extensive I/O options, including serial ports (RS-232/422/485) and digital displays via VGA and DVI, making it adaptable for diverse instrumentation setups. For data storage, the MIC-7700 supports various configurations, including 2.5" HDD/SSD, CFast, and mSATA, providing ample space and flexibility for data-intensive monitoring applications. Additionally, it features an input power range of 9 to 36 VDC, allowing it to function in varied field conditions, and is capable of expansion through Advantech i-Modules, accommodating additional PCIe and other I/O requirements.

In the Herøy FoU project, the MIC-7700's modularity, processing power, and connectivity capabilities enhance the DAQ system's overall reliability, supporting the precise acquisition and processing of data essential for Operational Modal Analysis and continuous structural monitoring.



Fig. 44 Cabin office by the bridge.



Fig. 45 Server.



Fig. 46 Sensors and DAQ before mounting.



Fig. 47 Local DAQ placed under the bridge.



Fig. 48 Example of sensor placement under the bridge.

5.2 Data Acquisition

As introduced in the previous chapters, the data acquisition system used for the experimental campaign consists of high-performance components. The system enables the acquisition of high-frequency data and extremely precise time synchronization, which allows consistent results in the dynamic identification activity, system components and configuration.

The system is made up of a MIC-7700 industrial server, five LEAP DAQ 8.32 units, five IEPE converters connected to the LEAP DAQ units, 32 monoaxial accelerometers PCB model 393B12m, LAN cables, and coaxial cables. The MIC-7700 processing module is the interface for all the LEAP DAQ nodes that are distributed on the structure and contains all the algorithms necessary for processing the accelerometer data to extract the dynamic properties. Each LEAP DAQ unit can manage up to a maximum of eight acquisition nodes.

5.2.1 Time Synchronization and Data Integrity

The LEAP DAQ units are connected to the MIC-7700 module as network devices. To obtain accurate synchronization of all channels, one of the control units is configured in master mode and generates a clock signal that is transmitted to the others via coaxial cable.

5.2.2 Sampling Frequency and Duration

The sampling frequency is set to 1000 Hz, which allows for filtering and subsampling the signals obtained to reduce noise. The raw signal is resampled to 20 Hz in the preprocessing phase before performing dynamic identification through OMA techniques. The duration of each single acquisition was chosen to be 30 minutes, which is a typical interval in OMA experimental campaigns.

5.3 Data Processing

The raw signals acquired by the accelerometers are carefully analysed to identify any sampling anomalies, spikes, synchronization problems, harmonics, or transients that could compromise the integrity of the data. The data are then resampled at 20 Hz, and each channel is associated with the corresponding degree of freedom in the geometric model of the structure.

After this phase, the Operational Modal Analysis algorithms are executed. Both rapid techniques such as FDD, which allows manual pick-picking of the frequencies, and more robust techniques, such as SSI, is exploited. SSI enables the construction of the stabilization diagram, which makes it possible to discriminate the structural modes from spurious modes generated by the algorithm. Once identified from the data, the natural frequencies, damping ratios and modal shapes are validated with simple metrics, by comparing the estimates obtained by varying the model order.

Chapter 6

The OMA Campaign



6 The OMA campaign

6.1 Introduction

Herøysund Bridge is a free-build bridge in Herøy municipality in Nordland county. The bridge was completed in 1966 (Table 6). The bridge is part of county road 828 and connects Sør-Herøy and Nord-Herøy. The Herøysund bridge is made of three branches (Fig. 49, Fig. 50 and Fig. 51), globally. The first branch, from axis 1 to axis 3, is a reinforcement concrete deck; the second branch, from axis 3 to axis 6, is a free-bridge post-tension concrete; the third branch, from axis 6 to axis 7, is a reinforcement concrete deck.

Table 6 Bridge data (https://www.wikiwand.com/no/Herøysundet_bru)

Type	road bridge, girder bridge
Place	Herøy
Opened	1966
Stretching	828
Length	153.9 meters
Free height	12 meters
Largest span	60 meters
Material	prestressed reinforced concrete
Traffic	1,200 (2021)
Herøysundet bridge	65°58'54"N 12°17'04"E

The use of the experimental test to gain knowledge about the dynamic response of the civil structure is a well-established practice. Assuming that the structure's dynamic behaviour can be expressed as a combination of modes, each one characterised by a set of parameters (natural frequency, damping ratio and mode shapes) whose values depend on geometry, material properties and boundary conditions, Experimental Modal Analysis (EMA) identifies those parameters from measurements of the applied forces. Even EMA has been applied in several fields the identification of modal parameters by EMA techniques became more challenging in civil engineering structures due to their size and frequency range.

Recently, Operation Modal Analysis (OMA) has been proposed for large structures. OMA can be defined as the modal identification procedure that allows the identification of modal properties on the base of the vibration response only. The main advantage of this technique is to assume that the white noise produced by wind, traffic and environmental unknown excitations let vibrate the structure without applying additional forces (from Fig. 49 to Fig. 51).

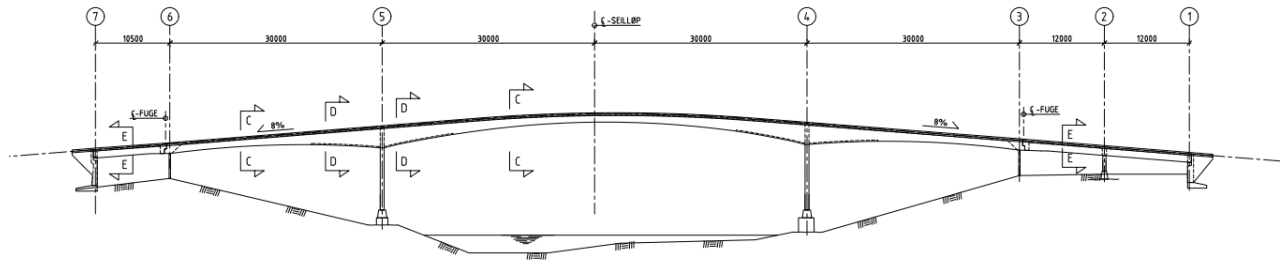


Fig. 49 Herøysund bridge, lateral view (Herøysund bru, korrosjon av etterspent armering FoU-programmet Bedre Bruvedlikehold 2017-2021, Statens Vegvesen Rapport Nr.843).



Fig. 50 a) Construction phase (1966), b) upgrading work (2020) (https://www.wikiwand.com/no/Herøysundet_bru).

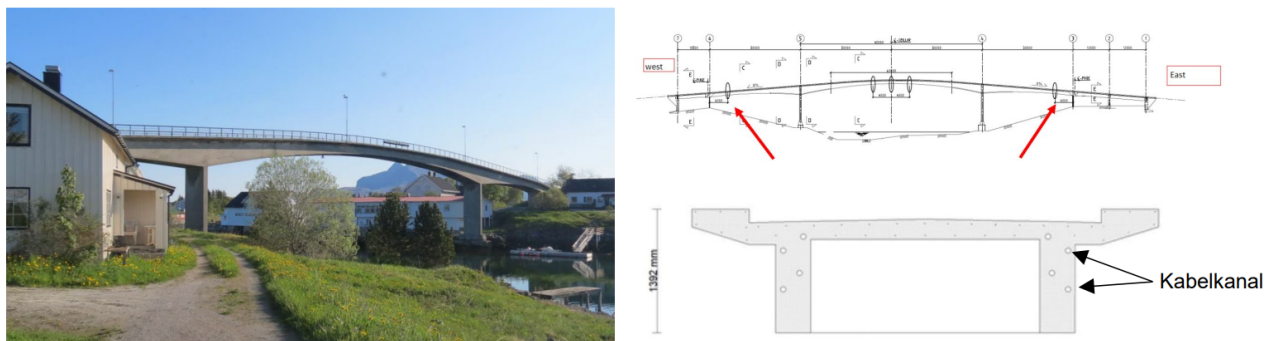


Fig. 51 Herøysund Bridge, image and section (Herøysund bru, korrosjon av etterspent armering FoU-programmet Bedre Bruvedlikehold 2017-2021, Statens Vegvesen Rapport Nr.843).

OMA techniques will be adopted for the dynamic identification of the bridge. In view of placing the sensors in appropriate positions, a simplified Finite Element (FE) or Discrete Macro-Element (DME) model will be adopted for preliminary frequency and modal estimation. The OMA campaign will be oriented to the identification of the modal parameters of the entire structure with a higher instrument density on the second,

and main, post-tensioned branch. An adequate number of sensor placements will be considered aiming to globally identify the fundamental modal shapes. It is worth noting that boundary conditions, local damages or post-tension forces may affect the modal parameters.

Data will be recorded with a sampling frequency of 1000Hz. Since traffic and wind forces may have different frequency ranges, the operational modal analysis will take into account the two different forces and the results will be compared and discussed in the final report.

ARTEMIS software and MATLAB routines will be adopted for performing the OMA analysis in the time and frequency domains.

6.2 Use of FEM and DMEM models for defining the sensor layout

Two modelling approaches have been involved in the preliminary analyses. The two models are based on different assumption. Specifically, the LUSAS software was engaged for modelling with FEM approach developing a shell-like model. The method is coherent with the already briefly introduced method at §0 of this report. The model was necessary for estimating the expected frequencies and the modal shapes.

The use of preliminary numerical models helps to defining the sensor layout that has to be considered on the structure. In this case, the more relevant modal shapes are reported in Fig. 52. All the estimated modes are coherent with the expected modes of similar bridges. In detail, the first and second modes are in-plane and out-of-plane flexural shapes at frequencies of $f_1=1,448$ [Hz] and $f_2=1,581$ [Hz]. The third mode is a second order in-plane flexural mode at the frequency of $f_3= 2,789$ [Hz]. The fourth mode is a torsional mode due to the out-of-plane piers behaviour at $f_4= 2,952$ [Hz]. The fifth mode is a pure torsional at $f_5= 3,969$ [Hz]. Lastly, a third order in-plane flexural mode is placed at $f_6= 4,365$ [Hz].

Aiming to verify the preliminary results an additional model has been developed by means of an alternative and less computational demanding procedure (DMEM reported at §3.2 of this document). The Fig. 53 and Fig. 53 summaries the modal results. The additional model confirmed the FEM results except for the order of the fifth and sixth modes.

All the mentioned results have been adopted for defining the sensor placement as described in the following section.

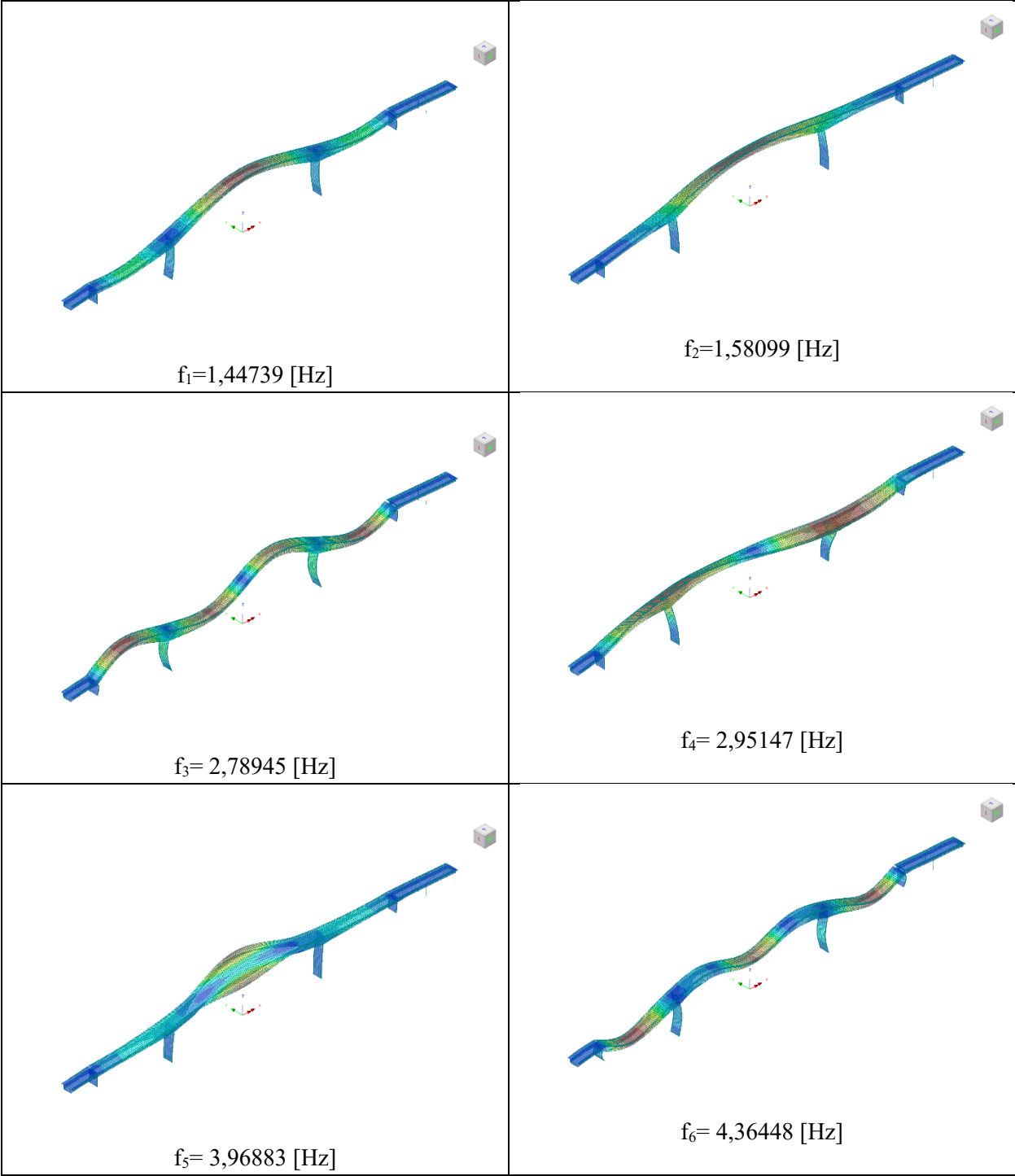


Fig. 52 LUSAS shell model modal shapes.

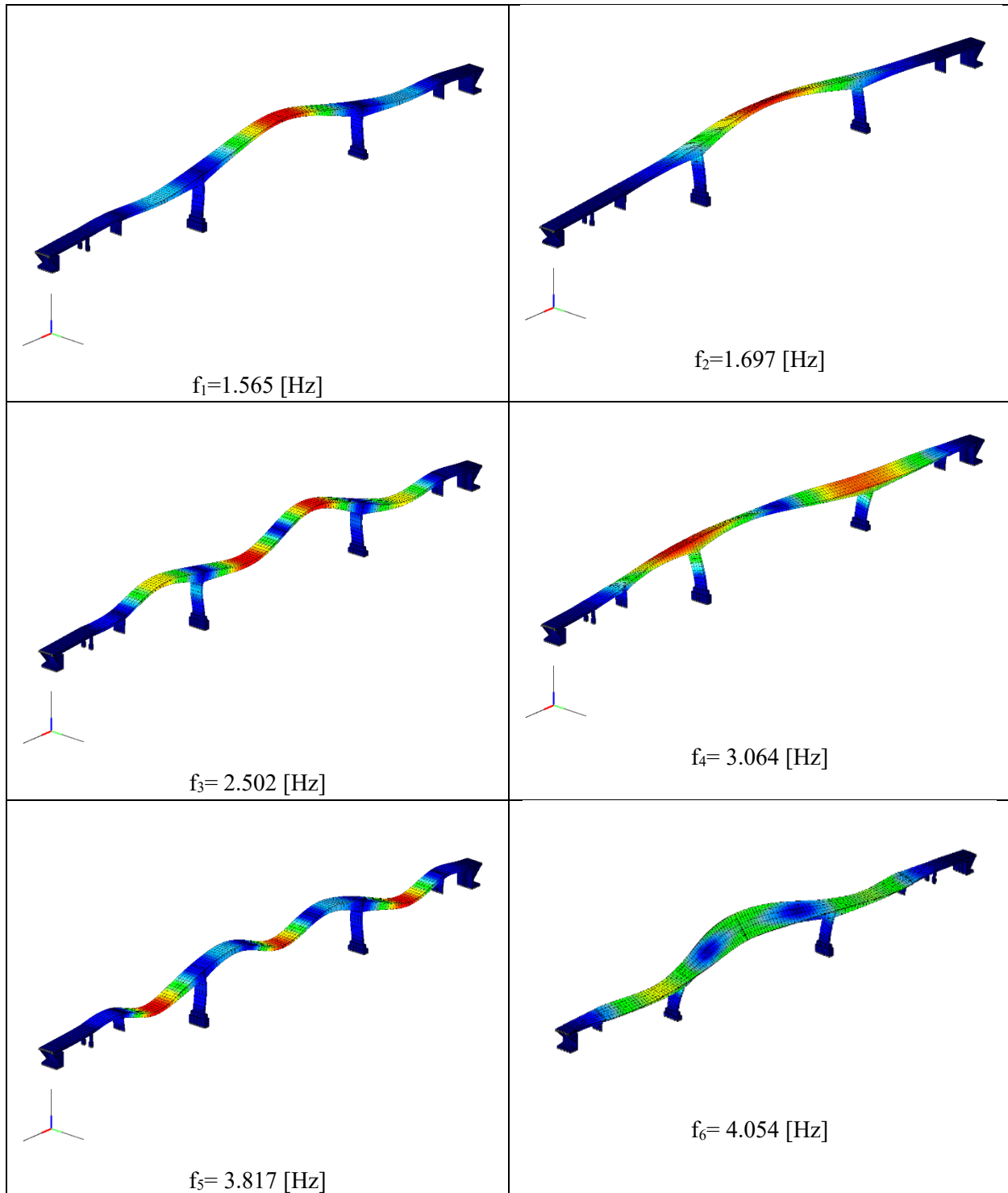


Fig. 53 HISTRA BRIDGE DMEM model modal shapes.

6.3 Sensor placement

This chapter describes the methods by which the sensors were positioned on the structure. It will examine both the initial strategy of positioning the accelerometers on the bridge deck and the solution implemented, which involved installing the sensors under the deck.

Preliminary strategy: installing the sensors on the bridge

In a preliminary phase of the project, the acquisition strategy involved installing the sensors on the bridge deck to proceed with a rapid positioning of the sensors without having to drill holes in the structure. For this purpose, a ground positioning system for the accelerometers was designed, consisting of an IPE 200 T-profile and aluminium cubes to mount the accelerometers. To ensure that the T-profile had no inherent modes of vibration within the characteristic frequency range of the bridge, a specific FEM model of the support was created.

Below is the list of components needed to mount the sensors:

- IPE 200 profile: resting on the bridge deck, it allows stable positioning of the sensors. It is equipped with holes on the base to allow, if necessary, anchoring to the ground using bolts (Ø8 mm). The vertical fin has a hole of size (Ø6 mm) for anchoring the aluminium cube on which the sensors are installed.
- Cubes (40 mm x 40 mm x 40 mm): these are small aluminium blocks that allow the sensors to be mounted in the X, Y and Z directions (Fig.54).

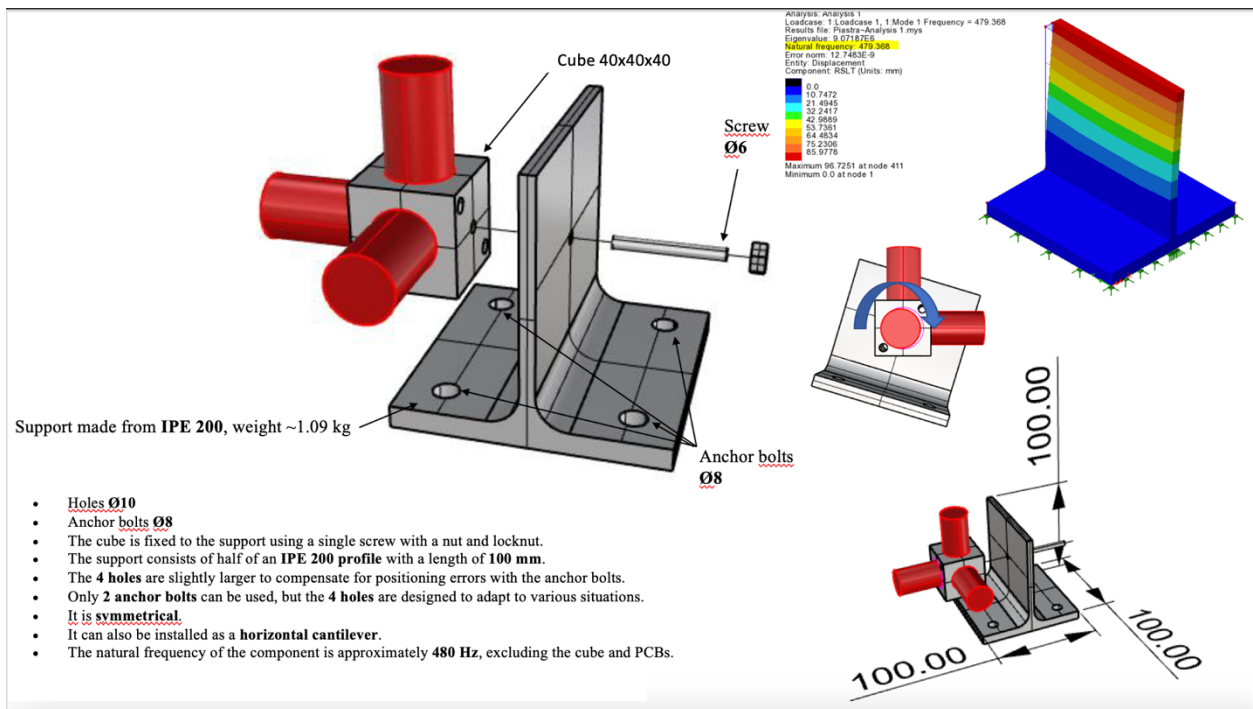


Fig. 54 Configuration of the T-shape plate and FEM results.

Finite Element Analysis (FEA) for Natural Frequency Evaluation

The FEM analysis performed on the IPE 200 profile made it possible to ensure that the natural frequencies of vibration of the support were not close to those of the structure. The analysis results show that the first natural frequency of the profile is 479.368 Hz, much higher than the frequency range where the dynamic response of the bridge is expected.

Challenges

Once on site and after having positioned a small number of sensors to perform test acquisitions, it was realized that the small size of the sidewalks combined with the high human activity made it impossible or impractical to install the sensors on the deck of the bridge without incurring the risk that the acquisitions would be compromised by any impacts or damage caused to the sensors by pedestrians.

Final Solution: Sensor Installation Beneath the Bridge

To get rid of the problem, it was decided to install the sensors under the bridge's deck by accessing it via scaffolding. Before proceeding, it was necessary to make changes to the installation plan and test the most effective anchoring system, both from a data quality and installation time point of view.

Evaluation of Mounting Configurations

Three possible installation solutions were tested:

- Configuration A: the IPE 200 T-profile was anchored to the surface using Ø8 mm bolts and then the cube anchored. Law configuration is the same as the preliminary one only the T-profile is now anchored to a vertical surface.
- Configuration B: the cube (40x40x40 mm) is anchored to the surface using a Ø6 mm bolt and high-performance glue.
- Configuration C: the cube (40x40x40 mm) is fixed to the surface only using high-performance glue.

Frequency Analysis and Final Choice

A frequency analysis was performed on a synchronized recording of the three solutions to validate the quality of the solutions under test. As shown in Fig. 58 the three solutions show a practically equivalent frequency content and for this reason it was decided to proceed with Configuration C which is the most efficient in terms of time.

The Fig. 55 shows the three test that were conducted with the tree methods. Each test analyses a different direction. The results have been analysed comparing the PSD. The results confirmed that the glue can be adopted with a consequent reduction of drillings.

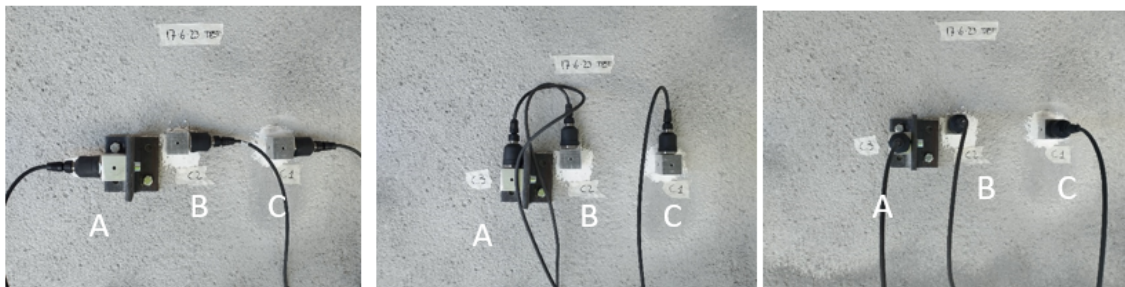


Fig. 55 Three tests layouts.



Fig. 56 Control of the sensor orientation.

The Fig. 57 reports the results of the test in X direction. The curves are coherent each one other. On the base of these results, the method C has been adopted.

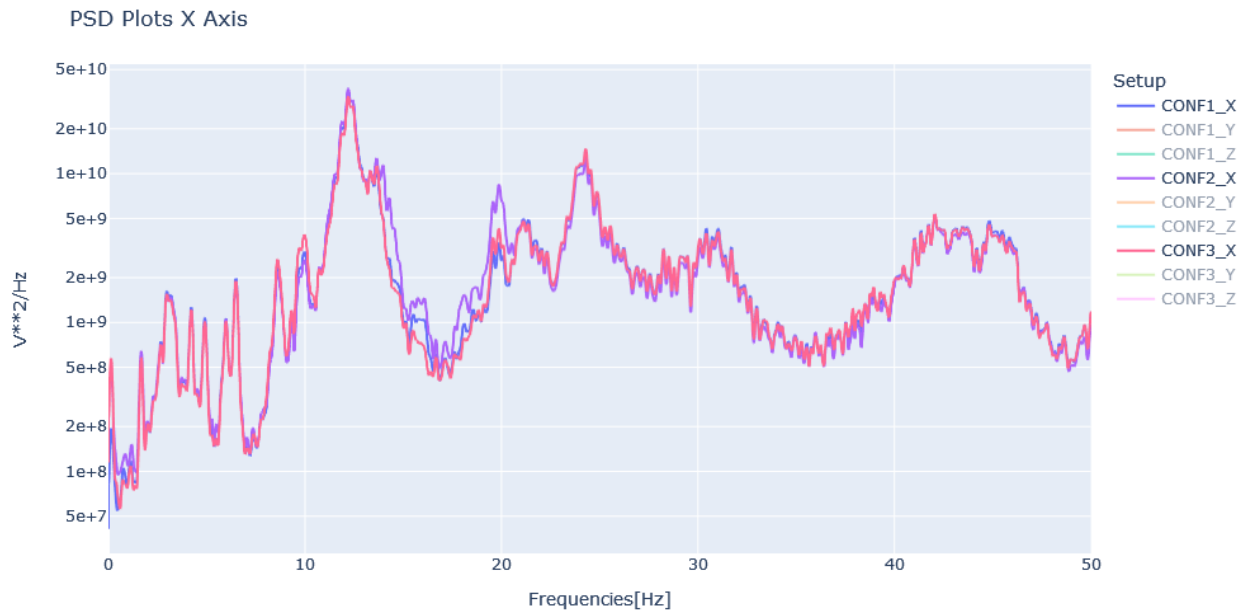


Fig. 57 PSD results for the X direction.

Thanks to the ability to quickly adapt the acquisition strategy to the site's specific characteristics, it was possible to acquire high-quality data for dynamic identification. Thanks to the simplicity and equivalence in performance of Configuration C consisting of an aluminium block plus glue, it was possible to proceed with mounting the sensors on the structure quickly and without delays, thus ensuring a successful experimental campaign.

Sensor Layout

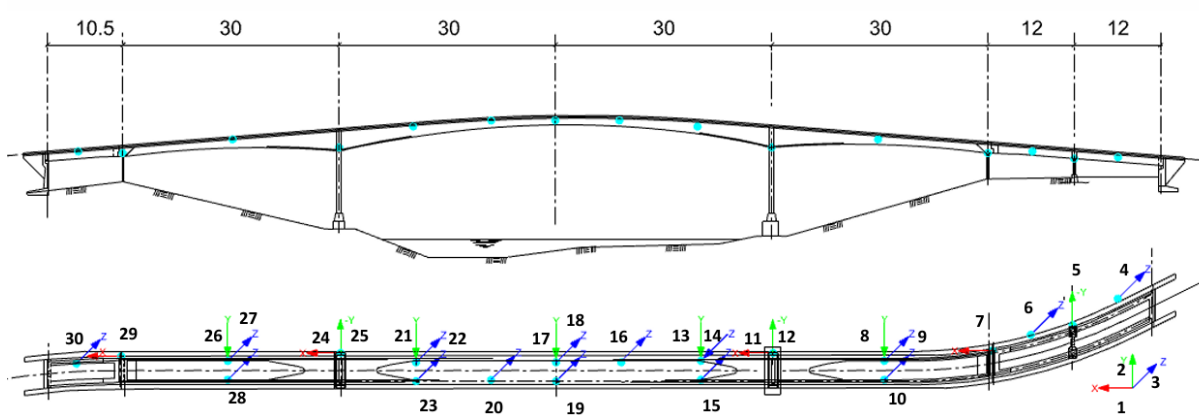


Fig. 58 Sensors' layout.

Table 7 Sensors' placements

Geometric Point	Survey	Point Acquisition	of	Sensor number	Structural Element F: Foundation P: Pier D: Deck S: Scaffolding	Axis	Sensor Serial Number
P1	18/06/2023	PU1		1	F	+X	70917
P1	18/06/2023	PU1		2	F	+Y	70920
P1	18/06/2023	PU1		3	F	+Z	68465
P2	18/06/2023	PU1		4	DI	+Z	70919
P3	18/06/2023	PU1		5	PI	-Y	70918
P4	18/06/2023	PU1		6	DII	+Z	70263
P5	18/06/2023	PU1		7	PII	+X	70262
P6	18/06/2023	PU2		8	DIII	+Y	71118
P6	18/06/2023	PU2		9	DIII	+Z	72620
P7	18/06/2023	PU2		10	DIII	+Z	68995
P8	18/06/2023	PU2		11	PIII	+X	68954
P8	18/06/2023	PU2		12	PIII	-Y	68466
P9	18/06/2023	PU3		13	DIV	+Y	68776
P9	18/06/2023	PU3		14	DIV	-Z	71200

Geometric Point	Survey	Point Acquisition	Sensor number	Structural Element F: Foundation P: Pier D: Deck S: Scaffolding	Axis	Sensor Serial Number
P10	18/06/2023	PU3	15	DIV	+Z	70261
P11	18/06/2023	PU3	16	DIV	+Z	71119
P12	18/06/2023	PU3	17	DIV	+Y	71270
P12	18/06/2023	PU3	18	DIV	+Z	71203
P13	18/06/2023	PU3	19	DIV	+Z	72610
P14	18/06/2023	PU4	20	DIV	+Z	72603
P15	18/06/2023	PU4	21	DIV	+Y	72609
P15	18/06/2023	PU4	22	DIV	+Z	72594
P16	18/06/2023	PU4	23	DIV	+Z	72593
P17	18/06/2023	PU4	24	PIV	+X	72597
P17	18/06/2023	PU4	25	PIV	-Y	72595
P18	18/06/2023	PU5	26	UI	+Y	72619
P18	18/06/2023	PU5	27	DV	+Z	72615
P19	18/06/2023	PU5	28	DV	+Z	72607
P20	18/06/2023	PU5	29	PV	+X	72612
P21	18/06/2023	PU5	30	DVI	+Z	72597



Fig. 59 Example of triaxial point of measure.

6.4 OMA results

A campaign of operational modal analyses was carried out by means of ARTeMIS software, with the objective of identifying the principal vibration mode of the bridge and investigating their variations over time.

The ten-day campaign analyzed the bridge acquiring data all day long. Due to the fact that heavy tracks cross the bridge in a not specific daily or night hours the identification campaign has been extended for 10 days.

The data has been elaborated in frequency and time domains. The Stabilization diagram of estimated state space models (SSI-UPC) is reported in Fig. 60 and the identified frequencies are summarized in Table 8.

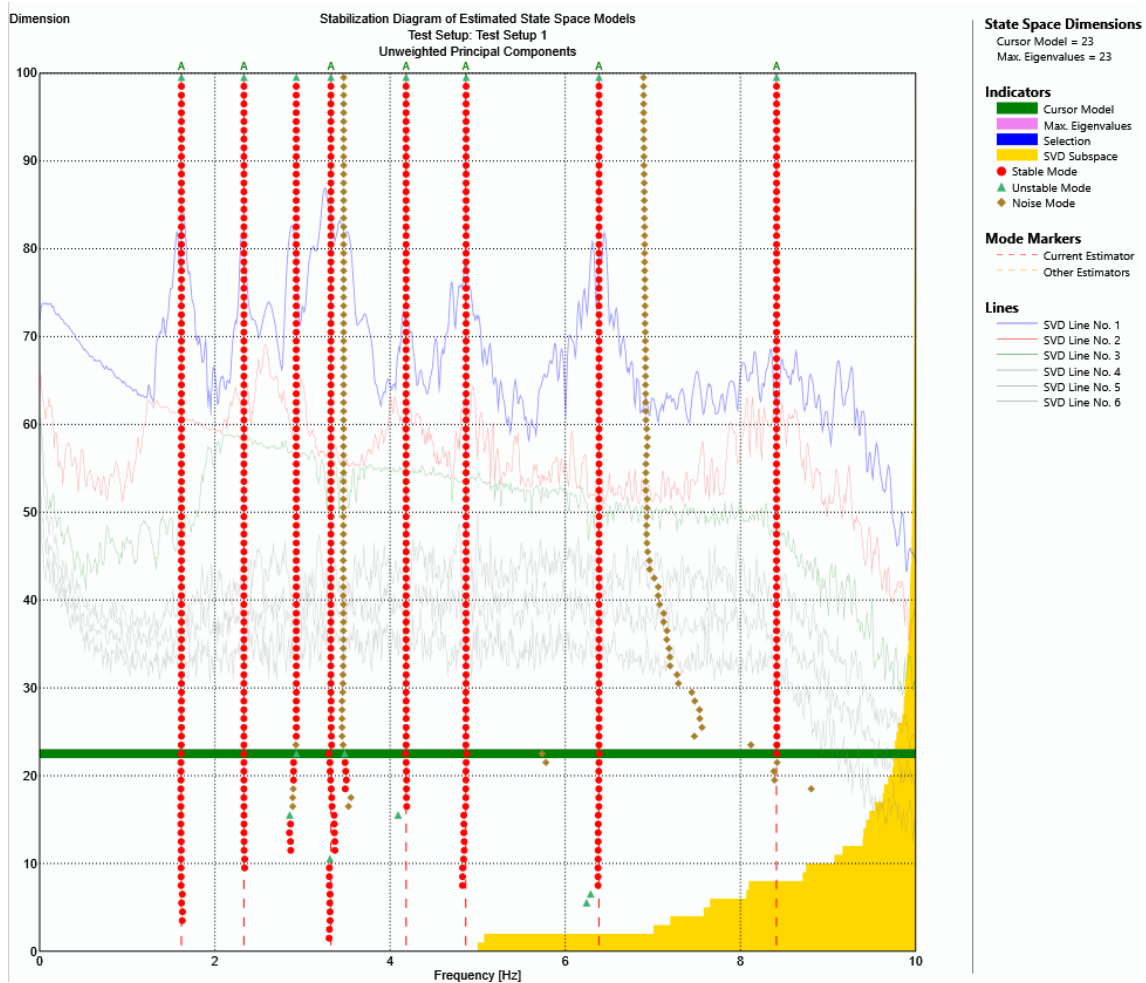


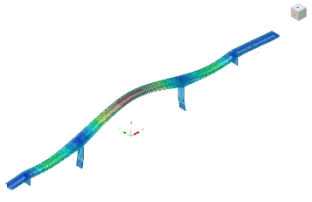
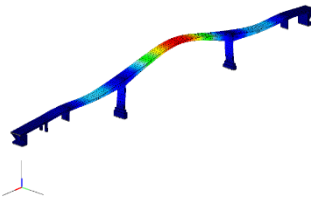
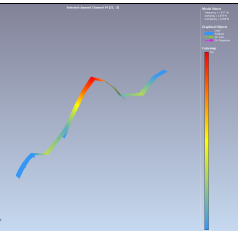
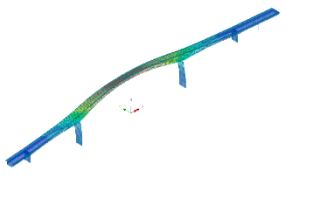
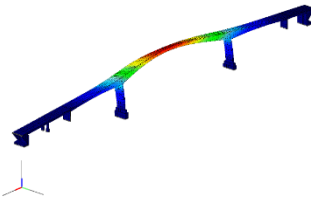
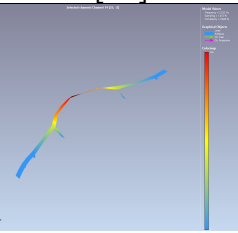
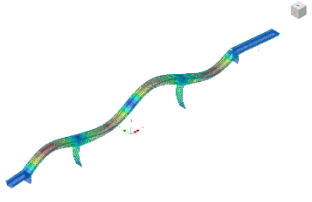
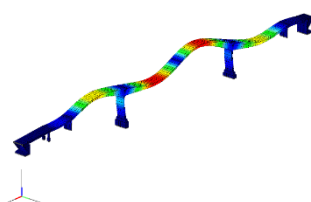
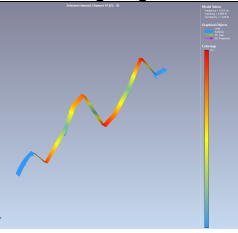
Fig. 60 Stabilization diagram of estimated state space models, SSI-UPC.

Table 8 Global modes

Frequency [Hz]	Damping [%]	Complexity [%]
1.617	2.878	0.256
2.332	1.472	0.943
3.325	4.689	1.426
4.183	1.677	6.268
4.864	1.823	3.786
6.384	1.307	1.018

As Table 9 summarises, the preliminary models fit correctly the real modal shapes. Some differences can be identified in the last two modes. In terms of frequencies the adopted elastic modulus underestimated the real stiffness of the structure that exposes higher frequencies values. Considering the MAC in Fig. 61 the modal shapes can be considered reliable and orthogonal each one other.

Table 9 Comparison of preliminary models and OMA results

LUSAS	HISTRA	ARTEMIS
 $f_1=1,448$ [Hz]	 $f_1=1.565$ [Hz]	 $f_1=1.617$ [Hz]
 $f_2=1,581$ [Hz]	 $f_2=1.697$ [Hz]	 $f_1=2.332$ [Hz]
 $f_3= 2,789$ [Hz]	 $f_3= 2.502$ [Hz]	 $f_1=3.325$ [Hz]

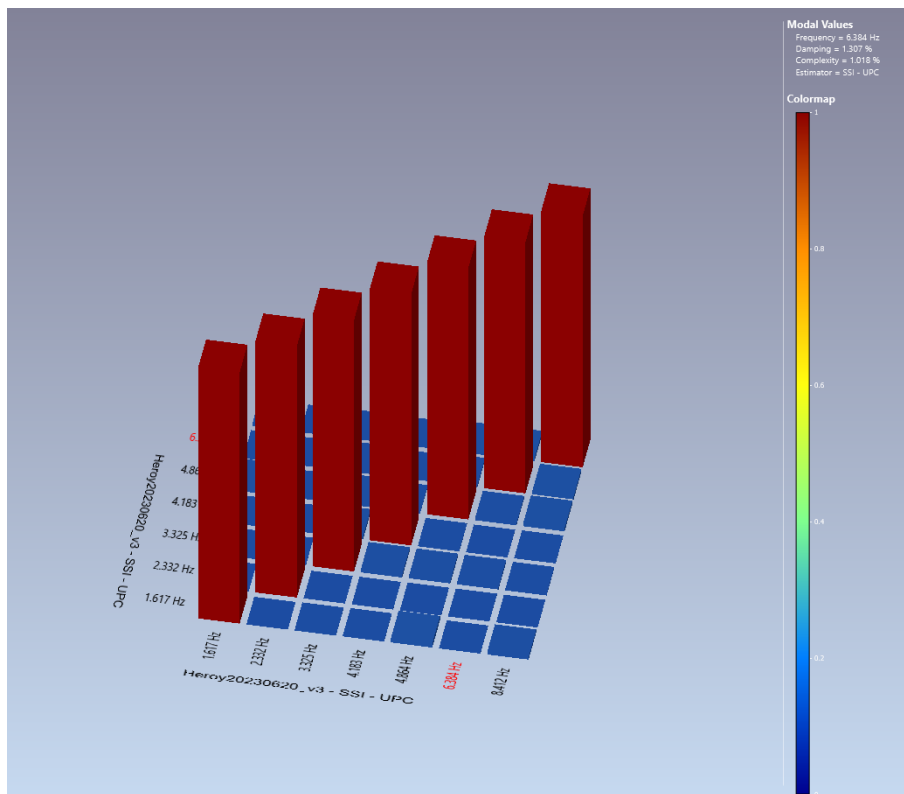
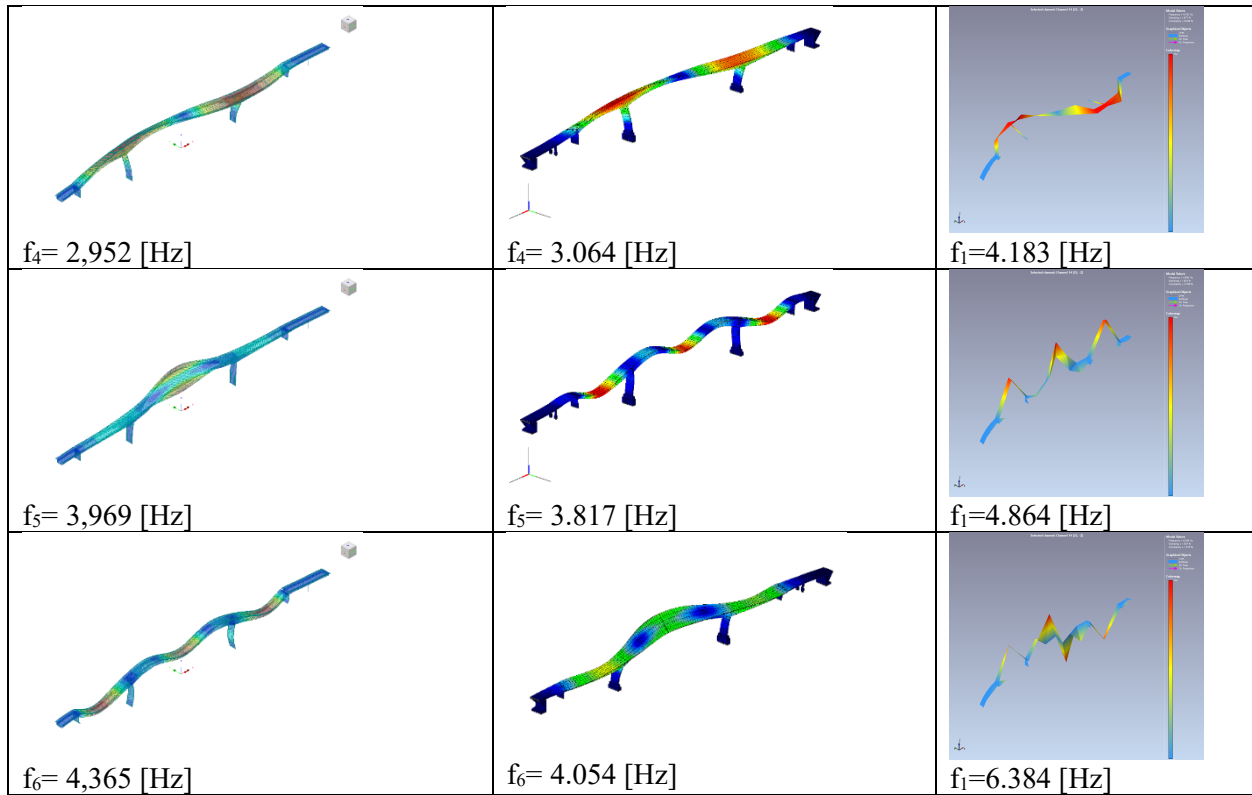


Fig. 61 Modal Assurance Criteria.

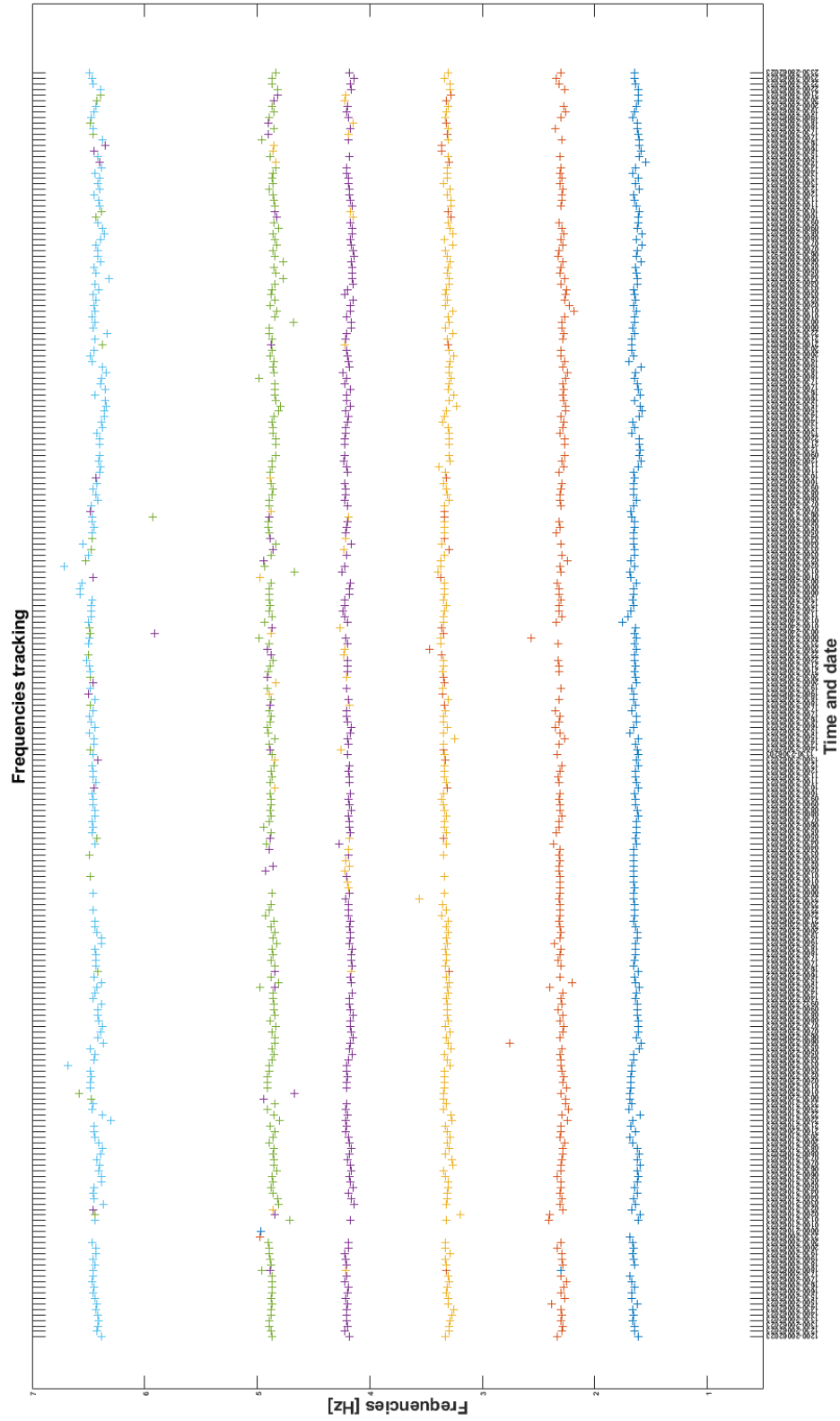


Fig. 62 Frequencies tracking.

6.5 Analysis of the Natural Frequency of a Bridge Using Statistical Methods

In this chapter, a statistical analysis of the historical series of the first six frequencies of the structure will be performed. We will first perform descriptive analyses, plot the historical series and verify the statistical normality of the data analyzing distributions and QQ-plots. We will also try to fit a class of additive models to break down the historical series into their constituent elements, i.e., trends and seasonality.

The flexibility of this class of models allows us to break down the historical series into interpretable components, which are:

- **Trends:** allows us to identify long-term trends in the data.
- **Seasonality:** allows us to model recurring patterns, for example, daily, weekly, and annual.

The model parameters are estimated using Bayesian methods, thus providing uncertainty intervals around the model's prediction.

This analysis is only a preliminary attempt. Subsequent studies will need to validate it using a longer data sample and possibly comparing the conclusions with numerical models and engineering approaches.

- **Preliminary data analysis**

The plot of the historical series shown in Fig. 63 highlights that, except the first fundamental frequency, which presents a relatively regular trend, the others are characterized by observations that deviate significantly from the underlying trend of the historical series

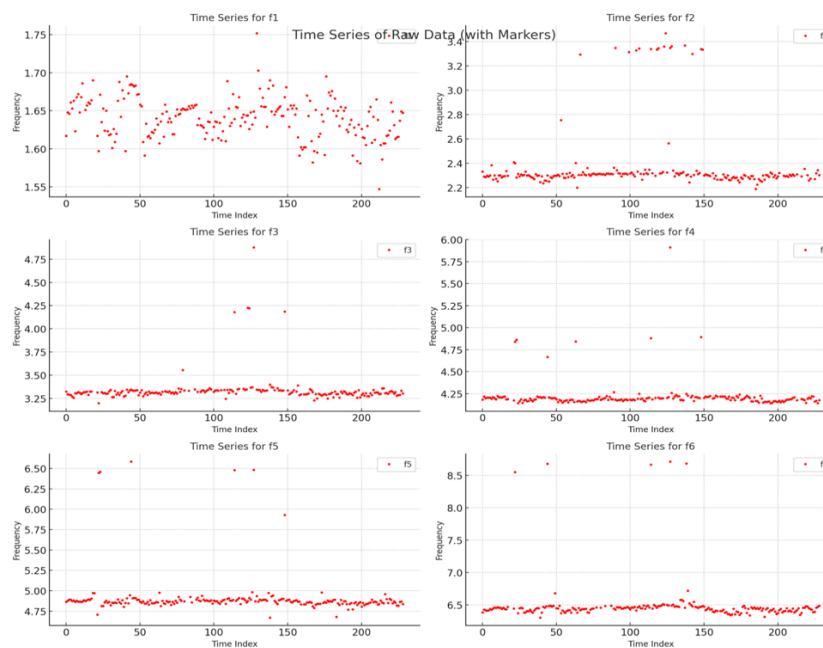


Fig. 63 Time series plot of the first six natural frequencies of the system.

This aspect is even more evident if we examine Fig. 64. In fact, it is clear that the only frequency to show a generally normal distribution is f1, while the others are characterised by non-normal and highly asymmetric distributions.

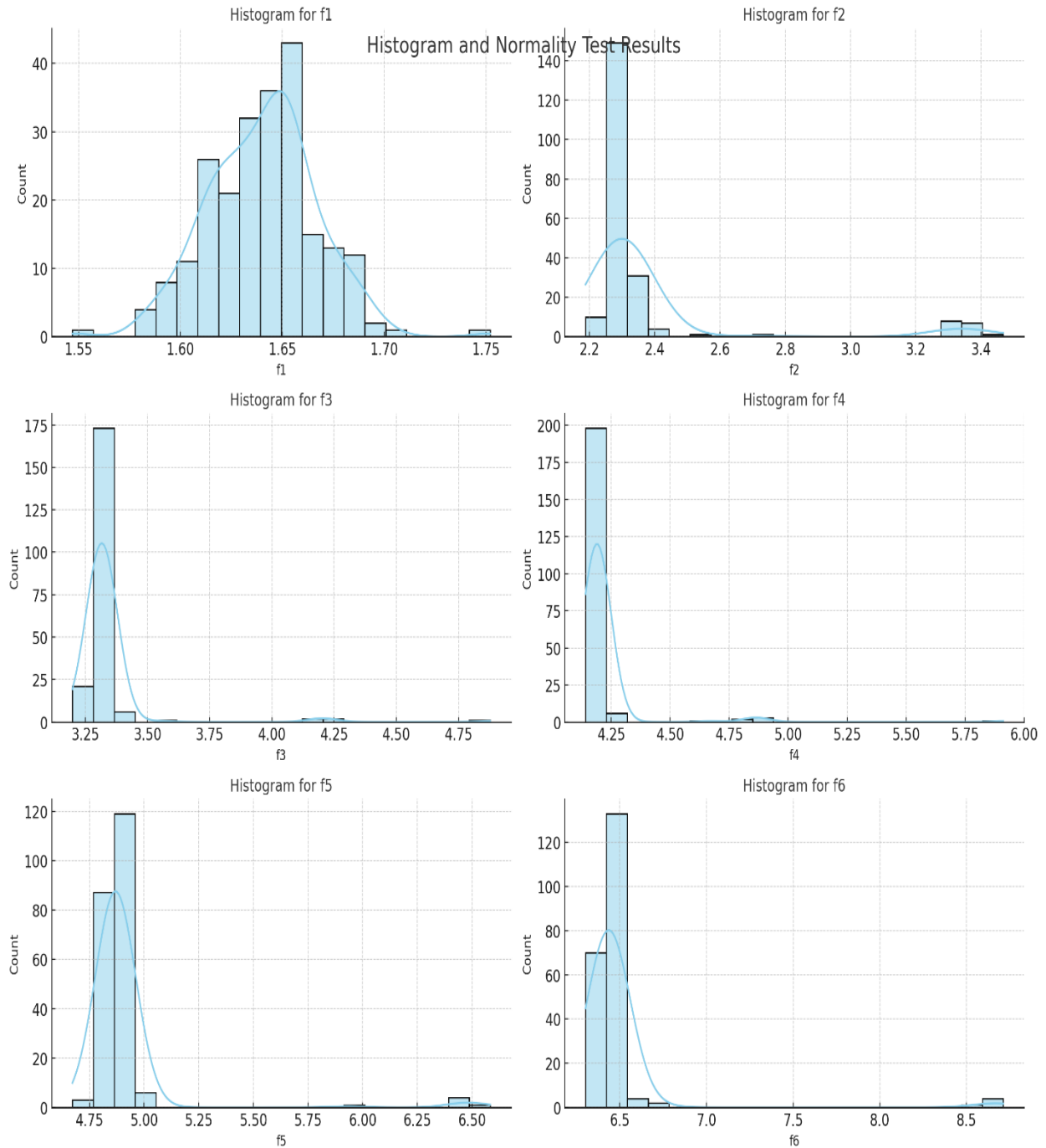


Fig. 64 Histograms and densities of the frequencies time series.

The QQ plot in Fig. 65 further confirms the deviation from normality of the statistical distributions of the frequencies from f2 to f7, where the only distribution that approximates a normal one is that of the frequency f1.

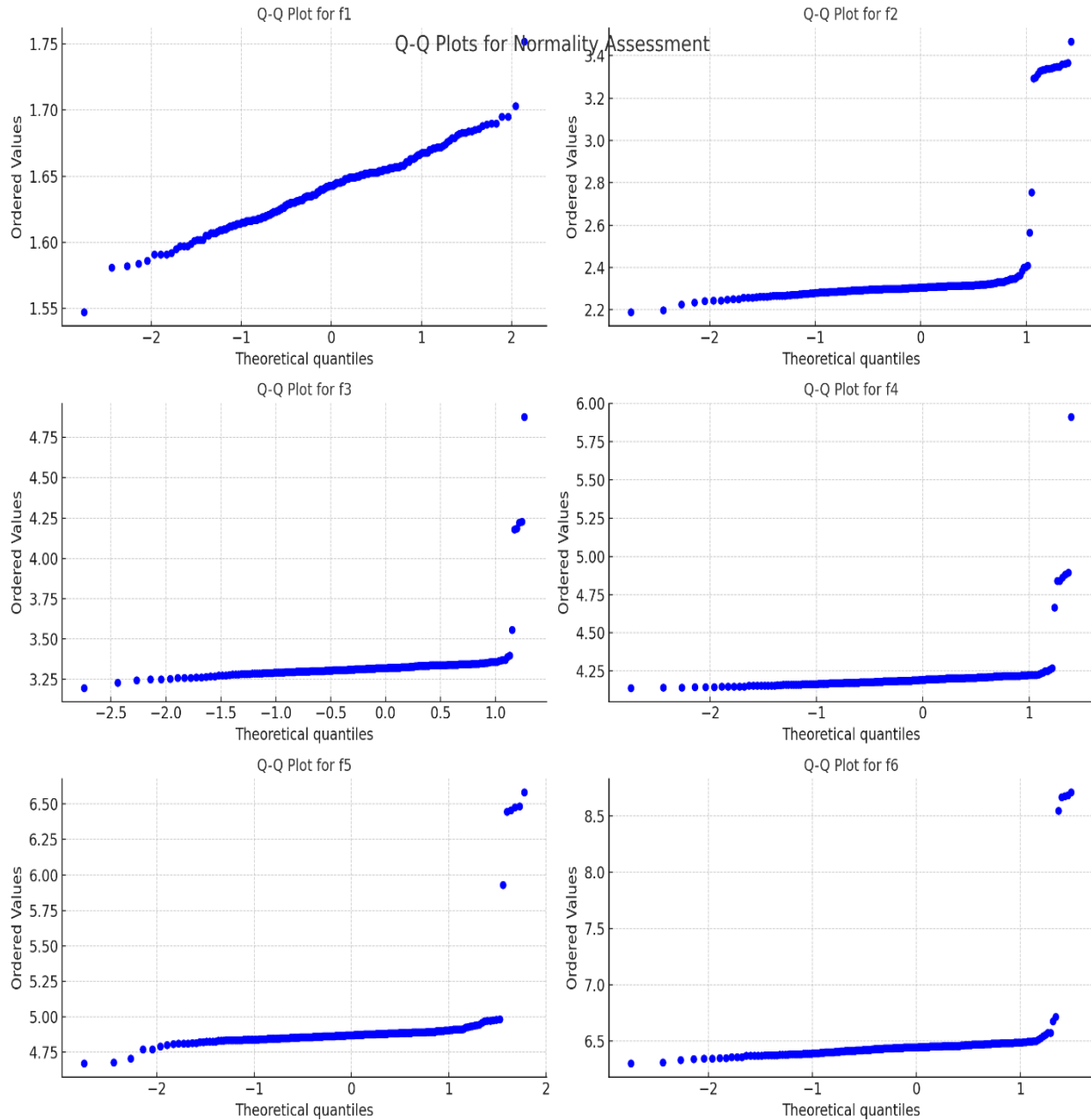


Fig. 65 Quantile-Quantile Plot of the frequencies.

It may be interesting to proceed with removing extreme values from the time series to see what happens to their statistical distributions after removing the outliers. In Fig. 66, the raw time series are plotted over the time series from which the outliers have been removed. It is possible to notice that the general trend of the time series is preserved, while the extreme values have been removed. Now, it is possible to plot the QQ-plots again to verify if the statistical distributions are closer to a normal one.

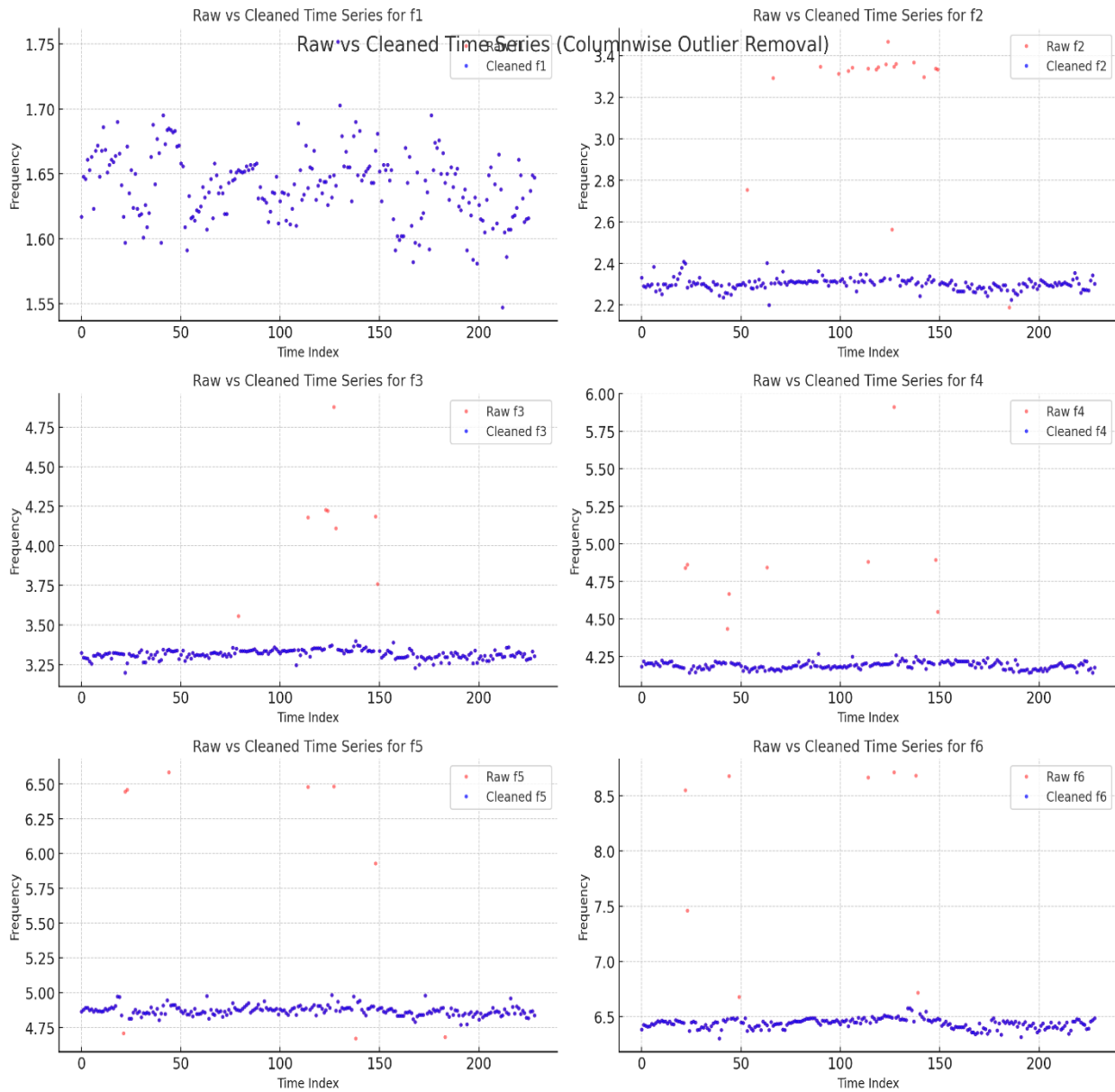


Fig. 66 Raw time series along with processed time series after outlier removal.

After removing the extreme values from the series, the QQ-plots in Fig. 67 show that the statistical distributions of the frequencies are closer to those of a normal distribution.

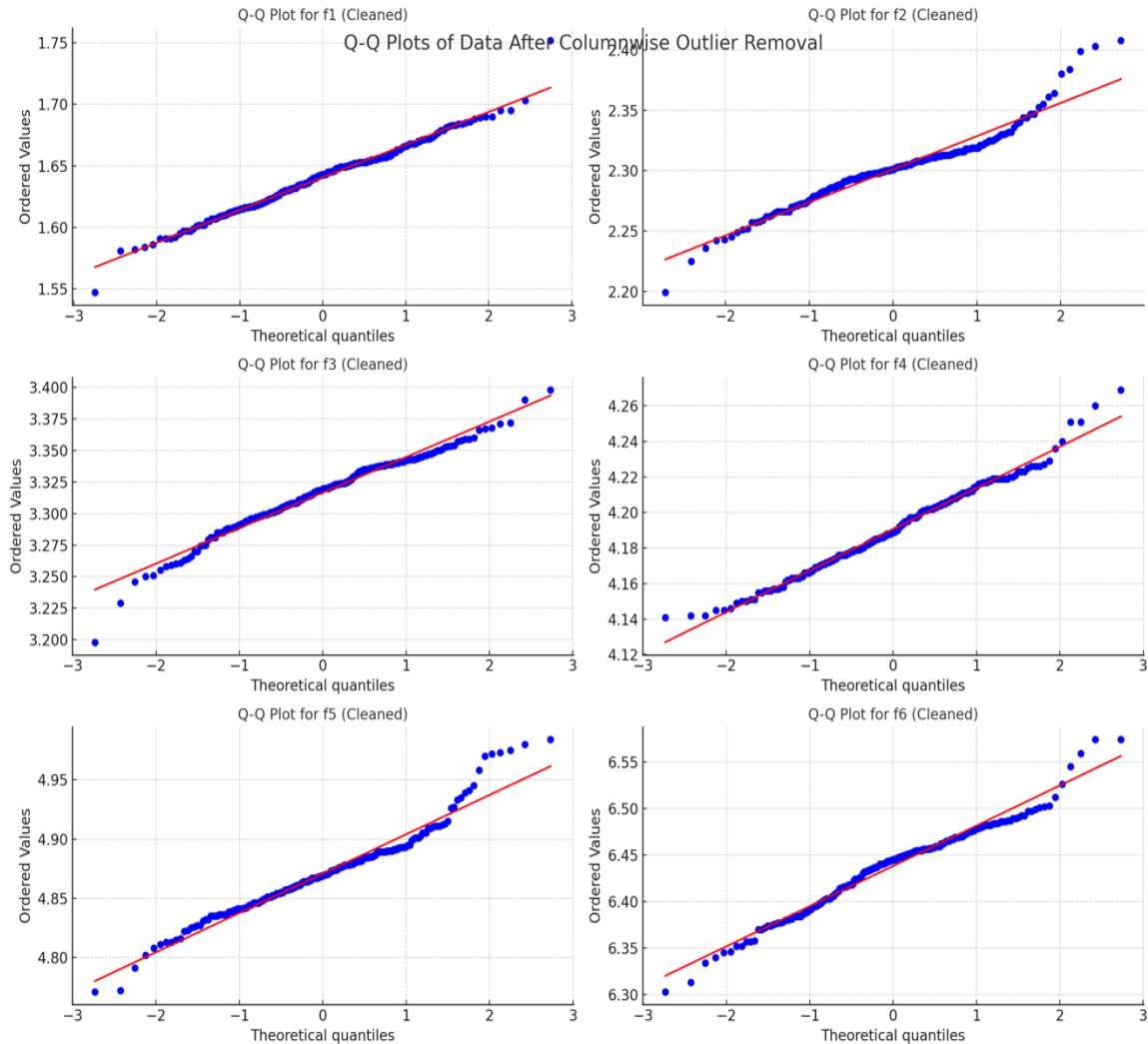


Fig. 67 QQ-plot after outlier removal.

This section presents the results of the model fitting on the historical series of frequencies. The analysis has only preliminary value and must be validated on future studies with more extensive data samples. The attempt was to apply a class of models capable of identifying the constituent components of the historical series under study, particularly in trend and seasonality. The analysis results for the first six natural frequencies of the bridge are reported below. Each analysis is composed of four graphs described below:

From Fig. 68 to Fig. 73: The figures show the frequencies sampled in the observation period, with a frequency of one every 30 min, represented by black dots. The figure also shows the model forecast, represented by the solid dark blue line and the credibility intervals plotted in light blue. From Fig. 74 to Fig. 79: The figures show the trends and estimated seasonality for each historical series.

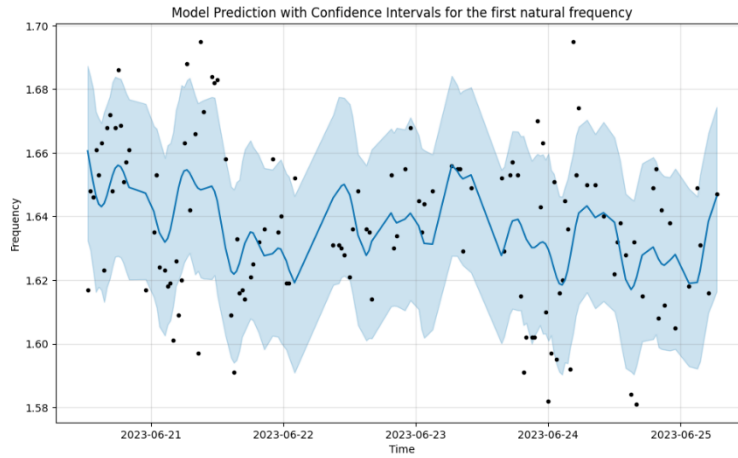


Fig. 68 Model prediction and uncertainties estimation for f_1 .

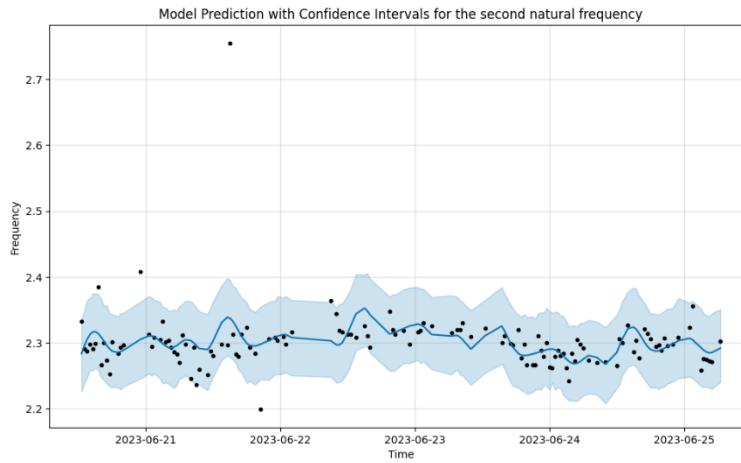


Fig. 69 Model prediction and uncertainties estimation for f_2 .

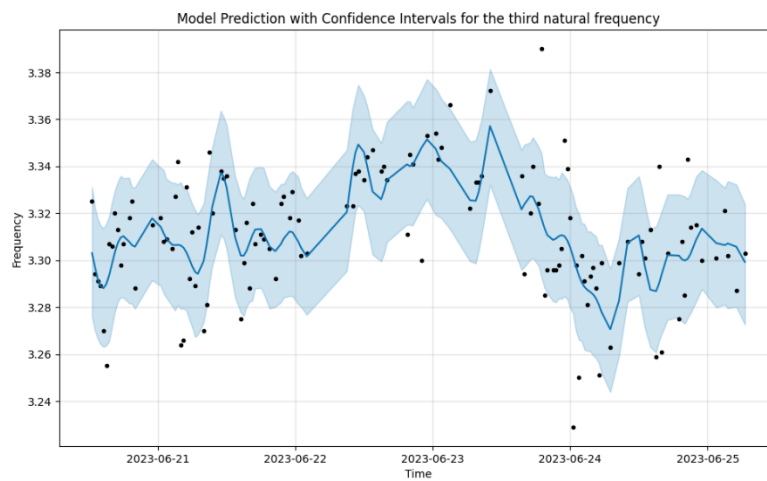


Fig. 70 Model prediction and uncertainties estimation for f_3 .

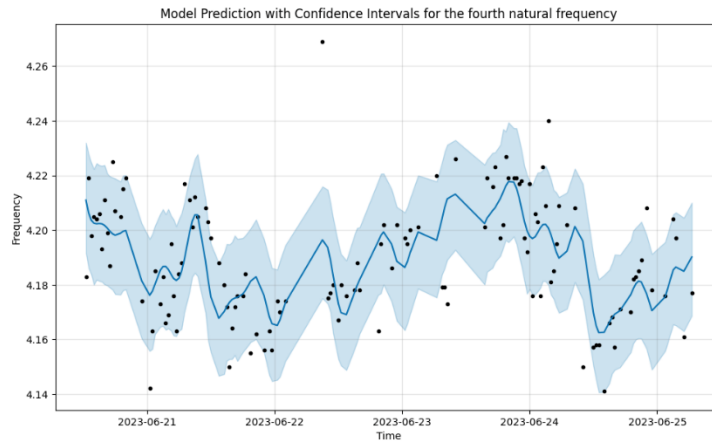


Fig. 71 Model prediction and uncertainties estimation f_4 .

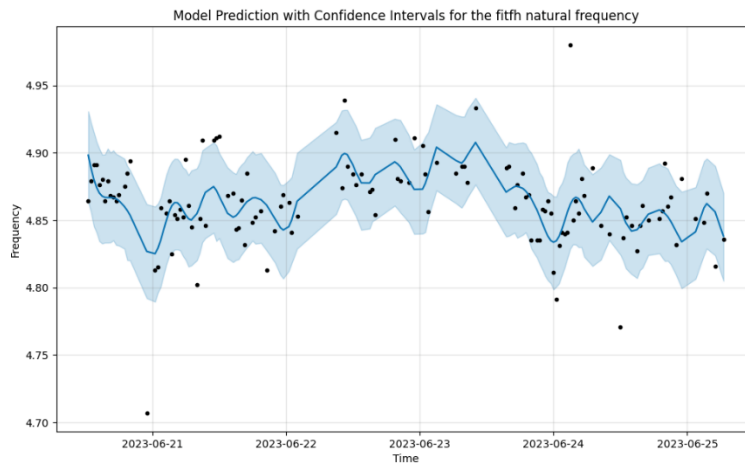


Fig. 72 Model prediction and uncertainties estimation for f_5 .

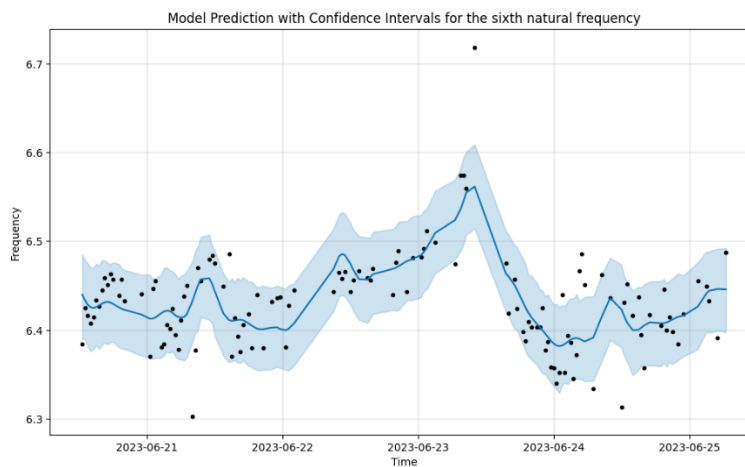


Fig. 73 Model prediction and uncertainties estimation for f_6 .

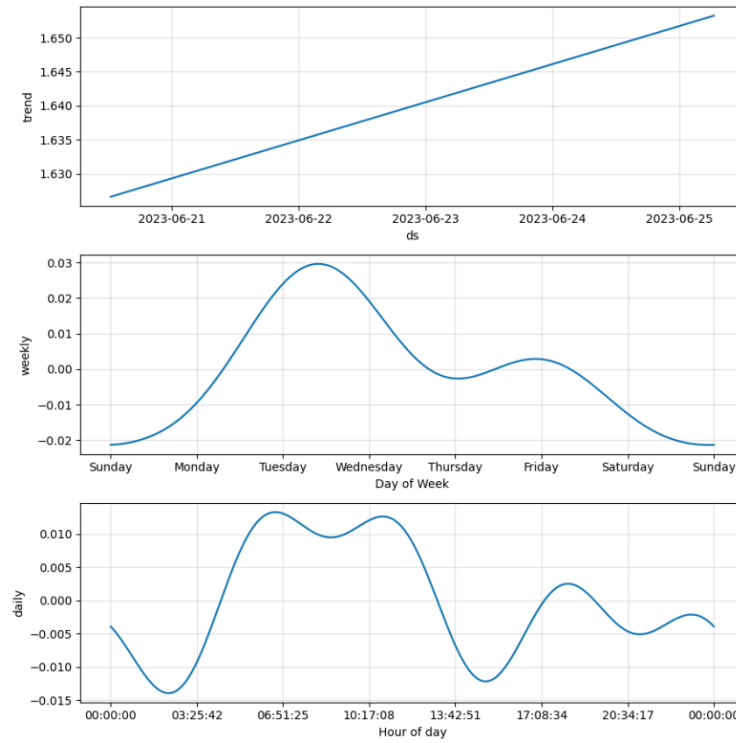


Fig. 74 Trend and seasonalities estimation for f_1 .

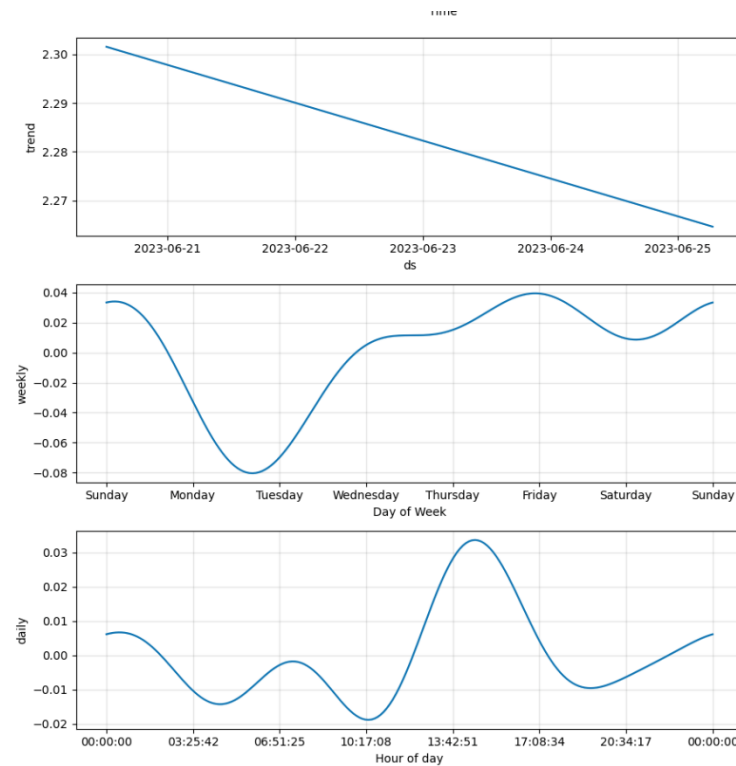


Fig. 75 Trend and seasonalities estimation for f_2 .

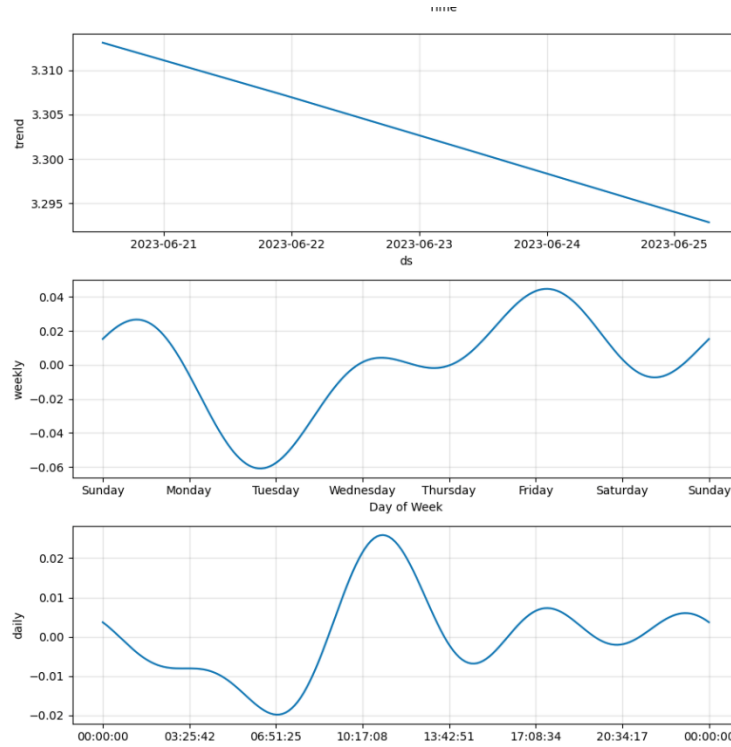


Fig. 76 Trend and seasonalities estimation for f_3 .

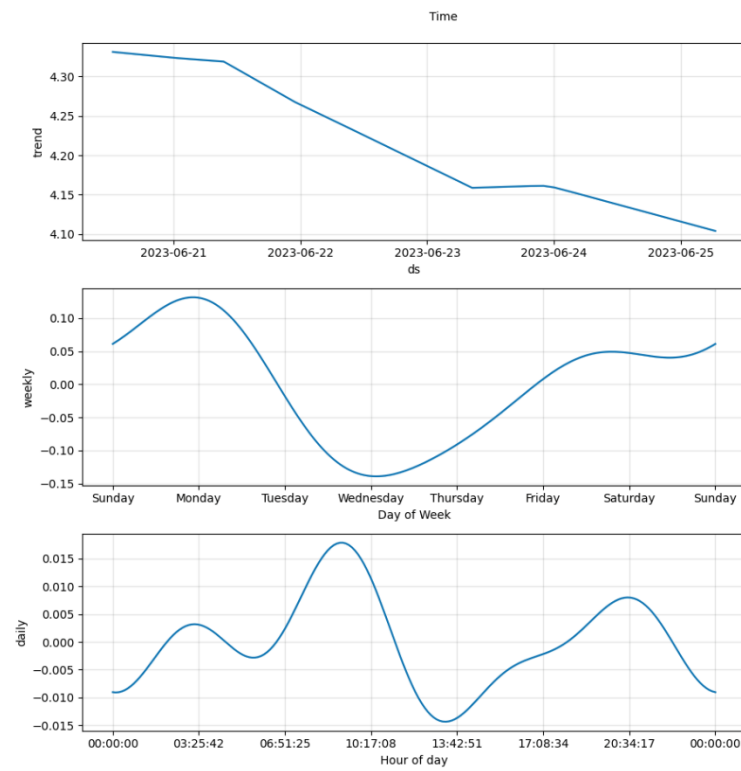


Fig. 77 Trend and seasonalities estimation for f_4 .

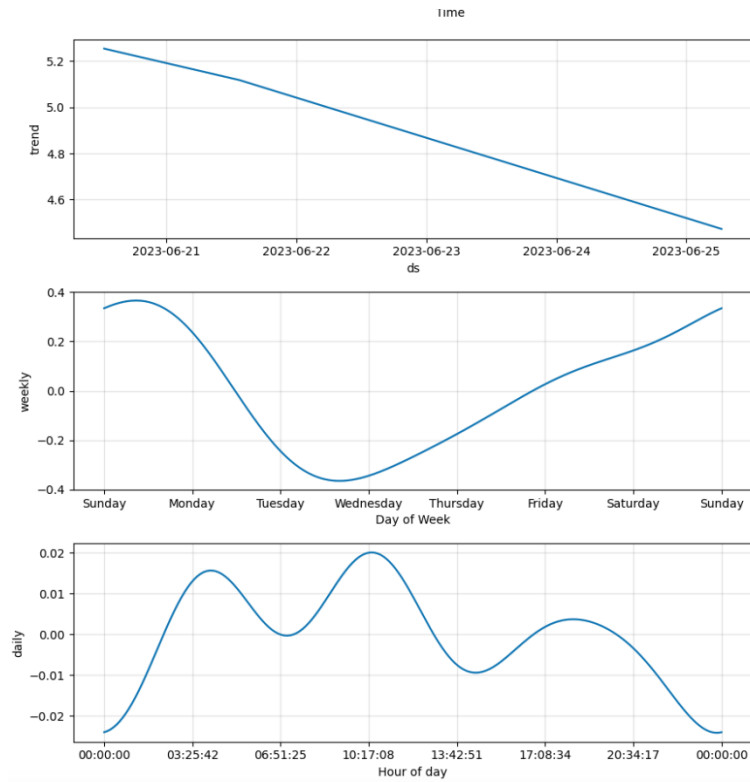


Fig. 78 Trend and seasonalities estimation for f5.

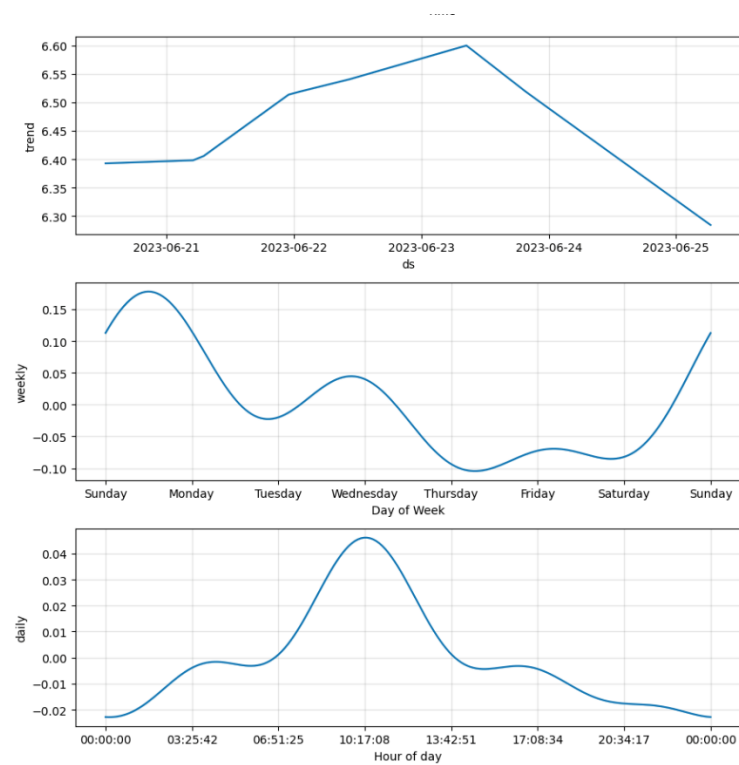


Fig. 79 Trend and seasonalities estimation for f6.



Chapter 7

Challenging problems and Proposed solutions



7 Challenging problems and proposed solutions

7.1 Optimal Sensor Placement

This aspect was investigated in the Master Thesis titled Optimal Sensor Placement Summary by the student Macdonald Nwamma and supervised by prof. Harpal Singh (UiT Narvik).

The study attempted to find the best sensor configuration for modal identification on the Herøysund Bridge. The objective was to increase the amount of data obtained from structural testing while reducing the number of sensors needed thereby reducing the cost of the sensor system. Four frequently used optimal sensor placement (OSP) methods, including the modal kinetic energy (MKE) method, the effective independent (EFI) method, minimum modal assurance criterion (MinMAC) method, and the information entropy (IE) method were explored and discussed. The EFI method was selected and applied on a beam model of the bridge, both with and without post-tension.

An algorithm was written on MatLAB using as input data the modal analysis results of the bridge obtained from ANSYS. A modified EFI method known as the effective independence driving point residue (EFI-DPR) method was also considered, and its final sensor locations set compared to those obtained from the EFI method. Both methods were validated by the condition number, trace, and determinant of the Fisher information matrix (FIM). Additionally, an interface was established to link ANSYS to MATLAB for the purpose of performing the sensor placement methods. The outcome of the Herøysund Bridge case study shows that the EFI-DPR method was the more effective than the EFI method because it maximizes its performance criterion.

In the thesis, four OSP methods, namely EFI, MKE, and MinMAC were discussed, and their underlying theories and formulas presented. Each of these methods offered a unique approach to optimal sensor placement. Different optimal sensor placement criteria utilized in the determination of suitability of sensor configuration was also discussed. The EFI method was selected for performing the optimal sensor placement on the Herøysund Bridge, and EFI-DPR method which is a modification of the former was also applied and results compared to those obtained from the EFI method.

Two different beam type FE model of the bridge were developed for this thesis. The two models were models of the bridge designed with and with no post-tensions. MATLAB code is developed to implement the OSP methods. Subsequently, both the EFI and EFI-DPR methods were executed on both model types. Both methods were iterative and ensures candidate sensor locations were reduced to a desire number. The process maximizes the determinant of the Fisher information matrix and leads to a corresponding minimization of the covariance matrix of the estimate error thereby resulting in the best estimate of the target modes. The final sensor configuration obtained from the application of these methods were evaluated to determine their effectiveness by utilizing the trace, determinant and condition number of the FIM.

Based on those analyses, the EFI-DPR method satisfied two out of the three evaluation criteria which includes the trace and determinant of the FIM proving to be a better method for maximizing the linear independence of mode shapes obtained from the model of the Herøysund Bridge.

Some results are reported from Fig. 80 to Fig. 83.

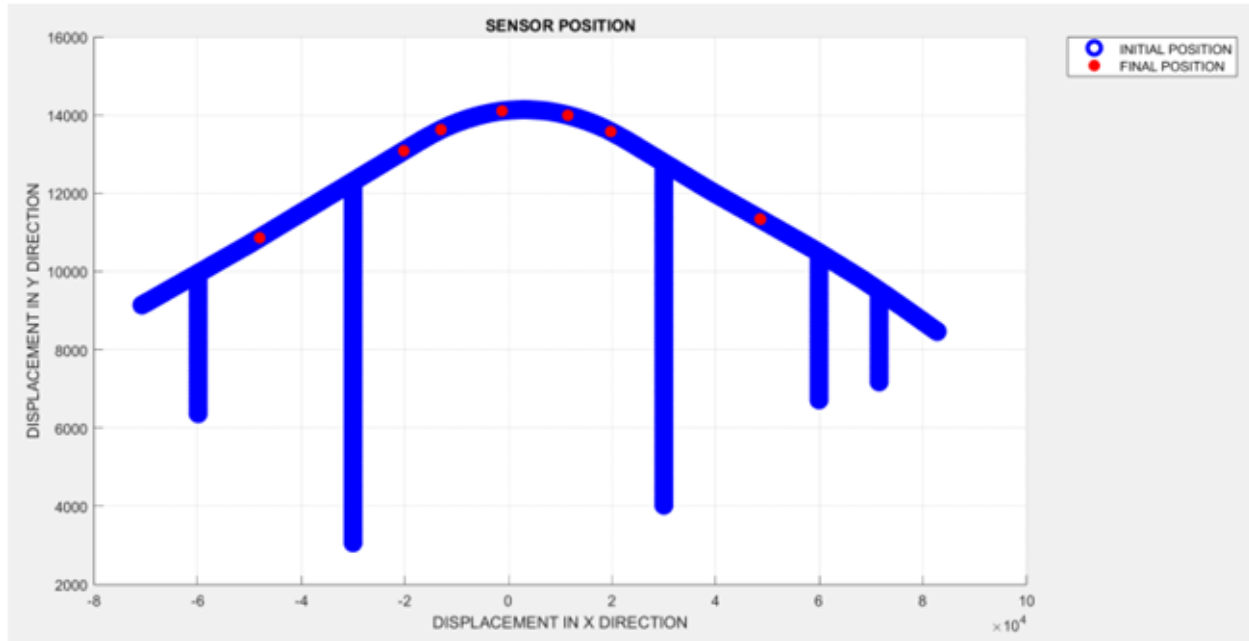


Fig. 80 Ten final sensor location for model WPT [8].

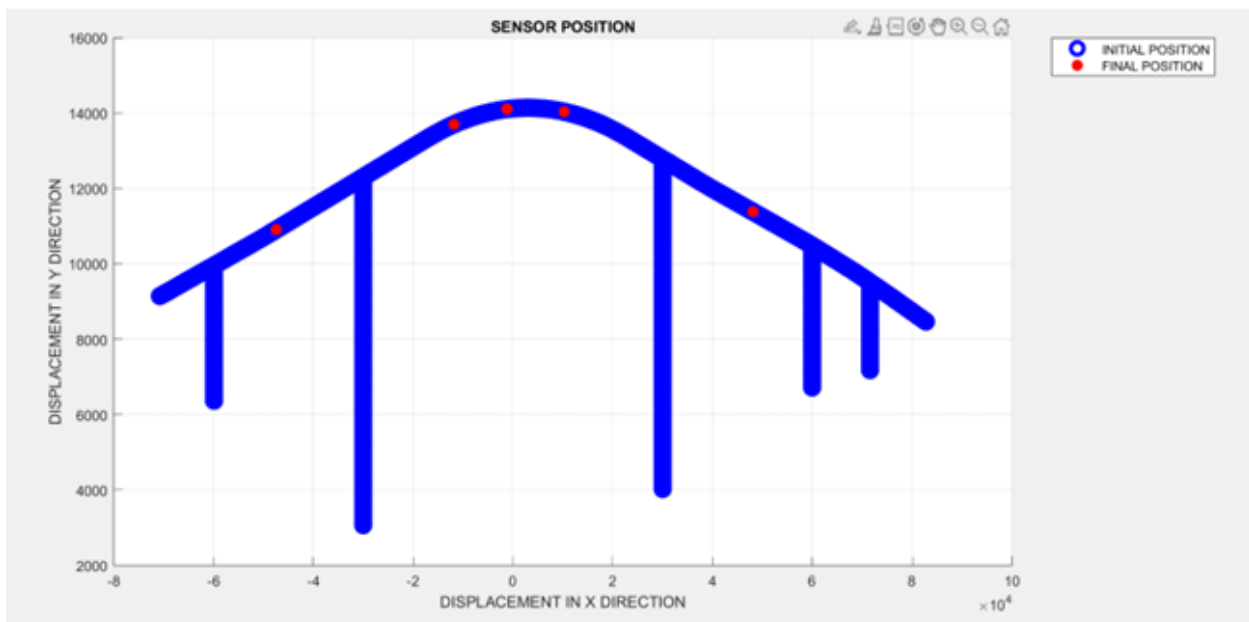


Fig. 81 Ten sensor locations for model WPT EFI-DPR method [8].

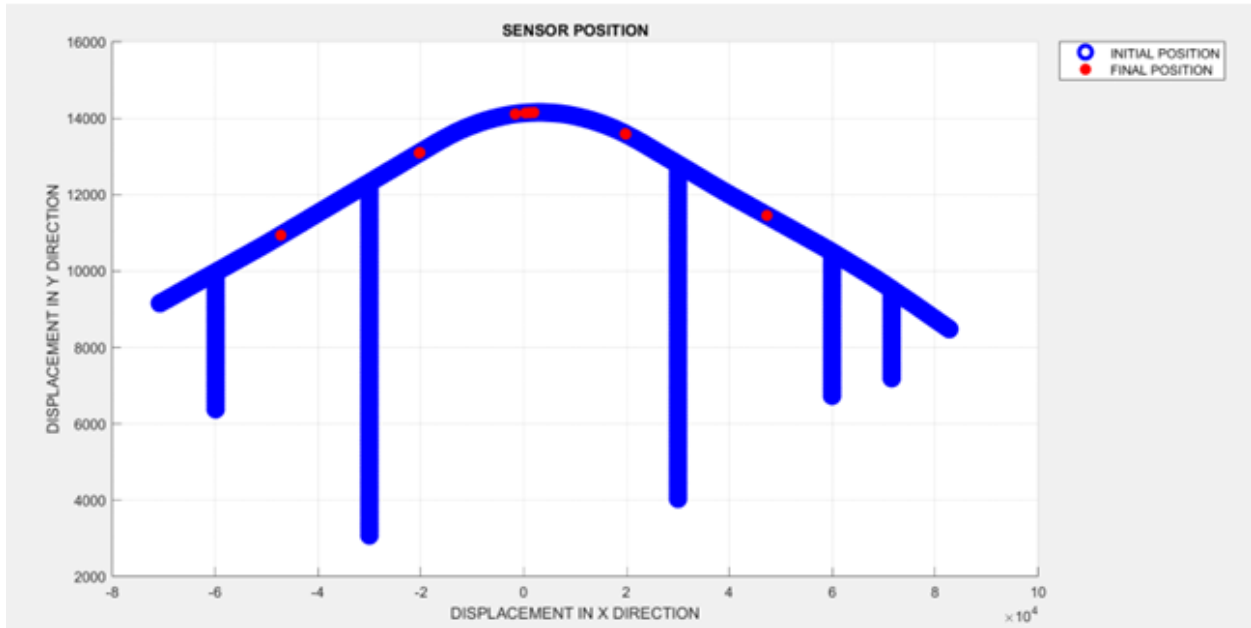


Fig. 82 Ten final sensor location for model WNPT [8].

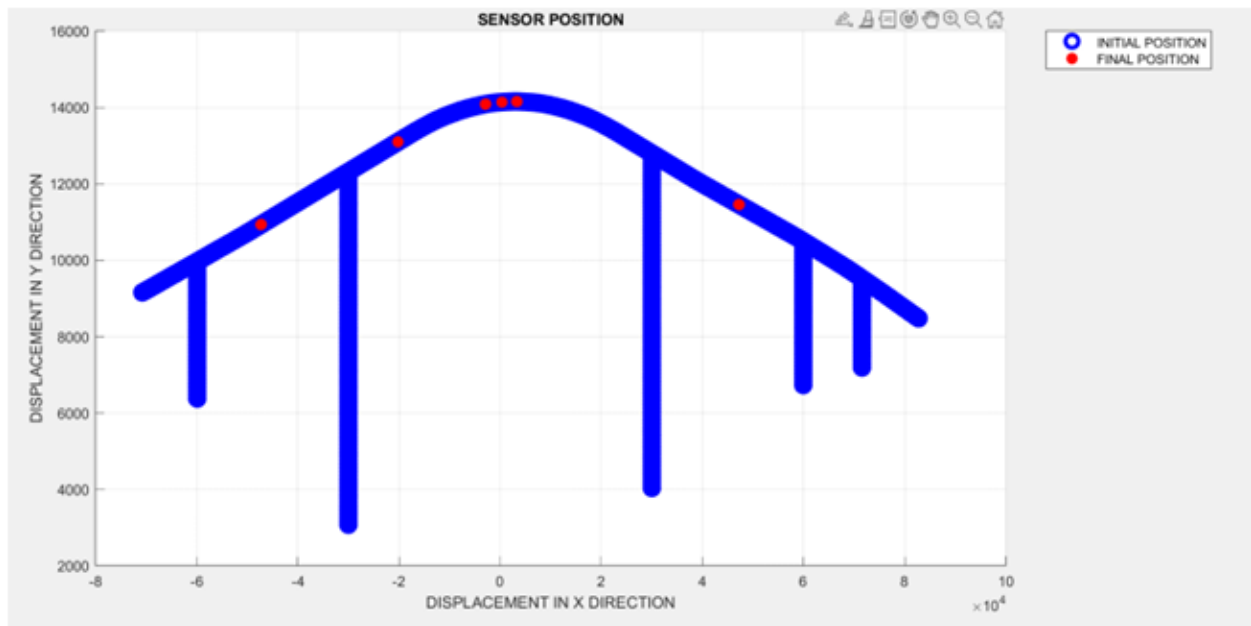


Fig. 83 Ten sensor location for model WNPT EFI-DPR method [8].

7.2 Model updating

The thesis **Development of Digital Twin of the Herøysund Bridge using Finite Element Model Updating** of Mohammadreza Khademi and supervised by prof. Harpal Singh (UiT Narvik), focused on developing a digital twin of the bridge. The aging of civil infrastructure presented significant challenges on a global scale, necessitating innovative research techniques for effective solutions. Governments increasingly allocated additional time and budgetary resources towards maintenance, repairs, or the construction of new structures to replace deteriorated or damaged ones.

This allocation was essential to ensure the provision of adequate services to citizens. Implementing a digital twin of any structure helps in structural health monitoring. This thesis aimed to build a digital twin of the Herøysund Bridge. Vibration data obtained from fieldwork was used for finite element model updating, making the updated finite element model more like the real-world behaviour of the bridge.

In this thesis, a comprehensive literature review was conducted on various methodologies, including experimental modal analysis, operational modal analysis, and finite element modal updating. Furthermore, a genetic optimization algorithm was used for the finite element model updating of the shell-based model of the Herøysund Bridge using MATLAB. The process of finite model updating, using a genetic algorithm, demonstrated promising results for the updated parameters.

The operational modal analysis was conducted on the vibration dataset (12-14/11/2023) from the Herøysund Bridge. Among all the techniques of OMA, SSI-UPCX was used in this thesis. This method identified the first three modal parameters that closely validated the shell-based FE model developed in the master thesis “Shell-based finite element modelling of Herøysund Bridge” by Zeeshan Azad.

Linear regression and Pearson correlation techniques were used to find a potential relation between environmental factors (temperature, wind speed, and humidity) and the extracted modal parameters. Since the dataset used was only for three days, no meaningful correlation was identified due to the lack of significant variation in the environmental factors.

A shell-based FE model was developed in ANSYS software. The Response Surface tool was employed to assess the sensitivity of this FE model to the parameters selected for updating (Young’s modulus, Poisson’s ratio, and density). A genetic algorithm developed in MATLAB was used for FE model updating. The MATLAB script was linked to the Response Surface tool of ANSYS software using a journal file. This link was used for updating the values of selected modal frequencies concerning the values of sensitive parameters in the initial FE model. Modal frequencies acquired were used to calculate fitness values. Convergence occurred after a few iterations, and an optimal solution was found for the sensitive parameters.

However, validating the optimal fitness function remains unaddressed in this thesis. This validation could be conducted by replacing the combination that yielded the highest fitness value, updating the model accordingly, and then comparing the similarities between the first and third mode shapes after modal analysis of the vibration data. This comparison uses the MAC value, which ranges from 0 to 1, indicating the degree of similarity between the two mode shapes. It is worth of mentioning, if the correct modes are selected on both sides to establish the fitness function, the described process for updating the FE model

should suffice. Utilizing the Modal Assurance Criterion formula (MAC value) would then serve primarily to provide additional assurance that the behaviour of the FE model is indeed converging.

Table 10 Updated values of Selected parameters [28]

Parameter's Name	Initial Value	Updated Value
Young's Modulus [MPa]	19360	20170
Poisson's Ratio	0.1414	0.1333
Density [kg/m ³]	2392	2316



Chapter 8

Conclusions and Lesson Learned



8 Conclusions and Lessons Learnt

The old Herøysund bridge in Nordland was chosen as a test pilot to find out how bridge disaster can be prevented in future. UiT The Arctic University of Norway, NTNU, SINTEF Narvik, Nordland Fylkes Kommune and Statens Vegvesen collaborated on a research project titled Herøy FoU that had a budget of just under 6 million NOK. UiT The Arctic University of Norway contributed on Work Package 1 i.e. Structural Health Monitoring and Work Package 2 i.e. Corrosion inspection, assessment and repair.

This report focuses on ambient vibration measurements and operational traffic loading using operational modal analysis (OMA).

The report describes the detailed investigation on the Herøysund bridge case study. The bridge was investigated by means of numerical models in linear and nonlinear field for the aims of the dynamic identification and during several master's degree theses. In terms of numerical modelling, different approaches, such the largely adopted FEM model and the more innovative DMEM, have been engaged for predicting and simulating the dynamic and static behaviour [23, 21, 28]. Three software have been adopted for the numerical simulations, HISTRA [29] (DMEM), LUSAS [22] (FEM) and ANSYS [30](FEM) and one for the OMA analysis, ARTEMIS [24]). All the model assumed a uniform concrete Young's modulus of 19360 MPa.

In terms of modal analysis, all the models identified comparable frequencies and modal shapes. Fig. 84 visually compares the frequency values to the identified ones. As the figure shows a good coherence can be noticed between the numerical models each one other. A significant difference between expected and identified can be observed at superior modes (6th mode). Table 11 reports the numerical values.

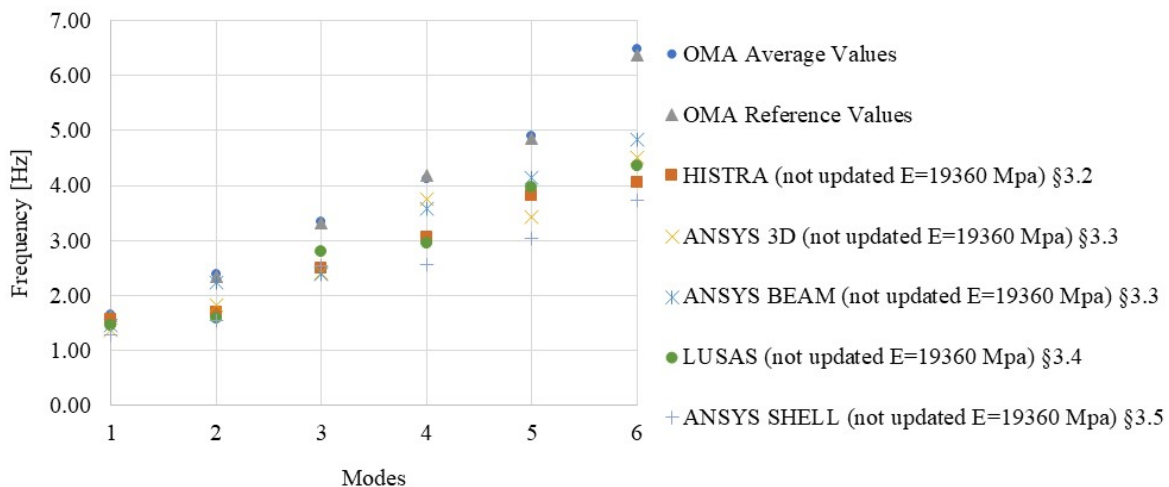
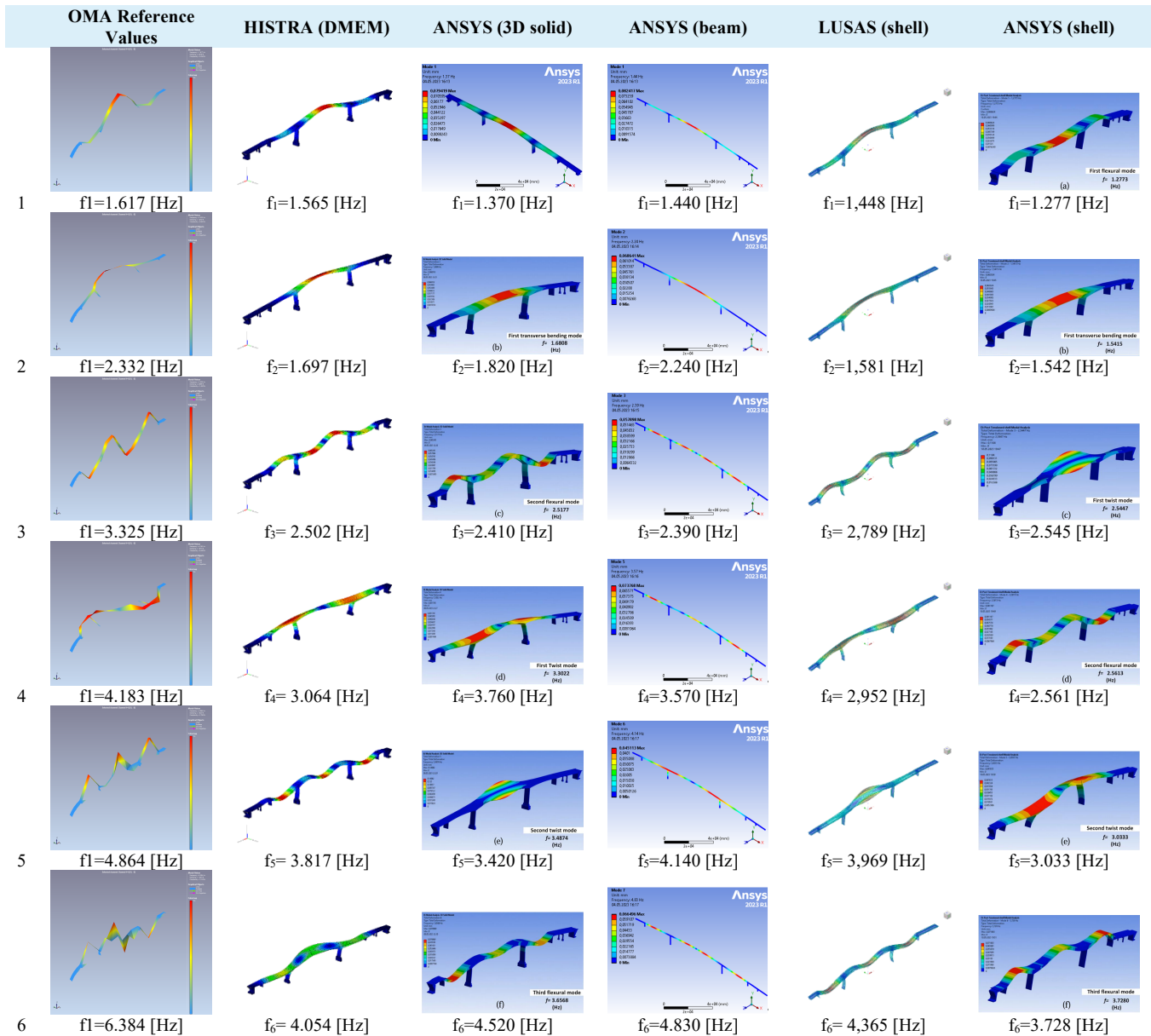


Fig. 84 Graphical comparison of frequencies.

Despite to the frequency differences, the modal shapes appear coherent in almost all the models and for the lower frequency values mainly.

Table 11 Frequencies values

	f ₁ Hz	f ₂ Hz	f ₃ Hz	f ₄ Hz	f ₅ Hz	f ₆ Hz
OMA Average Values	1.640	2.382	3.341	4.127	4.910	6.49
OMA Reference Values	1.617	2.332	3.325	4.183	4.864	6.384
HISTRA (not updated E=19360 Mpa) §3.2	1.565	1.697	2.502	3.064	3.817	4.054
ANSYS 3D (not updated E=19360 Mpa) §3.3	1.370	1.820	2.410	3.760	3.420	4.520
ANSYS BEAM (not updated E=19360 Mpa) §3.3	1.440	2.240	2.390	3.570	4.140	4.830
LUSAS (not updated E=19360 Mpa) §3.4	1.448	1.581	2,789	2,952	3,969	4,365
ANSYS SHELL (not updated E=19360 Mpa) §3.5	1.277	1.541	2.545	2.561	3.033	3.728



The consequence of this result is the need to update the model to calibrate the numerical model according to the OMA results. This aspect has been investigated (§7.2), leading to a calibration of the Young's modulus. In that master's thesis, the model updating procedures were developed for interacting with the ANSYS model. The initial supposed Young's modulus (19360 MPa) has been updated to the value of 20170 MPa.

From the point of the dynamic identification procedures (OMA) a short-term monitoring campaign (10 days) was carried out during June 2023. The already mentioned LUSAS and HISTRA models were specifically developed for defining the sensors placement layout. Before placing the sensors, a stainless T-shape base and an adjustable cube were designed.

An accurate evaluation of the effects of the mounting technique was investigated and results allowed to use the less invasive method, a bi-component glue. A total number of 30 mono-axial sensors were placed on the bridge, Fig. 85. The huge number of sensors represent a relevant economic issue in most real applications. Due to that a master thesis, reported in this document (§7.1), investigated possible strategies for the optimal sensor placement.

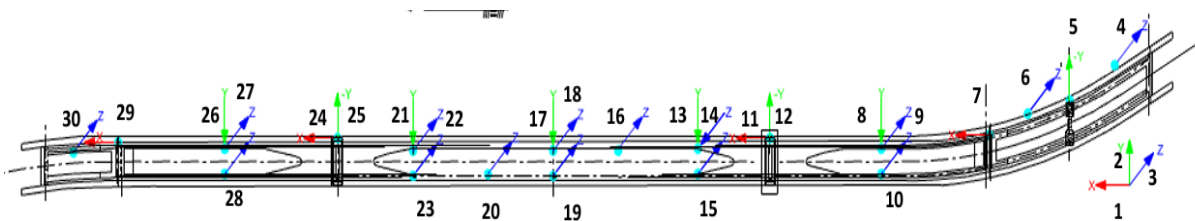


Fig. 85 Sensor layout.

The OMA results indicated consistent stability in the frequencies of the identified vibration modes. In most cases, these modes were reliably detected, demonstrating the robustness of the OMA and the accuracy of the sensors and acquisition architecture. However, one or more modes were not identified in a few instances. This failure to detect certain modes may be due to localized oscillations or spikes in the original data recordings, which can negatively affect the OMA results.

Notably, the first vibration mode was consistently identified across all analyses, maintaining a stable frequency with an average value of 1.64 Hz. This suggests that the first mode is particularly robust and unaffected by minor perturbations in the data. The second through sixth modes were also identified in most of the analyses, exhibiting minimal frequency variation, thus confirming the general stability of these modes over time.

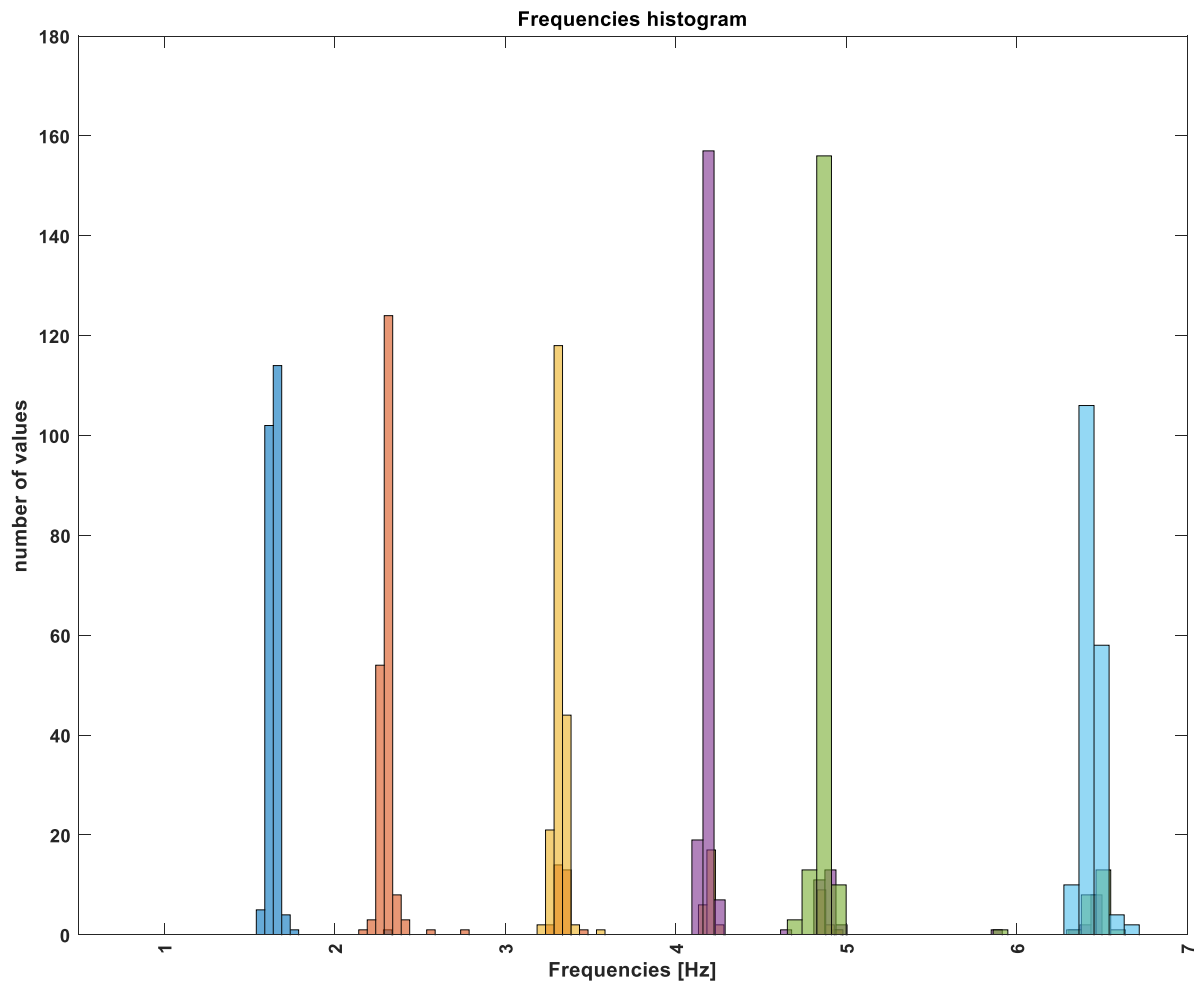


Fig. 86 Histogram of the identified frequencies.

Fig. 62 reports the ten-day long identification campaign in terms of identified frequencies. The frequencies remained stable throughout the observation period, except for a few values that traffic loads may influence. For instance, Fig. 87 report the variations of first and second frequencies. During the acquisition periods at 15:00 on 20 June 2023, 01:00 on 21 June 2023, 01:30 on 21 June 2023, 22:30 on 21 June 2023, 06:00 on 22 June 2023, 15:00 on 22 June 2023, and 00:00 on 24 June 2023, the first frequency showed a decrement, while the second frequency showed an increment. The yellow strips in the next figure highlight these phenomena.

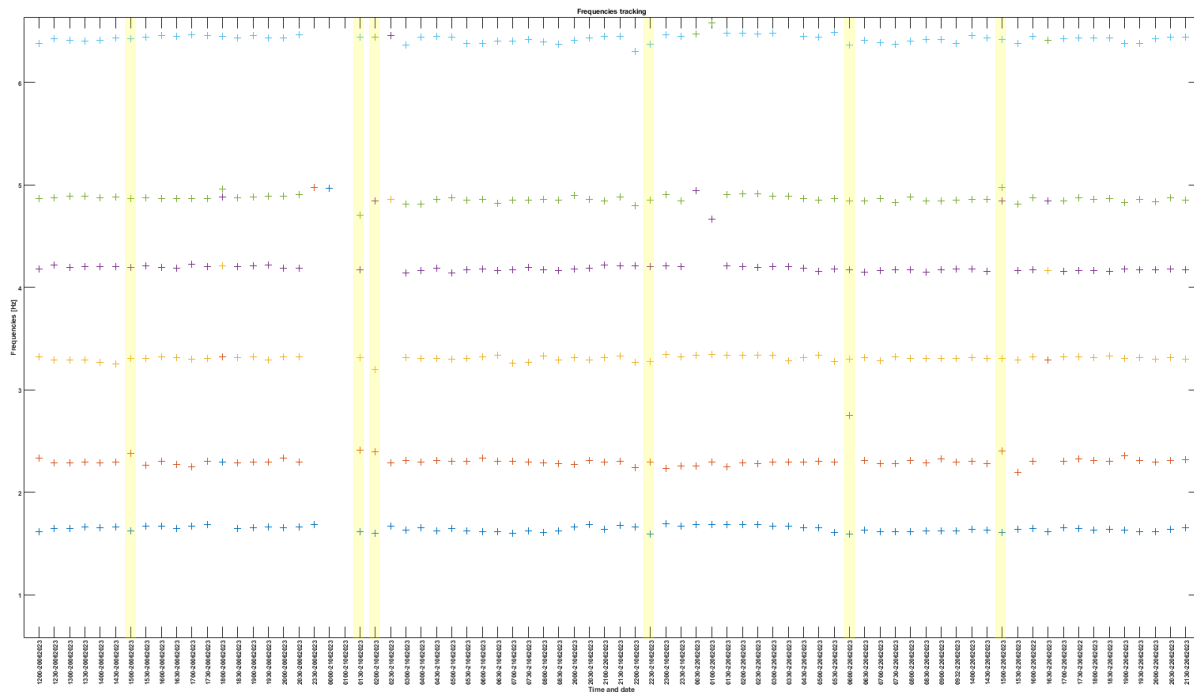


Fig. 87 Relevant variations.

For instance, at 15:00 on 20 June 2023 the first frequency decreases from 1.663 Hz to 1.623 Hz and the second increases from 2.299 Hz to 2.384 Hz. the acquisition period. This may represent a possible alert in a SHM system. Due to that a careful consideration on frequency and modal shapes must be done.

The figures from Fig. 88 to Fig. 91 show how the second modal shape changes significantly during this interval of acquisition. Considering that it is an out of plane flexural shape lead by the in-plane piers' stiffness the presence of damages that lead to non-symmetric responses can be supposed. These damages can be placed on piers, half joints or tendons. A long-term monitoring may help for identifying the correct damaged element.

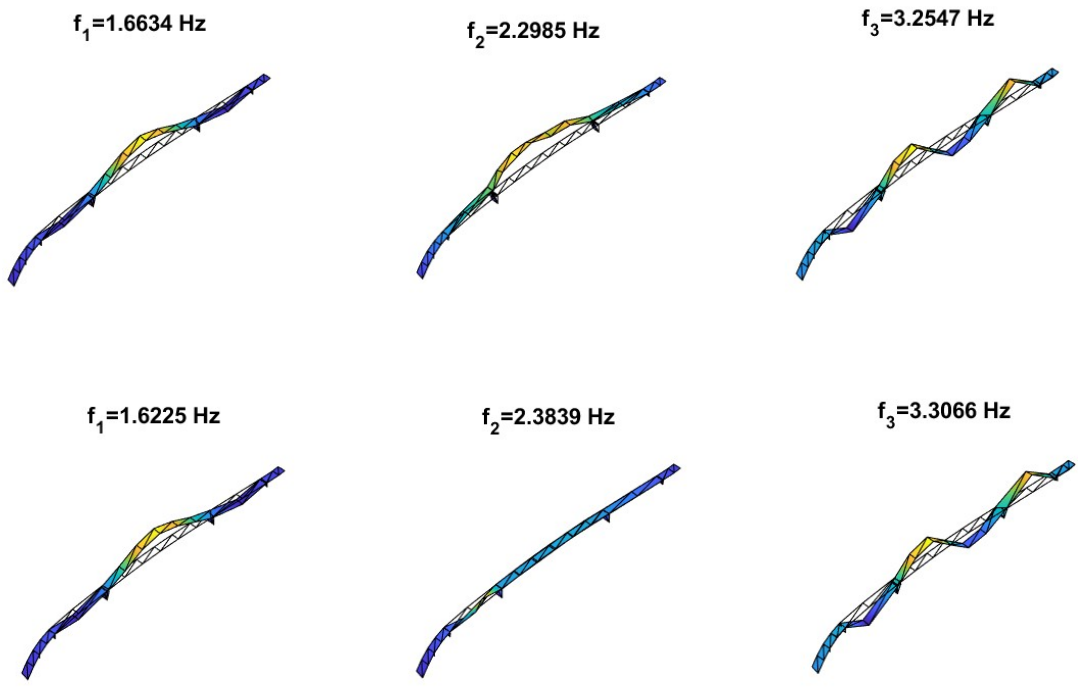


Fig. 88 Comparison of the three modal shapes identified at a) 14:30 and b) 15:00, 20th June 2023.

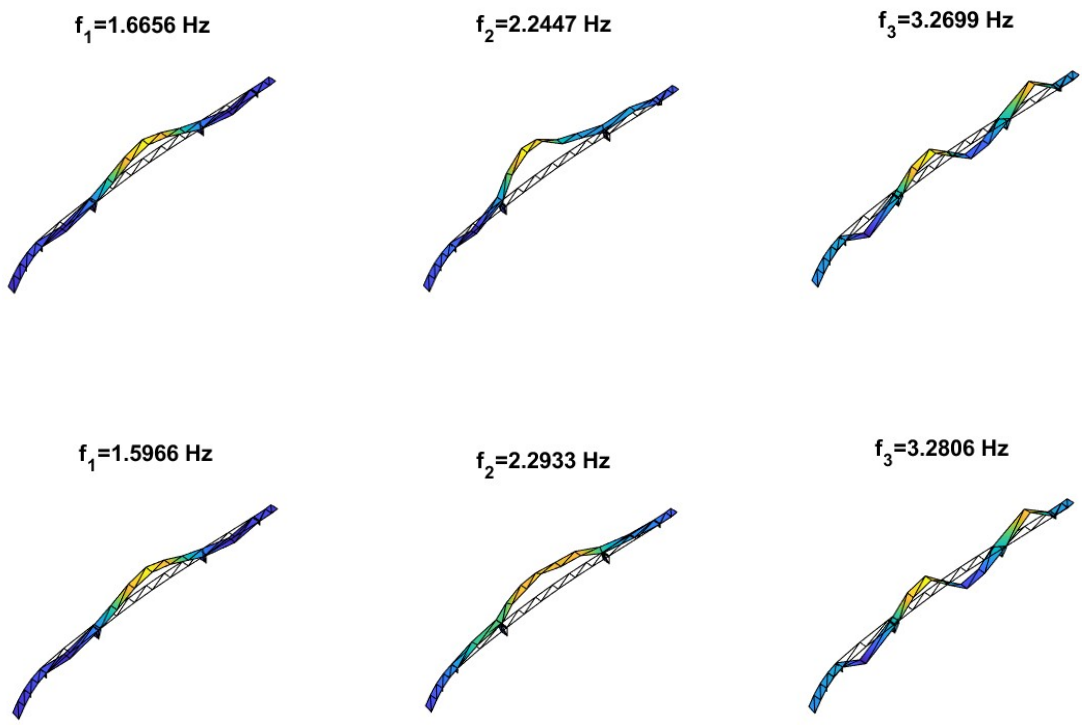


Fig. 89 Comparison of the three modal shapes identified at a) 22:00 and b) 22:30, 21st June 2023.

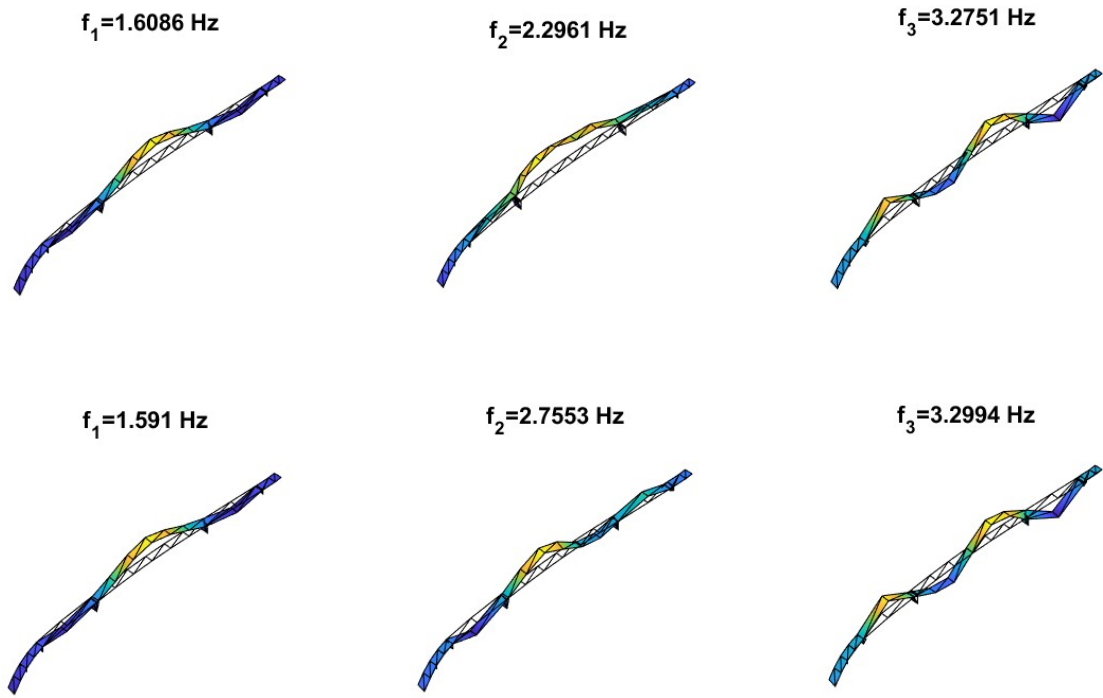


Fig. 90 Comparison of the three modal shapes identified at a) 05:30 and b) 06:00, 22nd June 2023

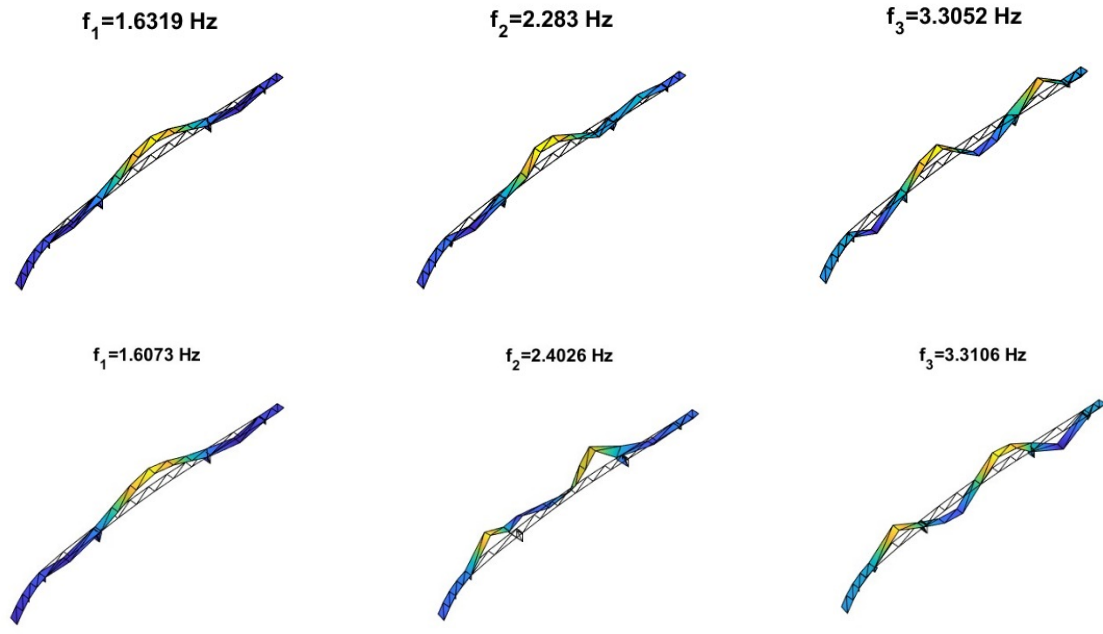


Fig. 91 Comparison of the three modal shapes identified at a) 14:30 and b) 15:00, 23rd June 2023

Lastly, a statistical analysis of the historical series has been performed. A descriptive analysis, a plot of the time series, and a check of the statistical normality of the data analyzing distributions and QQ-plots have been carried out. By means of additive models, trends and seasonality have been identified.

Even though the analysis is only a preliminary attempt, it gave us notable results. Subsequent studies can be needed to validate it using a longer data sample and possibly comparing the conclusions with numerical models and engineering approaches.

The statistical analysis identified credible intervals on the data that can be engaged for identifying outlier values.

For instance, Fig. 92 shows the statistical analysis of the first frequency. As the figure shows, some values are outside the accuracy limit. This approach may help define the thresholds for long-term monitoring better.

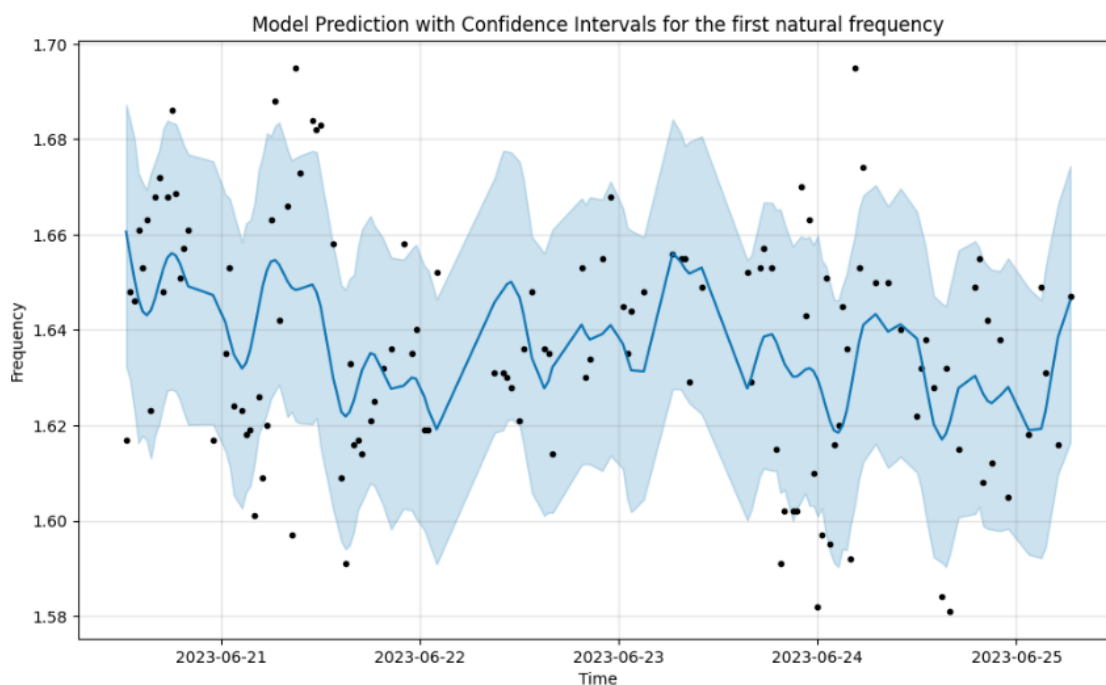


Fig. 92 Model prediction and uncertainties estimation for f_1

Finally, the Herøy FoU project further inspired to investigate problems concerning engineering mathematics such as [34], [35], [36], [37] and [38] that will be studied in the PhD. Thesis *Development of engineering and mathematical based methods for improved decision making in infrastructure maintenance*, Daniele Storni (In Progress).

Chapter 9

Meetings and

Dissemination of Knowledge



9 Dissemination of Knowledge

9.1 Meetings and fieldwork Herøy FoU

S.No.	Date	Event	Location
1	15/08/2022	Project Discussions	Digital
2	09-10/11/2022	Project Kick-off meeting	Mosjøen
3	24/11/2022	Scaffolding and dynamics	Digital
4	27/02/2023 02/03/2023	- Master thesis student visit	Mosjøen and Herøy
5	08/03/2023	Discussions on Installation of Sensors	Digital
6	30/03/2023	Discussion on Vibration Analysis Herøysund Bridge	Digital
7	14/04/2023	Discussion on OMA Activity Herøysund Bridge	Digital
8	11/06/2023 26/06/2023	- Field Work Herøysund Bridge	Herøy
9	28/06/2023 03/07/2023	- Installation of Permanent SHM system	Herøy
10	05/12/2023 06/12/2023	- Herøy FoU plenary meeting	UiT Narvik
11	15/01/2024 16/01/2024	- Project economy discussions and demounting of permanent SHM system	Mosjøen and Herøy
12	27/11/2024 28/11/2024	- End of project meeting	NTNU Trondheim

9.2 Public lectures and research discussions

1. Research Discussions, Meeting Kystverket, 11 November 2022, Kabelvåg.
2. Public Lecture, BA Dagen, 22 March 2023, UiT Campus Narvik.
3. Public Lecture, Visit of ministry of external affairs to UiT, 04 May 2023, UiT Tromsø.
4. Public Lecture, International workshop on technologies for sustainable development, 05-06 June 2023, UiT Campus Narvik.
5. Research Discussions, Meeting with H.E. Dr. B. Bala Bhaskar, Ambassador of the Republic of India to Norway, 27 June 2023, Oslo.
6. Research Discussions, Narvik Havn, 20 March 2024, Narvik.

7. Research Discussions, Norwegian Directorate of Railways, 16 April 2024, Narvik.
8. Research Discussions, 19 April 2024, South Asian University, New Delhi.
9. Research Discussions, UiT Delegation to India, 23 April 2024, Indian Institute of Technology, New Delhi.
10. Public Lecture, UiT Delegation to India, 24 April 2024, Norwegian Embassy, New Delhi.
11. Public Lecture, Indian Structural Health Monitoring Society, 28 June 2024, Online.
12. Research Discussions, IIT Hyderabad, 04 November 2024, Hyderabad, India.
13. Research Discussions, BITS Pilani Hyderabad Campus, 06 November 2024, Hyderabad, India.
14. Public Lecture, IIT (BHU) Varanasi, 07 November 2024, Varanasi, India.
15. Research Discussions with Smart Structures and Dynamics Laboratory, IIT-Delhi, 08 November 2024, New Delhi, India.

9.3 Conferences

1. INCPAA 2023: Mathematical problems in engineering, aerospace and sciences, 27-30 June 2023, Czech Technical University, Prague, Czech Republic.
2. The 50, 70, 80 Conference in Mathematics, 19-23 August 2024, Karlstad University, Karlstad, Sweden.
3. The International Association for Bridge and Structural Engineering (IBASE), 18-21 May 2025, Tokyo, Japan, Abstract Accepted.
4. Experimental Vibration Analysis for Civil Engineering Structures (EVACES), 02-04 July 2025, Porto, Portugal, Abstract Accepted.

9.4 Publications

1. *Analysis of civil engineering infrastructure in Norway with solutions based on structural health monitoring and artificial intelligence*, Kristoffer Tangrand and Harpal Singh, Journal of Non-Linear Studies, 2023.
2. *A comprehensive study of wavelets and artificial intelligence algorithms for SHM and its application to a concrete railway arch bridge*, Harpal Singh, Kristoffer Tangrand and Niklas Grip, AIP Conference Proceedings, INCPAA Prague 2023.
3. *Shell-based finite element modelling of Herøysund bridge in Norway*, Harpal Singh, Zeeshan Azad, Vanni Nicoletti, Journal of Modelling, 2024.
4. *Research on wavelets and artificial intelligence algorithms for structural health monitoring of concrete bridges*, Daniele Storni, Harpal Singh, Kristoffer Tangrand and Niklas Grip, Journal of Mathematics in Engineering, Science & Aerospace, 2024.
5. *A note on methods of analysis and function space used in some engineering problems*, Harpal Singh, The 50, 70,80 Conference in Mathematics, Karlstad, Accepted for Publication in conference proceedings, 2024.

6. *Modelling and dynamic identification of concrete bridge in cold climate region*, Daniele Storni, Giuseppe Occhipinti, Harpal Singh and Per Johan Nicklasson, The International Association for Bridge and Structural Engineering (IBASE), Tokyo, Japan, Paper in progress, 2025.
7. *Dynamic identification and long-term monitoring of post tensioned bridge in cold climate region*, Daniele Storni, Giuseppe Occhipinti and Harpal Singh, Experimental Vibration Analysis for Civil Engineering Structures (EVACES), Porto, Portugal, Paper in progress, 2025.

9.5 Master Thesis

1. *Shell based finite element modeling of Herøysund Bridge*, Zeeshan Azad, Master's Thesis in Engineering Design, UiT, May 2023.
2. *Beam based finite element modeling of Herøysund Bridge*, Patrick Norheim Berg, Master's Thesis in Engineering Design, UiT, May 2023.
3. *Review and application of optimal sensor placement on Herøysund Bridge*, Macdonald Nwamma, Master's Thesis in Engineering Design, UiT, May 2023.
4. *Development of digital twin of the Herøysund Bridge using finite element model updating*, Mohammadreza Khademi, Master's Thesis in Applied Computer Science, UiT, 2024.
5. *Numerical modelling of damage conditions on Herøysund Bridge in Herøy Municipality, Nordland Norway*, Christopher Odongo, Master's Thesis in Engineering Design, UiT, May 2024.

9.6 PhD thesis

Development of engineering and mathematical based methods for improved decision making in infrastructure maintenance, Daniele Storni, Work in Progress.



Chapter 10

References



10 References

- [1] H. Singh and N. Grip, “Recent trends in operation modal analysis techniques and its application on a steel truss bridge.,” *Nonlinear Studies* , vol. 26, no. 4, pp. 911-927, 2019.
- [2] K. Tangrand and H. Singh, “Analysis of civil engineering infrastructure in Norway with solutions based on structural health monitoring and artificial intelligence,” *Mathematics in Engineering, Science & Aerospace (MESA)*, vol. 14, no. 2, 2023.
- [3] L. H. Fredheim, “18-1069 HERØYSUND BRU,” 2017.
- [4] M. Holmqvist, D. I. Ab and R. Antonsen, “Herøysund bridge,” 2020.
- [5] A. Sveen, “18-1069 Herøysund bru. Bæreevneberegninger,” 2020.
- [6] AAS-Jacobsen, “Herøysund bru,” 2019.
- [7] Ingeniør Per Gulbrandsen AS, “Hovedpilarer m-fundamenter. Trykkplate. Formtegning,” 1965.
- [8] M. Nwamma, “Master Thesis: Optimal Sensor Placement,” UiT, Narvik, 2023.
- [9] C. Odongo, “Master Thesis: Numerical Modelling of Damage Conditions on Herøysund Bridge in Herøy Municipality, Nordland, Norway,” UiT , Narvik, 2024.
- [10] X. Kong, C. S. Cai and J. Hu, “The state-of-the-art on framework of vibration-based structural damage identification for decision making,” *Applied Sciences (Switzerland)*, vol. 7, no. 5, 2017.
- [11] A. Rytter, “Vibration based inspection of civil engineering structures,” AalborgUniversity, Denmark, 1993.
- [12] S. Caddemi, I. Calì, F. Cannizzaro, D. D'Urso, G. Occhipinti, B. Pantò, G. Pinaselli, D. Rapicavoli, G. Spirolazzi and R. Zurlo, “A ‘parsimonious’ 3d discrete macro-element method for masonry arch bridges,” in *10thInternational Masonry Conference*, Milan, 2018.
- [13] I. Calì, M. Marletta and B. Pantò, “A simplified model for the evaluation of the seismic behaviour of masonry buildings.,” pp. 1-17, 2005.
- [14] S. Caddemi, I. Calì, F. Cannizzaro, B. Pantò and D. Rapicavoli, “Discrete macroelement modeling,” in *Numerical modeling of masonry and historical structures: from theory to application*, G. M. Bahman Ghiassi, Ed., Elsevier, 2019.
- [15] B. Pantò, F. Cannizzaro, I. Calì and P. Lourenço, “Numerical and experimental validation of a 3D macro-model element method for the in-plane and out-of-plane behaviour of unreinforced masonry walls.,” *International Journal of Architectural Heritage*, vol. 11, no. 7, pp. 946-964, 2017.
- [16] B. Pantò, F. Cannizzaro, S. Caddemi and I. Calì, “3D macro-element modelling approach for seismic assessment of historical masonry churches,” *Advances in Engineering Software* , vol. 97, pp. 40-59, 2016.

- [17] S. Caddemi, I. Calìo, F. Cannizzaro and B. Pantò, “New Frontiers on Seismic Modeling of Masonry Structures,” *Front. Built Environ.*, 2017.
- [18] D. Rapticavoli, F. Cannizzaro, S. Caddemi and I. Calìo, “Discrete Macro-Element structural assessment of a railway masonry arch bridge subjected to pier settlements,” in *8th International Symposium on Life-Cycle Civil Engineering IALCCE 2023*, Milan, Italy, July 2-6 2023.
- [19] C. Chàcara, F. Cannizzaro, B. Pantò and I. Calìo, “Assessment of the dynamic response of unreinforced masonry structures using a macroelement modeling approach,” *Earthquake Engng Struct Dyn*, vol. 47, no. 12, pp. 1-21, 2018.
- [20] F. Cannizzaro, G. Occhipinti, D. Maltese, C. Oriti, D. Patanè, S. Caddemi and I. Cliò, “Modelling a reinforced concrete arch bridge by means of Discrete Macro-Element Model: the case of Giovanni XXIII bridge in Ragusa,” in *II FABRE Conference - Existing bridges, viaducts and tunnels: research, innovation adn application (FABRE24)*, 2024.
- [21] P. N. Berg, “Master Thesis: Beam Based Finite Element Modelling of Herøysund Bridge by and tutored,” UiT , Narvik, 2023.
- [22] FEA, “lusas.com,” [Online]. Available: https://www.lusas.com/products/options/masonry_bridge_wizard.html. [Accessed 05 08 2023].
- [23] Z. Azad, “Master Thesis: Shell-Based Finite Element Modelling of Herøysund Bridge,” UiT , Narvik, 2023.
- [24] SVIBS, “ARTEMIS Modal Help V3,” SVIBS.
- [25] G. James, T. Carne and J. Lauffer, “The Natural Excitation Technique (NExT) for Modal Parameter Extraction from Operating Structures. Modal Analysis,” *The International Journal of Analytical and Experimental Modal Analysis* , vol. 10, pp. 260-277, 1995.
- [26] S. Au, “Operational Modal Analysis: Modeling, Inference, Uncertainty Laws,” Springer, 2017.
- [27] S. Au, F. Zhang and Y. Ni, “Bayesian operational modal analysis: Theory, computation, practice.,” *Computer & Structures*, vol. 126, pp. 3-14, 2013.
- [28] M. Khademi, “Master Thesis: Development of Digital Twin of the Herøysund Bridge using Finite Element Model Updating,” UiT , Narvik.
- [29] GruppoSismica srl, *Histra - software for bridge modelling*, Catania, Italy.
- [30] ANSYS Inc., *ANSYS*.
- [31] H. Singh, Z. Azad and V. Nicoletti, “Shell-Based Finite Element Modeling of Herøysund Bridge in Norway,” *Modelling* , vol. 5, no. 1, pp. 71-84, 2023.
- [32] D. Storni, H. Singh, K. Tangrand and N. Grip, “Research on wavelets and artificial intelligence algorithms for structural health monitoring of concrete bridge,” *Journal| MESA*, vol. 15, no. 1, pp. 131-150, 2024.
- [33] V. Nicoletti, S. Quarchioni, R. Martini, F. Gara, L. Gaile and H. Singh, “A Novel Software Tool for the Optimal Sensor Placement in Civil Engineering Structures,” in *IOMAC* , 2024.
- [34] H. Singh, N. Grip and P. J. Nicklasson, “A comprehensive study of signal processing techniques of importance for operation modal analysis (OMA) and its application to a high-rise building.,” *Nonlinear Studies*, vol. 28, no. 2, 2021.

- [35] G. Akishev, L. E. Persson and H. Singh, “Inequalities for the Fourier coefficients in unbounded orthogonal systems in generalized Lorentz spaces.,” *Nonlinear Studies*, vol. 27, no. 4, 2020.
- [36] G. Akishev, L. E. Persson and H. Singh, “Some New Fourier and Jackson-Nikol’skii Type Inequalities In Unbounded Orthonormal Systems.,” *Constructive Mathematical Analysis* , vol. 4, no. 3, pp. 291-304., 2021.
- [37] N. Samko and H. Singh, “A note on contributions concerning nonseparable spaces with respect to signal processing within Bayesian frameworks.,” *Mathematical Methods in the Applied Sciences*, vol. 46, no. 1, pp. 1178-1184., 2023.
- [38] D. Baramidze, L. E. Persson, S. H. and G. Tephnadze, “Some new results and inequalities for subsequences of Nörlund logarithmic means of Walsh–Fourier series.,” *Journal of Inequalities and Applications* , vol. 30, no. 1, 2022.





Appendix 1


Sensor Placement Survey



11 Appendix 1: Sensor placement survey

Survey of the sensors placement	
Herøysund bridge	
Geometric Point	P1
Survey	18/06/2023
Point of Acquisition	PU1
Sensor number	1
Structural Element (F: Foundation, P:Pier, D:Deck, S:Scaffolding)	F
Axis	+X
Sensor owner	WISE
Sensor Serial Number	70917
Cable owner	WISE
Notes	External reference point at the base of abutment 1
Picture	
	


Survey of the sensors placement	
Herøysund bridge	
Geometric Point	P1
Survey	18/06/2023
Point of Aquisition	PU1
Sensor number	2
Structural Element (F: Foundation, P:Pier, D:Deck, S:Scaffolding)	F
Axis	+Y
Sensor owner	WISE
Sensor Serial Number	70920
Cable owner	WISE
Notes	Placed on foundation
Picture	
	


Survey of the sensors placement	
Herøysund bridge	
Geometric Point	P1
Survey	18/06/2023
Point of Aquisition	PU1
Sensor number	3
Structural Element (F: Foundation, P:Pier, D:Deck, S:Scaffolding)	F
Axis	+Z
Sensor owner	WISE
Sensor Serial Number	68465
Cable owner	WISE
Notes	Placed on foundation
Picture	
	

Survey of the sensors placement	
Herøysund bridge	
Geometric Point	P2
Survey	18/06/2023
Point of Aquisition	PU1
Sensor number	4
Structural Element (F: Foundation, P:Pier, D:Deck, S:Scaffolding)	DI
Axis	+Z
Sensor owner	WISE
Sensor Serial Number	70919
Cable owner	UIT
Notes	Right side of deck 1

Picture

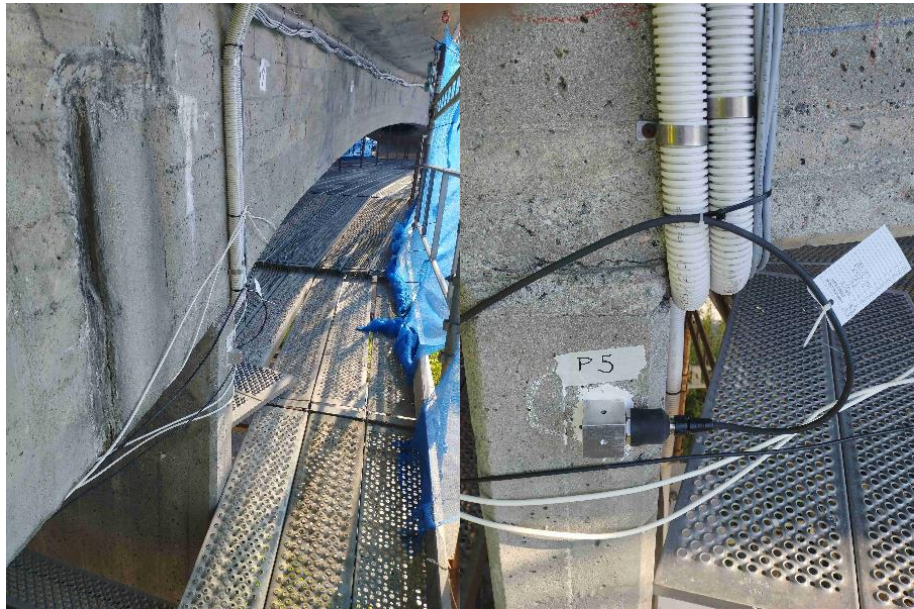



Survey of the sensors placement	
Herøysund bridge	
Geometric Point	P3
Survey	18/06/2023
Point of Aquisition	PU1
Sensor number	5
Structural Element (F: Foundation, P:Pier, D:Deck, S:Scaffolding)	PI
Axis	-Y
Sensor owner	WISE
Sensor Serial Number	70918
Cable owner	UIT
Notes	Positioned on the pile in the transverse direction. The pile is portal-shaped.
Picture	


Survey of the sensors placement	
Herøysund bridge	
Geometric Point	P4
Survey	18/06/2023
Point of Aquisition	PU1
Sensor number	6
Structural Element (F: Foundation, P:Pier, D:Deck, S:Scaffolding)	DII
Axis	+Z
Sensor owner	WISE
Sensor Serial Number	70263
Cable owner	WISE
Notes	Placed on a vertical crack on the right beam
Picture	
	


Survey of the sensors placement	
Herøysund bridge	
Geometric Point	P5
Survey	18/06/2023
Point of Aquisition	PU1
Sensor number	7
Structural Element (F: Foundation, P:Pier, D:Deck, S:Scaffolding)	PII
Axis	+X
Sensor owner	WISE
Sensor Serial Number	70262
Cable owner	WISE
Notes	Placed on the right side of the pier


Picture



Survey of the sensors placement	
Herøysund bridge	
Geometric Point	P6
Survey	18/06/2023
Point of Aquisition	PU2
Sensor number	8
Structural Element (F: Foundation, P:Pier, D:Deck, S:Scaffolding)	DIII
Axis	+Y
Sensor owner	WISE
Sensor Serial Number	71118
Cable owner	WISE
Notes	Right beam of the first deck
Picture	
	

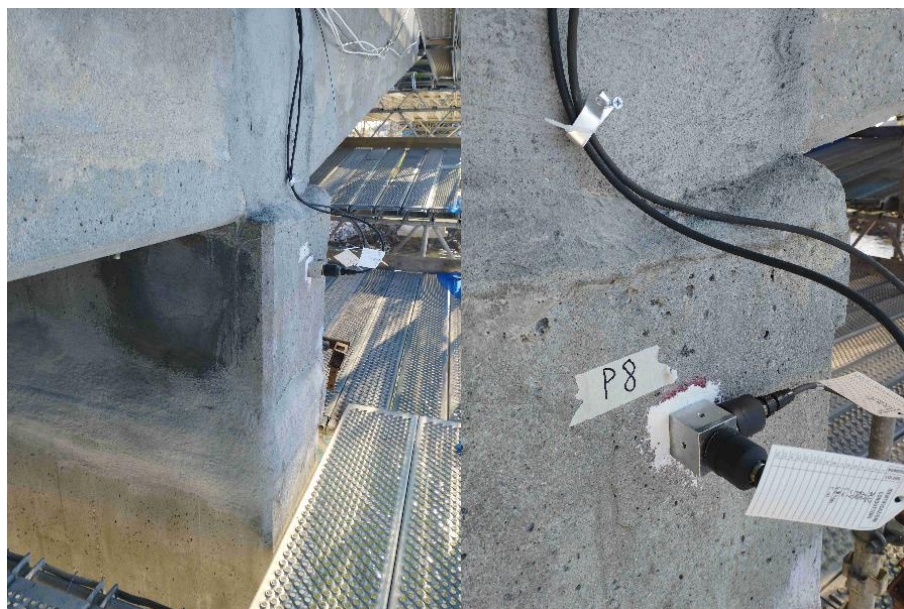
Survey of the sensors placement	
Herøysund bridge	
Geometric Point	P6
Survey	18/06/2023
Point of Aquisition	PU2
Sensor number	9
Structural Element (F: Foundation, P:Pier, D:Deck, S:Scaffolding)	DIII
Axis	+Z
Sensor owner	WISE
Sensor Serial Number	72620
Cable owner	WISE
Notes	Right beam vertical axis
Picture	
	

Survey of the sensors placement	
Herøysund bridge	
Geometric Point	P7
Survey	18/06/2023
Point of Aquisition	PU2
Sensor number	10
Structural Element (F: Foundation, P:Pier, D:Deck, S:Scaffolding)	DIII
Axis	+Z
Sensor owner	WISE
Sensor Serial Number	68955
Cable owner	WISE
Notes	Left side
Picture	
	

Survey of the sensors placement	
Herøysund bridge	
Geometric Point	P8
Survey	18/06/2023
Point of Aquisition	PU2
Sensor number	11
Structural Element (F: Foundation, P:Pier, D:Deck, S:Scaffolding)	PIII
Axis	+X
Sensor owner	WISE
Sensor Serial Number	68954
Cable owner	WISE
Notes	Bridge abutment wall in the riverbed. Extensive intervention areas for bar restoration can be identified
Picture	
	

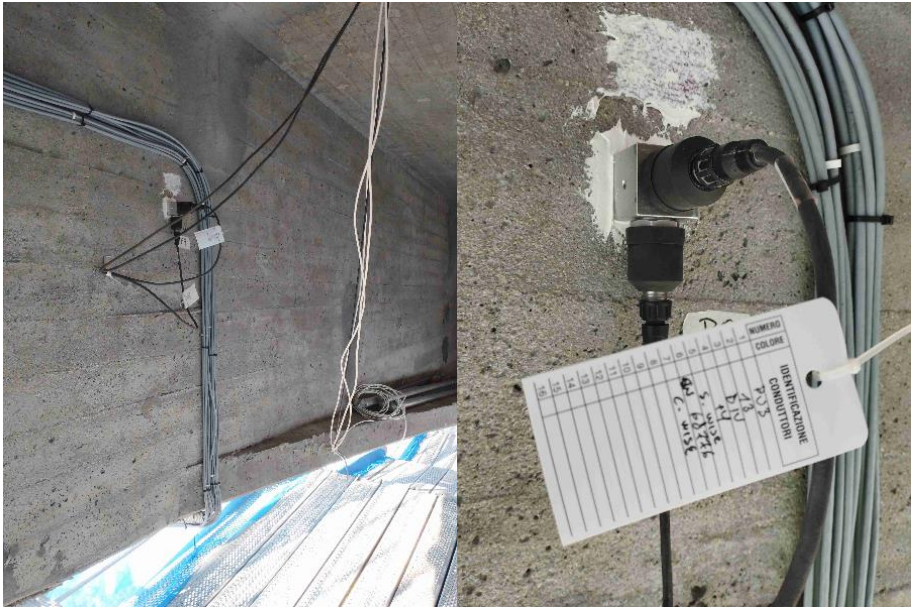
Survey of the sensors placement	
Herøysund bridge	
Geometric Point	P8
Survey	18/06/2023
Point of Aquisition	PU2
Sensor number	12
Structural Element (F: Foundation, P:Pier, D:Deck, S:Scaffolding)	PIII
Axis	-Y
Sensor owner	WISE
Sensor Serial Number	68466
Cable owner	WISE
Notes	Abutment in the riverbed, right side, widespread restoration interventions.

Picture



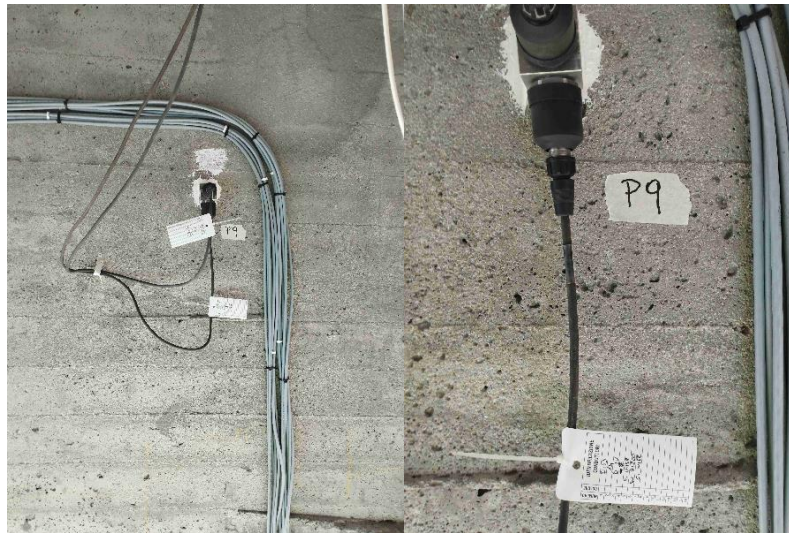
Survey of the sensors placement	
Herøysund bridge	
Geometric Point	P9
Survey	18/06/2023
Point of Aquisition	PU3
Sensor number	13
Structural Element (F: Foundation, P:Pier, D:Deck, S:Scaffolding)	DIV
Axis	+Y
Sensor owner	WISE
Sensor Serial Number	68776
Cable owner	WISE
Notes	At the end of the dovetail joint. All dovetail joints exhibit a central crack.


Picture





Survey of the sensors placement	
Herøysund bridge	
Geometric Point	P9
Survey	18/06/2023
Point of Aquisition	PU3
Sensor number	14
Structural Element (F: Foundation, P:Pier, D:Deck, S:Scaffolding)	DIV
Axis	-Z
Sensor owner	WISE
Sensor Serial Number	71200
Cable owner	WISE
Notes	Positioned downward to reduce interference with strain gauge cables.


Picture





Survey of the sensors placement	
Herøysund bridge	
Geometric Point	P10
Survey	18/06/2023
Point of Aquisition	PU3
Sensor number	15
Structural Element (F: Foundation, P:Pier, D:Deck, S:Scaffolding)	DIV
Axis	+Z
Sensor owner	WISE
Sensor Serial Number	70261
Cable owner	WISE
Notes	Left side
Picture	
	


Survey of the sensors placement	
Herøysund bridge	
Geometric Point	P11
Survey	18/06/2023
Point of Aquisition	PU3
Sensor number	16
Structural Element (F: Foundation, P:Pier, D:Deck, S:Scaffolding)	DIV
Axis	+Z
Sensor owner	WISE
Sensor Serial Number	71119
Cable owner	WISE
Notes	Right side
Picture	
	


Survey of the sensors placement	
Herøysund bridge	
Geometric Point	P12
Survey	18/06/2023
Point of Aquisition	PU3
Sensor number	17
Structural Element (F: Foundation, P:Pier, D:Deck, S:Scaffolding)	DIV
Axis	+Y
Sensor owner	WISE
Sensor Serial Number	71270
Cable owner	WISE
Notes	Right side centerline
Picture	

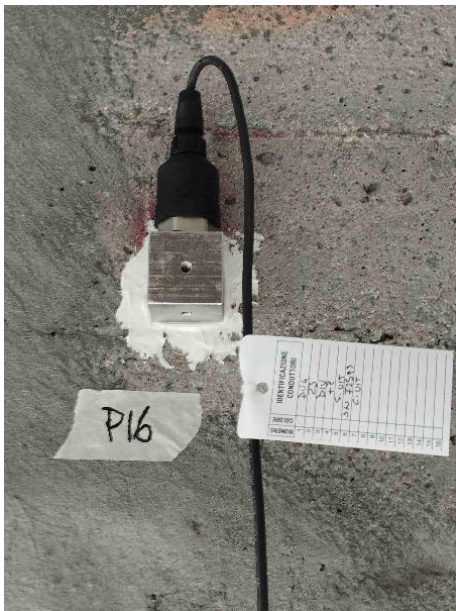
Survey of the sensors placement	
Herøysund bridge	
Geometric Point	P12
Survey	18/06/2023
Point of Aquisition	PU3
Sensor number	18
Structural Element (F: Foundation, P:Pier, D:Deck, S:Scaffolding)	DIV
Axis	+Z
Sensor owner	WISE
Sensor Serial Number	71203
Cable owner	UIT
Notes	Right side centerline
Picture	
	


Survey of the sensors placement	
Herøysund bridge	
Geometric Point	P13
Survey	18/06/2023
Point of Aquisition	PU3
Sensor number	19
Structural Element (F: Foundation, P:Pier, D:Deck, S:Scaffolding)	DIV
Axis	+Z
Sensor owner	UIT
Sensor Serial Number	72610
Cable owner	UIT
Notes	Left side centerline
Picture	
	


Survey of the sensors placement	
Herøysund bridge	
Geometric Point	P14
Survey	18/06/2023
Point of Aquisition	PU4
Sensor number	20
Structural Element (F: Foundation, P:Pier, D:Deck, S:Scaffolding)	DIV
Axis	+Z
Sensor owner	UIT
Sensor Serial Number	72603
Cable owner	UIT
Notes	Placed between post-tensioning cables and fiber band. Left side.
Picture	

Survey of the sensors placement	
Herøysund bridge	
Geometric Point	P15
Survey	18/06/2023
Point of Aquisition	PU4
Sensor number	21
Structural Element (F: Foundation, P:Pier, D:Deck, S:Scaffolding)	DIV
Axis	+Y
Sensor owner	UIT
Sensor Serial Number	72609
Cable owner	UIT
Notes	Right side
Picture	
	

Survey of the sensors placement	
Herøysund bridge	
Geometric Point	P15
Survey	18/06/2023
Point of Aquisition	PU4
Sensor number	22
Structural Element (F: Foundation, P:Pier, D:Deck, S:Scaffolding)	DIV
Axis	+Z
Sensor owner	UIT
Sensor Serial Number	72594
Cable owner	UIT
Notes	Left side
Picture	
	

Survey of the sensors placement	
Herøysund bridge	
Geometric Point	P16
Survey	19/06/2023
Point of Aquisition	PU4
Sensor number	23
Structural Element (F: Foundation, P:Pier, D:Deck, S:Scaffolding)	DIV
Axis	+Z
Sensor owner	UIT
Sensor Serial Number	72593
Cable owner	UIT
Notes	Cable to be fixed
<p>Picture</p> 	

Survey of the sensors placement	
Herøysund bridge	
Geometric Point	P17
Survey	18/06/2023
Point of Aquisition	PU4
Sensor number	24
Structural Element (F: Foundation, P:Pier, D:Deck, S:Scaffolding)	PIV
Axis	+X
Sensor owner	UIT
Sensor Serial Number	72597
Cable owner	UIT
Notes	Right side of the pier in the riverbed
Picture	


Survey of the sensors placement	
Herøysund bridge	
Geometric Point	P17
Survey	18/06/2023
Point of Aquisition	PU4
Sensor number	25
Structural Element (F: Foundation, P:Pier, D:Deck, S:Scaffolding)	PIV
Axis	-Y
Sensor owner	UIT
Sensor Serial Number	72595
Cable owner	UIT
Notes	Right side of the pier wall in the riverbed
Picture	
	

Survey of the sensors placement	
Herøysund bridge	
Geometric Point	P18
Survey	18/06/2023
Point of Aquisition	PU5
Sensor number	26
Structural Element (F: Foundation, P:Pier, D:Deck, S:Scaffolding)	DV
Axis	+Y
Sensor owner	UIT
Sensor Serial Number	72619
Cable owner	UIT
Notes	Right side



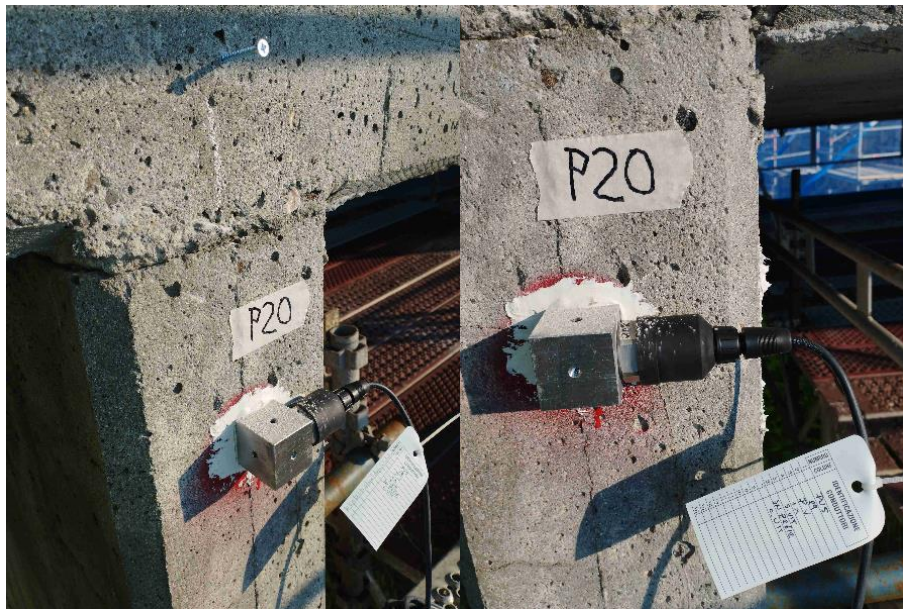
Survey of the sensors placement	
Herøysund bridge	
Geometric Point	P18
Survey	18/06/2023
Point of Aquisition	PU5
Sensor number	27
Structural Element (F: Foundation, P:Pier, D:Deck, S:Scaffolding)	DV
Axis	+Z
Sensor owner	UIT
Sensor Serial Number	72615
Cable owner	UIT
Notes	Right side



Survey of the sensors placement	
Herøysund bridge	
Geometric Point	P19
Survey	18/06/2023
Point of Aquisition	PU5
Sensor number	28
Structural Element (F: Foundation, P:Pier, D:Deck, S:Scaffolding)	DV
Axis	+Z
Sensor owner	UIT
Sensor Serial Number	72607
Cable owner	UIT
Notes	Left side
Picture	
	

Survey of the sensors placement	
Herøysund bridge	
Geometric Point	P20
Survey	18/06/2023
Point of Aquisition	PU5
Sensor number	29
Structural Element (F: Foundation, P:Pier, D:Deck, S:Scaffolding)	PV
Axis	+X
Sensor owner	UIT
Sensor Serial Number	72612
Cable owner	UIT
Notes	Pier wall right side

Picture



Survey of the sensors placement	
Herøysund bridge	
Geometric Point	P21
Survey	18/06/2023
Point of Aquisition	PU5
Sensor number	30
Structural Element (F: Foundation, P:Pier, D:Deck, S:Scaffolding)	DVI
Axis	+Z
Sensor owner	UIT
Sensor Serial Number	72597
Cable owner	UIT
Notes	Viaduct end right side centerline

Picture



Data and time	f1	f2	f3	f4	f5	f6	f7
20-Jun-2023 12:00:00	1,617	2,332	3,325	4,183	4,864	6,384	8,412
20-Jun-2023 12:30:00	1,648	2,290	3,294	4,219	4,879	6,425	8,624
20-Jun-2023 13:00:00	1,646	2,287	3,291	4,198	4,891	6,416	8,617
20-Jun-2023 13:30:00	1,661	2,298	3,289	4,205	4,891	6,408	8,546
20-Jun-2023 14:00:00	1,653	2,291	3,270	4,204	4,876	6,415	8,554
20-Jun-2023 14:30:00	1,663	2,299	3,255	4,206	4,880	6,434	8,636
20-Jun-2023 15:00:00	1,623	2,384	3,307	4,193	4,864	6,427	8,643
20-Jun-2023 15:30:00	1,668	2,266	3,306	4,211	4,879	6,445	8,587
20-Jun-2023 16:00:00	1,672	2,300	3,320	4,199	4,868	6,459	8,618
20-Jun-2023 16:30:00	1,648	2,273	3,313	4,187	4,867	6,451	8,687
20-Jun-2023 17:00:00	1,668	2,252	3,298	4,225	4,864	6,463	8,459
20-Jun-2023 17:30:00	1,686	2,301	3,307	4,207	4,869	6,457	8,643
20-Jun-2023 18:00:00	2,299	3,320	4,210	4,886	4,960	6,454	8,648
20-Jun-2023 18:30:00	1,651	2,284	3,318	4,205	4,875	6,439	8,619
20-Jun-2023 19:00:00	1,657	2,293	3,325	4,215	4,885	6,457	8,703
20-Jun-2023 19:30:00	1,661	2,296	3,288	4,219	4,894	6,433	8,558
20-Jun-2023 20:00:00	1,659	2,336	3,324	4,185	4,889	6,432	-
20-Jun-2023 20:30:00	1,664	2,297	3,324	4,189	4,905	6,469	-
20-Jun-2023 23:30:00	1,690		-		4,973	-	-
21-Jun-2023 00:00:00		-	-		4,970	-	-
21-Jun-2023 01:00:00	-	-	-	-	-	-	-
21-Jun-2023 01:30:00	1,617	2,408	3,315	4,174	4,707	6,441	8,508
21-Jun-2023 02:00:00	1,597	2,399	3,198	4,841	6,445	8,550	-
21-Jun-2023 02:30:00	1,671	2,285		4,862	-6,458	-	-
21-Jun-2023 03:00:00	1,635	2,313	3,318	4,142	4,813	6,370	8,418
21-Jun-2023 04:00:00	1,653	2,294	3,308	4,163	4,815	6,447	8,549
21-Jun-2023 04:30:00	1,624	2,308	3,309	4,185	4,859	6,455	8,496
21-Jun-2023 05:00:00	1,650	2,301	3,301	4,145	4,878	6,447	-
21-Jun-2023 05:30:00	1,623	2,304	3,305	4,173	4,855	6,381	8,516
21-Jun-2023 06:00:00	1,618	2,332	3,327	4,183	4,864	6,384	8,412
21-Jun-2023 06:30:00	1,619	2,301	3,342	4,166	4,825	6,406	8,454
21-Jun-2023 07:00:00	1,601	2,303	3,264	4,169	4,854	6,402	8,463
21-Jun-2023 07:30:00	1,626	2,293	3,266	4,195	4,851	6,424	8,511
21-Jun-2023 08:00:00	1,609	2,286	3,331	4,176	4,858	6,395	8,518
21-Jun-2023 08:30:00	1,620	2,282	3,292	4,163	4,852	6,378	8,498
21-Jun-2023 20:00:00	1,663	2,270	3,312	4,184	4,895	6,411	8,601
21-Jun-2023 20:30:00	1,688	2,311	3,289	4,188	4,861	6,438	8,577
21-Jun-2023 21:00:00	1,642	2,297	3,314	4,217	4,845	6,450	8,689
21-Jun-2023 21:30:00	1,677	2,301	3,330	4,208	4,884	6,448	-
21-Jun-2023 22:00:00	1,666	2,245	3,270	4,211	4,802	6,303	8,387
21-Jun-2023 22:30:00	1,597	2,293	3,281	4,201	4,851	6,377	8,628
21-Jun-2023 23:00:00	1,695	2,236	3,346	4,212	4,909	6,470	8,676

21-Jun-2023 23:30:00	1,673	2,259	3,320	4,205	4,846	6,455	8,640
22-Jun-2023 00:30:00	1,684	2,257	3,341		4,945	-6,476	-
22-Jun-2023 01:00:00	1,685	2,299	3,345	4,666	6,583	8,679	-
22-Jun-2023 01:30:00	1,684	2,251	3,338	4,208	4,909	6,480	8,667
22-Jun-2023 02:00:00	1,682	2,287	3,335	4,203	4,911	6,484	8,672
22-Jun-2023 02:30:00	1,683	2,280	3,336	4,197	4,912	6,475	8,695
22-Jun-2023 03:00:00	1,671	2,295	3,339	4,203	4,889	6,484	-
22-Jun-2023 03:30:00	1,672	2,297	3,285	4,201	4,893	6,679	-
22-Jun-2023 04:30:00	1,658	2,298	3,313	4,188	4,868	6,449	8,613
22-Jun-2023 05:00:00	1,656	2,306	3,339	4,156	4,854	6,444	-
22-Jun-2023 05:30:00	1,609	2,296	3,275	4,180	4,870	6,486	8,559
22-Jun-2023 06:00:00	1,591	2,755	3,299	4,172	4,843	6,370	8,497
22-Jun-2023 06:30:00	1,633	2,313	3,316	4,150	4,844	6,414	8,522
22-Jun-2023 07:00:00	1,616	2,282	3,288	4,164	4,865	6,393	8,503
22-Jun-2023 07:30:00	1,617	2,279	3,324	4,172	4,832	6,376	8,484
22-Jun-2023 08:00:00	1,614	2,313	3,307	4,176	4,885	6,406	8,492
22-Jun-2023 08:30:00	1,622	2,286	3,312	4,151	4,847	6,418	-
22-Jun-2023 09:00:00	1,621	2,323	3,311	4,176	4,848	6,418	8,465
22-Jun-2023 09:32:00	1,625	2,293	3,309	4,184	4,852	6,380	8,494
22-Jun-2023 14:00:00	1,640	2,304	3,317	4,179	4,863	6,456	-
22-Jun-2023 14:30:00	1,632	2,283	3,305	4,155	4,857	6,440	8,483
22-Jun-2023 15:00:00	1,607	2,403	3,311	4,842	4,975	6,423	-
22-Jun-2023 15:30:00	1,636	2,199	3,292	4,162	4,813	6,380	8,592
22-Jun-2023 16:00:00	1,646	2,305	3,321	4,171	4,877	6,452	-
22-Jun-2023 16:30:00	1,616	3,293		4,164	4,846	6,416	8,732
22-Jun-2023 17:00:00	1,658	2,305	3,327	4,156	4,842	6,432	8,721
22-Jun-2023 17:30:00	1,649	2,327	3,322	4,166	4,874	6,434	-
22-Jun-2023 18:00:00	1,635	2,308	3,318	4,163	4,860	6,436	8,678
22-Jun-2023 18:30:00	1,640	2,303	3,329	4,156	4,869	6,437	8,797
22-Jun-2023 19:00:00	1,635	2,361	3,308	4,179	4,826	6,384	-
22-Jun-2023 19:30:00	1,619	2,309	3,317	4,174	4,863	6,381	8,656
22-Jun-2023 20:00:00	1,619	2,298	3,302	4,170	4,841	6,428	8,637
22-Jun-2023 20:30:00	1,643	2,311	3,318	4,177	4,878	6,445	-
22-Jun-2023 21:30:00	1,652	2,316	3,303	4,174	4,853	6,445	8,682
22-Jun-2023 22:00:00	1,645	2,311	3,357	4,187	4,926	-	-
22-Jun-2023 22:30:00	1,646	2,307	3,323	4,189	4,890	6,459	-
22-Jun-2023 23:00:00	1,651	2,312	3,350	4,191	4,878	-	-
22-Jun-2023 23:30:00	1,653	2,314	3,558	4,214	-	-	-
23-Jun-2023 00:00:00	1,652	2,312	3,337	4,180	4,870	6,455	
23-Jun-2023 00:30:00	1,651	2,309		4,190	-	-	-
23-Jun-2023 01:00:00	1,652	2,312		4,196	-	-	-
23-Jun-2023 01:30:00	1,656	2,305	3,335	4,202		6,482	-
23-Jun-2023 02:00:00	1,653	2,316		4,223	4,927	-	-

23-Jun-2023 02:30:00	1,657	2,315		4,179	4,858	-	-
23-Jun-2023 03:00:00	1,654	2,311		4,216	-	-	-
23-Jun-2023 03:30:00	1,657	2,313	3,347	4,190		6,487	-
23-Jun-2023 04:00:00	1,658	2,311		4,188	4,893	-	-
23-Jun-2023 04:30:00	1,631	2,364	3,323	4,269	4,915	6,443	8,683
23-Jun-2023 05:00:00	1,640	3,347		4,184	4,881	6,424	-
23-Jun-2023 05:30:00	1,631	2,344	3,323	4,175	4,874	6,465	8,646
23-Jun-2023 06:00:00	1,630	2,318	3,337	4,177	4,939	6,458	8,701
23-Jun-2023 07:00:00	1,628	2,316	3,338	4,180	4,890	6,466	8,676
23-Jun-2023 08:00:00	1,613	2,293	3,320	4,187	4,877	6,444	-
23-Jun-2023 08:30:00	1,621	2,313	3,334	4,167	4,884	6,443	8,651
23-Jun-2023 09:00:00	1,636	2,313	3,344	4,180	4,876	6,456	8,666
23-Jun-2023 09:30:00	1,635	2,316	3,359	4,188	4,873	6,455	-
23-Jun-2023 10:00:00	1,648	2,308	3,347	4,176	4,884	6,467	8,619
23-Jun-2023 10:30:00	1,612	3,314			4,844	6,453	-
23-Jun-2023 11:00:00	1,629	2,315	3,323	4,182	4,881	6,432	-
23-Jun-2023 11:30:00	1,636	2,325	3,338	4,178	4,871	6,459	8,660
23-Jun-2023 12:00:00	1,635	2,310	3,340	4,188	4,873	6,456	8,674
23-Jun-2023 12:30:00	1,614	2,293	3,334	4,178	4,854	6,469	8,693
23-Jun-2023 13:00:00	1,634	3,327			4,841	6,414	8,612
23-Jun-2023 13:30:00	1,611	2,331	3,339	4,194	4,867	6,462	-
23-Jun-2023 14:00:00	1,623	3,342		4,251	4,886	6,479	-
23-Jun-2023 14:30:00	1,642	2,313	3,343	4,189	4,893	6,448	-
23-Jun-2023 15:00:00	1,610	2,266	3,246	4,197	4,842	6,449	-
23-Jun-2023 15:30:00	1,689	2,312	3,343	4,173	4,901	6,490	-
23-Jun-2023 16:00:00	1,653	2,347	3,311	4,163	4,910	6,440	8,656
23-Jun-2023 16:30:00	1,630	2,319	3,345	4,195	4,881	6,476	8,698
23-Jun-2023 17:00:00	1,634	2,312	3,341	4,202	4,879	6,489	8,689
23-Jun-2023 17:30:00	1,672	2,347	3,324	4,204	4,889	6,459	-
23-Jun-2023 18:00:00	1,639	3,339	4,180	4,881	6,479	8,668	-
23-Jun-2023 18:30:00	1,655	2,318	3,300	4,186	4,878	6,443	8,689
23-Jun-2023 19:00:00	1,654		3,349		4,895	6,497	-
23-Jun-2023 19:30:00	1,668	2,298	3,353	4,202	4,911	6,481	8,736
23-Jun-2023 20:00:00	1,630	3,333			4,836	6,456	-
23-Jun-2023 20:30:00	1,641	3,345		4,205	4,905	6,482	-
23-Jun-2023 21:00:00	1,645	2,316	3,354	4,197	4,905	6,482	8,699
23-Jun-2023 21:30:00	1,635	2,318	3,343	4,195	4,884	6,492	8,714
23-Jun-2023 22:00:00	1,644	2,330	3,348	4,200	4,856	6,512	8,722
23-Jun-2023 22:30:00	1,644	3,359	4,227		4,873	6,503	-
23-Jun-2023 23:00:00	1,626	3,468	4,221		4,911	-	-
23-Jun-2023 23:30:00	1,648	2,325	3,366	4,201	4,893	6,499	8,718
24-Jun-2023 00:00:00	1,632	2,564	3,371	4,211	4,984	6,489	-
24-Jun-2023 00:30:00	1,649	3,347	4,877	5,912	6,483	8,712	-

24-Jun-2023 01:00:00	1,641	3,361		4,260	4,871	6,492	-
24-Jun-2023 01:30:00	1,752	2,340	3,346	4,197	4,935	6,502	-
25-Jun-2023 11:30:00	1,703	2,293	3,343	4,219	4,867	6,472	-
25-Jun-2023 12:00:00	1,679	2,318	3,339	4,236	4,891	6,478	-
25-Jun-2023 12:30:00	1,656	2,315	3,322	4,220	4,885	6,474	8,678
25-Jun-2023 13:00:00	1,667	2,304	3,342	4,220	4,889	6,470	-
26-Jun-2023 00:00:00	1,655	2,319	3,333	4,179	4,890	6,574	8,584
26-Jun-2023 00:00:00	1,655	2,319	3,333	4,179	4,890	6,574	8,584
26-Jun-2023 00:30:00	1,629	2,330	3,336	4,173	4,878	6,559	8,379
26-Jun-2023 01:00:00	1,679	3,367			4,972	6,454	-
26-Jun-2023 01:30:00	1,690	2,300	3,398	4,251	4,672	8,685	-
26-Jun-2023 02:00:00	1,649	2,309	3,372	4,226	4,933	6,718	8,764
26-Jun-2023 02:30:00	1,683	2,243	3,368		4,941	6,526	-
26-Jun-2023 03:00:00	1,645	2,291	3,340	4,207	4,878	6,497	-
26-Jun-2023 03:30:00	1,649	3,298		4,229	4,859	6,478	-
26-Jun-2023 04:00:00	1,652	2,304	3,360	4,167	4,836	6,545	-
26-Jun-2023 04:30:00	1,654		3,338	4,211	4,884	6,467	8,833
26-Jun-2023 05:00:00	1,656	2,339	3,339	4,211	4,889	6,465	-
26-Jun-2023 05:30:00	1,643	2,311	3,335	4,206	4,902	6,451	-
26-Jun-2023 06:00:00	1,643	2,321	3,337	4,198	4,901	6,469	-
26-Jun-2023 06:30:00	1,668	3,338	4,185	4,893	5,931	6,470	-
26-Jun-2023 07:00:00	1,681	3,334			4,879	6,482	-
26-Jun-2023 07:30:00	1,652	2,300	3,336	4,201	4,889	6,475	8,534
26-Jun-2023 08:00:00	1,629	2,310	3,294	4,219	4,890	6,419	8,594
26-Jun-2023 08:30:00	1,657	2,305	3,308	4,212	4,865	6,435	-
26-Jun-2023 09:30:00	1,653	2,299	3,320	4,216	4,859	6,457	8,543
26-Jun-2023 10:00:00	1,657	2,296	3,340	4,223	4,876	6,424	8,584
26-Jun-2023 10:30:00	1,645		3,316		4,880	6,435	8,579
26-Jun-2023 11:00:00	1,653	2,319	3,324	4,197	4,885	6,398	8,593
26-Jun-2023 11:30:00	1,615	2,276	3,390	4,202	4,867	6,388	8,580
26-Jun-2023 12:00:00	1,591	2,297	3,285	4,227	4,869	6,409	8,565
26-Jun-2023 12:30:00	1,602	2,266	3,296	4,219	4,835	6,403	8,644
26-Jun-2023 12:30:00	1,599	-	-	-	-	-	-
26-Jun-2023 12:30:00	1,602	2,266	3,296	4,219	4,835	6,403	8,644
26-Jun-2023 12:30:00	1,602	2,266	3,296	4,219	4,835	6,403	8,644
26-Jun-2023 13:00:00	1,670	2,310	3,298	4,217	4,858	6,425	8,641
26-Jun-2023 13:30:00	1,643	2,288	3,305	4,218	4,857	6,377	-
26-Jun-2023 14:00:00	1,663	2,279	3,351	4,197	4,864	6,387	8,684
26-Jun-2023 14:30:00	1,610	2,300	3,339	4,192	4,855	6,358	8,618
26-Jun-2023 15:00:00	1,582	2,263	3,318	4,217	4,811	6,357	8,642
26-Jun-2023 15:30:00	1,597	2,262	3,229	4,176	4,791	6,340	8,617
26-Jun-2023 16:00:00	1,651	2,279	3,298	4,206	4,831	6,352	8,630
26-Jun-2023 16:30:00	1,595	2,288	3,250	4,203	4,841	6,440	8,637

26-Jun-2023 17:00:00	1,616	2,280	3,302	4,176	4,840	6,352	8,649
26-Jun-2023 17:30:00	1,620	2,283	3,291	4,223	4,841	6,394	8,633
26-Jun-2023 18:00:00	1,645	2,262	3,281	4,209	4,980	6,386	8,633
26-Jun-2023 18:30:00	1,636	2,242	3,293	4,240	4,850	6,345	8,617
26-Jun-2023 19:00:00	1,592	2,283	3,297	4,181	4,864	6,372	8,686
26-Jun-2023 19:30:00	1,695	2,272	3,288	4,185	4,855	6,467	8,652
26-Jun-2023 20:00:00	1,653	2,304	3,251	4,195	4,881	6,486	8,573
26-Jun-2023 20:30:00	1,674	2,297	3,299	4,209	4,868	6,451	8,704
26-Jun-2023 21:00:00	1,670		3,301	4,226	4,875	6,375	8,597
26-Jun-2023 21:30:00	1,676	2,286	3,314	4,214	4,867	6,440	-
26-Jun-2023 22:30:00	1,650	2,273	3,263	4,202	4,889	6,334	8,633
28-Jun-2023 00:00:00	1,666	2,296	3,326	4,166	4,892	6,459	-
28-Jun-2023 00:30:00	1,643	2,296	3,297	4,162	4,680	6,441	-
28-Jun-2023 01:00:00	1,650	2,270	3,299	4,208	4,846	6,462	8,578
28-Jun-2023 01:30:00	1,630	2,188	3,260	4,169	4,827	6,440	-
28-Jun-2023 02:00:00	1,655	2,225	3,326	4,169	4,887	6,450	-
28-Jun-2023 02:30:00	1,640	2,271	3,308	4,150	4,840	6,436	8,452
28-Jun-2023 03:00:00	1,650	2,257	3,329	4,226	4,874	6,456	-
28-Jun-2023 03:30:00	1,654	2,249	3,320	4,197	4,872	6,410	-
28-Jun-2023 04:00:00	1,625	2,300	3,299	4,149	4,839	6,442	-
28-Jun-2023 04:30:00	1,622	2,265	3,294	4,157	4,771	6,313	8,713
28-Jun-2023 05:00:00	1,632	2,305	3,308	4,158	4,837	6,431	8,331
28-Jun-2023 05:30:00	1,638	2,300	3,301	4,158	4,852	6,452	8,449
28-Jun-2023 06:00:00	1,591	2,288	3,285	4,163	4,772	6,391	-
28-Jun-2023 06:30:00	1,628	2,326	3,313	4,141	4,846	6,416	8,567
28-Jun-2023 07:00:00	1,618	2,314	3,325	4,145	4,861	6,418	-
28-Jun-2023 07:30:00	1,584	2,286	3,259	4,166	4,827	6,437	8,608
28-Jun-2023 08:00:00	1,632	2,303	3,340	4,168	4,846	6,395	8,615
28-Jun-2023 08:30:00	1,581	2,277	3,261	4,157	4,861	6,357	8,648
28-Jun-2023 09:00:00	1,626	2,292	3,288	4,157	4,808	6,374	-
28-Jun-2023 09:30:00	1,615	2,321	3,303	4,171	4,850	6,417	8,619
28-Jun-2023 10:00:00	1,614		3,281	4,151	4,823	6,437	8,635
28-Jun-2023 10:30:00	1,605		3,306	4,171	4,839	6,384	8,636
28-Jun-2023 11:00:00	1,630	2,298	3,274	4,155	4,841	6,401	-
28-Jun-2023 11:30:00	1,649	2,294	3,275	4,170	4,851	6,405	8,581
28-Jun-2023 12:00:00	1,655	2,296	3,308	4,182	4,857	6,446	8,524
28-Jun-2023 12:30:00	1,608	2,288	3,285	4,183	4,892	6,400	8,468
28-Jun-2023 13:00:00	1,642	2,307	3,343	4,185	4,860	6,415	8,553
28-Jun-2023 13:30:00	1,612	2,295	3,314	4,189	4,867	6,398	8,536
28-Jun-2023 14:00:00	1,665	2,308	3,315	4,202	4,861	6,444	-
28-Jun-2023 14:30:00	1,638	2,298	3,315	4,208	4,832	6,384	8,577
28-Jun-2023 15:00:00	1,547		3,297		4,836	6,396	8,538
28-Jun-2023 15:30:00	1,605	2,308	3,300	4,178	4,881	6,418	8,537

28-Jun-2023 16:00:00	1,586		3,358		4,857	6,446	-
28-Jun-2023 16:30:00	1,607		3,359		4,849	6,346	
28-Jun-2023 17:00:00	1,607	2,292	3,306	4,190	4,958	6,374	-
28-Jun-2023 17:30:00	1,617		3,311	4,186	4,900	6,455	8,538
28-Jun-2023 18:00:00	1,618	2,355	3,301	4,176	4,851	6,455	8,602
28-Jun-2023 18:30:00	1,624		3,321	4,146	4,901	6,479	-
28-Jun-2023 19:00:00	1,661	2,302	3,330	4,192	4,889	6,471	-
28-Jun-2023 19:30:00	1,649	2,258	3,321	4,204	4,848	6,449	8,536
28-Jun-2023 20:00:00	1,631	2,275	3,302	4,197	4,870	6,433	8,535
28-Jun-2023 20:30:00	1,613		3,319	4,221	4,854	6,424	8,611
28-Jun-2023 21:00:00	1,615		3,279	4,218	4,822	6,389	8,646
28-Jun-2023 22:00:00	1,616	2,271	3,287	4,161	4,816	6,391	8,445
28-Jun-2023 22:30:00	1,637	2,319	3,290	4,172	4,865	6,456	-
28-Jun-2023 23:00:00	1,649	2,344	3,334	4,142	4,867	6,469	-
28-Jun-2023 23:30:00	1,647	2,302	3,303	4,177	4,836	6,487	8,275

Appendix 2

Sensors' operating guide



12 Appendix 2: Sensors' operating guide

General OPERATING GUIDE

for use with

PIEZOELECTRIC ICP® ACCELEROMETERS

SPECIFICATION SHEET, INSTALLATION DRAWING
AND CALIBRATION INFORMATION ENCLOSED

PCB ASSUMES NO RESPONSIBILITY FOR DAMAGE CAUSED TO THIS PRODUCT AS A RESULT OF PROCEDURES THAT ARE INCONSISTENT WITH THIS OPERATING GUIDE.

1.0 INTRODUCTION

Congratulations on the purchase of a quality, ICP® acceleration sensor. In order to ensure the highest level of performance for this product, it is imperative that you properly familiarize yourself with the correct mounting and installation techniques before attempting to operate this device. If, after reading this manual, you have any additional questions concerning this sensor or its application, feel free to call a factory Application Engineer at 716-684-0001 or your nearest PCB sales representative.

2.0 ICP® ACCELEROMETERS

Powered by simple, inexpensive, constant-current signal conditioners, these sensors are easy to operate and interface with signal analysis, data acquisition and recording instruments. The following features further characterize ICP® sensors:

- Fixed voltage sensitivity, regardless of cable type or length.
- Low-impedance output signal, which can be transmitted over long cables in harsh environments with virtually no loss in signal quality.
- Two-wire operation with low cost coaxial cable, two-conductor ribbon wire or twisted-pair cabling.
- Low-noise, voltage-output signal compatible with standard readout, signal analysis, recording, and data acquisition equipment.
- Low cost per-channel - ICP® accelerometers require only an inexpensive, constant-current signal conditioner to operate.

- Intrinsic self-test feature – monitoring the sensor's output bias voltage provides an indication of proper operation, faulty condition, and bad cables.

In the rear of this manual you will find a **Specification Sheet**, which provides the complete performance characteristics of your particular sensor.

3.0 OPTIONAL FEATURES

Many sensors are supplied with standard, optional features. When listed before the model number, the following prefix letters indicate that the sensor is manufactured or supplied with a particular optional feature: "A" option: adhesive mount; "HT" option: extended high temperature range; "J" option: electrically ground isolated; "M" option: metric mounting thread; "Q" option: extended discharge time constant; "T" option: built-in transducer electronic data sheet (TEDS); and "W" option: attached, water-resistant cabling. Other prefix letters, such as "K", "KR", "GK", "GKR", "KL", and "GKL", indicate that the sensor is ordered in kit form, including interconnect cabling and signal conditioner. If you have any questions or concerns regarding optional features, consult the Vibration Division's product catalog or contact a PCB factory representative.

4.0 INSTALLATION OVERVIEW

When choosing a mounting method, consider closely both the advantages and disadvantages of each technique. Characteristics like location, ruggedness, amplitude range, accessibility, temperature, and portability are extremely critical. However, the most important and often overlooked consideration is the effect the mounting technique has on the high-frequency performance of the accelerometer.

* ICP is a registered trademark of PCB Group, Inc., which uniquely identifies PCB sensors that incorporate built-in microelectronics.

Shown in figure 1 are six possible mounting techniques and their effects on the performance of a typical piezoelectric accelerometer. (Note that not all of the mounting methods may apply to your particular sensor). The mounting configurations and corresponding graph demonstrate how the high-frequency response of the accelerometer may be compromised as mass is added to the system and/or the mounting stiffness is reduced.

NOTE: The low-frequency response is unaffected by the mounting technique. This roll-off behavior is typically fixed by the sensor's built-in electronics. However, when operating AC-coupled signal conditioners with readout devices having an input impedance of less than one megohm, the low frequency range may be affected. If necessary, contact a factory representative for further assistance.

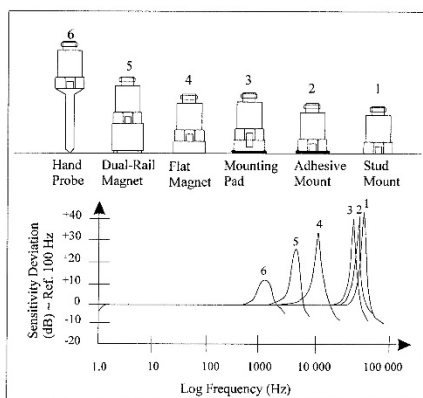


Figure 1. Assorted Mounting Configurations and Their Effects on High Frequency

4.1 STUD MOUNT

This mounting technique requires smooth, flat contact surfaces for proper operation and is recommended for permanent and/or secure installations. Stud mounting is also recommended when testing at high frequencies.

NOTE: Do NOT attempt mounting on curved, rough, or uneven surfaces, as the potential for misalignment and limited contact surface may significantly reduce the sensor's upper operating frequency range.

STEP 1: First, prepare a smooth, flat mounting surface, then drill and tap a mounting hole in the center of this area as shown in Figure 2 and in accordance with the enclosed **Installation Drawing**.

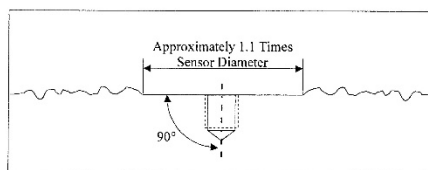


Figure 2. Mounting Surface Preparation

A precision-machined mounting surface with a minimum finish of 63 μin (0.00016 mm) is recommended. (If it is not possible to properly prepare the test structure mounting surface, consider adhesive mounting as a possible alternative). Inspect the area, checking that there are no burrs or other foreign particles interfering with the contact surface.

STEP 2: Wipe clean the mounting surface and spread on a light film of grease, oil, or similar coupling fluid prior to installation.

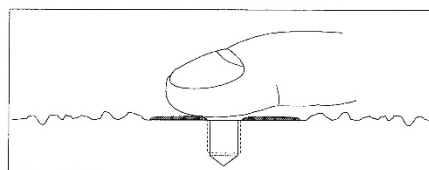


Figure 3. Mounting Surface Lubrication

Adding a coupling fluid improves vibration transmissibility by filling small voids in the mounting surface and increasing the mounting stiffness. For semi-permanent mounting, substitute epoxy or another type of adhesive.

STEP 3: Screw the mounting stud into the base of accelerometer and hand-tighten (this step is unnecessary for units having an integral mounting stud). Then, screw the sensor into the tapped hole that was prepared in the test object. Tighten the unit in place by applying, with a torque wrench, the recommended mounting torque, as listed on the enclosed **Installation Drawing**.

NOTE: It is important to use a torque wrench during this step. Under-torquing the sensor may not adequately couple the device; over-torquing may result in stud failure.

4.2 ADHESIVE MOUNT

Adhesive mounting is often used for temporary installation or when the test object surface cannot be adequately prepared for stud mounting. Adhesives like hot glue and wax perform well for temporary installations whereas two-part epoxies and quick-bonding gels (super glue) provide a more permanent installation. Two

techniques are used for adhesive mounting; they are via an adhesive mounting base (method 1 below) or direct adhesive mounting (method 2 below).

NOTE: *Adhesively mounted sensors often exhibit a reduction in high-frequency range. Generally, smooth surfaces and stiff adhesives provide the best high frequency response.*

METHOD 1 - Adhesive Mounting Base

This method involves attaching a base to the test structure, then securing the sensor to the base. This allows for easy removal of the accelerometer. Also, since many bases are manufactured of “hard-coated” aluminum, they provide electrical isolation to eliminate ground loops and reduce electrical interference that may propagate from the surface of the test object.

STEP 1: Prepare a smooth, flat mounting surface. A minimum surface finish of 63 μm (0.00016 mm) generally works best.

STEP 2: Stud-mount the sensor to the flat side of the appropriate adhesive mounting base according to the guidelines set forth in **STEPS 2** and **3** of the Stud Mount Procedure presented above.

STEP 3: Place a small portion of adhesive on the underside of the mounting base (the underside is discernable by the concentric grooves which are designed to accept the adhesive). Firmly press down on the assembly to displace any extra adhesive remaining under the base.

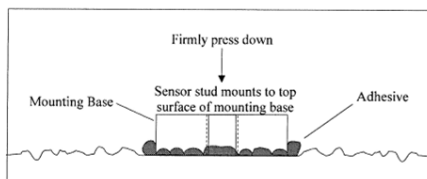


Figure 4. Mounting Base: Adhesive Installation

METHOD 2 - Direct Adhesive Mount

For restrictions of space or for convenience, most sensors can be adhesive-mounted directly to the test structure (an exception being units having integral mounting studs).

STEP 1: Prepare a smooth, flat mounting surface. A minimum surface finish of 63 μm (0.00016 mm) generally works best.

STEP 2: Place a small portion of adhesive on the underside of the sensor. Firmly press down on the top of the assembly to displace any adhesive. Be aware that

excessive amounts of adhesive can make sensor removal difficult. Also, adhesive that may invade the tapped mounting hole in the base of the sensor will compromise future ability to stud mount the unit.

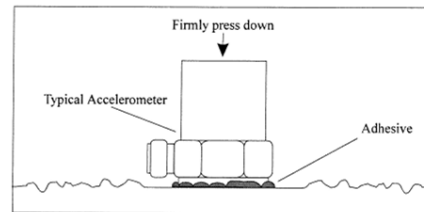


Figure 5. Direct Adhesive Mounting

4.2-1 ADHESIVE MOUNT REMOVAL (other than wax)

NOTE: *A debonder should always be used to avoid sensor damage.*

To avoid damaging the accelerometer, a debonding agent must be applied to the adhesive prior to sensor removal. With so many adhesives in use (everything from super glues, dental cement, epoxies, etc), there is no universal debonding agent available. The debonder for the Loctite 454 adhesive that PCB offers is Acetone. If you are using anything other than Loctite 454, you will have to check with the individual manufacturers for their debonding recommendations. The debonding agent must be allowed to penetrate the surface in order to properly react with the adhesive, so it is advisable to wait a few minutes before removing the sensor.

After the debonding agent has set, you can use an ordinary open-end wrench if the accelerometer has a hex base or square base, or the supplied removal tool for teardrop accelerometers. After attaching either, use a gentle shearing (or twisting) motion (by hand only) to remove the sensor from the test structure.

4.3 MAGNETIC MOUNT

Magnetic mounting provides a convenient means for making quick, portable measurements and is commonly used for machinery condition monitoring, predictive maintenance, spot checks, and vibration trending applications.

NOTE: *The correct magnet choice and an adequately prepared mounting surface are critical for obtaining reliable measurements, especially at high frequencies. Poor installations can cause as much as a 50% drop in the sensor frequency range.*

Not every magnet is suitable for all applications. For example, rare earth magnets are commonly used because

of their high strength. Flat magnets work well on smooth, flat surfaces, while dual-rail magnets are required for curved surfaces such as motor housings and pipes. In the case of non-magnetic or rough surfaces, it is recommended that the user first weld, epoxy, or otherwise adhere a steel mounting pad to the test surface. This provides a smooth location for mounting and a target to insure that subsequent measurements for trending purposes are taken at the same location.

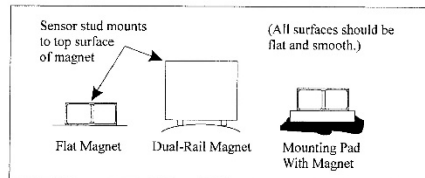


Figure 6. Magnet Types

STEP 1: Prepare a smooth, flat mounting surface. A minimum surface finish of 63 μm (0.00016 mm) generally works best. After cleaning the surface and checking for burrs, apply a light film of silicone grease, machine oil, or similar-type coupling fluid.

STEP 2: After choosing the correct magnet type, inspect the magnet, verifying that its mounting surfaces are flat and smooth.

STEP 3: Stud-mount the accelerometer to the appropriate magnet according to the guidelines set forth in STEP 3 of the above Stud Mount Procedure.

STEP 4: To avoid damage to the sensor, install the magnet/sensor assembly to the prepared test surface by gently “rocking” or “sliding” it into place.

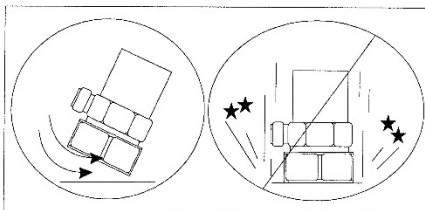


Figure 7. Magnet Mounting

CAUTION: Magnetically mounting of an accelerometer has the potential to generate very high (and very damaging) acceleration (g) levels. To prevent such damage, exercise caution and install the assembly gently by rocking it into place. If shock is expected to be a particular concern, use a sensor with built-in shock protection. For further assistance, contact a factory representative.

4.4 HANDHELD OR PROBE TIP MOUNT

This method is NOT recommended for most applications. Both the accuracy and repeatability at low (<5 Hz) and high frequency (>1 kHz) ranges are questionable. It is generally used only for machinery condition monitoring, when installation space is restricted, or other portable trending applications. The technique, however, can be useful for initially determining locations of greatest vibration to establish a permanent sensor installation point.

5.0 CABLING

Care and attention to cable installation and cable condition is essential as the reliability and accuracy of any measurement system is no better than that of its weakest link. Do to the nature of vibration measurements, all sensor cables will ultimately fatigue and fail. Good installation practice will extend the life of a cable, however, it is highly recommended to keep spare cables on hand to enable continuation of the test in the event of a cable failure.

STEP 1: Ascertain that you have the correct cable type.

One cable type cannot satisfy all applications. ICP[®] sensors can be operated with any ordinary two-wire or coaxial cable. Special, low-noise cables that are typically recommended for use with high-impedance, charge-output sensors can also be used. For applications requiring conformity to CE , low noise cables are essential. Industrial applications often require shielded, twisted-pair cables to reduce the effects of EMI and RFI that is present near electrical motors and machinery. Teflon-jacketed cabling may be necessary to withstand corrosive environments and higher temperatures. Consult the Vibration Division’s product catalog for more information about cables or feel free to contact a factory representative for a specific recommendation on cables that are best suited for your application.

STEP 2: Connect the cable to the accelerometer.

A small amount of thread-locking compound placed on the connector threads prior to attachment helps secure the cable during testing. In wet, oily, or dirty environments, the connection can be sealed with silicone rubber sealant, O-rings, and flexible, heat-shrink tubing.

Coaxial Cables: Make connection by inserting the cable’s connector pin into the sensor’s mating socket. Then thread the connector into place by turning the cable connector’s outer shell onto the accelerometer’s electrical connector.

NOTE: Do not spin the accelerometer while holding the cable connector stationary, as this will cause undue

friction on the center pin of the cable connector and lead to premature fatigue.

Multi-pin connectors: Make connection by inserting the sensor's mating pins onto the cable connector's mating sockets. Then thread the connector into place by turning the cable connector's outer shell onto the accelerometer's electrical connector.

Pigtail Connections: Certain miniature accelerometers and shock sensors are provided with lightweight cables attached to "Pigtail" connections. This type of connection reduces overall weight and incidence of connection intermittency under shock conditions. In the event of a cable or connection failure, the cables may be repaired in the field simply by re-soldering the stripped leads to the exposed pins on the sensor. (Check the **Installation Drawing** to determine signal and ground pins). In many cases, it is also helpful to protect the solder joint with heat-shrink tubing or epoxy.

NOTE: If you do not have the experience or resources to attach pigtail leads, consult PCB to discuss factory attachment. Damage to internal electronics may be caused by excessive heat during soldering and such failure is not covered by warranty.

STEP 3: Route the cable to the signal conditioner, making certain to relieve stress on the sensor/cable connection. Also, minimize cable motion by securing it with tape, clamps or ties at regular intervals.

Common sense should be used to avoid physical damage and minimize electrical noise. For instance, avoid routing cables near high-voltage wires. Do not route cables along floors or walkways where they may be stepped on or become contaminated. To avoid ground loops, shielded cables should have the shield grounded at one end only, typically at the signal conditioner.

STEP 4: Finally, connect the remaining cable end to the signal conditioner. It is good practice to dissipate any electrical charge that may have accumulated in the cable by shorting the signal pin to the ground pin or shell prior to attachment.

6.0 POWERING

All ICP® sensors require constant current excitation for proper operation. For this reason, use only PCB constant-current signal conditioners or other approved constant-current sources. A typical system schematic is shown in Figure 8.

NOTE: Damage to the built-in electronics resulting from the application of incorrect power, or the use of an unapproved power source, is NOT covered by warranty.

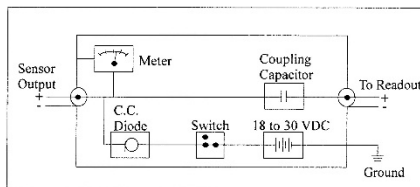


Figure 8. Typical System Schematic

The power supply consists of a current-regulated, 18 to 30 VDC source. This power is regulated by a current-limiting circuit, which provides the constant-current excitation required for proper operation of ICP® sensors. In general, battery-powered devices offer versatility for portable, low-noise measurements, whereas line-powered units provide the capability for continuous monitoring. Consult the Vibration Division's product catalog for more information about signal conditioners.

NOTE: Under no circumstances should a voltage be supplied to an ICP® accelerometer without a current-regulating diode or equivalent electrical circuit. This may include ohmmeters, multi-meters and continuity testers.

Meters or LEDs are used on PCB signal conditioners to monitor the bias voltage on the sensor output signal, to check sensor operation, and detect cable faults. Normally, a "yellow" reading indicates an open circuit; "green" indicates normal operation; and "red" indicates either a short or overload condition. Finally, a capacitor at the output stage of the device removes the sensor output bias voltage from the measurement signal. This provides a zero-based, AC-coupled output signal that is compatible with most standard readout devices.

NOTE: Units having a low bias voltage may be in the "red," when actually they are working properly. If suspect, the bias voltage can be checked with a voltmeter attached to a "T" connector installed on the input connector to the signal conditioner.

Note: For readout devices having an input impedance near one gigohm (as encountered with some A to D converters), it may be necessary to place a one megohm resistor in parallel to the readout input to eliminate slow turn-on and signal drift.

Today, many FFT analyzers, data acquisition modules, and data collectors have the proper constant-current excitation built-in for direct use with ICP® sensors. Before using this feature, however, check that the supply voltage and constant current are within acceptable limits for use with your particular sensor. (Check enclosed **Specification Sheet**). Please contact the respective signal

conditioner manufacturer or check the product manual for more information.

7.0 OPERATING

After completing the system setup, switch on the signal conditioner and allow 1 to 2 minutes for the system to stabilize. The meter (or LED) on the signal conditioner should be reading “green.” This indicates proper operation and you may begin taking measurements. If a faulty condition is indicated (red or yellow reading), first check all system connections, then check the functionality of the cable and signal conditioner. If the system still does not operate properly, consult a PCB factory representative.

NOTE: Always operate the accelerometer within the limitations listed on the enclosed *Specification Sheet*. Operating the device outside these parameters can cause temporary or permanent damage to the sensor.

8.0 ACCELEROMETER CALIBRATION

Accelerometer calibration provides, with a definable degree of accuracy, the necessary link between the physical quantity being measured and the electrical signal generated by the sensor. In addition, other useful information concerning operational limits, physical parameters, electrical characteristics, or environmental influences may also be determined. Without this link, analyzing data becomes a nearly impossible task. Fortunately, most sensor manufacturers provide a calibration record that documents the exact characteristics of each sensor. (The type and amount of data varies depending on the manufacturer, sensor type, contractual regulations, and other special requirements).

Under normal conditions, piezoelectric sensors are extremely stable, and their calibrated performance characteristics do not change over time. However, the sensor may be temporarily or permanently affected by harsh environments influences or other unusual conditions that may cause the sensor to experience dynamic phenomena outside of its specified operating range. This change manifests itself in a variety of ways, including: a shift of the sensor resonance due to a cracked crystal; a temporary loss of low-frequency measuring capability due to a drop in insulation resistance; or total failure of the built-in microelectronic circuit due to a high mechanical shock.

For these reasons, it is recommended that a recalibration cycle be established for each accelerometer. This schedule is unique and is based on a variety of factors, such as: extent of use, environmental conditions, accuracy requirements, trend information obtained from previous calibration records, contractual regulations, frequency of “cross-checking” against other equipment, manufacturer recommendation, and any risk associated with incorrect

readings. International standards, such as ISO 10012-1, provide insight and suggest methods for determining recalibration intervals for most measuring equipment. With the above information in mind and under “normal” circumstances, PCB conservatively suggests a 12- to 24-month recalibration cycle for most piezoelectric accelerometers.

NOTE: It is good measurement practice to verify the performance of each accelerometer with a *Handheld Shaker* or other calibration device before and after each measurement. The PCB *Handheld Shaker* operates at a fixed frequency and known amplitude (1.0 g) to provide a quick check of sensor sensitivity.

8.1 RECALIBRATION SERVICE

PCB offers recalibration services for our piezoelectric accelerometers, as well as units produced by other manufacturers. Our internal metrology laboratory is certified to ISO 9001, accredited by A2LA to ANSI/IEC 17025 and ANSI/NCSL Z540-1, complies with ISO 10012-1 (and former MIL-STD-45662A), and uses equipment directly traceable to NIST. Our investment in equipment, traceability and conformance to industry standards ensures accurate calibration against relevant specifications, in a timely fashion.

8.2 BACK-TO-BACK CALIBRATION THEORY

Many companies choose to purchase the equipment necessary to perform the recalibration procedure in house. While this may result in both a savings of time and money, it has also been attributed to incorrect readings and costly errors. Therefore, in an effort to prevent the common mistakes associated with customer-performed calibration, this document includes a broad overview of the Back-to-Back Calibration technique. This technique provides a quick and easy method for determining the sensitivity of a test accelerometer over a wide frequency range.

Back-to-Back Calibration is perhaps the most common method for determining the sensitivity of piezoelectric accelerometers. This method relies on a simple comparison to a previously calibrated accelerometer, typically referred to as a reference standard.

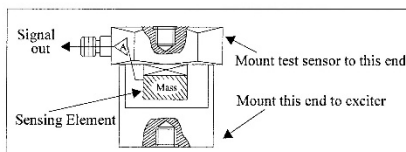


Figure 9. Reference Standard Accelerometer

These high-accuracy devices, which are directly traceable to a recognized standards laboratory, are designed for stability, as well as configured to accept a test accelerometer. By mounting a test accelerometer to the reference standard and then connecting this combination to a suitable vibration source, it is possible to vibrate both devices and compare the data as shown in Figure 10. (Test set-ups may be automated and vary, depending on the type and number of accelerometers being calibrated).

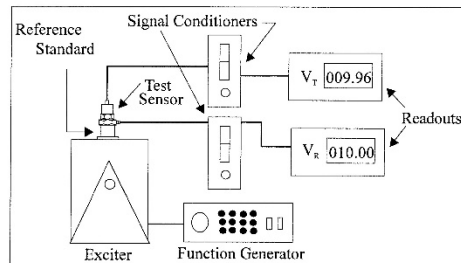


Figure 10. Typical Back-to-Back Calibration System

Because the acceleration is the same on both sensors, the ratio of their outputs (V_T/V_R) must also be the ratio of their sensitivities. With the sensitivity of the reference standard (S_R) known, the exact sensitivity of the test sensor (S_T) is easily calculated by using the following equation:

$$S_T = S_R (V_T/V_R)$$

By varying the frequency of the vibration, the sensor may be calibrated over its entire operating frequency range. The typical response of an unfiltered accelerometer is shown in Figure 11.

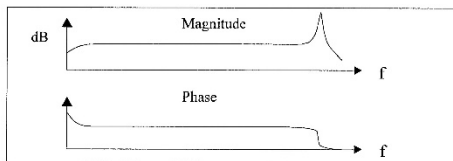


Figure 11. Typical Test Accelerometer Response

8.3 PCB CALIBRATION PROCEDURE

Numerous precautions are taken at PCB to insure accurate and repeatable results. This section provides a brief overview of the primary areas of concern.

Since the Back-to-Back Calibration technique relies on each sensor experiencing an identical acceleration level, proper mounting of the test sensor to the reference standard is imperative. Sensors with mounting holes are attached directly to the reference standard with a stud

tightened to the recommended mounting torque. A shouldered mounting stud is typically used to prevent the stud from "bottoming out" in the hole. Both mounting surfaces are precision-machined and lapped to provide a smooth, flat interface according to the manufacturer's specification. A thin layer of silicone grease is placed between the mating surfaces to fill any imperfections and increase the mounting stiffness. The cables are stress-relieved by first routing them to the shaker head, then to a nearby stationary location. This reduces cable motion, which is especially important when testing charge output sensors, and helps to prevent extraneous motion or stresses from being imparted into the system. A typical set-up is shown in Figure 12.

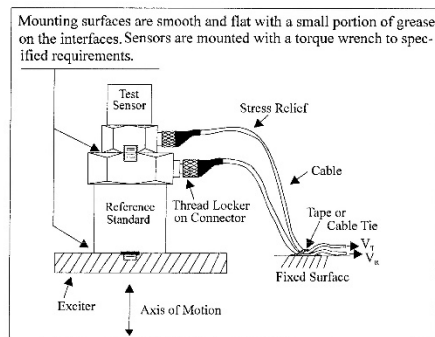


Figure 12. Typical Calibration Set-Up

Adhesively mounted sensors use similar practices. However, in this case, a small portion of quick-bonding gel, or similar temporary adhesive, is used to attach the test sensor to a reference standard designed with a smooth, flat mounting surface.

In addition to mounting, the selection of the proper equipment is critical. Some of the more important considerations include: 1) the reference standard must be specified and previously calibrated over the frequency and/or amplitude range of interest; 2) the shaker should be selected to provide minimal transverse (lateral) motion and minimal distortion; and 3) the quality of the meters, signal generator, and other devices should be selected so as to operate within the limits of permissible error.

8.4 COMMON MISTAKES

Most calibration errors are caused by simply overlooking some of the fundamental principals of dynamics. This section attempts to address some of the more common concerns.

For stud-mount sensors, always mount the accelerometer directly to the reference standard. Ensure that the mounting surfaces are smooth, flat, and free of any burrs. Always use a

coupling fluid, such as silicone grease, in the mounting interface to maintain a high mounting stiffness. Mount the sensor according to the manufacturer's recommended mounting torque. DO NOT use any intermediate mounting adaptors, as the mounted resonant frequency may be reduced, and thereby compromise the high-frequency performance. If necessary, use adaptor studs.

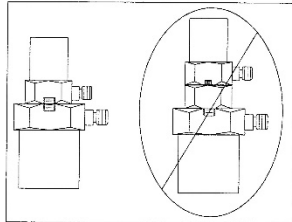


Figure 13. Stud Mounting

For adhesive mount sensors, use a thin, stiff layer of temporary adhesive such as quick-bonding gel or superglue. DO NOT use excessive amounts of glue or epoxy, as the mounting stiffness may be reduced and compromise high-frequency performance. It may also damage the sensor during removal.

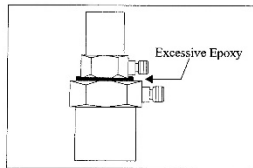


Figure 14. Incorrect Adhesive Mounting

Triaxial accelerometers should always be mounted directly to the reference standard. Unless absolutely required, DO NOT use adaptors to re-orient the sensor along the axis of motion, as the mounting stiffness may be altered. The vibration at the test sensor's sensing element may differ from the vibration at the reference standard due to a "cantilever" effect, seen in Figure 15.

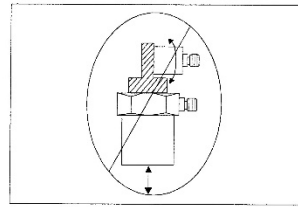


Figure 15. Mounting Triaxial Sensors (Incorrect)

Understand Back-to-Back Calibration limitations. Do not expect the uncertainty of calibration to be any better than $\pm 2\%$. (In fact, the uncertainty may be as high as $\pm 3\%$ or $\pm 4\%$ for frequencies < 10 Hz or > 2 kHz.) Since large sensors may affect high-frequency accuracy, verify that the test sensor does not mass load the reference standard. Validate your calibration system with another accelerometer prior to each calibration session. Check with the manufacturer for exact system specifications.

8.5 CONCLUSIONS

Without an adequate understanding of dynamics, determining what, when, and how to test a sensor is a difficult task. Therefore, each user must weigh the cost, time, and risk associated with self-calibration versus utilizing the services of an accredited laboratory.

9.0 SERVICE

See the supplement sheet, contained in this manual, for information on our warranty, service, repair, and return policies and instructions.

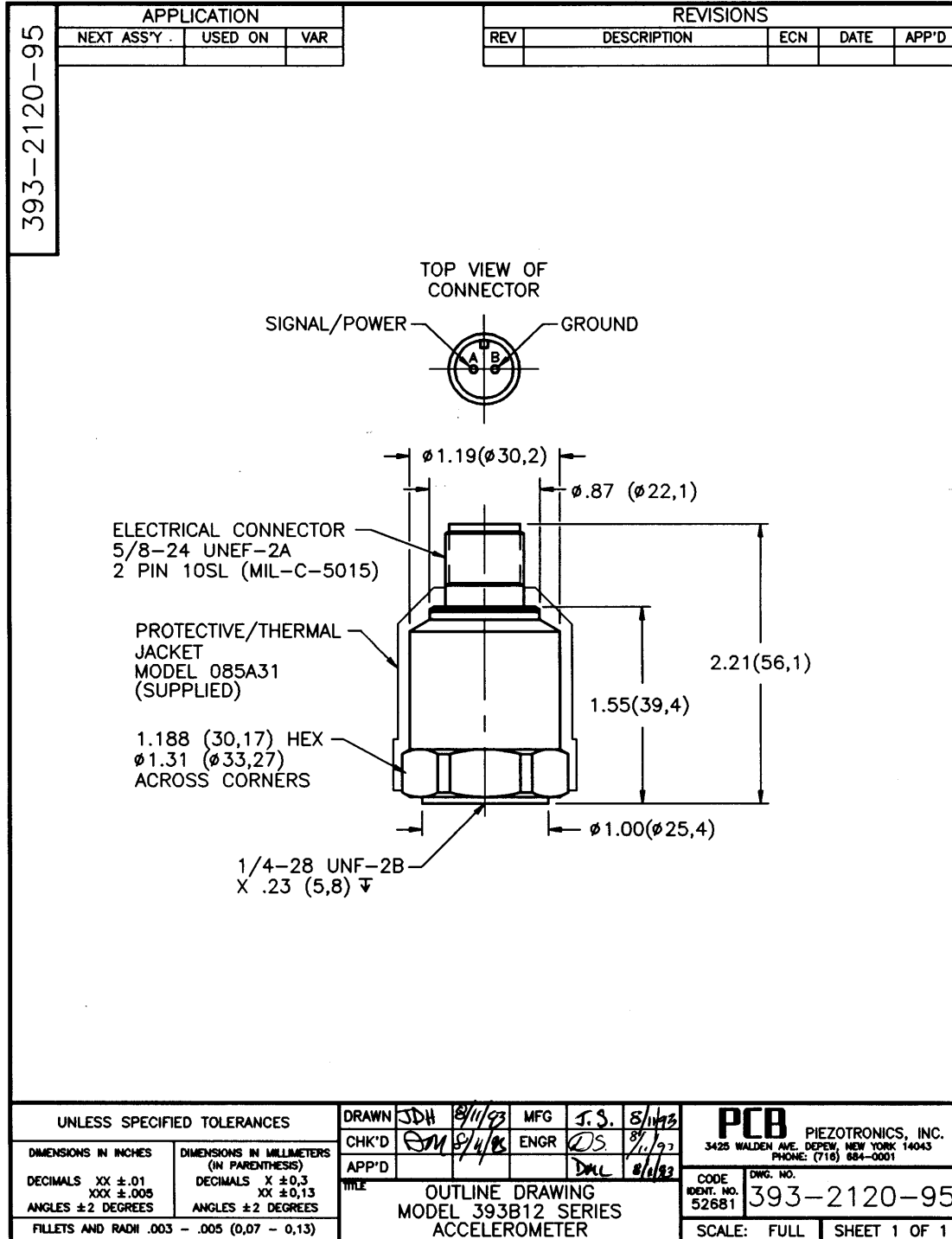
When unexpected measurement problems arise, call our 24-hour SensorLineSM to discuss your immediate dynamic instrumentation needs with a factory representative. Dial 716-684-0001.

Appendix 3

Sensors Technical Drawings



13 Appendix 3: Sensors Technical drawings



081-XXXX-90

PCB Piezotronics Inc. owns proprietary rights in the information disclosed herein. Neither it nor any reproduction thereof will be disclosed to others without the written consent of PCB Piezotronics Inc.

REVISIONS	
REV	DESCRIPTION
P	UPDATE DRAWING
	DNI 25686

STANDARD STUD MOUNT

MOUNTING THREAD	SEE DRAWING
S-40	A
M3 X 0.50	B
10-32	C
M5 X 0.80	D
1/4-28	E
M8 X 1.00	F

"A" S-40 MOUNTING INSTRUCTIONS
(METRIC DIMENSIONS IN BRACKETS)

MOUNTING HOLE PREPARATION:
 $\phi .10$ (.0257)
 X .20 (.51) ∇ MIN.
 S-40 UNC-2B
 X .15 (.38) ∇ MIN.

4.) RECOMMENDED MOUNTING TORQUE:
4-5 INCH POUNDS
(45-55 NEWTON CENTIMETERS).

"B" M3 X 0.50 MOUNTING INSTRUCTIONS
(ENGLISH DIMENSIONS IN BRACKETS)

MOUNTING HOLE PREPARATION:
 $\phi .21$ (.099)
 X 4.4 (1.8) ∇ MIN.
 M3 X 0.50-6H
 X 3.3 (.13) ∇ MIN.

4.) RECOMMENDED MOUNTING TORQUE:
45-55 NEWTON CENTIMETERS
(4-5 INCH POUNDS).

"C" 10-32 MOUNTING INSTRUCTIONS
(METRIC DIMENSIONS IN BRACKETS)

MOUNTING HOLE PREPARATION:
 $\phi .159$ (.04)
 X .23 (.58) ∇ MIN.
 10-32 UNF-2B
 X .15 (.38) ∇ MIN.

4.) RECOMMENDED MOUNTING TORQUE:
10-20 INCH POUNDS
(113-225 NEWTON CENTIMETERS).

"D" M5 X 0.80 MOUNTING INSTRUCTIONS
(ENGLISH DIMENSIONS IN BRACKETS)

MOUNTING HOLE PREPARATION:
 $\phi .422$ (.166)
 X 7.62 (.300) ∇ MIN.
 M5 X 0.8-6H
 X 5.08 (.200) ∇ MIN.

4.) RECOMMENDED MOUNTING TORQUE:
113-225 NEWTON CENTIMETERS
(10-20 INCH POUNDS).

INTEGRAL STUD MOUNT

MOUNTING THREAD	SEE DRAWING
S-40	A
M3 X 0.50	B
10-32	C
M5 X 0.80	D
1/4-28	E
M8 X 1.00	F

"THRU-BOLT" STUD MOUNT

BOLT THREAD	SEE DRAWING
10-32	C
1/4-28	E
M6 X 1.00	F
M8 X 1.25	F

"E" 1/4-28 MOUNTING INSTRUCTIONS
(METRIC DIMENSIONS IN BRACKETS)

MOUNTING HOLE PREPARATION:
 $\phi .21$ (.054)
 X .20 (.7) ∇ MIN.
 1/4-28 UNF-2B
 X .20 (.5) ∇ MIN.

4.) RECOMMENDED MOUNTING TORQUE:
2-5 FOOT POUNDS
(3-7 NEWTON METERS).

"F" M6 X 0.75, M6 X 1.00, M8 X 1.25 MOUNTING INSTRUCTIONS
(ENGLISH DIMENSIONS IN BRACKETS)

M6 X 0.75 MOUNTING HOLE PREPARATION:
 $\phi .51$ (.029)
 X 7.62 (.300) ∇ MIN.
 M6 X 0.75-6H
 X 5.08 (.200) ∇ MIN.

M8 X 1.00 MOUNTING HOLE PREPARATION:
 $\phi .75$ (.026)
 X 8.64 (.340) ∇ MIN.
 M8 X 1.25-6H
 X 5.00 (.197) ∇ MIN.

4.) RECOMMENDED MOUNTING TORQUE:
3-7 NEWTON METERS (2-5 FT POUNDS).

"G" MOUNTING INSTRUCTIONS FOR SPECIAL THREAD LENGTHS
(METRIC DIMENSIONS IN BRACKETS)

MOUNTING HOLE PREPARATION:
 ϕ DRILL DIA.
 X "C" ∇ MIN.
 TAP
 X "B" ∇ MIN.
 THREAD DEPTH = 8 x X + 1 THREAD PITCH
 DRILL DEPTH = C + 8 x 3 THREAD PITCH
 SEE A-F FOR APPROPRIATE DRILL AND TAP
 THREAD PITCH = 1/TP [P]

3.) FOR BEST RESULTS, PLACE A THIN LAYER OF SILICONE GREASE (OR EQUIVALENT) ON INTERFACE PRIOR TO MOUNTING.

∇ MOUNTING SURFACE SHOULD BE FLAT TO WITHIN .001 (0.03) TIR OVER DIM 'A' WITH A $\sqrt{.161}$ OR BETTER FINISH FOR BEST RESULTS.

∇ DRILL PERPENDICULAR TO MOUNTING SURFACE TO WITHIN $\pm 1^\circ$.

UNLESS OTHERWISE SPECIFIED TOLERANCES ARE:		DRAWN	CHECKED	ENGINEER
DIMENSIONS IN INCHES	DIMENSIONS IN MILLIMETERS [IN BRACKETS]	JDM	EGR	JJD
DECIMALS .XX ±.01 XXX ±.005	DECIMALS X 1.0 ± 0.3 XX ± 0.13			
ANGLES ± 2 DEGREES	ANGLES ± 2 DEGREES	TITLE		
FILLET AND RADIUS .003 - .005	FILLET AND RADIUS 0.07 - 0.13	INSTALLATION DRAWING FOR STANDARD 081 SERIES MOUNTING		

PCB PIEZOTRONICS

3425 WALDEN AVE. DEPEW, NY 14043
 (716) 684-0001 E-MAIL: sales@pcc.com

CODE: 081-XXXX-90
 DRAWING NO. 92681

SCALE: N.T.S. SHEET 1 OF 1

Appendix 4

Sensors Calibration Certificate



14 Appendix 4: Sensors Calibration Certificate

~Calibration Certificate~

Sensor Information

Model Number: 393B12
 Serial Number: 68465
 Manufacturer: PCB
 Description: ICP® Accelerometer

Calibration Data

Sensitivity @ 100 Hz: 10,521 mV/g
 1,073 mV/m/s²
 Phase @ 100 Hz: -0.93 deg.
 Test Level: 0.30 g

Transducer Specifications

Amp. Range: ± 0.5 g
 Resolution: 0.000008 g
 Resonant Freq: ≥ 10000 Hz
 Temp. Range: -46 to 82 °C
 -50 to 180 °F
 Axis: Uni-Axial

Data Table

Freq. (Hz)	Deviation (%)	Phase (deg)
0.5	-0.9396	4.5258
1	-1.3105	2.0868
2	-1.4437	0.8135
3	-1.3642	0.5134
4	-1.4635	0.2943
5	-1.5040	0.1718
6.3	-1.4715	0.0619
7	-1.6190	0.0170
8	-1.6391	-0.0506
10	-1.6350	-0.0693
30	0.0019	-0.3695
50	-0.1443	-0.6212
100	0.0000	-0.9288
200	-0.4918	-1.7149
300	-0.8479	-2.4788
400	-0.9847	-3.1033
500	-1.1122	-3.6439
600	-1.0446	-4.3087
700	-1.1426	-4.9182
800	-1.1134	-5.5774
900	-1.0457	-6.2115
1000	-1.0122	-6.8005

Phase Response

Amplitude Response

Notes

Results relate only to the items calibrated.
 This certificate may not be reproduced except in full, without written permission.
 Method: Back-to-Back Comparison Calibration per ISO 16063 Part 21.
 This calibration was performed with TMS 9155 Calibration Workstation 2 version 7.0.2.
 Proficiency in calibration traceable to PTB (17014/17004) and NIST (683/287323).
 Back-to-Back Comparison Calibration per ISO 16063-21
 Procedure Used: PRD-P220 or PRD-P239
 Measurement uncertainty (95% confidence level with coverage factor 2) for frequency ranges tested during calibration are as follows: 0.5-1 Hz; 1.1%; >1-10 Hz; ± 0.8%; 11-99 Hz; ± 1.2%; 100 Hz; ± 0.75%; 101-920 Hz; ± 1.0%; 921-5000 Hz; ± 1.4%; 5001-10,000 Hz; ± 1.9%; 10,001-15,000 Hz; ± 2.2%; 15,001-20,000 Hz; ± 2.8%.
 Phase uncertainty: 0.5-10 Hz; 1.0°, 11-99 Hz; 1.5°, 100-4999 Hz; 1.3°, 5000-20,000 Hz; 2.8°

Unit Condition
 As Found: In Tolerance
 As Left: In Tolerance

Lab Conditions

Temperature: 73 (23) °F (°C)
 Humidity: 25 %

Cal Date: 21-Mar-23
 Due Date:

Customer

Wise/Daniele Storni

Technician Notes

Approval Information

Technician: Tyler Stratman
 Approval:

10310 Aerohub Boulevard
 Cincinnati, OH 45215
 Ph: 513.351.9919
 www.modalshop.com

2649.01
 Calibration Laboratory

Cal ID: 59395

Page 1 of 1

~Calibration Certificate~

Sensor Information

Model Number: 393B12
Serial Number: 68466
Manufacturer: PCB

Description: ICP® Accelerometer

Calibration Data

Sensitivity @ 100 Hz: 10,254 mV/g
1,046 mV/m/s²
Phase @ 100 Hz: -0.90 deg.
Test Level: 0.30 g

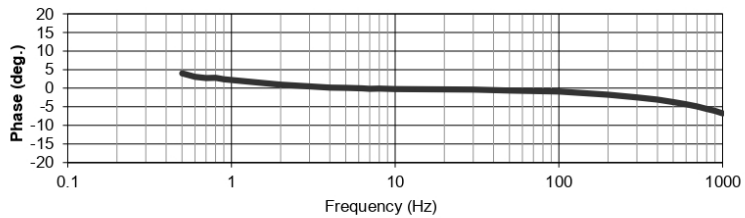
Transducer Specifications

Amp. Range: ± 0.5 g
Resolution: 0.000008 g
Resonant Freq: ≥ 10000 Hz
Temp. Range: -46 to 82 °C
-50 to 180 °F
Axis: Uni-Axial

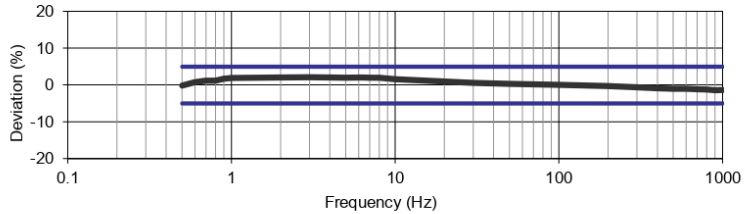
Data Table

Freq. (Hz)	Deviation (%)	Phase (deg)
0.5	-0.1985	4.0229
1	1.9086	2.2095
2	2.0074	0.9214
3	2.1056	0.4602
4	1.9942	0.1877
5	1.9637	0.0856
6.3	2.0230	-0.0536
7	1.9229	-0.1575
8	1.9712	-0.1340
10	1.5779	-0.2408
30	0.5272	-0.3484
50	0.3171	-0.6315
100	0.0000	-0.8978
200	-0.2814	-1.7633
300	-0.6487	-2.4584
400	-0.9267	-3.0626
500	-1.0147	-3.7177
600	-1.0649	-4.3211
700	-1.1496	-4.9200
800	-1.2748	-5.5698
900	-1.3839	-6.1237
1000	-1.3752	-6.7312

Phase Response



Amplitude Response



Notes

Results relate only to the items calibrated.
This certificate may not be reproduced except in full, without written permission.
Method: Back-to-Back Comparison Calibration per ISO 16063 Part 21.
This calibration was performed with TMS 9155 Calibration Workstation 2 version 7.0.2.
Proficiency in calibration traceable to PTB (17014/17004) and NIST (683/287323).
Back-to-Back Comparison Calibration per ISO 16063-21
Procedure Used: PRD-P220 or PRD-P239
Measurement uncertainty (95% confidence level with coverage factor 2) for frequency ranges tested during calibration are as follows: 0.5-1 Hz; 1.1%; >1-10 Hz; ± 0.8%, 11-99 Hz; ± 1.2%, 100 Hz; ± 0.75%, 101-920 Hz; ± 1.0%, 921-5000 Hz; ± 1.4%, 5001-10,000 Hz; ± 1.9%, 10,001-15,000 Hz; ± 2.2%, 15,001-20,000 Hz; ± 2.8%.
Phase uncertainty: 0.5-10 Hz; 1.0°, 11-99 Hz; 1.5°, 100-4999 Hz; 1.3°, 5000-20,000 Hz; 2.8°

Unit Condition

As Found: In Tolerance
As Left: In Tolerance

Lab Conditions

Temperature: 71 (22) °F (°C)
Humidity: 44 %

Customer

Wise/Daniele Storni

Cal Date: 23-Mar-23
Due Date:

Technician Notes

Approval Information

Technician: Tyler Stratman
Approval: *[Signature]*

10310 Aerohub Boulevard
Cincinnati, OH 45215
Ph: 513.351.9919
www.modalshop.com



Cal ID: 59437

~Calibration Certificate~

Sensor Information

Model Number: 393B12
Serial Number: 68776
Manufacturer: PCB

Description: ICP® Accelerometer

Calibration Data

Sensitivity @ 100 Hz: 10,771 mV/g
1,098 mV/m/s²
Phase @ 100 Hz: -0.97 deg.
Test Level: 0.30 g

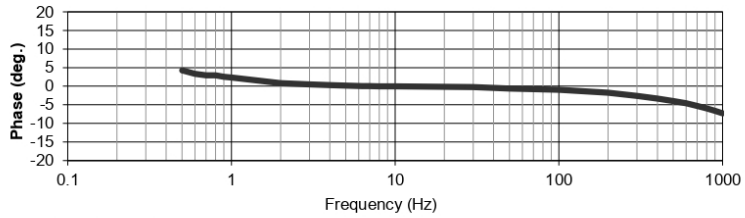
Transducer Specifications

Amp. Range: ± 0.5 g
Resolution: 0.000008 g
Resonant Freq: ≥ 10000 Hz
Temp. Range: -46 to 82 °C
-50 to 180 °F
Axis: Uni-Axial

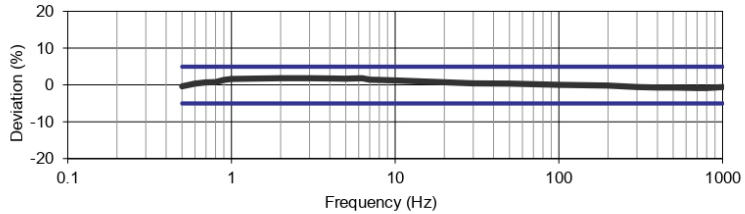
Data Table

Freq. (Hz)	Deviation (%)	Phase (deg)
0.5	-0.3769	4.2997
1	1.6200	2.3200
2	1.8192	0.8241
3	1.8494	0.4925
4	1.7289	0.2692
5	1.7019	0.1679
6.3	1.7896	0.0554
7	1.4269	0.0329
8	1.3386	-0.0269
10	1.2067	-0.0642
30	0.4469	-0.2551
50	0.3635	-0.6025
100	0.0000	-0.9670
200	-0.2088	-1.7539
300	-0.5670	-2.6236
400	-0.6940	-3.3196
500	-0.6992	-3.9828
600	-0.7667	-4.6123
700	-0.8138	-5.2887
800	-0.8255	-5.9523
900	-0.7409	-6.6394
1000	-0.5789	-7.2821

Phase Response



Amplitude Response



Notes

Results relate only to the items calibrated.
This certificate may not be reproduced except in full, without written permission.
Method: Back-to-Back Comparison Calibration per ISO 16063 Part 21.
This calibration was performed with TMS 9155 Calibration Workstation 2 version 7.0.2.
Proficiency in calibration traceable to PTB (17014/17004) and NIST (683/287323).
Back-to-Back Comparison Calibration per ISO 16063-21
Procedure Used: PRD-P220 or PRD-P239
Measurement uncertainty (95% confidence level with coverage factor 2) for frequency ranges tested during calibration are as follows: 0.5-1 Hz; 1.1%; >1-10 Hz; ± 0.8%, 11-99 Hz; ± 1.2%, 100 Hz; ± 0.75%, 101-920 Hz; ± 1.0%, 921-5000 Hz; ± 1.4%, 5001-10,000 Hz; ± 1.9%, 10,001-15,000 Hz; ± 2.2%, 15,001-20,000 Hz; ± 2.8%.
Phase uncertainty: 0.5-10 Hz; 1.0°, 11-99 Hz; 1.5°, 100-4999 Hz; 1.3°, 5000-20,000 Hz; 2.8°

Unit Condition

As Found: In Tolerance
As Left: In Tolerance

Lab Conditions

Temperature: 74 (23) °F (°C)
Humidity: 25 %

Customer

Wise/Daniele Storni

Cal Date: 21-Mar-23
Due Date:

Technician Notes

Approval Information

Technician: Tyler Stratman
Approval: *[Signature]*

10310 Aerohub Boulevard
Cincinnati, OH 45215
Ph: 513.351.9919
www.modalshop.com



Cal ID: 59398

~Calibration Certificate~

Sensor Information

Model Number: 393B12
Serial Number: 68955
Manufacturer: PCB

Description: ICP® Accelerometer

Calibration Data

Sensitivity @ 100 Hz: 10,243 mV/g
1,044 mV/m/s²
Phase @ 100 Hz: -1.01 deg.
Test Level: 0.30 g

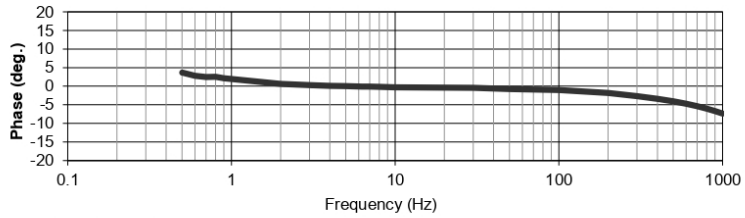
Transducer Specifications

Amp. Range: ± 0.5 g
Resolution: 0.000008 g
Resonant Freq: ≥ 10000 Hz
Temp. Range: -46 to 82 °C
-50 to 180 °F
Axis: Uni-Axial

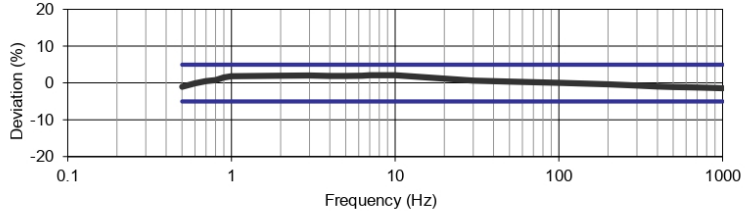
Data Table

Freq. (Hz)	Deviation (%)	Phase (deg)
0.5	-1.0152	3.6906
1	1.8213	1.9416
2	1.9562	0.6199
3	2.0227	0.3176
4	1.9149	0.1248
5	1.8886	0.0227
6.3	1.9686	-0.0802
7	2.1054	-0.1177
8	2.1238	-0.1639
10	2.1170	-0.2764
30	0.5984	-0.4474
50	0.3791	-0.7533
100	0.0000	-1.0057
200	-0.3836	-1.8392
300	-0.6957	-2.6857
400	-0.9926	-3.3720
500	-1.1224	-4.0533
600	-1.1592	-4.7220
700	-1.2177	-5.3921
800	-1.2812	-6.0238
900	-1.3561	-6.6799
1000	-1.3856	-7.3329

Phase Response



Amplitude Response



Notes

Results relate only to the items calibrated.
This certificate may not be reproduced except in full, without written permission.
Method: Back-to-Back Comparison Calibration per ISO 16063 Part 21.
This calibration was performed with TMS 9155 Calibration Workstation 2 version 7.0.2.
Proficiency in calibration traceable to PTB (17014/17004) and NIST (683/287323).
Back-to-Back Comparison Calibration per ISO 16063-21
Procedure Used: PRD-P220 or PRD-P239
Measurement uncertainty (95% confidence level with coverage factor 2) for frequency ranges tested during calibration are as follows: 0.5-1 Hz; 1.1%; >1-10 Hz; ± 0.8%, 11-99 Hz; ± 1.2%, 100 Hz; ± 0.75%, 101-920 Hz; ± 1.0%, 921-5000 Hz; ± 1.4%, 5001-10,000 Hz; ± 1.9%, 10,001-15,000 Hz; ± 2.2%, 15,001-20,000 Hz; ± 2.8%.
Phase uncertainty: 0.5-10 Hz; 1.0°, 11-99 Hz; 1.5°, 100-4999 Hz; 1.3°, 5000-20,000 Hz; 2.8°

Unit Condition

As Found: In Tolerance
As Left: In Tolerance

Lab Conditions

Temperature: 74 (24) °F (°C)
Humidity: 24 %

Customer

Wise/Daniele Storni

Cal Date: 21-Mar-23
Due Date:

Technician Notes

Approval Information

Technician: Tyler Stratman
Approval: *[Signature]*

10310 Aerohub Boulevard
Cincinnati, OH 45215
Ph: 513.351.9919
www.modalshop.com



Cal ID: 59396

~Calibration Certificate~

Sensor Information

Model Number: 393B12
Serial Number: 70262
Manufacturer: PCB

Description: ICP® Accelerometer

Calibration Data

Sensitivity @ 100 Hz: 10,373 mV/g
1,058 mV/m/s²
Phase @ 100 Hz: -0.92 deg.
Test Level: 0.30 g

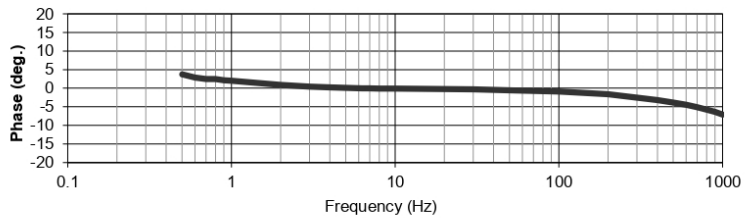
Transducer Specifications

Amp. Range: ± 0.5 g
Resolution: 0.000008 g
Resonant Freq: ≥ 10000 Hz
Temp. Range: -46 to 82 °C
-50 to 180 °F
Axis: Uni-Axial

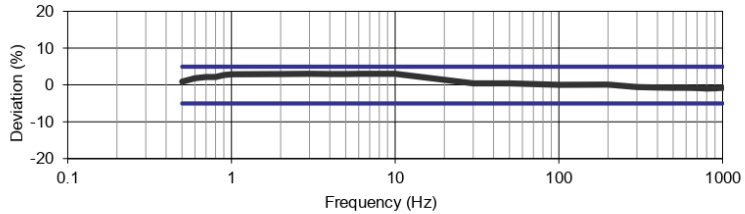
Data Table

Freq. (Hz)	Deviation (%)	Phase (deg)
0.5	0.8908	3.7764
1	2.8678	1.9965
2	2.9523	0.8580
3	3.0572	0.4444
4	2.9379	0.1963
5	2.9620	0.0745
6.3	3.0463	-0.0337
7	3.0171	-0.0610
8	2.9953	-0.1130
10	3.0285	-0.1320
30	0.3984	-0.2810
50	0.3985	-0.5965
100	0.0000	-0.9192
200	0.0809	-1.6057
300	-0.5526	-2.5213
400	-0.6874	-3.1729
500	-0.7658	-3.8310
600	-0.7602	-4.4440
700	-0.8647	-5.0980
800	-0.9334	-5.7545
900	-0.8861	-6.3662
1000	-0.7695	-7.0327

Phase Response



Amplitude Response



Notes

Results relate only to the items calibrated.
This certificate may not be reproduced except in full, without written permission.
Method: Back-to-Back Comparison Calibration per ISO 16063 Part 21.
This calibration was performed with TMS 9155 Calibration Workstation 2 version 7.0.2.
Proficiency in calibration traceable to PTB (17014/17004) and NIST (683/287323).
Back-to-Back Comparison Calibration per ISO 16063-21
Procedure Used: PRD-P220 or PRD-P239
Measurement uncertainty (95% confidence level with coverage factor 2) for frequency ranges tested during calibration are as follows: 0.5-1 Hz; 1.1%; >1-10 Hz; ± 0.8%, 11-99 Hz; ± 1.2%, 100 Hz; ± 0.75%, 101-920 Hz; ± 1.0%, 921-5000 Hz; ± 1.4%, 5001-10,000 Hz; ± 1.9%, 10,001-15,000 Hz; ± 2.2%, 15,001-20,000 Hz; ± 2.8%.
Phase uncertainty: 0.5-10 Hz; 1.0°, 11-99 Hz; 1.5°, 100-4999 Hz; 1.3°, 5000-20,000 Hz; 2.8°

Unit Condition

As Found: In Tolerance
As Left: In Tolerance

Lab Conditions

Temperature: 70 (21) °F (°C)
Humidity: 50 %

Customer

Wise/Daniele Storni

Cal Date: 24-Mar-23
Due Date:

Technician Notes

Approval Information

Technician: Tyler Stratman
Approval: *[Signature]*

10310 Aerohub Boulevard
Cincinnati, OH 45215
Ph: 513.351.9919
www.modalshop.com



Cal ID: 59462

~Calibration Certificate~

Sensor Information

Model Number: 393B12
Serial Number: 70263
Manufacturer: PCB

Description: ICP® Accelerometer

Calibration Data

Sensitivity @ 100 Hz: 10,613 mV/g
1,082 mV/m/s²
Phase @ 100 Hz: -0.99 deg.
Test Level: 0.30 g

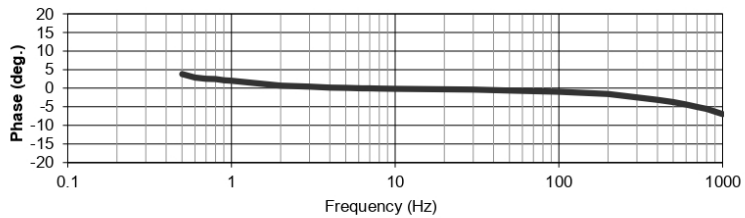
Transducer Specifications

Amp. Range: ± 0.5 g
Resolution: 0.000008 g
Resonant Freq: ≥ 10000 Hz
Temp. Range: -46 to 82 °C
-50 to 180 °F
Axis: Uni-Axial

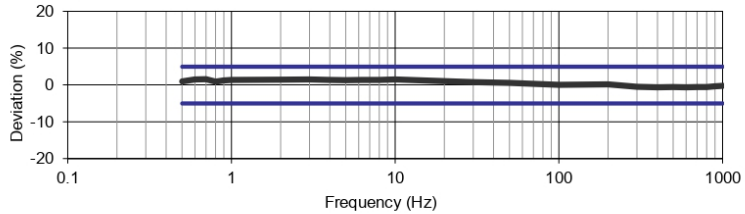
Data Table

Freq. (Hz)	Deviation (%)	Phase (deg)
0.5	0.9721	3.8348
1	1.3367	1.9824
2	1.4155	0.6876
3	1.4576	0.3956
4	1.3338	0.1870
5	1.2823	0.0859
6.3	1.3472	-0.0086
7	1.3440	-0.0319
8	1.3699	-0.0872
10	1.5045	-0.1721
30	0.7872	-0.3831
50	0.5323	-0.6327
100	0.0000	-0.9934
200	0.1626	-1.5424
300	-0.5332	-2.4837
400	-0.6110	-3.1333
500	-0.6001	-3.7480
600	-0.6212	-4.4186
700	-0.5843	-5.0412
800	-0.5723	-5.5914
900	-0.3858	-6.2708
1000	-0.2191	-6.9150

Phase Response



Amplitude Response



Notes

Results relate only to the items calibrated.
This certificate may not be reproduced except in full, without written permission.
Method: Back-to-Back Comparison Calibration per ISO 16063 Part 21.
This calibration was performed with TMS 9155 Calibration Workstation 2 version 7.0.2.
Proficiency in calibration traceable to PTB (17014/17004) and NIST (683/287323).
Back-to-Back Comparison Calibration per ISO 16063-21
Procedure Used: PRD-P220 or PRD-P239
Measurement uncertainty (95% confidence level with coverage factor 2) for frequency ranges tested during calibration are as follows: 0.5-1 Hz; 1.1%; >1-10 Hz; ± 0.8%, 11-99 Hz; ± 1.2%, 100 Hz; ± 0.75%, 101-920 Hz; ± 1.0%, 921-5000 Hz; ± 1.4%, 5001-10,000 Hz; ± 1.9%, 10,001-15,000 Hz; ± 2.2%, 15,001-20,000 Hz; ± 2.8%.
Phase uncertainty: 0.5-10 Hz; 1.0°, 11-99 Hz; 1.5°, 100-4999 Hz; 1.3°, 5000-20,000 Hz; 2.8°

Unit Condition

As Found: In Tolerance
As Left: In Tolerance

Lab Conditions

Temperature: 73 (23) °F (°C)
Humidity: 25 %

Customer

Wise/Daniele Storni

Cal Date: 21-Mar-23
Due Date:

Technician Notes

Approval Information

Technician: Tyler Stratman
Approval: *[Signature]*

10310 Aerohub Boulevard
Cincinnati, OH 45215
Ph: 513.351.9919
www.modalshop.com



Cal ID: 59394

~Calibration Certificate~

Sensor Information

Model Number: 393B12
Serial Number: 70918
Manufacturer: PCB

Description: ICP® Accelerometer

Calibration Data

Sensitivity @ 100 Hz: 10,536 mV/g
1,074 mV/m/s²
Phase @ 100 Hz: -0.96 deg.
Test Level: 0.30 g

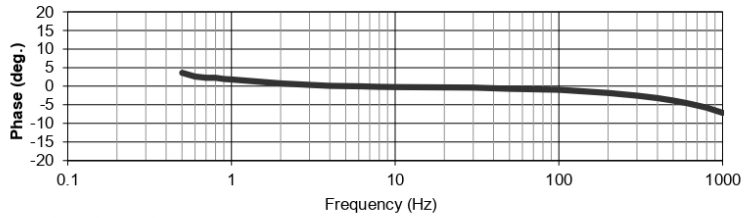
Transducer Specifications

Amp. Range: ± 0.5 g
Resolution: 0.000008 g
Resonant Freq: ≥ 10000 Hz
Temp. Range: -46 to 82 °C
-50 to 180 °F
Axis: Uni-Axial

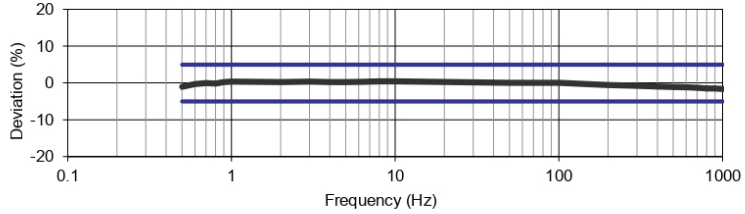
Data Table

Freq. (Hz)	Deviation (%)	Phase (deg)
0.5	-1.0360	3.6161
1	0.3435	1.7909
2	0.2508	0.7327
3	0.3403	0.3666
4	0.2529	0.1222
5	0.2084	0.0275
6.3	0.2912	-0.0649
7	0.3575	-0.1119
8	0.3985	-0.1737
10	0.4364	-0.2232
30	0.1745	-0.3435
50	0.0064	-0.6927
100	0.0000	-0.9632
200	-0.5506	-1.8420
300	-0.7918	-2.5652
400	-1.0042	-3.2321
500	-1.1333	-3.8816
600	-1.1568	-4.5192
700	-1.3188	-5.1983
800	-1.4755	-5.7843
900	-1.4934	-6.4684
1000	-1.5884	-7.1520

Phase Response



Amplitude Response



Notes

Results relate only to the items calibrated.
This certificate may not be reproduced except in full, without written permission.
Method: Back-to-Back Comparison Calibration per ISO 16063 Part 21.
This calibration was performed with TMS 9155 Calibration Workstation 2 version 7.0.2.
Proficiency in calibration traceable to PTB (17014/17004) and NIST (683/287323).
Back-to-Back Comparison Calibration per ISO 16063-21
Procedure Used: PRD-P220 or PRD-P239
Measurement uncertainty (95% confidence level with coverage factor 2) for frequency ranges tested during calibration are as follows: 0.5-1 Hz; 1.1%; >1-10 Hz; ± 0.8%, 11-99 Hz; ± 1.2%, 100 Hz; ± 0.75%, 101-920 Hz; ± 1.0%, 921-5000 Hz; ± 1.4%, 5001-10,000 Hz; ± 1.9%, 10,001-15,000 Hz; ± 2.2%, 15,001-20,000 Hz; ± 2.8%.
Phase uncertainty: 0.5-10 Hz; 1.0°, 11-99 Hz; 1.5°, 100-4999 Hz; 1.3°, 5000-20,000 Hz; 2.8°

Unit Condition

As Found: In Tolerance
As Left: In Tolerance

Lab Conditions

Temperature: 71 (21) °F (°C)
Humidity: 35 %

Customer

Wise/Daniele Storni

Cal Date: 22-Mar-23
Due Date:

Technician Notes

Approval Information

Technician: Tyler Stratman
Approval: *[Signature]*

10310 Aerohub Boulevard
Cincinnati, OH 45215
Ph: 513.351.9919
www.modalshop.com



Cal ID: 59421

~Calibration Certificate~

Sensor Information

Model Number: 393B12
Serial Number: 71118
Manufacturer: PCB

Description: ICP® Accelerometer

Calibration Data

Sensitivity @ 100 Hz: 10,090 mV/g
1,029 mV/m/s²
Phase @ 100 Hz: -0.91 deg.
Test Level: 0.30 g

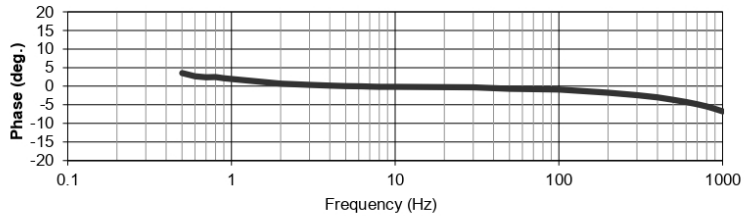
Transducer Specifications

Amp. Range: ± 0.5 g
Resolution: 0.000008 g
Resonant Freq: ≥ 10000 Hz
Temp. Range: -46 to 82 °C
-50 to 180 °F
Axis: Uni-Axial

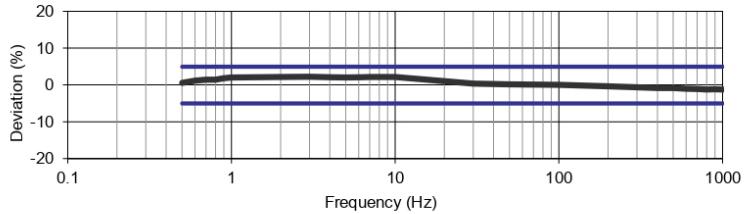
Data Table

Freq. (Hz)	Deviation (%)	Phase (deg)
0.5	0.5310	3.5610
1	2.0066	1.9394
2	2.1712	0.6644
3	2.2242	0.3547
4	2.1027	0.1519
5	2.0482	0.0486
6.3	2.0813	-0.0609
7	2.1296	-0.0840
8	2.1501	-0.1503
10	2.1601	-0.1926
30	0.3242	-0.2946
50	0.1268	-0.6803
100	0.0000	-0.9058
200	-0.3980	-1.7207
300	-0.6164	-2.3821
400	-0.8560	-3.0370
500	-0.8624	-3.6480
600	-1.0350	-4.2812
700	-1.0994	-4.8676
800	-1.2194	-5.4545
900	-1.1991	-6.1010
1000	-1.2235	-6.7137

Phase Response



Amplitude Response



Notes

Results relate only to the items calibrated.
This certificate may not be reproduced except in full, without written permission.
Method: Back-to-Back Comparison Calibration per ISO 16063 Part 21.
This calibration was performed with TMS 9155 Calibration Workstation 2 version 7.0.2.
Proficiency in calibration traceable to PTB (17014/17004) and NIST (683/287323).
Back-to-Back Comparison Calibration per ISO 16063-21
Procedure Used: PRD-P220 or PRD-P239
Measurement uncertainty (95% confidence level with coverage factor 2) for frequency ranges tested during calibration are as follows: 0.5-1 Hz; 1.1%; >1-10 Hz; ± 0.8%, 11-99 Hz; ± 1.2%, 100 Hz; ± 0.75%, 101-920 Hz; ± 1.0%, 921-5000 Hz; ± 1.4%, 5001-10,000 Hz; ± 1.9%, 10,001-15,000 Hz; ± 2.2%, 15,001-20,000 Hz; ± 2.8%.
Phase uncertainty: 0.5-10 Hz; 1.0°, 11-99 Hz; 1.5°, 100-4999 Hz; 1.3°, 5000-20,000 Hz; 2.8°

Unit Condition

As Found: In Tolerance
As Left: In Tolerance

Lab Conditions

Temperature: 72 (22) °F (°C)
Humidity: 26 %

Customer

Wise/Daniele Storni

Cal Date: 21-Mar-23
Due Date:

Technician Notes

Approval Information

Technician: Tyler Stratman
Approval: *[Signature]*

10310 Aerohub Boulevard
Cincinnati, OH 45215
Ph: 513.351.9919
www.modalshop.com



2649.01
Calibration Laboratory

Cal ID: 59407

~Calibration Certificate~

Sensor Information

Model Number: 393B12
Serial Number: 71119
Manufacturer: PCB

Description: ICP® Accelerometer

Calibration Data

Sensitivity @ 100 Hz: 10,312 mV/g
1,052 mV/m/s²
Phase @ 100 Hz: -1.02 deg.
Test Level: 0.30 g

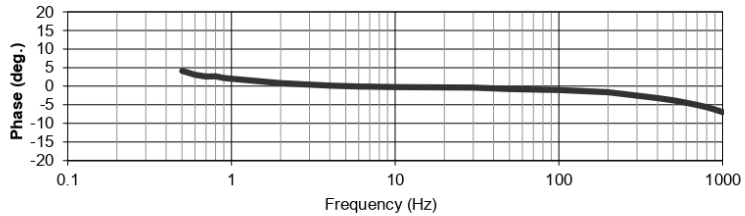
Transducer Specifications

Amp. Range: ± 0.5 g
Resolution: 0.000008 g
Resonant Freq: ≥ 10000 Hz
Temp. Range: -46 to 82 °C
-50 to 180 °F
Axis: Uni-Axial

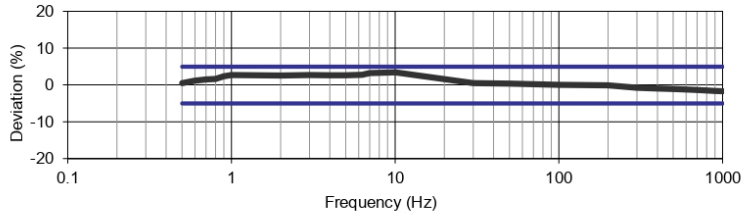
Data Table

Freq. (Hz)	Deviation (%)	Phase (deg)
0.5	0.4617	4.1757
1	2.6565	1.9987
2	2.5870	0.8168
3	2.6977	0.3922
4	2.6335	0.1469
5	2.5953	0.0196
6.3	2.7246	-0.0832
7	3.1989	-0.1224
8	3.3103	-0.1684
10	3.4516	-0.2361
30	0.5143	-0.3465
50	0.3776	-0.7361
100	0.0000	-1.0223
200	-0.1110	-1.6412
300	-0.7640	-2.5479
400	-1.0005	-3.1753
500	-1.1374	-3.8222
600	-1.2717	-4.4567
700	-1.3766	-5.0591
800	-1.5372	-5.6567
900	-1.6170	-6.2926
1000	-1.6780	-6.9021

Phase Response



Amplitude Response



Notes

Results relate only to the items calibrated.
This certificate may not be reproduced except in full, without written permission.
Method: Back-to-Back Comparison Calibration per ISO 16063 Part 21.
This calibration was performed with TMS 9155 Calibration Workstation 2 version 7.0.2.
Proficiency in calibration traceable to PTB (17014/17004) and NIST (683/287323).
Back-to-Back Comparison Calibration per ISO 16063-21
Procedure Used: PRD-P220 or PRD-P239
Measurement uncertainty (95% confidence level with coverage factor 2) for frequency ranges tested during calibration are as follows: 0.5-1 Hz; 1.1%; >1-10 Hz; ± 0.8%, 11-99 Hz; ± 1.2%, 100 Hz; ± 0.75%, 101-920 Hz; ± 1.0%, 921-5000 Hz; ± 1.4%, 5001-10,000 Hz; ± 1.9%, 10,001-15,000 Hz; ± 2.2%, 15,001-20,000 Hz; ± 2.8%.
Phase uncertainty: 0.5-10 Hz; 1.0°, 11-99 Hz; 1.5°, 100-4999 Hz; 1.3°, 5000-20,000 Hz; 2.8°

Unit Condition

As Found: In Tolerance
As Left: In Tolerance

Lab Conditions

Temperature: 71 (22) °F (°C)
Humidity: 45 %

Customer

Wise-Daniele Storni

Cal Date: 24-Mar-23
Due Date:

Technician Notes

Approval Information

Technician: Tyler Stratman
Approval: *[Signature]*

10310 Aerohub Boulevard
Cincinnati, OH 45215
Ph: 513.351.9919
www.modalshop.com



Cal ID: 59460

~Calibration Certificate~

Sensor Information

Model Number: 393B12
Serial Number: 71200
Manufacturer: PCB

Description: ICP® Accelerometer

Calibration Data

Sensitivity @ 100 Hz: 10,109 mV/g
1,031 mV/m/s²
Phase @ 100 Hz: -0.94 deg.
Test Level: 0.30 g

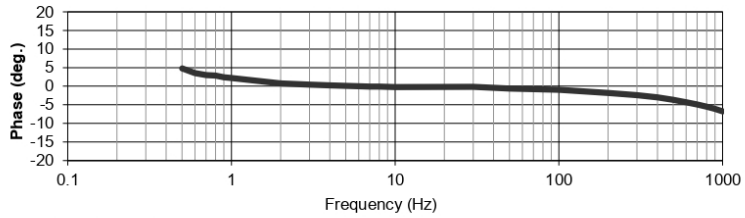
Transducer Specifications

Amp. Range: ± 0.5 g
Resolution: 0.000008 g
Resonant Freq: ≥ 10000 Hz
Temp. Range: -46 to 82 °C
-50 to 180 °F
Axis: Uni-Axial

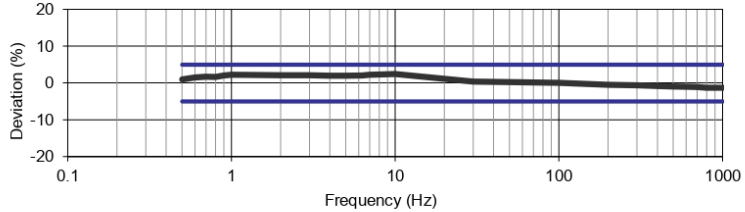
Data Table

Freq. (Hz)	Deviation (%)	Phase (deg)
0.5	0.9243	4.8258
1	2.1955	2.1865
2	2.0740	0.7660
3	2.0949	0.4365
4	1.9851	0.1928
5	1.9396	0.1001
6.3	2.0153	-0.0264
7	2.2178	-0.0745
8	2.2985	-0.1281
10	2.4481	-0.2332
30	0.3627	-0.2011
50	0.1904	-0.6343
100	0.0000	-0.9401
200	-0.5095	-1.8250
300	-0.6203	-2.4186
400	-0.8535	-3.0271
500	-0.9553	-3.6577
600	-1.0442	-4.3102
700	-1.1217	-4.8882
800	-1.3026	-5.5330
900	-1.2944	-6.1190
1000	-1.3095	-6.7356

Phase Response



Amplitude Response



Notes

Results relate only to the items calibrated.
This certificate may not be reproduced except in full, without written permission.
Method: Back-to-Back Comparison Calibration per ISO 16063 Part 21.
This calibration was performed with TMS 9155 Calibration Workstation 2 version 7.0.2.
Proficiency in calibration traceable to PTB (17014/17004) and NIST (683/287323).
Back-to-Back Comparison Calibration per ISO 16063-21
Procedure Used: PRD-P220 or PRD-P239
Measurement uncertainty (95% confidence level with coverage factor 2) for frequency ranges tested during calibration are as follows: 0.5-1 Hz; 1.1%; >1-10 Hz; ± 0.8%, 11-99 Hz; ± 1.2%, 100 Hz; ± 0.75%, 101-920 Hz; ± 1.0%, 921-5000 Hz; ± 1.4%, 5001-10,000 Hz; ± 1.9%, 10,001-15,000 Hz; ± 2.2%, 15,001-20,000 Hz; ± 2.8%.
Phase uncertainty: 0.5-10 Hz; 1.0°, 11-99 Hz; 1.5°, 100-4999 Hz; 1.3°, 5000-20,000 Hz; 2.8°

Unit Condition

As Found: In Tolerance
As Left: In Tolerance

Lab Conditions

Temperature: 72 (22) °F (°C)
Humidity: 26 %

Customer

Wise/Daniele Storni

Cal Date: 21-Mar-23
Due Date:

Technician Notes

Approval Information

Technician: Tyler Stratman
Approval: *[Signature]*

10310 Aerohub Boulevard
Cincinnati, OH 45215
Ph: 513.351.9919
www.modalshop.com



Cal ID: 59405

~Calibration Certificate~

Sensor Information

Model Number: 393B12
Serial Number: 71201
Manufacturer: PCB

Description: ICP® Accelerometer

Calibration Data

Sensitivity @ 100 Hz: 9,685 mV/g
987.5 mV/m/s²
Phase @ 100 Hz: -0.84 deg.
Test Level: 0.30 g

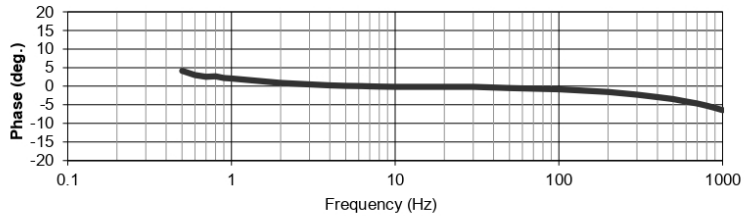
Transducer Specifications

Amp. Range: ± 0.5 g
Resolution: 0.000008 g
Resonant Freq: ≥ 10000 Hz
Temp. Range: -46 to 82 °C
-50 to 180 °F
Axis: Uni-Axial

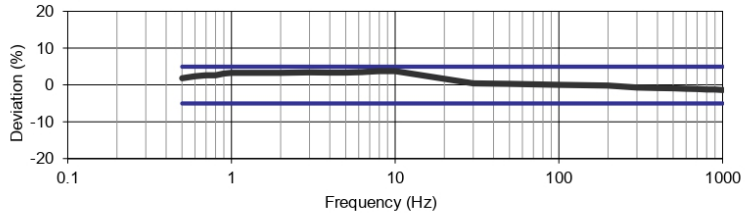
Data Table

Freq. (Hz)	Deviation (%)	Phase (deg)
0.5	1.7898	4.1295
1	3.3166	2.0374
2	3.2655	0.9113
3	3.4185	0.5016
4	3.3690	0.2346
5	3.3274	0.1159
6.3	3.4615	0.0054
7	3.6440	-0.0260
8	3.7241	-0.0834
10	3.7724	-0.1422
30	0.4498	-0.1969
50	0.3102	-0.5201
100	0.0000	-0.8417
200	-0.1994	-1.5543
300	-0.6813	-2.2659
400	-0.8263	-2.9201
500	-0.9202	-3.4813
600	-1.0715	-4.1128
700	-1.1264	-4.6826
800	-1.2415	-5.2708
900	-1.2555	-5.8530
1000	-1.3392	-6.4090

Phase Response



Amplitude Response



Notes

Results relate only to the items calibrated.
This certificate may not be reproduced except in full, without written permission.
Method: Back-to-Back Comparison Calibration per ISO 16063 Part 21.
This calibration was performed with TMS 9155 Calibration Workstation 2 version 7.0.2.
Proficiency in calibration traceable to PTB (17014/17004) and NIST (683/287323).
Back-to-Back Comparison Calibration per ISO 16063-21
Procedure Used: PRD-P220 or PRD-P239
Measurement uncertainty (95% confidence level with coverage factor 2) for frequency ranges tested during calibration are as follows: 0.5-1 Hz; 1.1%; >1-10 Hz; ± 0.8%, 11-99 Hz; ± 1.2%, 100 Hz; ± 0.75%, 101-920 Hz; ± 1.0%, 921-5000 Hz; ± 1.4%, 5001-10,000 Hz; ± 1.9%, 10,001-15,000 Hz; ± 2.2%, 15,001-20,000 Hz; ± 2.8%.
Phase uncertainty: 0.5-10 Hz; 1.0°, 11-99 Hz; 1.5°, 100-4999 Hz; 1.3°, 5000-20,000 Hz; 2.8°

Unit Condition

As Found: In Tolerance
As Left: In Tolerance

Lab Conditions

Temperature: 71 (22) °F (°C)
Humidity: 48 %

Customer

Wise/Daniele Storni

Cal Date: 24-Mar-23
Due Date:

Technician Notes

Approval Information

Technician: Tyler Stratman
Approval: *[Signature]*

10310 Aerohub Boulevard
Cincinnati, OH 45215
Ph: 513.351.9919
www.modalshop.com



Cal ID: 59461

~Calibration Certificate~

Sensor Information

Model Number: 393B12
Serial Number: 71203
Manufacturer: PCB

Description: ICP® Accelerometer

Calibration Data

Sensitivity @ 100 Hz: 10,186 mV/g
1,039 mV/m/s²
Phase @ 100 Hz: -1.00 deg.
Test Level: 0.30 g

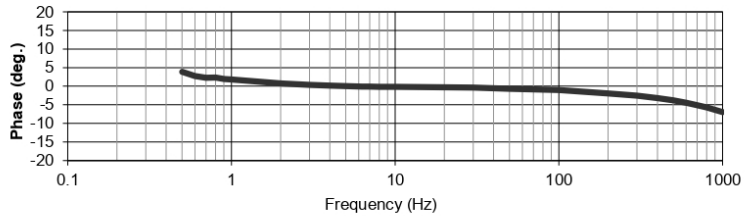
Transducer Specifications

Amp. Range: ± 0.5 g
Resolution: 0.000008 g
Resonant Freq: ≥ 10000 Hz
Temp. Range: -46 to 82 °C
-50 to 180 °F
Axis: Uni-Axial

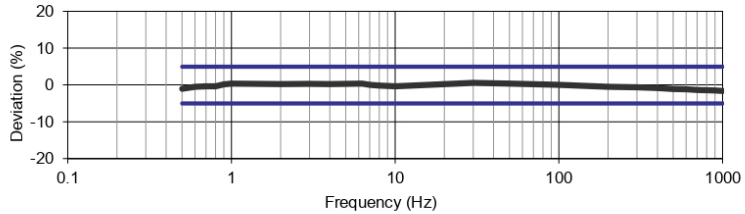
Data Table

Freq. (Hz)	Deviation (%)	Phase (deg)
0.5	-1.0124	3.8829
1	0.3635	1.7922
2	0.2219	0.7498
3	0.3169	0.3476
4	0.2547	0.1294
5	0.2670	0.0190
6.3	0.3632	-0.0852
7	-0.0080	-0.1061
8	-0.1465	-0.1610
10	-0.4063	-0.1525
30	0.5801	-0.3655
50	0.3743	-0.6732
100	0.0000	-0.9994
200	-0.5266	-1.9233
300	-0.6479	-2.5707
400	-0.8240	-3.2235
500	-1.1139	-3.8203
600	-1.1711	-4.4408
700	-1.3536	-5.0935
800	-1.4351	-5.6948
900	-1.5218	-6.3598
1000	-1.5954	-6.9594

Phase Response



Amplitude Response



Notes

Results relate only to the items calibrated.
This certificate may not be reproduced except in full, without written permission.
Method: Back-to-Back Comparison Calibration per ISO 16063 Part 21.
This calibration was performed with TMS 9155 Calibration Workstation 2 version 7.0.2.
Proficiency in calibration traceable to PTB (17014/17004) and NIST (683/287323).
Back-to-Back Comparison Calibration per ISO 16063-21
Procedure Used: PRD-P220 or PRD-P239
Measurement uncertainty (95% confidence level with coverage factor 2) for frequency ranges tested during calibration are as follows: 0.5-1 Hz; 1.1%; >1-10 Hz; ± 0.8%, 11-99 Hz; ± 1.2%, 100 Hz; ± 0.75%, 101-920 Hz; ± 1.0%, 921-5000 Hz; ± 1.4%, 5001-10,000 Hz; ± 1.9%, 10,001-15,000 Hz; ± 2.2%, 15,001-20,000 Hz; ± 2.8%.
Phase uncertainty: 0.5-10 Hz; 1.0°, 11-99 Hz; 1.5°, 100-4999 Hz; 1.3°, 5000-20,000 Hz; 2.8°

Unit Condition

As Found: In Tolerance
As Left: In Tolerance

Lab Conditions

Temperature: 72 (22) °F (°C)
Humidity: 34 %

Customer

Wise/Daniele Storni

Cal Date: 22-Mar-23
Due Date:

Technician Notes

Approval Information

Technician: Tyler Stratman
Approval: *[Signature]*

10310 Aerohub Boulevard
Cincinnati, OH 45215
Ph: 513.351.9919
www.modalshop.com



Cal ID: 59416

